Preparation of Microcellular Injection Molded Foams with High Performance

By

Minghui Wu, BEng.

A thesis submitted to the University of Nottingham Ningbo China

for the degree of Doctor of Philosophy

April 2024

Abstract

Microcellular plastic foams are applied in a wide range of applications due to their enhanced toughness, good sound insulation properties and electrical properties. It is well known that cell structure would strongly influence the properties of polymer foams. However, there are still fewer studies related to the effect of cell size on the properties of polymer foams under a constant void fraction (VF). To achieve foams with high performance, the effect of cell structure on the impact strength, electrical properties and sound insulation properties was studied systematically in this research.

(a) Effect of cell structure on impact strength:

First, the cell structure and impact strength of poly(lactic acid)/poly(butylene adipate-co-terephthalate) (PLA/PBAT) blend foams under different content of compatibilizer were compared. The obtained PLA blend foams displayed a super high impact strength of 49.1 kJ/m^2, 9.3 and 6.4 times that of the unmodified PLA/PBAT blend and its corresponding foam, respectively. It proved that enhancing interfacial adhesion and reducing cell size could improve the impact strength of PLA/PBAT foams.

Then, to explore the relationship between cell size and impact toughness, PLA/PBAT foams with different cell sizes but a constant VF were prepared. When the cell size was smaller than a critical value, the foam would be tough; when the cell size was greater than the critical value, the foam would be brittle. In other words, there was a brittle-tough transition at the critical cell size. For foams with cell sizes

below the critical value, the proximity of the cells facilitated a robust interaction of stress fields generated by adjacent cells, coupled with the beneficial role of rubber particles in hindering the progression of cell-induced crazes to cracks, absorbing significant energy. For foams with cell sizes above the critical value, however, the cell-induced crazes could directly develop into cracks due to the negligible interaction, leading to a low impact strength.

Finally, the combined effects of the PLA crystallinity and cell size on the impact strength of PLA/PBAT foams were studied. The PLA crystallinity was tailored by carbon dioxide (CO_2) treatment and cell size was well controlled by changing processing parameters. As expected, the brittle-tough transition can be found by reducing cell size regardless of the degree of PLA crystallinity. When the cell size was above 12 μm, the impact strength was almost unchanged by varying cell size, since those foams were all fractured through crazing. When cell size was below 12 μm, the impact strength was significantly enhanced by improving the PLA crystallinity due to the transformation of the fracture mechanism from multiple crazing to shear yielding.

(b) Effect of cell structure on electrical properties:

Polypropylene/carbon nanostructure (PP/CNS) nanocomposite foams with a fixed VF were produced using core-back foaming injection molding (FIM) technique, and their cell sizes were well-controlled by modifying the nitrogen (N_2) content. The results revealed that as the cell size increased from 71 to 317 μm, the EC and EMI shielding effectiveness (SE) increased from 1.43×10^{-3} to 5.07×10^{-3} S/cm and from 48.5 to 59.2 dB, respectively. The enhanced EC was attributed to the slightly aligned

CNS and the shorter actual conductive paths.

(c) Effect of cell structure on sound insulation properties:

PP/mica composite foams with different VFs and cell sizes were obtained using core-back FIM. The results showed that increasing the VF (the sample thickness increased but the sample density remained constant) could enhance the sound transmission loss (STL) from 16.8 dB for PP solid to 29.9 dB for PP foam with 75% VF. In addition, reducing the cell size and adding mica could also improve the STL due to the increase in reflection and scattering of sound waves in cells.

In summary, it has been demonstrated that polymer foams with high performance in terms of impact toughness, electrical properties and soundproofing properties can be achieved by tailoring cell size. This study provided a deeper understanding of the cell structure-properties relationship for polymer foams.

Achievements

Journal papers

1. **Minghui Wu**, Qian Ren, Xiuyu Zhu, Wanwan Li, Haibin Luo, Fei Wu, Long Wang*, Wenge Zheng, Pin Cui, Xiaosu Yi, Super toughened blends of poly(lactic acid) and poly(butylene adipate-co-terephthalate) injection-molded foams via enhancing interfacial compatibility and cellular structure, Int. J. Biol. Macromol. 245 (2023) 125490. https://doi.org/10.1016/j.ijbiomac.2023.125490
2. **Minghui Wu**, Qian Ren, Peng Gao, Wenyu Ma, Bin Shen*, Long Wang*, Wenge Zheng*, Pin Cui, Xiaosu Yi*, Enhanced electrical conductivity and EMI shielding performance through cell size-induced CNS alignment in PP/CNS foam, Compos. Commun. 43 (2023) 101716. https://doi.org/10.1016/j.coco.2023.101716
3. Long Wang*, **Minghui Wu**, Qian Ren, Zhengsheng Weng, Wanwan Li, Xiuyu Zhu, Wenge Zheng, Xiaosu Yi, Strong and high void fraction PP/CNS nanocomposite foams fabricated by core-back foam injection molding, J. Appl. Polym. Sci. 140(8) (2023) e53521. https://doi.org/10.1002/app.53521
4. **Minghui Wu**, Qian Ren, Xueyun Li, Peng Gao, Long Wang*, Wenge Zheng, Ping Cui, Xiaosu Yi, Wei Yang*, Supertough Polylactide Blend Foams with Controlled Cell Size, Macromolecules 57(21) (2024) 10432-10441. https://doi.org/10.1021/acs.macromol.4c02051
5. **Minghui Wu**, Qian Ren, Xueyun Li, Peng Gao, Long Wang*, Wenge Zheng, Ping Cui, Xiaosu Yi*, Toughened polylactide blend foams: Combined effects of cell size and matrix crystallization. (In preparation)

Acknowledgments

Firstly, I would like to thank my main supervisors, Prof. Xiaosu Yi, Prof. Pin Cui, Prof. Wenge Zheng, and Prof. Long Wang, who offered me the opportunity to study in the Advanced Composites Group of UNNC and Advanced Polymer Processing Group of Ningbo Institute of Materials Technology & Engineering, CAS. I take this opportunity to express my sincere appreciation for their invaluable guidance, suggestions, discussion, continuous encouragement and great care for author's studies and life.

Sincere gratitude is given to Prof. Bin Shen, Prof. Fei Wu, and Dr. Xiaoling Liu, for their helpful advice and discussions.

My sincere appreciation also goes to my colleagues and friends, Baohai Pan, Zhenwu Wang, Qian Ren, Penke Huang, Liyue Zhang, Zhao Liu, Lu Tong, Zhengshen Weng, etc., for their kind assistance in my studies and life. I also want to thank the members of staff, Jianming Guan, Yajin Fang, Saihua Li, Xin Wang, etc., who supported me through my research projects.

Most important of all, I express my deep gratitude to my parents and sisters for their understanding and encouragement.

Finally, the National Natural Science Foundation of China (52003280), Zhejiang Provincial Natural Science Foundation of China (LQ21B040003), the S&T Innovation 2025 Major Special Programme of Ningbo (2021Z052) and other funding bodies are all acknowledged for financial support to my PhD study.

Table of Contents

Abstract ..... **i**
Achievements ..... **iv**
Acknowledgments ..... **v**
Table of Contents ..... **vi**
List of Figures ..... **x**
List of Tables ..... **xvi**
List of Abbreviations ..... **xvii**
List of Symbols ..... **xx**
Chapter 1: Introduction **1**
1.1. Background 1
1.2. Aims and objectives 3
1.3. Thesis structure 4
1.4. References 6
Chapter 2: Literature review **8**
2.1. Foam-processing methods 8
2.1.1. Batch foaming 8
2.1.2. Extrusion foaming 10
2.1.3. FIM 11
2.1.4. Cell structure regulation in core-back FIM 13
2.2. Polymeric foam toughening technology 19
2.2.1. Blending 19
2.2.2. Adding inorganic fillers 23
2.2.3. Tailoring crystallization 25
2.2.4. Adjusting cell structure 26
2.3. Methods for improving EC of CPC foams 30
2.3.1. Polymer modification 31
2.3.2. Cell structure modification 32
2.4. Methods for improving sound insulation properties of polymer foams 36
2.4.1. Adding fillers 39
2.4.2. Adjusting cell structure 40
2.4.3. Multilayer structure design 41
2.5. Conclusions 46
2.6. References 46
Chapter 3: Super toughened blends of PLA and PBAT injection-molded foams via enhancing interfacial compatibility and cellular structure **55**
3.1. Abstract 56
3.2. Introduction 56

3.3. Experimental section 60
3.3.1. Materials 60
3.3.2. Blend preparation 60
3.3.3. Core-back FIM process 61
3.3.4. Fourier transform infrared spectrometry (FTIR) and ^{1}H nuclear magnetic resonance (NMR) 62
3.3.5. Gel permeation chromatography (GPC) 63
3.3.6. Extraction in chloroform 63
3.3.7. PLA/PBAT blend morphology analysis 63
3.3.8. Rheological behavior analysis 63
3.3.9. Foam morphology characterization 64
3.3.10. Thermal analysis 65
3.3.11. Mechanical test 65
3.4. Results and discussion 65
3.4.1. Reaction between PLA/PBAT and ADR 65
3.4.2. Phase morphology of PLA/PBAT blends 71
3.4.3. Rheology behavior of PLA/PBAT blends 73
3.4.4. Cellular structure of injection-molded foams 75
3.4.5. Crystallization behaviors 79
3.4.6. Tensile properties 80
3.4.7. Impact properties 82
3.5. Conclusion 90
3.6. References 91
Chapter 4: Cell structure and adhesion in polymer blend foams: Cell size-induced brittle-tough transition 97
4.1. Abstract 98
4.2. Introduction 99
4.3. Experimental section 102
4.3.1. Materials 102
4.3.2. Blend preparation 102
4.3.3. FIM with core-back operation 102
4.3.4. PLA/PBAT blend morphology analysis 104
4.3.5. Rheological behavior analysis 105
4.3.6. Foam characterization 105
4.3.7. Thermal analysis 106
4.3.8. Mechanical properties 107
4.4. Results and discussion 107
4.4.1. Phase morphology 107
4.4.2. Rheological behavior 109
4.4.3. Cellular structure 110
4.4.4. Thermal behavior 116
4.4.5. Impact strength 118
4.4.6. Discussion 122
4.5. Conclusion 126
4.6. References 127

Chapter 5: Toughened polylactide blend foams: Combined effects of cell size and matrix crystallization 131

5.1. Abstract 132

5.2. Introduction 132

5.3. Experimental section 135

5.3.1. Materials 135
5.3.2. Blend preparation 135
5.3.3. Core-back FIM process 136
5.3.4. CO_2 treatment 137
5.3.5. SEM 137
5.3.6. DSC 139
5.3.7. Wide-angle X-ray diffraction (WAXD) 139
5.3.8. Mechanical test 140

5.4. Results and discussion 141

5.4.1. Cell structure evolution during CO_2 treatment 141
5.4.2. Crystalline structure development during CO_2 treatment 143
5.4.3. Phase morphology changes during CO_2 treatment 145
5.4.4. Mechanical properties induced by PLA matrix crystallinity 147
5.4.5. Discussion 153

5.5. Conclusion 155

5.6. References 155

Chapter 6: Enhanced EC and EMI shielding performance through cell size-induced CNS alignment in PP/CNS foam 160

6.1. Abstract 161

6.2. Introduction 161

6.3. Experimental section 165

6.3.1. Materials 165
6.3.2. Sample preparation 165
6.3.3. Thermal analysis 168
6.3.4. Rheological analysis 168
6.3.5. SEM 168
6.3.6. Transmission electron microscope (TEM) 169
6.3.7. EC and EMI shielding performance measurement 170

6.4. Results and discussion 170

6.4.1. CNS dispersion in PP matrix 170
6.4.2. Cell structure 171
6.4.3. EC of PP/CNS foams 174
6.4.4. EMI shielding performance 179

6.5. Conclusion 183

6.6. References 183

Chapter 7: Enhanced sound insulation properties of PP/mica foams by controlling cell structure 190

7.1. Abstract 191

7.2. Introduction 191

7.3. Experimental section 193
7.3.1. Materials 193
7.3.2. Blend preparation 193
7.3.3. Core-back FIM 194
7.3.4. SEM 194
7.3.5. Dynamic mechanical analysis (DMA) 195
7.3.6. Characterization of sound insulation 195
7.4. Results and discussion 196
7.4.1. Mica dispersion in PP matrix 196
7.4.2. Cell structure 197
7.4.3. Sound insulation properties 202
7.5. Conclusion 206
7.6. References 206
Chapter 8: Conclusions and future work 211
8.1. Conclusions 211
8.2. Future work 213

List of Figures

Fig. 2-1. Schematic of pressure-induced batch foaming[3].....9

Fig. 2-2. Schematic of temperature-induced batch foaming[3].....10

Fig. 2-3. Schematic of tandem extrusion foaming[6].....11

Fig. 2-4. Schematic of FIM[6].....12

Fig. 2-5. Schematic of low-pressure FIM[11].....12

Fig. 2-6. Schematic of core-back FIM: (a) mold filling and the formation of gate-nucleated cells due to pressure drop over the gate; (b) full-shot; (c) collapse and dissolution of gate-nucleated nucleated cells, (d) complete disappearance of nucleated cells (formation of one-phase melt/gas solution); (e) nucleation of secondary cells due to the core-back (or mold-opening) operation; (f) cell growth. (The hatched area shows the formed skin layer).[15].....13

Fig. 2-7. (a) Open and (b) closed cell structure[16].....14

Fig. 2-8. The cell structure of the PEBA foams fabricated by core-back FIM using a same core-back distance but different gas concentrations: (a) 0.3 wt%, (b) 0.6 wt%, and (c) 0.8 wt%[12].....16

Fig. 2-9. The cellular morphology of the PEBA foams fabricated by core-back FIM using various packing pressures: (a) 15 MPa, (b) 20 MPa, and (c) 25 MPa[12].....16

Fig. 2-10. SEM micrographs of PP/NA foams fabricated at a foaming temperature of (a, a') 101 ℃, (b, b') 95 ℃, and (c, c') 90 ℃, respectively. (a–c), and (a'–c') are taken from the views parallel and perpendicular to the core-back direction, respectively[27].....17

Fig. 2-11. SEM micrographs of the cross-section of LCBPP foams in the core layer at expansion ratios of (a, a') 2-fold, (b, b') 5-fold, (c, c') 7-fold, and (d, d') 10-fold at a fixed dwelling time of 3 s (foaming temperature = 109 ℃). (a−d) and (a'−d') are taken from the views parallel and perpendicular to the core-back direction, respectively[28].....18

Fig. 2-12. (a) SEM images of foam with expansion ratio of 4.5-fold (PP3). (b) OCC and the expansion ratio of PP foams[29].....18

Fig. 2-13. (a) Elongation at break, (b) Young’ s modulus, and (c) tensile toughness for PP/HDPE blends at various composition ratios. (d) Examples of injection molded parts before and after tensile test to demonstrate the significant ductility improvement of microcellular 75/25 PP/HDPE blend[32].....20

Fig. 2-14. (a) SEM images of the 75/25 PP/HDPE foamed part at different elongations. (b) Schematic of the ductility enhancing mechanism by microcellular foam structure[32].....21

Fig. 2-15. SEM micrograph of PP/PTFE composites with (a) 1 wt% and (b) 5 wt% PTFE after etching PP matrix using xylene[34].....22

Fig. 2-16. Foam structure comparisons of the injection molded PP/PTFE composite foams: (a) cell size and (b) cell density. (c) Gardner impact strength of the prepared foams[34].....23

Fig. 2-17. Representative SEM micrographs of (a) neat PLA (b) PLA – 0.25 wt% clay, (c) PLA – 0.5 wt% clay, (d) PLA – 1 wt% clay, (e) LCB-PLA, (f) LCB-PLA – 0.25 wt% clay, (g) LCB-PLA – 0.5 wt% clay, and (h) LCB-PLA – 1 wt% clay[39]. 24

Fig. 2-18. Schematic of shish-kebab structure formation in LOPPM processing and nanoscale cells formation during foaming[41]. 25

Fig. 2-19. Schematic of the preparation process. (a) PIF processing and (b) supercritical CO_2 foaming[43]. 26

Fig. 2-20. SEM images of the impact-fractured surfaces of the solid PP (PP1) and PP foams (PP6–PP9). The relative density of PP6. PP7, PP8, and PP9 were 0.67, 0.62, 0.38 and 0.04. The scale bar in PP1 is 100 μm; the scale bar in PP6 – PP8 is 30 μm; and the scale bar in PP9 is 500 μm[49]. 28

Fig. 2-21. Mechanical behavior at high strain rates divided by the square of the relative density for both PMMA solid and for PMMA microcellular and nanocellular foams[50]. 30

Fig. 2-22. SEM images from hybrid nanocomposite specimen with 5.0%wt GNPs and 0.5%wt CNTs. (a) Flexible CNTs connecting large two-dimensional (2D) GNPs (b) A CNT cluster connecting three GNPs[59]. 32

Fig. 2-23. EC for solid EP/F-MWCNT composites and foamed composites with various F-MWCNT content[65]. 33

Fig. 2-24. EC of PP/MWCNT nanocomposites with different vol.% MWCNT as a function of relative density[67]. 35

Fig. 2-25. (I) TEM images illustrating MWCNT alignment in solid and foamed PP/MWCNT (1.28 vol.%) nanocomposites. The relative density of (a), (b) and (c) are 1, 0.7 and 0.2, respectively. (II) 2-D conceptualization of the evolution of MWCNT interconnection with foaming. The relative density of (a), (b) and (c) are 1, 0.7 and 0.2, respectively[67]. 36

Fig. 2-26. General variation of the transmission loss with frequency for a homogeneous material[72]. 38

Fig. 2-27. Schematic of sound transmission in (a) solid and (b) foamed samples..... 39

Fig. 2-28. Laminar morphologies of PVC composites with different layer numbers. A: 2-layer; B: 4-layer; C: 8-layer; D: 16-layer[87]. 43

Fig. 2-29. Schematic of sound transmission path in PVC multilayered composite. A: 8-layer; B: 16-layer; C: close-up image of A; D: close-up image of B[87]. 44

Fig. 2-30. (a) Schematic of the apparatus for PIF processing; (b) Schematic illustration of PIF PP/POE foam preparation. The SEM image of the cross-section of PP/POE(c), PP/POE foam(d), PP/POE foam at high magnification (e), PIF PP/POE (f), PIF PP/POE foam (g), PIF PP/POE foam at high magnification(h)[88]. 45

Fig. 3-1. Structure of PBAT, PLA and ADR, where R1 – R5 are H, CH_3, a higher alkyl group, or combinations of them; R6 is an alkyl group, and *x*, *y*, and *z* are each between 1 and 20. 60

Fig. 3-2. FTIR spectra of samples: (a) ADR, PBAT, PLA and B1.5; (b) B, B0.5, B1 and B1.5..... 67

Fig. 3-3. ^{1}H NMR spectra for (a) pure PBAT, (b) pure PLA, (c) pure ADR, and (d, d') B0 and B1.5. 69

Fig. 3-4. Possible reactions between PLA/PBAT and ADR during reactive extrusion. 70

Fig. 3-5. SEM images of the unfoamed specimens (a, a') B, (b, b') B0.5, (c, c') B1 and (d, d') B1.5. (a-d) and (a'-d') were taken from the views perpendicular and parallel to the flow direction, respectively. 72

Fig. 3-6. SEM images of (a) B, (b) B0.5, (c) B1 and (d) B1.5 obtained from the view parallel to the flow direction. 73

Fig. 3-7. The rheological behavior of B, B0.5, B1 and B1.5 specimens as a function of frequency at 190 ℃: (a) complex viscosity (η^*), (b) storage modulus (G'), and (c) Han plot. 74

Fig. 3-8. Typical SEM images of (a, a') B, (b, b') B0.5, (c, c') B1 and (d, d') B1.5 foams. (a'-d') were the magnified images of (a-d). 76

Fig. 3-9. (a) Cell size and (b) cell density of B, B0.5, B1 and B1.5 foams. 76

Fig. 3-10. Rheological behavior of PLA and PBAT with various ADR content as a function of temperature at a frequency of 1 rad/s. 78

Fig. 3-11. Schematic of the formation mechanism of the bimodal cell structure for the modified PLA/PBAT blends: (a, a') Cell nucleation, (b, b') Cell growth, (c, c') Final cell structure. 78

Fig. 3-12. First heating curves (10 ℃/min) of the unfoamed specimens (a) B, B0.5, B1, and B1.5 and (b) their corresponding foamed samples. 80

Fig. 3-13. (a) Tensile strength and (b) elongation at break of the unfoamed specimens B, B0.5, B1, B1.5 and their corresponding foamed samples. 81

Fig. 3-14. Stress-strain curves of (a) B, B0.5, B1, B1.5 and (b) their corresponding foamed samples. 81

Fig. 3-15. Impact strength of the unfoamed specimens (a) B, B0.5, B1, B1.5 and (b) their corresponding foamed samples. 83

Fig. 3-16. SEM images of impact-fractured surfaces of (a) B, (b) B0.5, (c) B1, (d) B1.5. Number 1 represent the whole impact-fractured surface morphology at low magnification. Number 2, 3, and 4 represent the magnified images obtained from the crack initiation zone (position A), the early crack propagation zone (position B) and the later crack propagation zone (position C), respectively. 85

Fig. 3-17. SEM images of impact-fractured surfaces of (a) B foam, (b) B0.5 foam, (c) B1foam, (d) B1.5 foam. Number 1 represent the whole impact-fractured surface morphology at low magnification. Number 2, 3, and 4 represent the magnified images obtained from the crack initiation zone (position A), the early crack propagation zone (position B) and the later crack propagation zone (position C), respectively. 87

Fig. 3-18. SEM images of (a) B, (b) B0.5, (c) B1, (d) B1.5 foam at the early crack propagation zone. 88

Fig. 3-19. (a) Schematic of sample position for SEM. SEM images of (b, d) B1 foam and (c, e) B1.5 foam in whitened region perpendicular to the impact-fractured surface. 89

Fig. 3-20. Schematic of the impact-fractured surface morphology of PLA/PBAT blend foams. 90

Fig. 4-1. (a) Schematic of SENTB. (b) A typical load-displacement curve..... 107

Fig. 4-2. Phase morphology of (a, a') PLA/PBAT, (b, b') PLA/PBAT/ADR, and (c–e) PLA/PBAT foams with various cell sizes: (c) 43.6 μm, (d) 19.2 μm, and (e) 11.2 μm. (a–e) obtained by SEM, and (a', b') by TEM. The VF of PLA/PBAT foams was 30%. 109

Fig. 4-3. The dependence angular frequencies of (a) complex viscosity and (b) storage modulus at 190 ℃. 110

Fig. 4-4. SEM images of PLA/PBAT foams with different cell sizes and a fixed VF of 30%. 111

Fig. 4-5. SEM images of PLA/PBAT foams with different cell sizes and a fixed VF of 40%. 112

Fig. 4-6. Cell size distribution of PLA/PBAT foams with a VF of 30%. 112

Fig. 4-7. Cell size distribution of PLA/PBAT foams with a VF of 40%. 113

Fig. 4-8. Cell size dependence of cell density and cell wall thickness for PLA/PBAT foams with VF of (a) 30% and (b) 40%.....113

Fig. 4-9. SEM images of PLA/PBAT/ADR foams with different cell sizes and a fixed VF of 30%.....114

Fig. 4-10. SEM images of PLA/PBAT/ADR foams with different cell sizes and a fixed VF of 40%. 115

Fig. 4-11. Cell size distribution of PLA/PBAT/ADR foams with a VF of 30%. 115

Fig. 4-12. Cell size distribution of PLA/PBAT/ADR foams with a VF of 40%. 116

Fig. 4-13. Cell size dependence of cell density and cell wall thickness for PLA/PBAT/ADR foams with VF of (a) 30% and (b) 40%.....116

Fig. 4-14. First heating curves of obtained foams with different cell sizes under VFs of 30% and 40%: (a) PLA/PBAT foams, (b) PLA/PBAT/ADR foams. 117

Fig. 4-15. Impact strength of (a, b) PLA/PBAT foams and (d, e) PLA/PBAT/ADR foams: (a, c) impact strength *vs.* cell size, (b, d) specific impact strength *vs.* cell size. Dashed line represents the solid sample. 119

Fig. 4-16. SEM images of impact fractured surfaces of (a, b) PLA/PBAT foams and (c, d) PLA/PBAT/ADR foams. (a'– d') are the enlarged images of (a– d), respectively. The VF of all samples was 30%. 121

Fig. 4-17. (a, c) Load-displacement curves and (b, d) variation of fracture energy parameters (E, E_i and E_p) of foams with various cell sizes: (a, b) PLA/PBAT foams, (b, d) PLA/PBAT/ADR foams. The VF of all samples was 40%. 122

Fig. 4-18. Schematics of stress concentration (a) around a rubber particle and between two rubber particles. (c) Schematics of stress field distribution before and after reducing cell size. 124

Fig. 4-19. Schematic of the cell size-induced toughening mechanism of (a, b) PLA/PBAT foams and (c, d) PLA/PBAT/ADR. 126

Fig. 5-1. Illustration of CO_2 treatment equipment. 137

Fig. 5-2. Illustration of SENTB test..... 140

Fig. 5-3. (a–f) SEM images of untreated PLA/PBAT foams with different cell sizes and (a'–f') their corresponding cell size distribution. The VF of all samples was ~40%..... 142

Fig. 5-4. (a–f) SEM images of CO_2 treated PLA/PBAT foams with different cell sizes and (a'–f') their corresponding cell size distribution. The VF of all samples was ~28%..142

Fig. 5-5. Comparison of cell size of PLA/PBAT foams before and after CO_2 treatment. Sample a–f correspond to SEM a–f in Fig. 5-3 and 5-4. 143

Fig. 5-6. First heating curves of PLA/PBAT foams (a) before and (b) after CO_2 treatment. 144

Fig. 5-7. 1-D WAXD diffraction profiles of PLA/PBAT foams before and after CO_2 treatment. 145

Fig. 5-8. SEM image of solid and foamed PLA/PBAT foams (a–d) before and (e–h) after CO_2 treatment. (a, e) were obtained from solid samples. The cell sizes of untreated foams (b, c, d) were 22.8, 15.3 and 6.4 μm, respectively. The cell sizes of treated foams (f, g, h) were 23.6, 14.6 and 6.3 μm, respectively. 147

Fig. 5-9. Notched Izod impact strength as a function of cell size for foams with (a) low and (b) high PLA crystallinity. (c) Specific impact strength as a function of cell size for foams with low and high PLA crystallinity. 148

Fig. 5-10. SEM images of impact-fractured surfaces of PLA/PBAT foams with various cell sizes: (a) 15.3 μm, (b) 14.6 μm, (c) 6.4 μm, and (d) 6.3 μm. (a, c) and (b, d) had low and high PLA crystallinity, respectively. (a'–d') were the magnified images of (a–d). 149

Fig. 5-11. SEM images of cross sections underneath the impact-fractured surfaces for PLA/PBAT foams with various cell sizes: (a) 15.3 μm, (b) 14.6 μm, (c) 6.4 μm, and (d) 6.3 μm. (a, c) and (b, d) had low and high PLA crystallinity, respectively. 151

Fig. 5-12. Schematic of the impact-fractured surfaces for PLA/PBAT foams with different cell sizes and various PLA crystallinity. 152

Fig. 5-13. SEM images taken from the polished surfaces of PLA/PBAT foams with various cell sizes: (a) 15.3 μm, (b) 14.6 μm, (c) 6.4 μm, and (d) 6.3 μm. (a, c) and (b, d) had low and high PLA crystallinity, respectively. (a'–d') were the magnified images of (a–d). 153

Fig. 6-1. Schematic of the preparation process of PP/CNS nanocomposite foams. 166

Fig. 6-2. Schematic of mold cavity and specimen preparations. 167

Fig. 6-3. SEM images of PP/CNS nanocomposite. (b) is the magnified image of one section of (a). 171

Fig. 6-4. Rheological behavior of pure PP and PP/CNS nanocomposite. 172

Fig. 6-5. Crystallization behavior of pure PP and PP/CNS nanocomposite in (a) 1^{st} cooling and (b) 2^{nd} heating. 173

Fig. 6-6. SEM images of (a) PP and (b–d) PP/CNS nanocomposite foams fabricated under various N_2 content: (a)1 wt%, (b) 0.6 wt%, (c) 0.8 wt%, (d) 1 wt%. (a1—d1) were the corresponding cell size distribution of (a—d). 173

Fig. 6-7. (a) Optical photograph of foamed sample. SEM images of the surface layer of PP/CNS foams under N_2 content of (b) 0.6 wt%, (c)0.8 wt% and (d) 1 wt%. (e) Surface layer thickness of PP/CNS foams fabricated under different N_2 content. 174

Fig. 6-8. EC of PP/CNS solid and foamed samples as a function of (a) N_2 content and (b) Cell size. 175

Fig. 6-9. SEM images of the cell wall for PP/CNS foams with different cell sizes: (a) 317 μm, (b) 142μm, (c, d) 71 μm. 177

Fig. 6-10. TEM images of PP/CNS foams with different cell wall thicknesses: (a) 0.8 μm, (b) over 40 μm. (b1-b4) are the magnified images captured from different distances from cell boundary in (b): (b1) 0 μm, (b2) 6 μm, (b3) 11 μm, (b4) 17 μm..... 178

Fig. 6-11. (a) Schematic diagram of the degree of CNS orientation at different locations away from the boundary of cell. (b, c) CNS dispersion in PP matrix of cell wall with (b) small and (c) large thickness. (d, e) Conductive path of PP/CNS foams with (d) small cell size (thin cell wall) and (e) big cell size (thick cell wall). 179

Fig. 6-12. (a-c) EMI shielding properties of PP/CNS nanocomposite and the corresponding foams in X band: (a) SE total, (b) SE abs and SE ref, (c) R' and A' coefficients. (d) Comparison of the EMI shielding performance of our result with other reported CPC foams. The reference numbers listed in Table 6-3. 181

Fig. 7-1. SEM images of (a) mica particles and (b) PP/mica composite foam. (b') is the magnification of one section of (b)..... 197

Fig. 7-2. SEM images of core layers of pure PP and PP/mica composite foams at various VFs. 198

Fig. 7-3. SEM images of surface layers of pure PP and PP/mica composite foams at various VFs. 199

Fig. 7-4. Changes of (a) cell size, (b) cell density, and (c) skin layer thickness of pure PP and PP/mica composite foams at various VFs. 199

Fig. 7-5. SEM images of core layers of pure PP and PP30 foams with various cell sizes at a fixed VF of 67%..... 200

Fig. 7-6. SEM images of surface layers of pure PP and PP30 foams with various cell sizes at a fixed VF of 67%..... 201

Fig. 7-7. (a, b) Cell size dependence of cell density for (a) pure PP foams and (b) PP30 foams. (c, d) Cell size dependence of cell wall thickness for (c) pure PP foams and (d) PP30 foams. VF is fixed at 67%. 201

Fig. 7-8. Sound insulation properties of PP and PP/mica composite foams under different VF: (a) PP foams, (b) PP10 foams, (c) PP30 foams, and (d) average STL value. 203

Fig. 7-9. (a) Volume density of PP and PP/mica composites. (b) The storage modulus and (c) loss modulus-temperature curves of PP and PP/mica composites. 204

Fig. 7-10. Sound insulation properties of PP and PP/mica composite foams under different cell sizes: (a) PP foams, (b) PP30 foams, and (c) average STL value..... 205

Fig. 7-11. The schematic diagram of sound waves transmission path by the effect of (a) reducing cell size and (b) introducing mica. 206

List of Tables

Table 3-1. Processing parameters used for the FIM experiments. 62
Table 3-2. Density and VF of the unfoamed and foamed samples 62
Table 3-3. Molecular weight of PLA/PBAT blends with different ADR content. 71
Table 3-4. Thermal parameters of B, B0.5, B1, B1.5 and their corresponding foamed samples from DSC curves 80
Table 4-1. Density and VF of foamed samples 103
Table 4-2. Processing parameters used for the FIM experiments. 103
Table 5-1. Processing parameters used for the FIM experiments. 136
Table 5-2. Thermal parameters of PLA/PBAT foams before and after CO_2 treatment 144
Table 6-1. Processing parameters used in the core-back FIM process. 167
Table 6-2. Cell structure parameters of PP and PP/CNS foams 173
Table 6-3. Comparison of the EMI shielding performance of CPC foams. 182
Table 7-1. Processing parameters used for the FIM experiments. 194

List of Abbreviations

1D	One-dimensional
2D	Two-dimensional
ABS	Poly(acrylonitrile-co-butadiene-co-styrene)
CB	Carbon black
CF	Carbon fiber
CNF	Carbon nanofibers
CNS	Carbon nanostructure
CNT	Carbon nanotubes
CO_2	Carbon dioxide
CPC	Conductive polymer composite
DSC	Differential scanning calorimeter
EC	Electrical conductivity
EGMA	Poly(ethylene-co-glycidyl methacrylate)
EMI	Electromagnetic interference
EVA	Ethylene-co-vinyl acetate
FIM	Foam injection molding
FTIR	Fourier transform infrared spectrometry
GNP	Graphene nanoplatelet
GPC	Gel permeation chromatography
HDPE	High-density polyethylene
HGB	Hollow glass bead

LCBPP	Long-chain branched polypropylene
LDPE	Low-density polyethylene
LOPPM	Loop oscillating push-pull molding
MBS	Methyl methacrylate-butadiene-styrene
MWCNT	Multiwalled carbon nanotube
N_2	Nitrogen
NA	Nucleating agent
NMR	Nuclear magnetic resonance
OCC	Open-cell content
PBAT	Poly(butylene adipate-co-terephthalate)
PC	Polycarbonate
PDI	Polydispersity index
PE	Polyethylene
PEBA	Polyether block amide
PEI	Polyetherimide
PET	Polyethylene terephthalate
PHA	Polyhydroxyalkanoate
PHBV	Poly(3-hydroxybutyrate-co-3-hydroxy-valerate)
phr	Parts per hundred rubber
PIF	Pressure-induced-flow
PLA	Polylactic acid
PMMA	Polymethyl methacrylate
POE	Polyolefin elastomer

PP	Polypropylene
PS	Polystyrene
PTFE	Polytetrafluoroethylene
PU	Polyurethane
PVC	Polyvinyl chloride
PVDF	Polyvinylidene fluoride
RE	Reflection coefficient
SAN	Acrylonitrile-styrene
SBS	Styrene-butadiene-styrene
SCF	Supercritical fluid
SE	Shielding effectiveness
SEM	Scanning electron microscopy
SENTB	Single-edge notched three-point bending
SiCnw	Silicon carbide nanowire
STL	Sound transmission loss
TEM	Transmission electron microscopy
VF	Void fraction
WAXD	Wide-angle X-ray diffraction

List of Symbols

a	Length
A'	Coefficients of absorption
b	Wideth
c	Sound speed
d	Average cell size
D_w	Weight-average particle size
E	Elastic modulus
Ei	Incident acoustic power
Et	Transmitted acoustic power
f	Frequency
Φ	Expansion ratio
γ	Impedance ratio
h	Thickness
ρ_m	Surface density
n	Number of cells
N_0	Cell density
ρ	Density
R'	Coefficients of reflection
T'	Coefficients of transmission
v	Poisson ratio

V_{closed}	Closed volume that cannot be penetrated by the pressurized nitrogen
$V_{geometric}$	Geometric volume
X_c	Degree of crystallinity
Y	Area
Z	Acoustic impedance
τ	Cell wall thickness
ρ_m	Density of the solid (unfoamed)
ρ_f	Density of the foam
ΔH_m	Enthalpy of melting
ΔH_c	Enthalpy of crystallization
ΔH_m^0	Melting enthalpy of completely crystalline polymer
ω_f	Weight percent

Chapter 1: Introduction

1.1. Background

Microcellular plastic foams, which were first invented by Suh et al. of Massachusetts Institute of Technology (MIT) in 1979, refer to any polymer with small cells ranging from 0.1 to 10 μm and a high cell density in the range of 10^9-10^{15} cells/cm^3[1]. The target behind the invention of microcellular plastic foams was to prepare a plastic material consuming less polymer without sacrificing mechanical properties. Unexpectedly, microcellular plastic foams also show additional advantages, such as enhanced toughness, good thermal insulation, and sound insulation properties in comparison to their solid samples[2]. Thus, microcellular plastic foams are applied in a wide range of applications, including packaging, automobile, sporting equipment, thermal and sound insulators[3]. Besides, adding conductive fillers can further augment the functionality of microcellular plastic foams. It has been proved that the introduction of cell structure into conductive polymer composites (CPC) can offer substantial advantages in electromagnetic interference (EMI) shielding applications[4].

In recent years, commonly used semicrystalline polymers, such as PP and polylactic acid (PLA), have been widely used to prepare foam materials due to their excellent properties, including high stiffness and strength. However, the inherent low toughness hinders their foams' wide applications. Thus, many methods such as blending rubber or soft thermoplastics (e.g. polyethylene (PE) and poly(3-

hydroxybutyrate-co-3-hydroxy-valerate) (PHBV)), compounding inorganic fillers (e.g. talc and clay), and tailoring crystallization (e.g. crystal NA), were applied to improve the toughness of foams [2, 5-7]. However, those methods would also influence the crystallization and the foaming process of polymer, since the modifications could accelerate the crystallization behavior, improve the melt strength, and thus enhance the cell nucleation and reduce the cell size [8, 9]. As a result, the toughness of polymer foams was influenced by several factors, including cell structure and the added filler.

CPC foam, as a kind of electromagnetic shielding material, has became a hotspot in recent years due to its advantageous attributes, including lightweight, corrosion resistance and good processability, compared with metal-based material[10]. Frequently used conductive fillers include carbon black (CB), carbon fiber (CF), carbon nanotubes (CNT), graphene, carbon nanofibers (CNF) and Mxene[11]. Generally, electrical conductivity (EC) greatly affects EMI shielding. Increasing conductive filler content in CPC foams was an effective way to enhance EC. However, a high content of conductive filler would seriously impair the processability of CPCs. Tailoring the cell structure could also promote the EC of CPC foams. For example, Hamidinejad et al[12] proved that foaming can greatly improve the EC and lower the percolation threshold of high-density polyethylene/graphene nanoplatelet (HDPE/GNP) composite foams. Furthermore, Wang et al[13-15] investigated the effect of VF on the EC of CPC foams, and found that increasing VF (below 20%) improved EC, while further increase in VF (>30%) led to a decrease in the EC. Besides, the model prediction results were in good

agreement with the experimental data for CPC foams. It should be noticed that cell size would vary with VF. However, the effect of cell size on EC was not discussed in the reported literature.

Compared with the traditional devices adopted for soundproofing (e.g. metallic and inorganic materials), polymeric foams have gotten much attention due to their advantages including low density and good processability[16]. Adding inorganic fillers has been frequently applied to enhance the sound insulation properties of polymer and polymeric foams since it could improve the stiffness and density of samples[17, 18]. Besides, regulating the cell structure could also improve the sound insulation properties of polymeric foams. Generally, the sound insulation properties improved with the increase of VF, since the thickness of the tested samples was also increased, which would prolong the transmission pathway of sound waves[19, 20]. It is indicated by many reports that the soundproofing performance can be improved by decreasing the cell size of foams[18, 20]. However, the reduced cell size was caused by adding additional filler, and the VF was also varied simultaneously in some cases.

Obviously, cell structure parameters including cell size, cell density and density (or VF) would strongly influence the properties of polymeric foams, such as toughness, electrical properties and sound insulation properties. However, the research about the relationship between cell size and properties is still in its infancy.

1.2. Aims and objectives

This research aims to investigate the effect of cell size on the impact strength,

electrical and sound insulation properties, when the VF is fixed. The corresponding enhancement mechanisms are to be further discussed. There are 3 specific objectives as follows:

(a) To investigate the relationship between cell size and impact strength when the VF is consistent. Furthermore, the effect of polymer crystallization on impact toughness is also considered.

(b) To study the influence of cell size on electrical properties (e.g. EC and EMI shielding property) of CPC foams at a fixed VF.

(c) To investigate the effect of cell size on sound insulation properties of polymer composite foams while keeping the VF constant.

1.3. Thesis structure

Chapter 1 describes the background of this research, aim and objectives, and the structure of the thesis.

Chapter 2 covers the development of foaming injection molding technology. Literature reviews of the methods for improving impact toughness, electrical and sound insulation properties of polymeric foams are also included in this chapter.

Chapter 3 illustrates the characteristics of PLA/PBAT foams with different chain extender content, such as cell morphology, crystallinity and mechanical properties. The effect of chain extender content on the cell structure and mechanical properties of PLA/PBAT foams is investigated.

Chapter 4 compares the impact strength of PLA/PBAT foams with various cell sizes while keeping the VF constant. The toughening mechanism is proposed based on the characterization of impact-fractured surfaces and single-edge notched three-point bending (SENTB) technique.

Chapter 5 investigates the combined effects of cell size and matrix crystallization on the impact strength of PLA/PBAT foams. Comparisons of cell size-impact strength changing patterns under different PLA crystallinity are conducted to study the difference in terms of impact strength and impact-fractured surface. The synergistic toughening mechanism of cell size and matrix crystallinity for PLA/PBAT foams is proposed.

Chapter 6 illustrates the effect of cell size on the electrical properties of PP/CNS foams. According to the observation of the dispersion of CNS in PP/CNS foams with various cell size, the mechanism of cell size-induced conductivity enhancement is proposed.

Chapter 7 comprehensively studies the effect of VF, mica content and cell size on sound insulation properties of PP/mica composite foams. The mechanism of improving the sound insulation performance is discussed through the characterization of cell structure, and mica dispersion in the PP matrix.

Chapter 8 includes the main conclusions of the thesis and further perspectives.

1.4. References

[1] N.P. Suh, Impact of microcellular plastics on industrial practice and academic research, Macromol. Symp. 201(1) (2003) 187-202. https://doi.org/10.1002/masy.200351122

[2] L. Wang, Y. Hikima, S. Ishihara, M. Ohshima, Fabrication of lightweight microcellular foams in injection-molded polypropylene using the synergy of long-chain branches and crystal nucleating agents, Polymer 12 (2017) 119-127. https://doi.org/10.1016/j.polymer.2017.09.025

[3] M. Antunes, J.I. Velasco, Multifunctional polymer foams with carbon nanoparticles, Prog. Polym. Sci. 39(3) (2014) 486-509. https://doi.org/10.1016/j.progpolymsci.2013.11.002

[4] X. Jia, Y. Li, B. Shen, W. Zheng, Evaluation, fabrication and dynamic performance regulation of green EMI-shielding materials with low reflectivity: A review, Composites, Part B 233 (2022) 109652. https://doi.org/10.1016/j.compositesb.2022.109652

[5] X. Sun, H. Kharbas, J. Peng, L.-S. Turng, Fabrication of super ductile polymeric blends using microcellular injection molding, Manuf. Lett. 2(2) (2014) 64-68. https://doi.org/10.1016/j.mfglet.2014.02.002

[6] X. Sun, H. Kharbas, J. Peng, L.-S. Turng, A novel method of producing lightweight microcellular injection molded parts with improved ductility and toughness, Polymer 56 (2015) 102-110. https://doi.org/10.1016/j.polymer.2014.09.066

[7] J. Zhao, Y. Qiao, G. Wang, C. Wang, C.B. Park, Lightweight and tough PP/talc composite foam with bimodal nanoporous structure achieved by microcellular injection molding, Mater. Des. 195 (2020) 109051. https://doi.org/10.1016/j.matdes.2020.109051

[8] M.-H. Wu, C.-C. Wang, C.-Y. Chen, Preparation of high melt strength polypropylene by addition of an ionically modified polypropylene, Polymer 202 (2020) 122743. https://doi.org/10.1016/j.polymer.2020.122743

[9] A. Rizvi, A. Tabatabaei, M.R. Barzegari, S.H. Mahmood, C.B. Park, In situ fibrillation of CO2-philic polymers: Sustainable route to polymer foams in a continuous process, Polymer 54(17) (2013) 4645-4652. https://doi.org/10.1016/j.polymer.2013.06.023

[10] G. Sang, P. Xu, T. Yan, V. Murugadoss, N. Naik, Y. Ding, Z. Guo, Interface Engineered Microcellular Magnetic Conductive Polyurethane Nanocomposite Foams for Electromagnetic Interference Shielding, Nano-Micro Lett. 13(1) (2021) 153. https://doi.org/10.1007/s40820-021-00677-5

[11] B. Zhao, M. Hamidinejad, S. Wang, P.W. Bai, R.C. Che, R. Zhang, C.B. Park, Advances in

electromagnetic shielding properties of composite foams, J. Mater. Chem. A 9(14) (2021) 8896-8949. https://doi.org/10.1039/d1ta00417d

[12] M. Hamidinejad, B. Zhao, A. Zandieh, N. Moghimian, T. Filleter, C.B. Park, Enhanced Electrical and Electromagnetic Interference Shielding Properties of Polymer–Graphene Nanoplatelet Composites Fabricated via Supercritical-Fluid Treatment and Physical Foaming, ACS Appl. Mater. Interfaces 10(36) (2018) 30752-30761. https://doi.org/10.1021/acsami.8b10745

[13] S. Wang, A. Ameli, V. Shaayegan, Y. Kazemi, Y. Huang, H.E. Naguib, C.B. Park, Modelling of Rod-Like Fillers' Rotation and Translation near Two Growing Cells in Conductive Polymer Composite Foam Processing, Polymers 10(3) (2018) 261. https://doi.org/10.3390/polym10030261

[14] S. Wang, Y. Huang, E. Chang, C. Zhao, A. Ameli, H.E. Naguib, C.B. Park, Evaluation and modeling of electrical conductivity in conductive polymer nanocomposite foams with multiwalled carbon nanotube networks, Chem. Eng. J. 411 (2021) 128382. https://doi.org/10.1016/j.cej.2020.128382

[15] S. Wang, Y. Huang, C. Zhao, E. Chang, A. Ameli, H.E. Naguib, C.B. Park, Theoretical modeling and experimental verification of percolation threshold with MWCNTs' rotation and translation around a growing bubble in conductive polymer composite foams, Compos. Sci. Technol. 199 (2020) 108345. https://doi.org/10.1016/j.compscitech.2020.108345

[16] S. Hu, J. Cai, G. Liao, Q. Fu, Preparation and Sound Insulation Performance of Superfine Metal Powder/Nitrile-Butadiene Rubber-Polyvinyl Chloride Microcellular Foaming Material, Adv. Polym. Technol. 2019 (2019) 7608641. https://doi.org/10.1155/2019/7608641

[17] J.-Z. Liang, X.-H. Jiang, Soundproofing effect of polypropylene/inorganic particle composites, Composites, Part B 43(4) (2012) 1995-1998. https://doi.org/10.1016/j.compositesb.2012.02.020

[18] L. Xu, T. Han, J. Li, Y. Xiong, S. Guo, The cell growth-induced orientation of mica in lightweight flexible poly (vinyl chloride) foams and its enhancement on sound insulation, Compos. Sci. Technol. 145 (2017) 78-88. https://doi.org/10.1016/j.compscitech.2017.03.037

[19] D. Jahani, A. Ameli, M. Saniei, W. Ding, C.B. Park, H.E. Naguib, Characterization of the Structure, Acoustic Property, Thermal Conductivity, and Mechanical Property of Highly Expanded Open-Cell Polycarbonate Foams, Macromol. Mater. Eng. 300(1) (2015) 48-56. https://doi.org/10.1002/mame.201400125

[20] J. Zhao, G. Wang, Z. Chen, Y. Huang, C. Wang, A. Zhang, C.B. Park, Microcellular injection molded outstanding oleophilic and sound-insulating PP/PTFE nanocomposite foam, Composites, Part B 215 (2021) 108786. https://doi.org/10.1016/j.compositesb.2021.108786

Chapter 2: Literature review

2.1. Foam-processing methods

The traditional foam-processing techniques used for microcellular polymer foam preparation include batch foaming, extrusion foaming, and foam injection molding (FIM). Generally, batch foaming is just used for research purposes, and extrusion foaming and FIM are mainly used for foam production. The most commonly used physical blowing agents are CO_2 and N_2, in the supercritical fluid (SCF) state. This is because the SCF state provides the fluid with increased diffusivity and solubility[1].

2.1.1. Batch foaming

Batch foaming is a batch-wise process conducted in a closed vessel. It is a non-continuous foam-processing technique since the saturation and foaming of polymer samples occur separately. The batch foaming is usually classified as pressure-induced (one-step) and temperature-induced (two-step).

2.1.1.1. Pressure-induced (one-step) method

In this method, a polymer sample is placed in an autoclave and saturated with a blowing agent. Once the sample is completely saturated, the autoclave depressurizes rapidly at a high pressure reduction rate, leading to the occurrence of cell nucleation and its following growth. Finally, the sample is cooled in water to stabilize the cell structure[2, 3]. Fig. 2-1 shows a schematic of pressure-induced batch foaming.

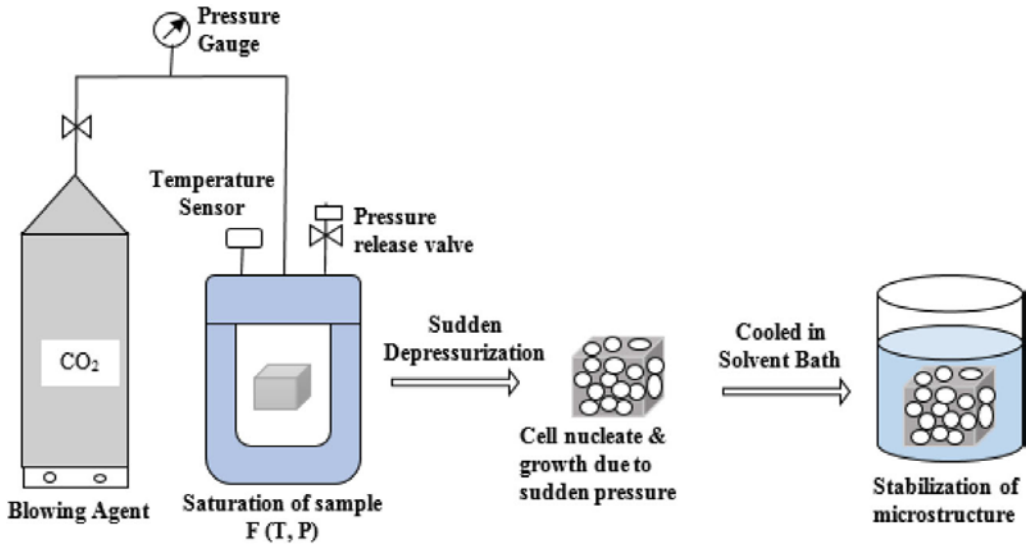

Fig. 2-1. Schematic of pressure-induced batch foaming[3].

2.1.1.2. Temperature-induced (two-step) method

In the temperature-induced method, the polymer sample is usually saturated at a temperature below the glass transition temperature of the polymer matrix. The sample is taken out from the autoclave once the sample is completely saturated. Then, the saturated sample is dipped in a hot oil bath to induce cell nucleation and cell growth due to the high temperature gradient[3, 4]. The bath temperature is usually above the glass transition temperature of the sample. Fig. 2-2 shows a schematic of temperature-induced batch foaming.

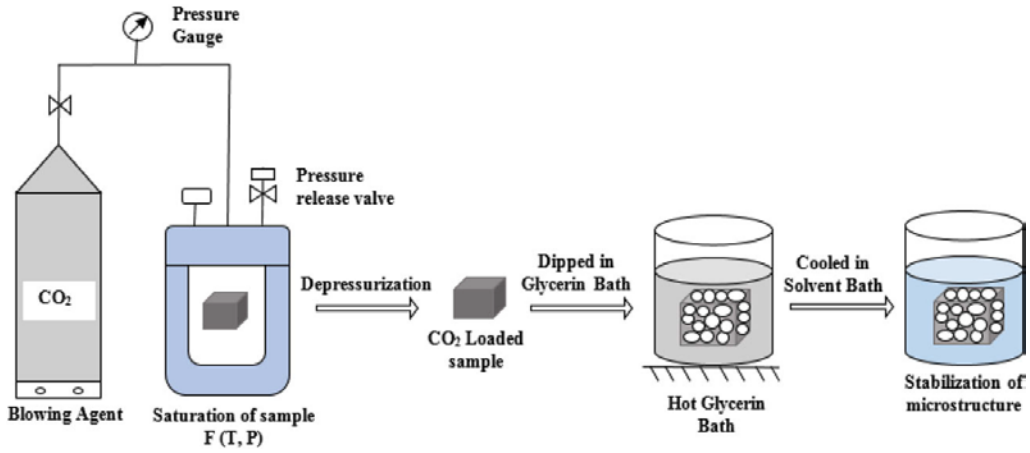

Fig. 2-2. Schematic of temperature-induced batch foaming[3].

2.1.2. Extrusion foaming

Extrusion foaming is a continuous process, consisting of an extruding unit, gas injection unit and die-shaping unit[5]. The tandem foam extrusion lines (Fig. 2-3) are mostly used in industries. The polymer pellets are added into the first barrel through hopper and get melted due to the high temperature. Then, the blowing agent is injected into the melt and a homogenous polymer/gas mixture is formed due to the shearing action of the screw. In the second barrel, the temperature of the polymer/gas mixture is reduced to suppress the cell coalescence. The melt pump regulates the melt flow rate of the mixture. As the homogenous molten mixture leaves the die, the rapid pressure drop leads to the occurrence of cell nucleation and growth.

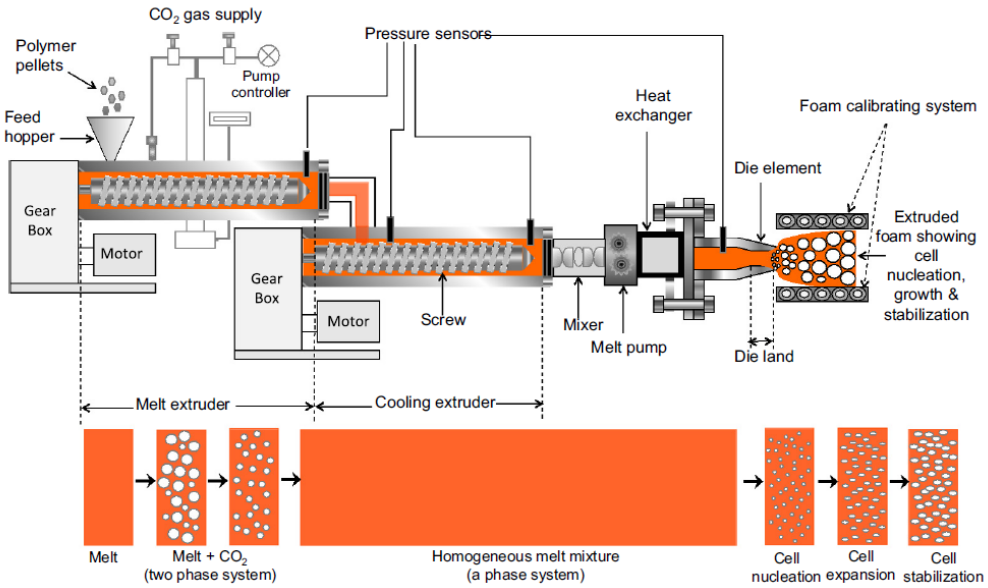

Fig. 2-3. Schematic of tandem extrusion foaming[6].

2.1.3. FIM

FIM is one of the most promising available technologies since it can be applied to prepare lightweight foams with three-dimensional geometries in rapid production cycles[7]. FIM is an extension of the traditional injection molding but with the addition of a gas injection unit. It consists of the injection unit and the clamping unit, as Fig. 2-4 shows[6]. There are two major approaches to conducting FIM experiments including low-pressure FIM and core-back (or mold-opening) FIM.

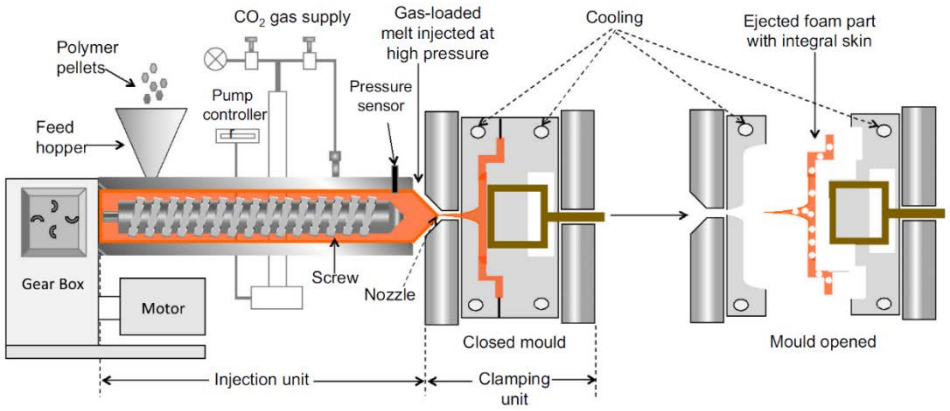

Fig. 2-4. Schematic of FIM[6].

2.1.3.1. Low-pressure FIM

In low-pressure FIM[8-10], a short-shot, which means the melt/gas mixture cannot completely fill the mold cavity, is injected into the mold cavity, and the cell nucleation occurs at the gate due to the low pressure of mold cavity. Fig. 2-5 shows the schematic of low-pressure[11]. As depicted, gate-nucleated cells grow, become elongated, and coalesce during their travel along the cavity, leading to a non-uniform cell structure.

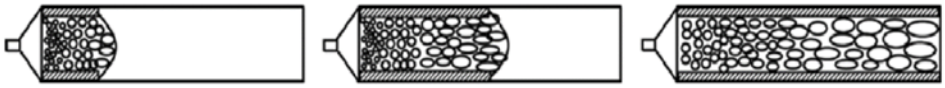

Fig. 2-5. Schematic of low-pressure FIM[11].

2.1.3.2. Core-back FIM

In core-back FIM or mold-opening FIM[12-14], surprisingly, a well uniform cell structure can be achieved. Fig. 2-6 illustrates the schematic of core-back FIM[15]. Usually, core-back FIM process is composed of four stages, including injection, dwelling, core-back (or mold-opening) and cooling. First, a full-shot is used to fill the entire cavity and cell nucleation occurs at the gate (Fig. 2-6a and b). The gate-nucleated cells will dissolve back into the melt due to the high packing pressure during the dwelling stage (Fig. 2-6c and d). Then, the cell nucleation is induced by core-back (mold-opening) operation, and a very uniform cell structure can be achieved after cooling(Fig. 2-6e and f).

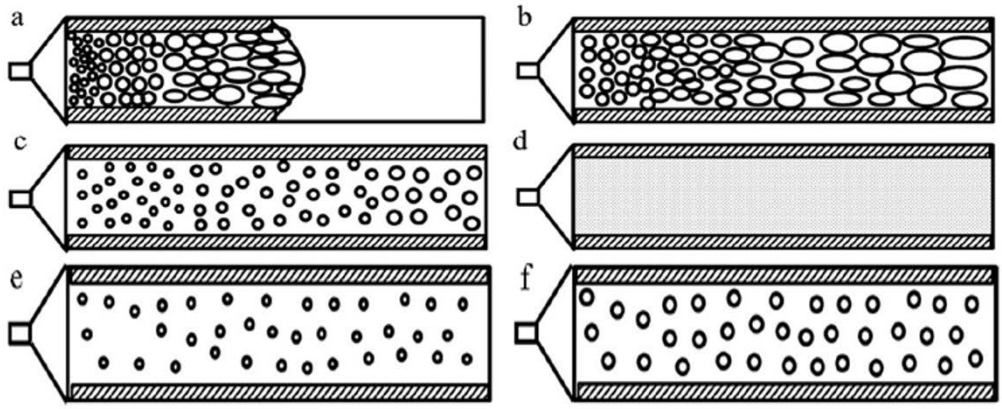

Fig. 2-6. Schematic of core-back FIM: (a) mold filling and the formation of gate-nucleated cells due to pressure drop over the gate; (b) full-shot; (c) collapse and dissolution of gate-nucleated nucleated cells, (d) complete disappearance of nucleated cells (formation of one-phase melt/gas solution); (e) nucleation of secondary cells due to the core-back (or mold-opening) operation; (f) cell growth. (The hatched area shows the formed skin layer).[15]

Compared with batch foaming and extrusion foaming, FIM shows great advantages in the preparation of foams with precise dimensions, especially for core-back FIM. By controlling the core-back distance during the core-back FIM process, foams with the desired expansion ratio can be easily obtained. Therefore, in this study, core-back FIM technique was applied to prepare foams and to study the relationship between cell size and properties of polymer foams.

2.1.4. Cell structure regulation in core-back FIM

2.1.4.1. Cell structure parameters

The properties of foams are directly related to the cell structure of foam: open-cell content (OCC), cell size, cell size distribution, cell density, VF or expansion ratio, and cell wall thickness.

(a) OCC: Two distinct structures can be observed in foamed samples, including closed-cell structure and open-cell structure, as shown in Fig. 2-7. Closed-cell structure consists of cells that isolated from each other, while the cells are connected with each other. In this content, OCC is proposed. It is defined as the ratio of open volume to total volume for a foam, and is determined using the following equation:

$$OCC = \left(1 - V_{closed} / V_{geometric}\right) \tag{2-1}$$

where V_{closed} is the closed volume that cannot be penetrated by the pressurized nitrogen and $V_{geometric}$ the geometric volume of the sample.

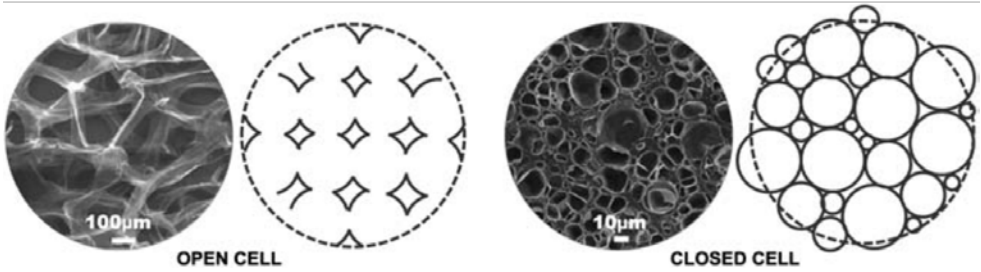

Fig. 2-7. (a) Open and (b) closed cell structure[16].

(b) Cell size and cell density: Cell density N_0 defined as the number of cells per unit volume of unfoamed polymer, is determined according to the following equation.:

$$N_0 = \left(\frac{n}{A}\right)^{3/2} \Phi \tag{2-2}$$

where n is the number of cells in the micrograph, A the area of the selected micrograph, Φ the expansion ratio of the foamed sample. Generally, cell size and cell density are inversely correlated for foams with a fixed density.

(c) Expansion ratio and VF: The Φ is calculated using equation:

$$\Phi = \frac{\rho_s}{\rho_f} \tag{2-3}$$

where ρ_s and ρ_f are the density of the solid and its foamed sample, respectively. The VF, which is defined as the ratio of the volume of voids in the foam to the total volume of the foam, is determined using equation:

$$VF = \frac{\rho_f}{\rho_s} \tag{2-4}$$

2.1.4.2. Effect of process parameters on cell structure

The cell structure (e.g. cell size and VF) can be well controlled by tailoring the process parameters (e.g. gas content, packing pressure, dwelling time and core-back distance) in core-back FIM process. According to the traditional cell nucleation theory[17-20] in polymer foaming, improving physical blowing agent is an effective ways to accelerate cell nucleation. In specific, driving force for cell nucleation increases with a higher blowing agent content, and the number of nucleated cells increase, resulting a higher cell density [15, 17, 21]. Wang et al.[12] investigated the effect of N_2 content on the cell structure of polyether block amide (PEBA) foams, and found that with the increase of N_2 content from 0.3 to 0.8 wt%, the cell size greatly reduced from 162 to 39 μm (Fig. 2-8).

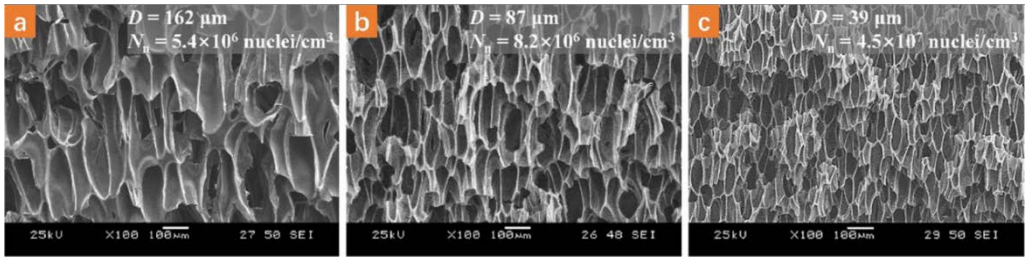

Fig. 2-8. The cell structure of the PEBA foams fabricated by core-back FIM using a same core-back distance but different gas concentrations: (a) 0.3 wt%, (b) 0.6 wt%, and (c) 0.8 wt%[12].

Generally, the gate-nucleated cells would dissolve back into the melt during dwelling step, and then the secondary foaming initiated by the core-back operation. Obviously, a higher pressure drop rate could be achieved by increasing packing pressure, which is favorable to the cell nucleation and thus reduces the cell size and increases the cell density of foam[22, 23]. For instance, Wang et al.[12] reported that the cell size of reduced from 83 to 40 μm by improving the packing pressure from 15 to 25 MPa, as shown in Fig. 2-9.

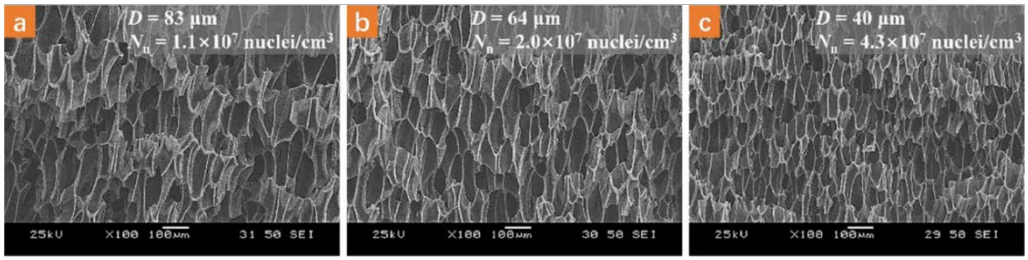

Fig. 2-9. The cellular morphology of the PEBA foams fabricated by core-back FIM using various packing pressures: (a) 15 MPa, (b) 20 MPa, and (c) 25 MPa[12].

During the dwelling step, the temperature of polymer/gas mixture in the mold cavity will drop rapidly and approach the mold temperature. Thus, the foaming temperature as well as the melt strength in the polymer can be controlled. If the used polymer is semicrystalline polymer, the non-isothermal crystallization would occur simultaneously. The formation of crystals could act as heterogeneous NA to offer a large number of nucleation sites during foaming[4, 24, 25]. Thus, changing the

dwelling time is a common method to control the cell structure[26, 27]. Wang et al.[27] investigated the influence of dwelling time on the cell structure of PP/NA foams. They found that by increasing the dwelling time from 3.4 s to 4.2 s, the foaming temperature (the polymer/gas mixture temperature after dwelling stage, the mold temperature was set as 40 ℃) decreased from 101 ℃ to 90 ℃ (measured by a temperature sensor), leading to the distinct improvement of cell structure (the cell density increased from 1.1×10^{9} to 4.2×10^{10} cells/cm^{3}), as depicted in Fig. 2-10.

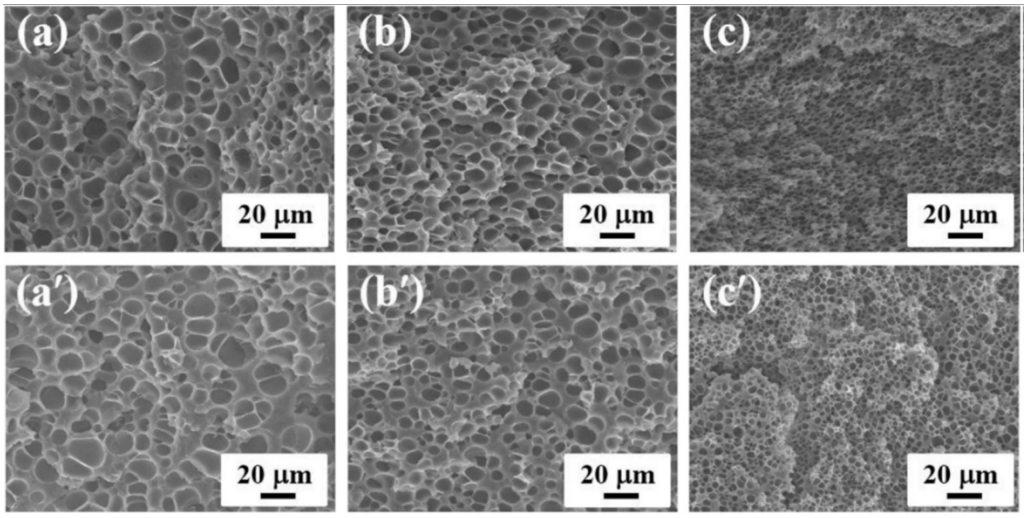

Fig. 2-10. SEM micrographs of PP/NA foams fabricated at a foaming temperature of (a, a') 101 ℃, (b, b') 95 ℃, and (c, c') 90 ℃, respectively. (a–c), and (a'–c') are taken from the views parallel and perpendicular to the core-back direction, respectively[27].

The VF or expansion ratio can be precisely controlled by changing the core-back distance. However, the other cell structure parameters such as cell size and OCC would also change with the increase of expansion ratio. Wang et al.[28] studied the cell structure of long-chain branched polypropylene (LCBPP) under different expansion ratios, as shown in Fig. 2-11. 2-fold expansion foams showed a spherical

cell shape. When the expansion ratio increased to 5-fold, elliptical cells could be found. With the further increase of expansion ratio, cells were greatly elongated along the core-back direction due to the extensional stress induced by the core-back operation. Increasing the expansion ratio would also lead to the transition of cell structure from closed cell structure to open cell structure. Jahani et al.[29] reported that the OCC improved to about 70%, when the expansion ratio increased to 4.5-fold (Fig. 2-12).

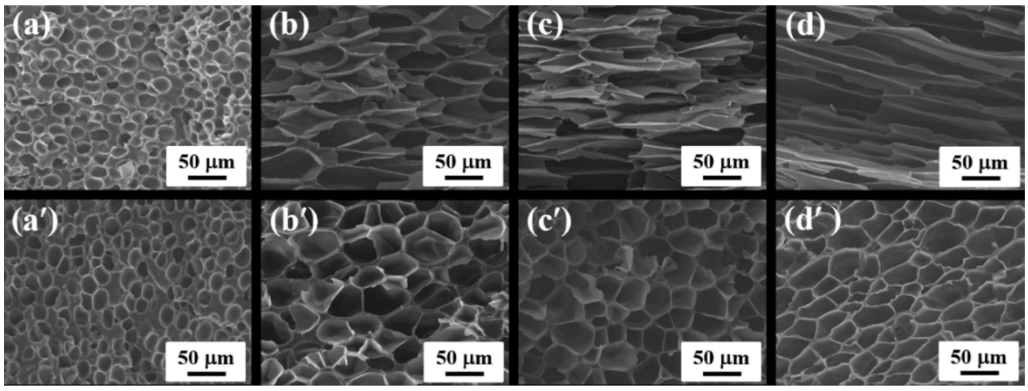

Fig. 2-11. SEM micrographs of the cross-section of LCBPP foams in the core layer at expansion ratios of (a, a') 2-fold, (b, b') 5-fold, (c, c') 7-fold, and (d, d') 10-fold at a fixed dwelling time of 3 s (foaming temperature = 109 °C). (a−d) and (a'−d') are taken from the views parallel and perpendicular to the core-back direction, respectively[28].

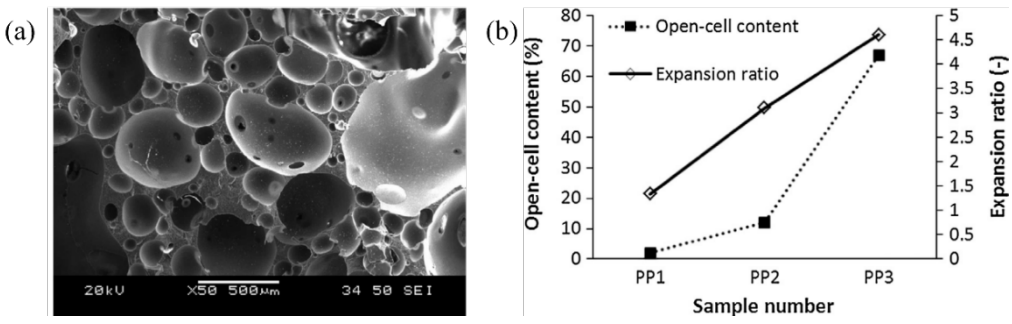

Fig. 2-12. (a) SEM images of foam with expansion ratio of 4.5-fold (PP3). (b) OCC and the expansion ratio of PP foams[29].

2.2. Polymeric foam toughening technology

In recent years, PP and PLA have been extensively used to fabricate foams. However, their inherent brittleness hampers their foams' wide applications. Up to now, sufficient articles published just focused on the modification of cell structure, and only a few attempts have conducted to improve the toughness of foams. The major methods can be divided into four kinds: blending, adding inorganic fillers, tailoring crystallization, and adjusting cell structure.

2.2.1. Blending

It is well known that incorporating rubber particles into the polymer matrix is effective in toughening polymer[30, 31]. Sun et al.[32, 33] proved that this method can be used to toughen foams. PP/HDPE blend foams with different HDPE content (0, 25, 50, 75, 100 wt%) were prepared, and the tensile test results showed that PP/HDPE (75/25) exhibited the highest elongation at break of 690%, as shown in Fig. 2-13. Further investigation about the morphology under different elongation showed that the PP/HDPE (75/25) foams were greatly fibrillated along the tensile load direction in the necking region (Fig. 2-14a). The authors proposed that a microcellular structure (cell size < 100 μm) with a sub-micron scale immiscible secondary phase (HDPE phases with cell size below 1 μm) was the key to increase toughness (Fig. 2-14b). Under loading, the debonding of the second phases were beneficial to the interconnection of micro-sized cells to form channels, so that the stretched part became a bundle of fibrils, leading to a significant improvement in

toughness. Furthermore, similar results can be found in PP/low-density polyethylene (LDPE) and PP/PHBV blend foams[33].

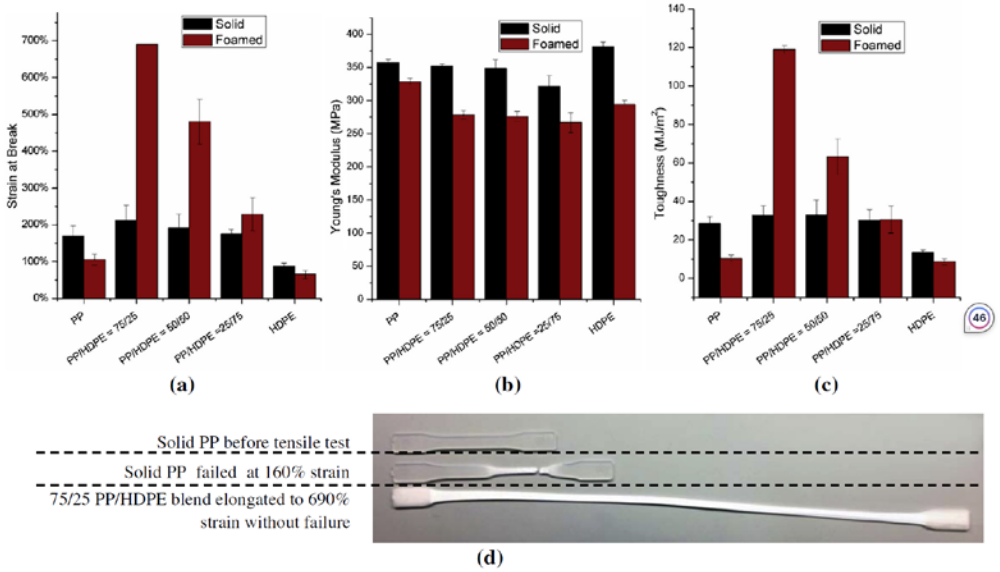

Fig. 2-13. (a) Elongation at break, (b) Young's modulus, and (c) tensile toughness for PP/HDPE blends at various composition ratios. (d) Examples of injection molded parts before and after tensile test to demonstrate the significant ductility improvement of microcellular 75/25 PP/HDPE blend[32].

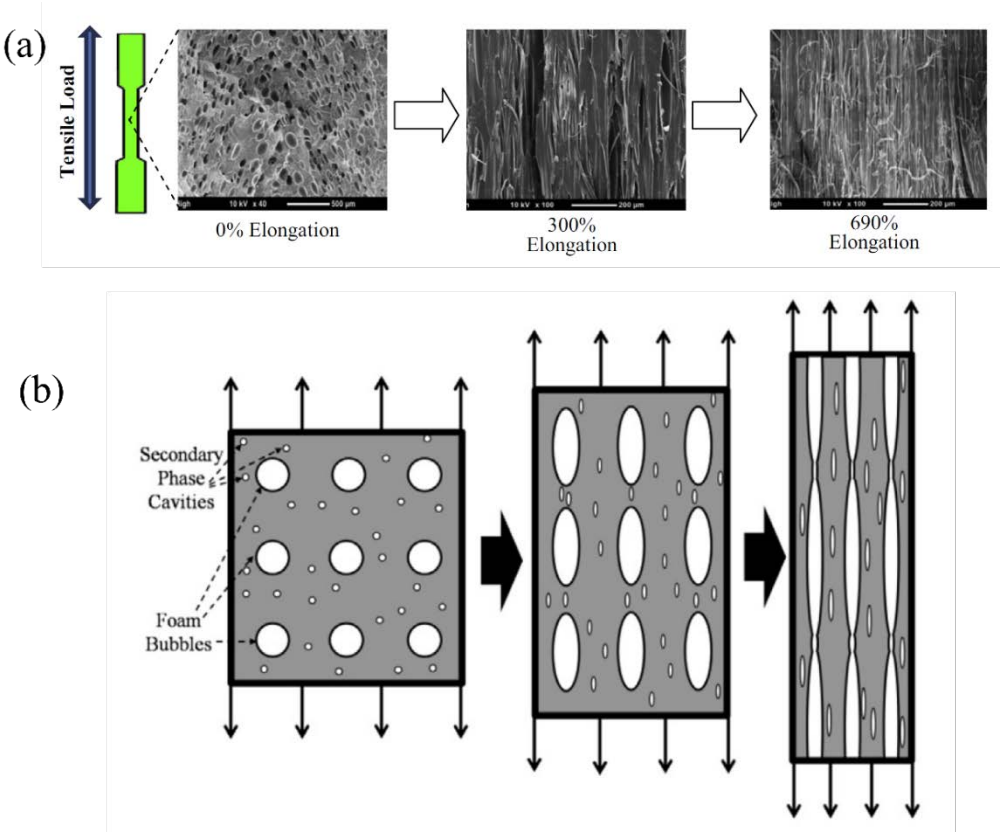

Fig. 2-14. (a) SEM images of the 75/25 PP/HDPE foamed part at different elongations. (b) Schematic of the ductility enhancing mechanism by microcellular foam structure[32].

It has been reported that in situ fibrillation method based on polymer blending of a second-phase polymer can enhance the impact toughness of foams[34, 35]. Zhao et al.[34] found that the in-situ fibrillated PP/polytetrafluoroethylene (PTFE) composites can be simply prepared through a co-rotating twin-screw extruder (Fig. 2-15). The well dispersed PTFE fibrils significantly enhanced crystallization and melt strength of PP, leading to the refined cell structure and enhanced impact strength (Fig. 2-16). By adding 5 wt% PTFE, the impact strength increased by more than 250%. The enhancement in toughness was attributed to the three reasons. First, the introduction of PTFE fibrils could refine the crystals and thus improve the

roughness of PP matrix. Second, the existing of PTFE fibrils reduced the cell size, which could prevent the foams from crack initiation and propagation during the impact test. Third, the weak cohesive forces between PTFE chains was favorable for the sliding of PP crystals，especially for high PTFE content. Wang et al.[35] prepared nanofibrillar PLA/polyethylene terephthalate (PET) by using core-back FIM, and found that the Izod impact strength increased by more than 6 times compared with PLA foam obtained by regular foaming injection mold. The combined effects of the existing of the tough PET nanofibrils, refined crystals and reduced cell size leaded to the improvement of impact strength.

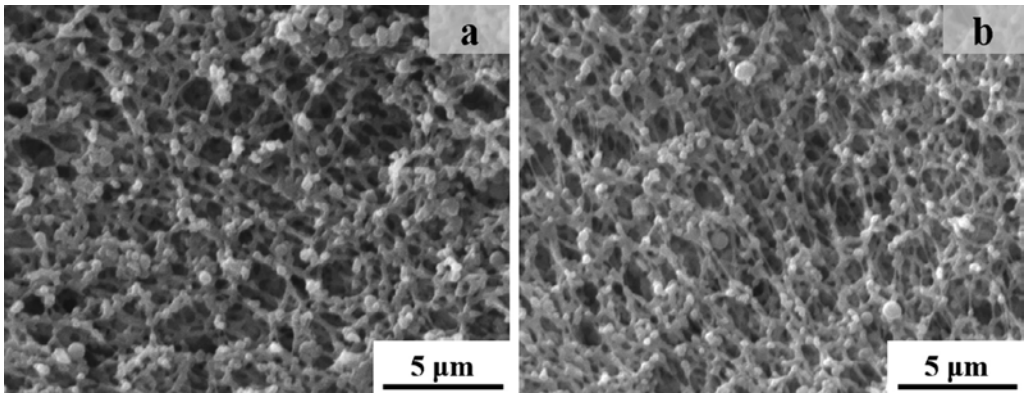

Fig. 2-15. SEM micrograph of PP/PTFE composites with (a) 1 wt% and (b) 5 wt% PTFE after etching PP matrix using xylene[34].

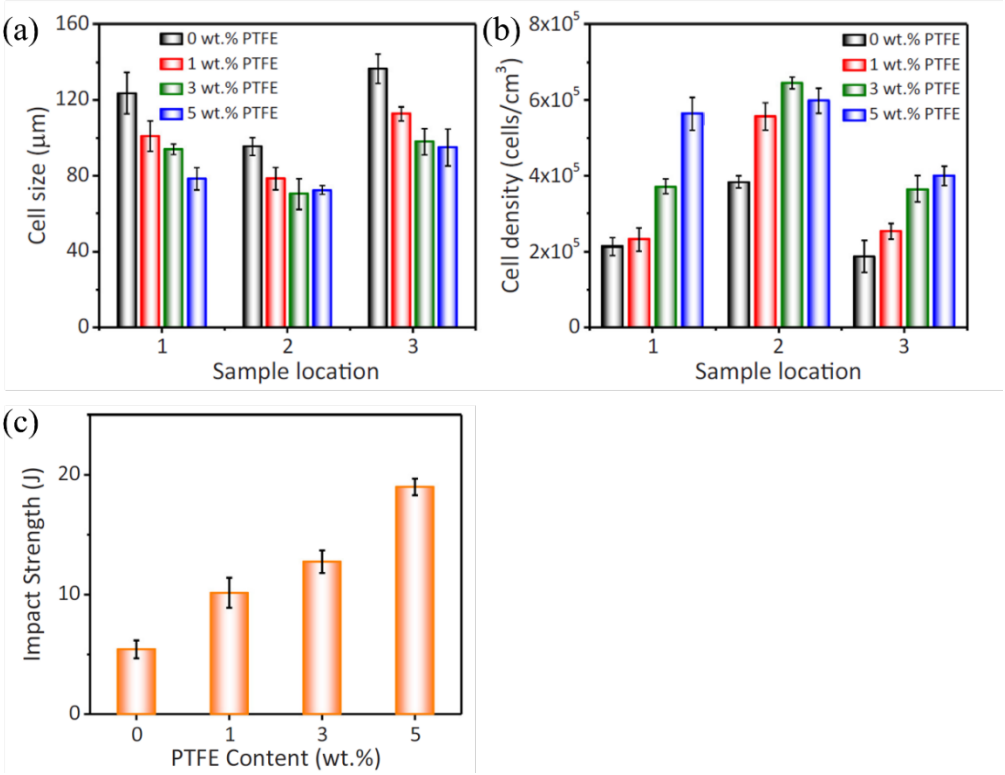

Fig. 2-16. Foam structure comparisons of the injection molded PP/PTFE composite foams: (a) cell size and (b) cell density. (c) Gardner impact strength of the prepared foams[34].

2.2.2. Adding inorganic fillers

The introduction of inorganic fillers into polymer can effectively promote the foamability of polymer since it could not only enhance melt strength but also act as cell NAs during foaming process[36, 37]. For semicrystalline polymers such PP and PLA, inorganic fillers could also accelerate the crystallization behavior, and further improve the foamability[38]. Thus, a uniform cell structure with small cell size can be obtained, which may be beneficial to the improvement of impact strength.

Najafi et al.[39] added nanoclay into linear PLA and long chain branched (LCB) PLA, and investigated their effects on cell structure and impact strength. The results

showed that PLA/clay nanocomposite foams showed a lower specific impact strength than that of solid counterparts, due to the poor cell structure (Fig. 2-17). However, The specific impact strength of LCB-PLA/clay nanocomposite foams improved after adding clay, and the LCB-PLA foam containing 0.5 wt% clay presented the highest impact strength of 19.1 (kJ m^{-2})/(kg m^{-3}), exhibiting an increase of 37% in comparison to LCB-PLA foam. The underlying toughening mechanism was that the uniform distributed smaller-sized cells could improve the energy dissipation. Wang et al.[40] investigated the effect of particle size on the impact toughness of PP/talc composites foams. The PP/nano-talc composite foam depicted a significantly improved impact strength compared with he PP/micro-talc composite foam, even they had a similar cell structure. It may be attributed to the fact that nano talc can reduce the crystal size of PP and strengthen shear slipping of polymer chains, leading to the enhancement of energy absorption.

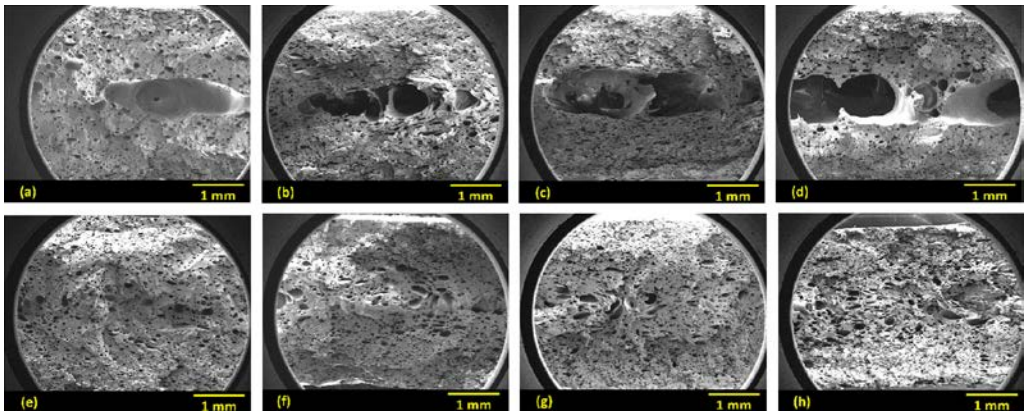

Fig. 2-17. Representative SEM micrographs of (a) neat PLA (b) PLA–0.25 wt% clay, (c) PLA–0.5 wt% clay, (d) PLA–1 wt% clay, (e) LCB-PLA, (f) LCB-PLA–0.25 wt% clay, (g) LCB-PLA–0.5 wt% clay, and (h) LCB-PLA–1 wt% clay[39].

2.2.3. Tailoring crystallization

For semicrystalline polymer foams, the transition of crystal structure from spherulite to oriented microfiber structure could significantly promote the impact strength. Mi et al.[41] first prepared highly oriented PP samples with shish-kebab crystalline structure using a self-developed loop oscillating push-pull molding (LOPPM) device. The shish-kebab crystal has highly oriented chains of polymer molecules (shish) surrounded by plate-like lamellar crystals with periodic distances (kebabs)[42]. Then, the LOPPM-PP was foamed through batch foaming, resulting in the formation of nano cells with cell size of 55.3 nm. LOPPM-PP foam showed impact strength of 23.9 kj/m^2, which was 7.5 and 1.6 times that of solid PP and LOPPM-PP, respectively. Fig. 2-18 shows the schematic of shish-kebab structure formation in LOPPM processing and nanoscale cells formation during foaming. The enhanced toughness was attributed to the shish-kebab structure as well as the nano sized cells. Xiang et al.[43] prepared strong tough PLA foams by using pressure-induced-flow (PIF) processing followed by supercritical CO_2 foaming (Fig. 2-19). Due to the oriented crystals as well as the presence of both micron and nano cells, the PLA foam obtained at 40 ℃ showed a great impact strength of 32.3 kJ/m^2.

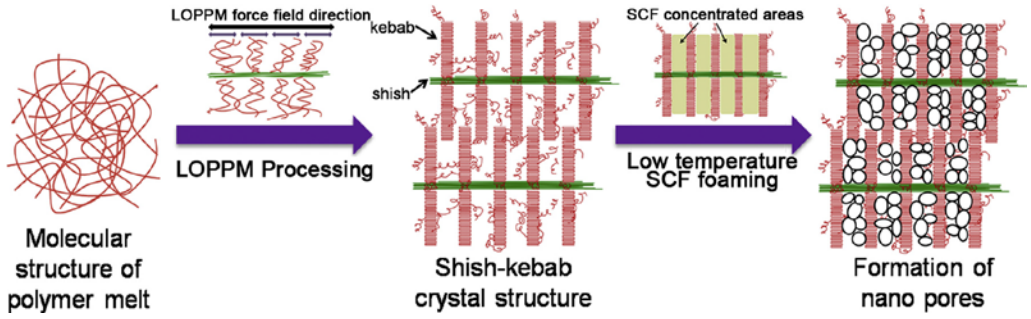

Fig. 2-18. Schematic of shish-kebab structure formation in LOPPM processing and nanoscale cells formation during foaming[41].

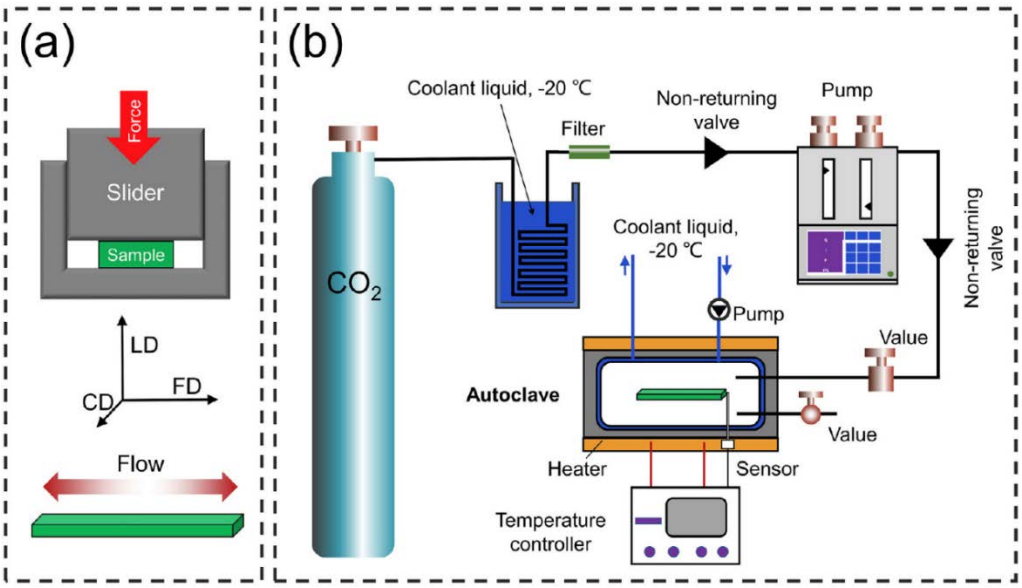

Fig. 2-19. Schematic of the preparation process. (a) PIF processing and (b) supercritical CO_2 foaming[43].

2.2.4. Adjusting cell structure

Usually, the dependence between density and the physical properties of porous materials can be well formulated by the Gibson and Ashby equation [44]:

$$P_f = C \cdot P_s \cdot \left(\frac{\rho_f}{\rho_s} \right)^n \tag{2-5}$$

where P_f and P_s are the properties of a porous material and the corresponding solid material, respectively. C and n usually take values of about 1 and 2, respectively. Thus, the trend of reducing impact toughness as a function of decreased density (or increased VF) has been extensively reported in PET, polyvinyl chloride (PVC), polycarbonate (PC), polystyrene (PS) microcellular foams[45-48]. However, Bao et al. [49] prepared PP foams with different cell sizes (1–50 μm) and relative densities (0.04–0.86) and found that with the decrease in relative density, the impact strength

first improved before a relative density of about 0.6 and then reduced. Those PP foams with enhanced impact strength all presented small cell sizes (< 10 μm), which could initiate plastic deformation and thus absorb a lot of energy. Fig. 2-20 shows the SEM images of the impact-fractured surfaces of the solid PP and PP foams. It indicated that except for relative density, cell size would also influence the impact strength. Thus, it is necessary to decouple the contributions of relative density and cell size on the impact strength of foams.

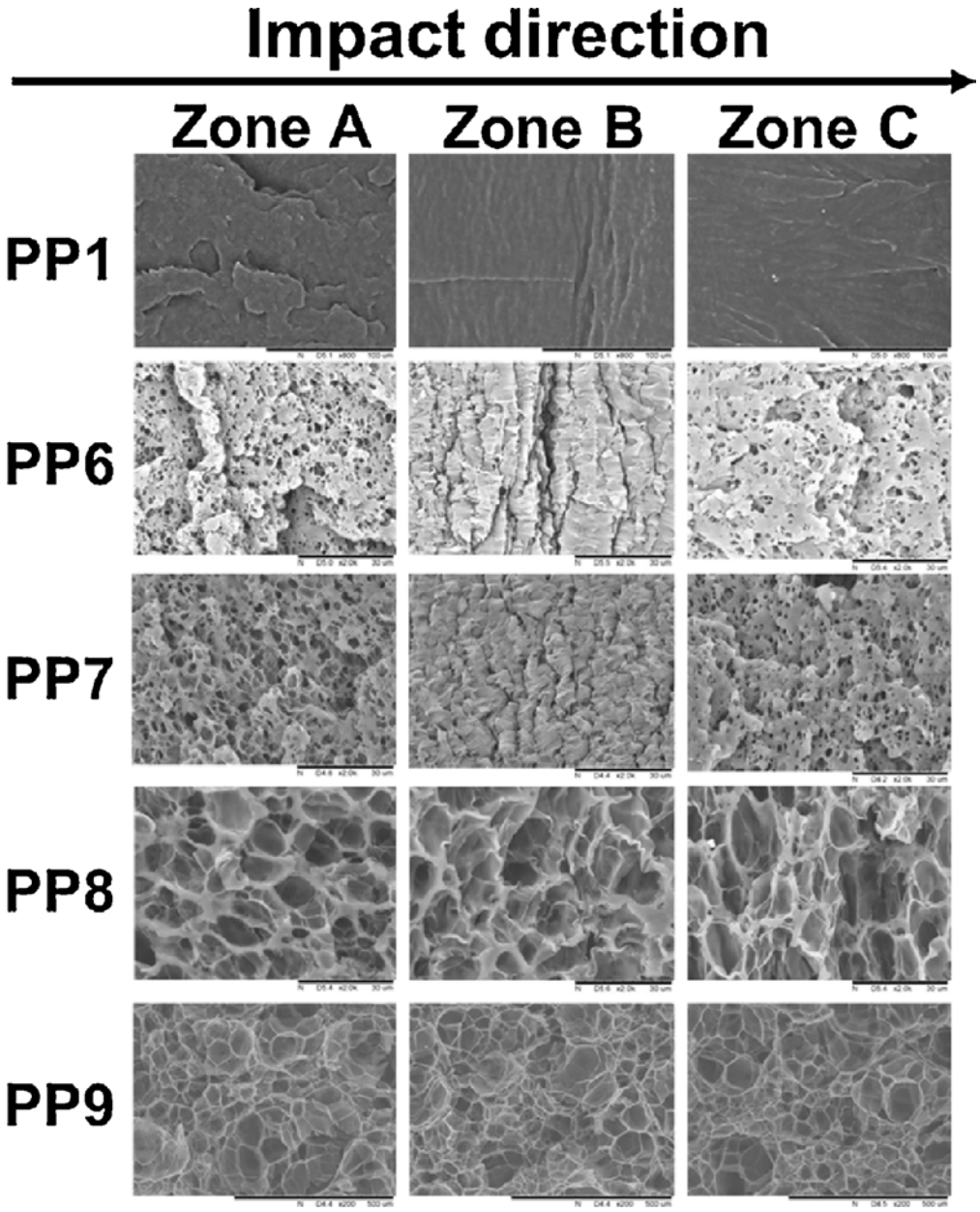

Fig. 2-20. SEM images of the impact-fractured surfaces of the solid PP (PP1) and PP foams (PP6–PP9). The relative density of PP6. PP7, PP8, and PP9 were 0.67, 0.62, 0.38 and 0.04. The scale bar in PP1 is 100 μm; the scale bar in PP6–PP8 is 30 μm; and the scale bar in PP9 is 500 μm[49].

May be due to the difficulty of preparing foams with various cell sizes for a constant

density through bath foaming, the researches about the relationship between cell size and impact strength are still rare. Notario et al.[50] fabricated several polymethyl methacrylate (PMMA) foams with cell sizes ranging from 200 nm to 11 μm and relative densities of about 0.5, and proved that the nanocellular foams presented a higher impact strength in comparison with micro cellular foams, as shown in Fig. 2-21. Similar result was reported by Miler et al.[51] for polyetherimide (PEI) foams. They observed that the impact strength of nanocellular foams were higher than microcellular ones at the same relative density. However, contradictory results have emerged regarding the effect of cell size on impact strength for microcellular foams. Barlow et al[52] prepared PC foams with different cell sizes (6–18 μm) while maintaining a constant relative density (0.7), and found that the impact strength enhanced with the increase of cell size. Conversely, Bao et al compared the impact strength of PS foams with different cell sizes and the same relative density, revealing a decline in impact strength with the enlargement of cell size at the same relative density (0.3 or 0.56). In a word, no conclusive results in the relation between cell size and impact strength were found and more work is needed.

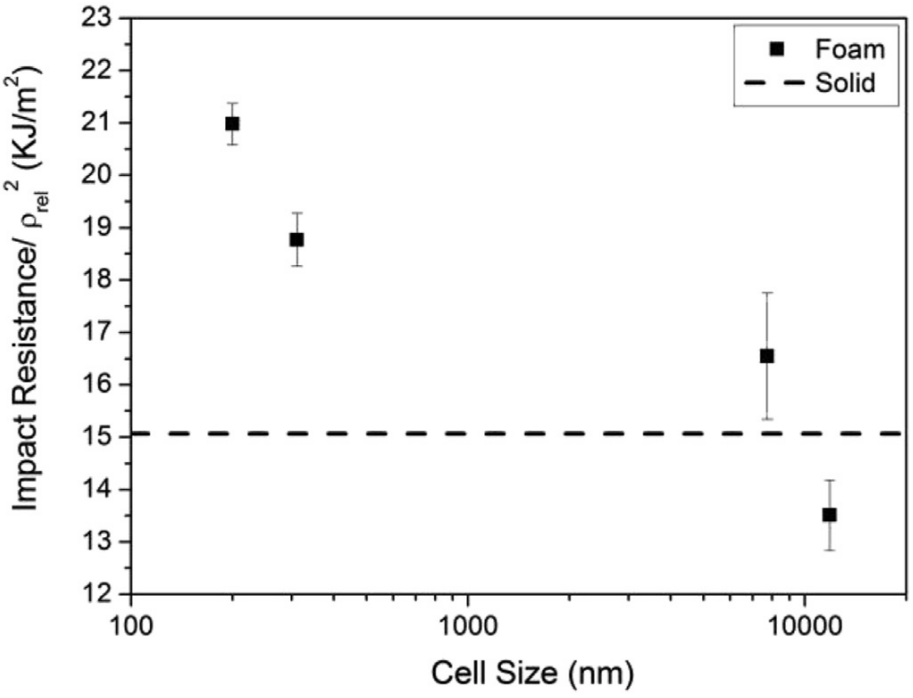

Fig. 2-21. Mechanical behavior at high strain rates divided by the square of the relative density for both PMMA solid and for PMMA microcellular and nanocellular foams[50].

2.3. Methods for improving EC of CPC foams

In recent years, the popularity of wireless communication equipment and electronic components has led to serious electromagnetic pollution, threatening the function of electronic devices and the health of human being[53, 54]. Therefore, there is an urgent need for electromagnetic shielding materials to attenuate electromagnetic waves and reduce electromagnetic radiation. Compared to the traditional metal-based materials, CPC foams have gained special attention, owing to their advantages of light weight, chemical corrosion resistance, easy processability and low cost[55, 56]. To obtain desirable EMI shielding properties, it is important to fabricate CPC

foams with an effective conductive network at low filler loading. Generally, several methods have been developed to increase EC of CPC foams, including polymer modification and cell structure modification.

2.3.1. Polymer modification

The polymer modification methods are referring to the introduction of conductive fillers into the polymer matrix. When the conductive filler content reaches a critical value, the interconnected network of conductive fillers is built up, and thus the insulating polymer becomes a CPC. This mechanism can be explained by electrical percolation threshold theory. The commonly used conductive fillers include CB, CF, CNT, graphene, CNF and MXene. Generally, the higher length-to width aspect ratio leads to a low electrical percolation threshold[57, 58]. Thus, adding CNT into polymer always has a lower electrical percolation threshold in comparison with the introduction of graphene.

The incorporation of other conductive fillers into original carbon networks has been dominated as an effective method to improve EC. Safdari et al.[59] compared the electrical properties of epoxy/CNT, epoxy/GNP, and bybrid epoxy/GNP/CNT composites, and both experimental and computational results suggested that adding a small amount of nanofiller could greatly increase the EC of the hybrid composites by several orders of magnitudes. Fig. 2-22 shows that CNTs could connect with sounding GNPs to form a percolation network. Ma et al.[60] prepared polyvinylidene fluoride/multiwalled carbon nanotubes/graphene (PVDF/MWCNT/graphene) foam via a new water vapor-induced phase separation method. With a filler content of 16 wt%, the EC of PVDF/WMCNT/graphene foam

was as high as 20.8 S/m, while that of PVDF/graphene foam and PVDF/WMCNT foam was just 5.6 and 8.9 S/m. Owing to the effective conductive network of hybrid fillers, PVDF/WMCNT/graphene foam with a thickness of 2 mm depicted an EMI SE of 28.5 dB. Similar results also can be found in poly(acrylonitrile-co-butadiene-co-styrene) (ABS)/CB/WMCNT, PVDF/graphene/silicon carbide nanowire (SiCnw) and PDMS/MWCNT/cotton fibers composites[61-63].

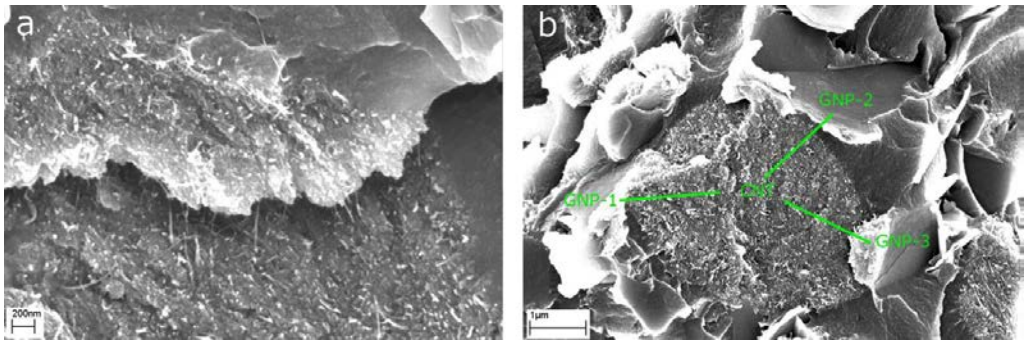

Fig. 2-22. SEM images from hybrid nanocomposite specimen with 5.0%wt GNPs and 0.5%wt CNTs. (a) Flexible CNTs connecting large two-dimensional (2D) GNPs (b) A CNT cluster connecting three GNPs[59].

2.3.2. Cell structure modification

It has been widely accepted that foaming could improve electrical properties of CPCs owning to the excluded volume effect[64]. Li et al.[65] fabricated epoxy/functionalized MWCNT (F-MWCNT) microcellular foams through a supercritical CO_2 foaming method, and found that the electrical percolation threshold reduced from 0.32 to 0.21 vol% after foaming, as shown in Fig. 2-23. This is because foaming can orient the conductive fillers around cells, promoting the formation of a more impactful conductive path in CPCs, leading to the improvement of EC and EMI SE. Hamidinejad et al.[66] studied the effect of foaming on the

electrical properties of HDPE/GNP foams, and the results showed that the EC was increased by up to 9 orders of magnitude and the electrical percolation threshold are reduced by 62%. The highest EMI SE of 31.6 dB was obtained for HDPE/GNP (19 vol%) composite foam, while that of solid counterparts was just 21.8 dB.

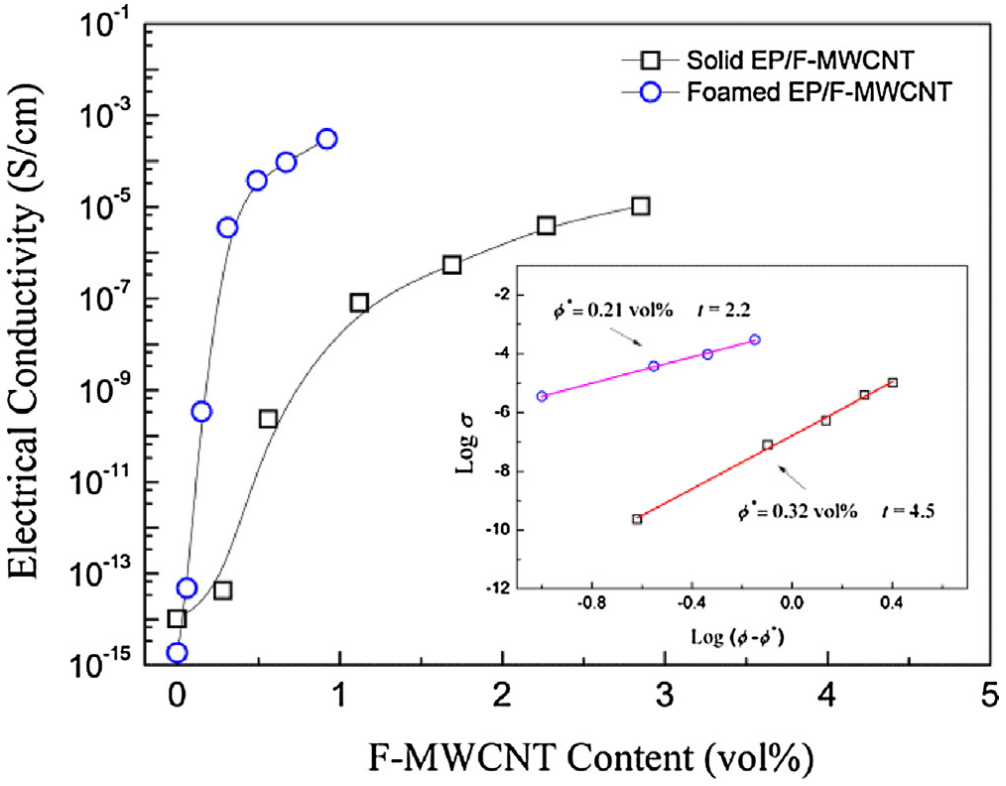

Fig. 2-23. EC for solid EP/F-MWCNT composites and foamed composites with various F-MWCNT content[65].

The electrical properties are also influenced by the relative density (or VF) of CPC foams. Ameli et al.[67] prepared PP/MWCNT foams with various relative density (0.1–1) and investigated the evolution of electrical properties with relative density. The results (Fig. 2-24) showed that as the relative density decreased from 1 (solid) to 0.8, the EC initially increased due the slight orientation of MWCNTs around the cells, which were favorable for the MWCNT interconnections. However, with the

further decrease of relative density, the EC gradually decreased due to the full orientation of MWCNTs perpendicular to the radial direction, resulting in a reduction in MWCNT interconnections. Fig. 2-25 shows the evolution of the MWCNT dispersion with foaming. In foaming process, the biaxial stretching leaded to the slight orientation of MWCNTs around the cells while the cell-to cell compression made them close to each other, increasing the interconnections of WMCNT and the EC. When the relative density below an optimum value, the MWCNTs were fully oriented perpendicular to the cell radius, leading to the destruction of conductive path. Thus, the EC became to decrease. Similar results have been reported in PS/WMCNT and Polyurethane (PU)/MWCNT composite foams[68, 69]. Considering the effect of location and orientation of conductive filler on the EC of CPC foams, Monte Carlo simulations were applied to investigate the EC under various VFs[69-71]. The model predictions were in good agreement with the experimental results. Therefore, choosing the optimum relative density (or VF) is one of the key factors to obtain CPC foams with enhanced electrical properties.

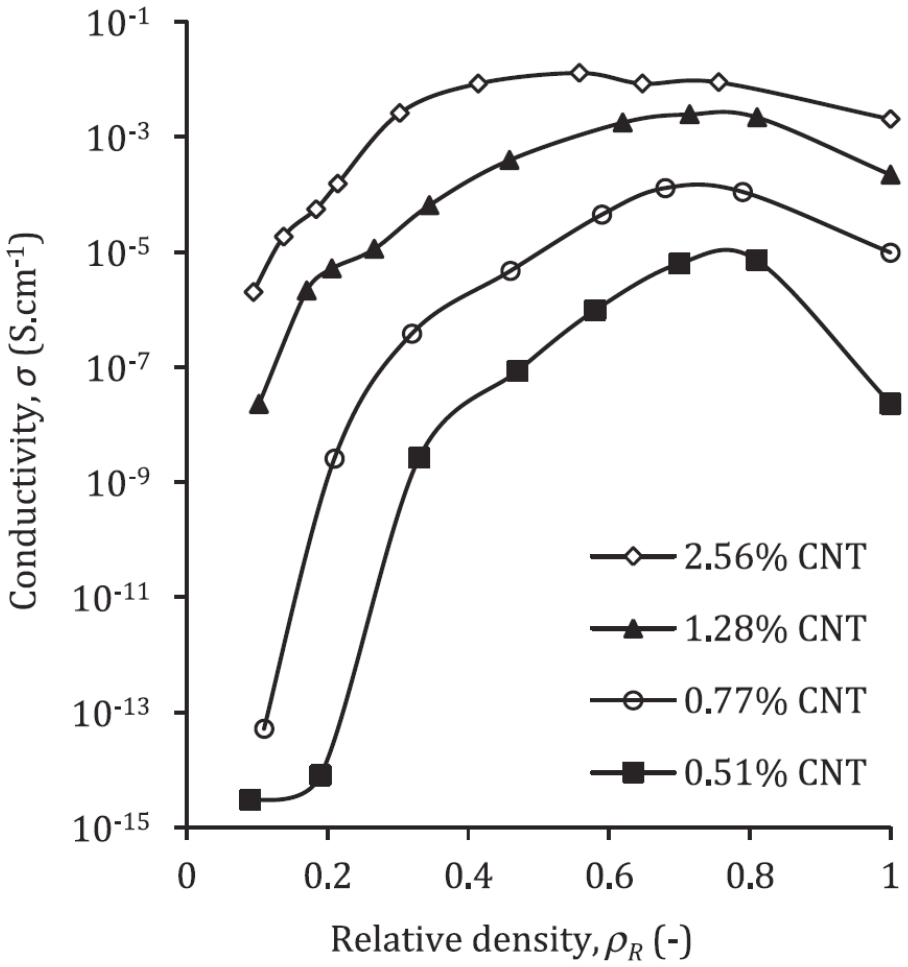

Fig. 2-24. EC of PP/MWCNT nanocomposites with different vol.% MWCNT as a function of relative density[67].

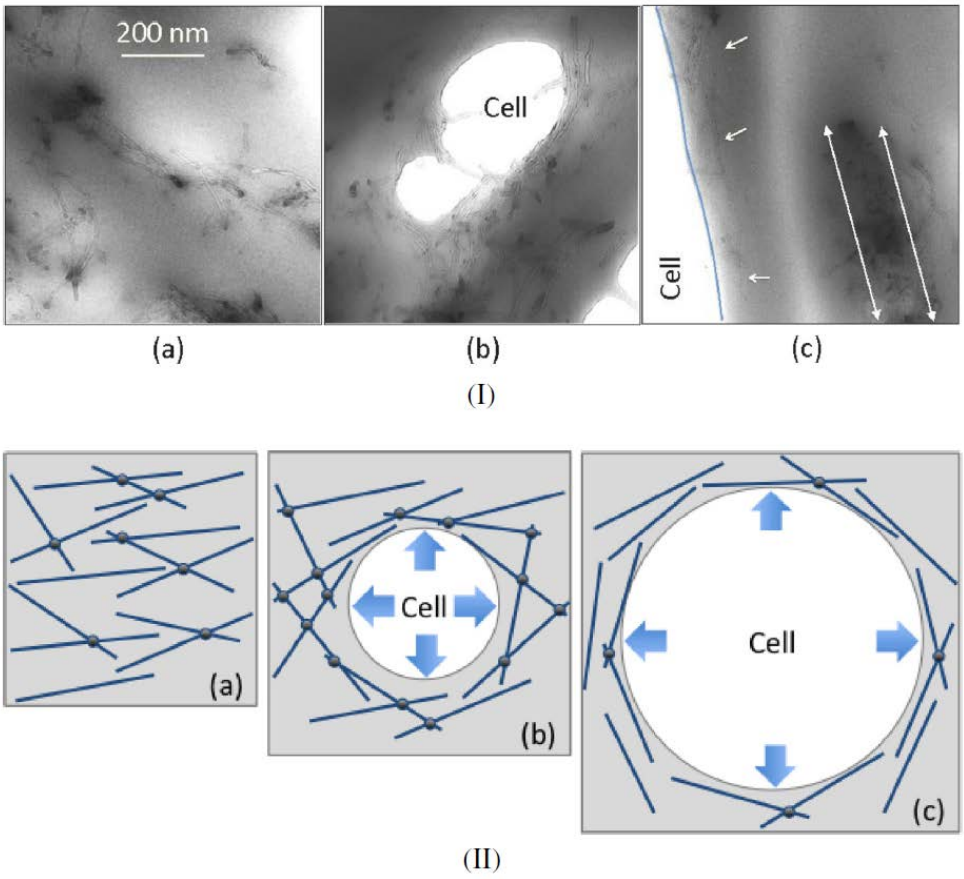

Fig. 2-25. (I) TEM images illustrating MWCNT alignment in solid and foamed PP/MWCNT (1.28 vol.%) nanocomposites. The relative density of (a), (b) and (c) are 1, 0.7 and 0.2, respectively. (II) 2-D conceptualization of the evolution of MWCNT interconnection with foaming. The relative density of (a), (b) and (c) are 1, 0.7 and 0.2, respectively[67].

2.4. Methods for improving sound insulation properties of polymer foams

In recent years, noise pollution has become one of the major concerns of environmental issues and personal unhealthiness, and polymeric soundproofing

materials have been extensively used in noise control applications[30]. Sound insulation properties of the samples are characterized by STL, which defined as the logarithmic ratio of the incident acoustic power (Ei) to transmitted acoustic power (Et) as illustrated in Eq.:

$$STL = 10\log_{10}\frac{E_i}{E_t} \tag{2-6}$$

where E_i and E_t are the incident sound energy and transmitted sound energy, respectively. For certain incident sound waves, the bigger the STL value, the better the sound insulation properties.

The general variation of the STL with frequency for a homogeneous material is depicted in Fig. 2-26. It is noticed that there are three general regions and two special frequencies[72, 73]:

(a) Region I: stiffness-controlled region. The STL is controlled mainly by the stiffness of the panel. For a given frequency, a higher stiffness will lead to a higher STL.

(b) Resonant frequency (f_r): It is calculated using equation:

$$f_r = \frac{Bh}{2\pi ab}\sqrt{\frac{E}{\rho\left(1-v^2\right)}} \tag{2-7}$$

where B=10.4; h, a, b, E, ρ, v are the thickness, length, wideth, elastic modulus, density and Poisson ratio of panel, respectively.

(c) Region II: mass-controlled region. The STL is determined by the mass of the panel. The STL for normal incidence (STL_n) is determined by equation:

$$STL_n = 20\lg\left(\rho_m \cdot f\right) - 43 \tag{2-8}$$

where m and f are the surface density of panel and frequency. The STL for random incidence can be calculated through the following expression:

$$STL = STL_n - 5 \tag{2-9}$$

In this region, if the frequency is doubled the STL will increase by 6 dB/octave.

(d) Critical frequency: When the frequency of the sound wave improves in the mass-controlled region, the wavelength of bending waves in the material will get close to that in the air. The occurrence of the equality of both wavelengths will lead to the panel vibrating, resulting the significant decrease in STL.

(e) Region III: damping-controlled region. The STL is strongly related to the frequency of the incident sound waves and the internal damping of the panel material.

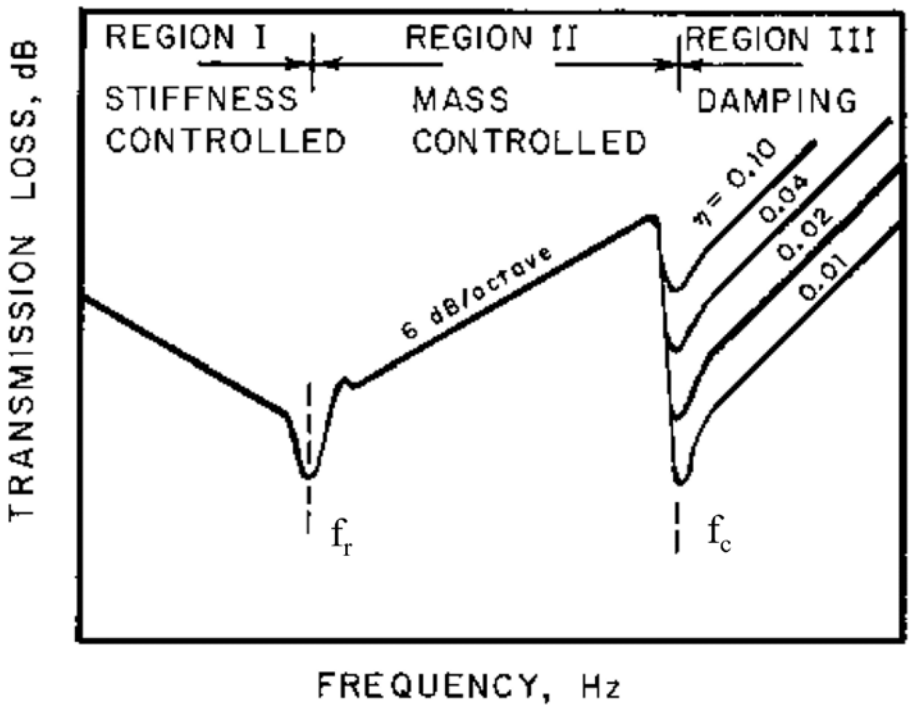

Fig. 2-26. General variation of the transmission loss with frequency for a homogeneous material[72].

Compared with the solid polymers, polymer foams depicted the reduced density and enhanced sound insulation properties [74]. For polymer foams, the acoustic impedance mismatch between air and polymer leads to the partial reflection of sound waves at the interface and prolongs the sound propagation path (Fig. 2-27), enhancing the dissipation of sound energy[75]. The main approaches for increasing sound insulation properties of polymer foams involve adding fillers, adjusting cell structure and multilayer structure design.

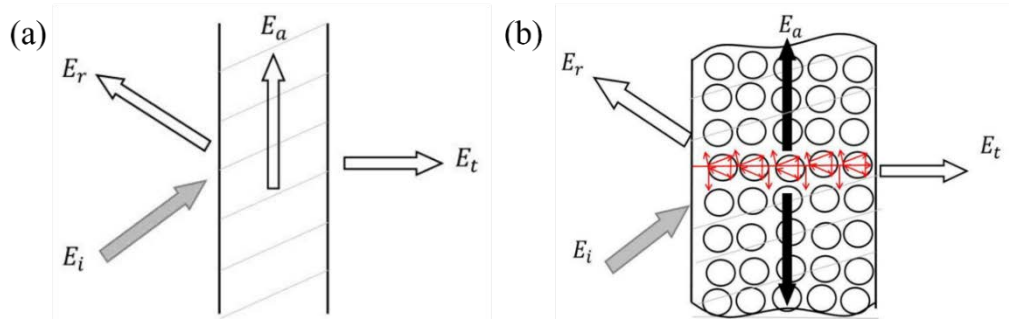

Fig. 2-27. Schematic of sound transmission in (a) solid and (b) foamed samples.

2.4.1. Adding fillers

Filling inorganic fillers, including mica, glass bead, calcium carbonate ($CaCO_3$), hollow glass bead (HGB), CNT, and clay, into polymer materials can enhance the sound insulation properties of polymer foams by increasing their density and stiffness[76-78]. Xu et al.[77] studied the effect of mica content on the sound insulation performance of PVC/mica composite foams. By adding 10 wt% mica, the STL of PVC/mica composite foams increased from 23 to 28 dB. Liao et al.[79] reported that the STL of nitrile tubber/PVC/heavy metal particles composite foams improved from 21 to 30 dB when the content of heavy metal particles increased from 0 to 30 phr. Except for inorganic fillers, organic fillers can also be added in

polymer foams to improve the STL. Chen et al. found that the PU foam containing 8 wt% bamboo chips showed a high STL of 18.9 dB, an increase of 80% in comparison with PU foam.

2.4.2. Adjusting cell structure

Generally, the sound insulation properties improved with the increase of VF, since the thickness of the tested samples was also increased, which would prolong the transmission pathway of sound waves[80-82]. Jahani et al.[80] prepared PC foams with different expansion rate by using core-back FIM. The foams exhibited the same weigh, and their thickness was increased with increasing expansion ratio. The results showed that the STL improved with the increase of expansion ratio. It could be attributed to the elongation of the propagation path of sound waves. Wu et al.[82] reported that the STL of PP foams improved from 18 to 35 dB by increasing the expansion ratio from 1 to 4.5-fold. Xue et al.[83] fabricated epoxy foams with different density using non-traditional expandable microspheres. When the foam density reduced from 0.97 to 0.66 g/cm^3, the STL greatly improved from 16 to 28 dB. With the further reduction of foam density from 0.66 to 0.59 g/cm^3, however, the STL gradually decreased to 22 dB. The impaired sound insulation performance could be attributed to the breakage of some microspheres at low foam density, which would extremely shorten the propagation path of sound wave and weaken the sound reflection.

Zhao et al.[81] prepared PP/PTFE foams with various PTFE content using core-back FIM. The results showed that at a given expansion ratio, with the increase of PTFE content, the cell size decreased, leading to the improvement of STL. However,

it did not reveal the relationship between cell size and STL, since PTFE content was also a variable. Xu et al. prepared PVC/mica (90/10) composite foams using chemical foaming method. By increasing the foaming time, the cell size and foam density of samples reduced, resulting in the enhanced STL. The authors attributed this to the cell growth-induced orientation of mica in cell walls (caused by the small cell size). However, the thickness of sample was also increased by increasing foaming time, and this factor had not been considered. Based on the previous analysis, the relationship between cell size and STL at a given expansion ratio is still not clear.

2.4.3. Multilayer structure design

Promoting the sound insolation properties of polymer by structure design has gained attentions in recent years. Multilayered composites with cell structure may have great potential in achieving excellent sound insulation properties[74, 84]. It is because the sound waves would reflect at the interface between two mediums (e.g. polymer/air, or two different polymers) due to the acoustic impedance mismatch, prolonging the sound transmission path. Besides, it is well known that partial sound wave energy dissipates as energy owning to viscous friction between polymer chains and air friction in cells[85, 86]. Thus, the longer sound transmission path is beneficial to the consumption of sound wave energy.

The acoustic impedance (Z) of a medium depends on the density (ρ) and sound speed (c) of the medium, as illustrated in equation:

$$Z = \rho c \tag{2-10}$$

For solid medium, the longitudinal sound speed is calculated using the following

equation:

$$c = \sqrt{\frac{E(1-v)}{\rho(1+v)(1-2v)}} \tag{2-11}$$

where v and E are the sound speed and elastic modulus of the sample, respectively. The impedance ratio of adjacent mediums (γ) and the reflection coefficient of sound energy at the interface (RE) of two mediums can be calculated by the equations:

$$\gamma = Z_a / Z_b \tag{2-12}$$

$$RE = \left(\frac{Z_b - Z_a}{Z_b + Z_a} \right)^2 \tag{2-13}$$

where Z_a and Z_b are the acoustic impedance of medium a and medium b, respectively. Obviously, the bigger the impedance mismatch is, the more repeated reflections of sound waves at the interfaces are. Repeated reflections can prolong the sound transmission path, leading to the improvement of air fraction, viscoelastic damping and sound dissipation.

Han et al.[87] prepared PVC-based foam/film alternating multilayered composites using multilayered co-extrusion system and studied their sound insulation properties. They reported that the STL of foam/film multilayered composites were higher than that of unfoamed film/film multilayered composites. In addition, with the increase of layer number from 2 to16 (Fig. 2-28), the STL of the composite gradually improved from 22.4 to 26.2 dB. It can be attributed to the fact that increasing the layer and interface number enhanced the sound reflection at interfaces and elongated the sound propagation path, leading to the improvement of sound dissipation. However, with the further increase of layer number, the STL of 16-layer composite

reduced to 24.7 dB due to the reduction of reflection and scattering of sound waves in the cells, as shown in Fig. 2-29. Du et al.[88] investigated the sound insulation performance of PP/polyolefin elastomer (POE) blend foams with multi-layer-oriented structure. First, PP/POE blend with multi-layer-oriented structure (Fig. 2-30e) was obtained through pressure induced flow (PIF) process (Fig. 2-30a). Then, cell structure was introduced into PP/POE blend using supercritical CO_2 foaming process (Fig. 2-30b). The multi-layer-oriented structure of PP/POE foam (Fig. 2-30g and h) significantly improved the reflection of sound waves and thus led to enhanced STL. The resulting PIF PP/POE foam showed a super high STL of 103.6 dB, which was 67.2 dB higher than PP/POE foam.

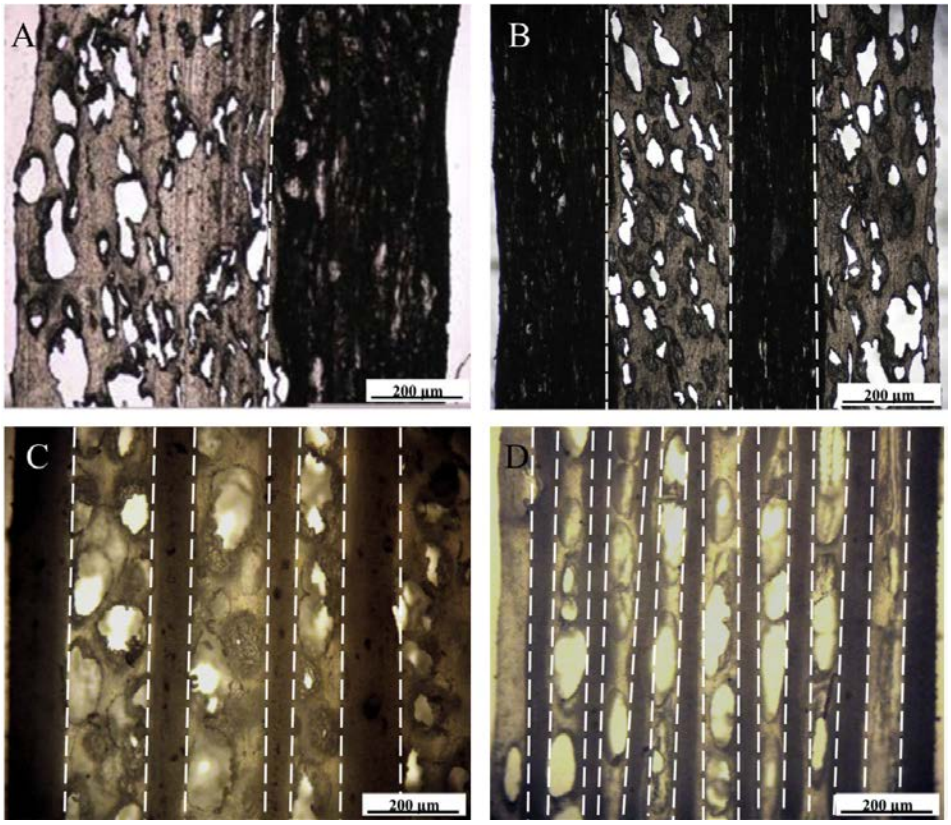

Fig. 2-28. Laminar morphologies of PVC composites with different layer numbers. A: 2-layer; B: 4-layer; C: 8-layer; D: 16-layer[87].

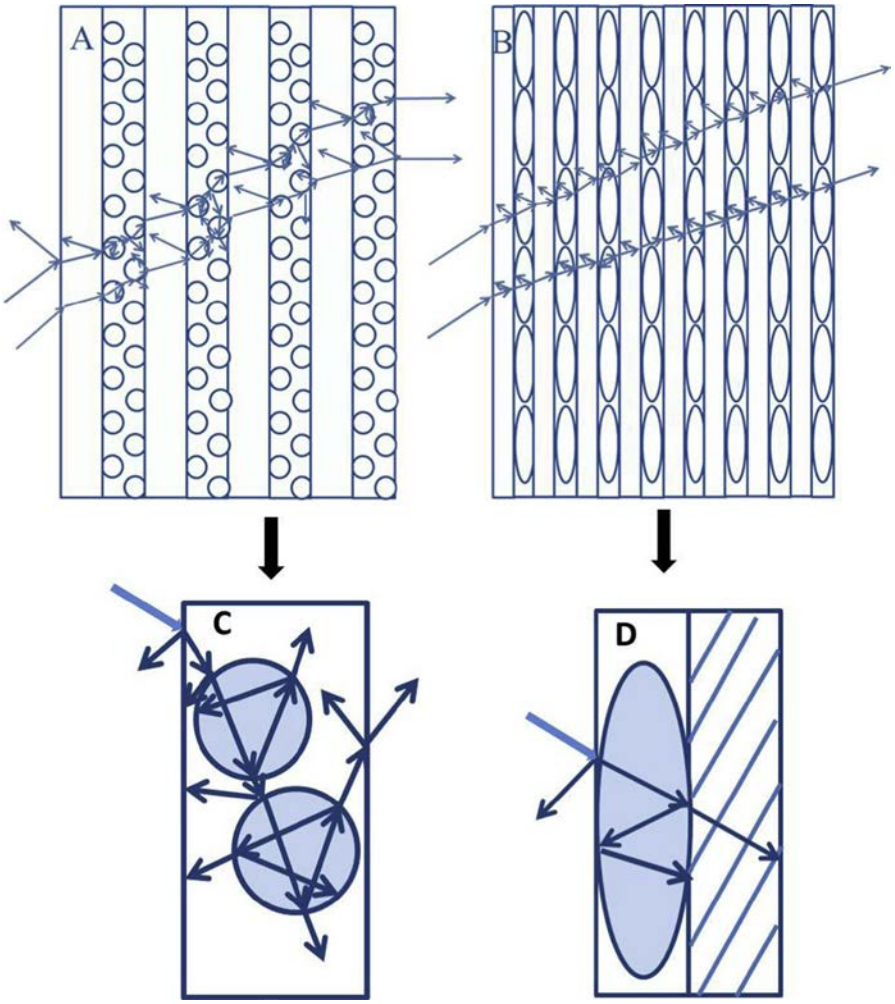

Fig. 2-29. Schematic of sound transmission path in PVC multilayered composite. A: 8-layer; B: 16-layer; C: close-up image of A; D: close-up image of B[87].

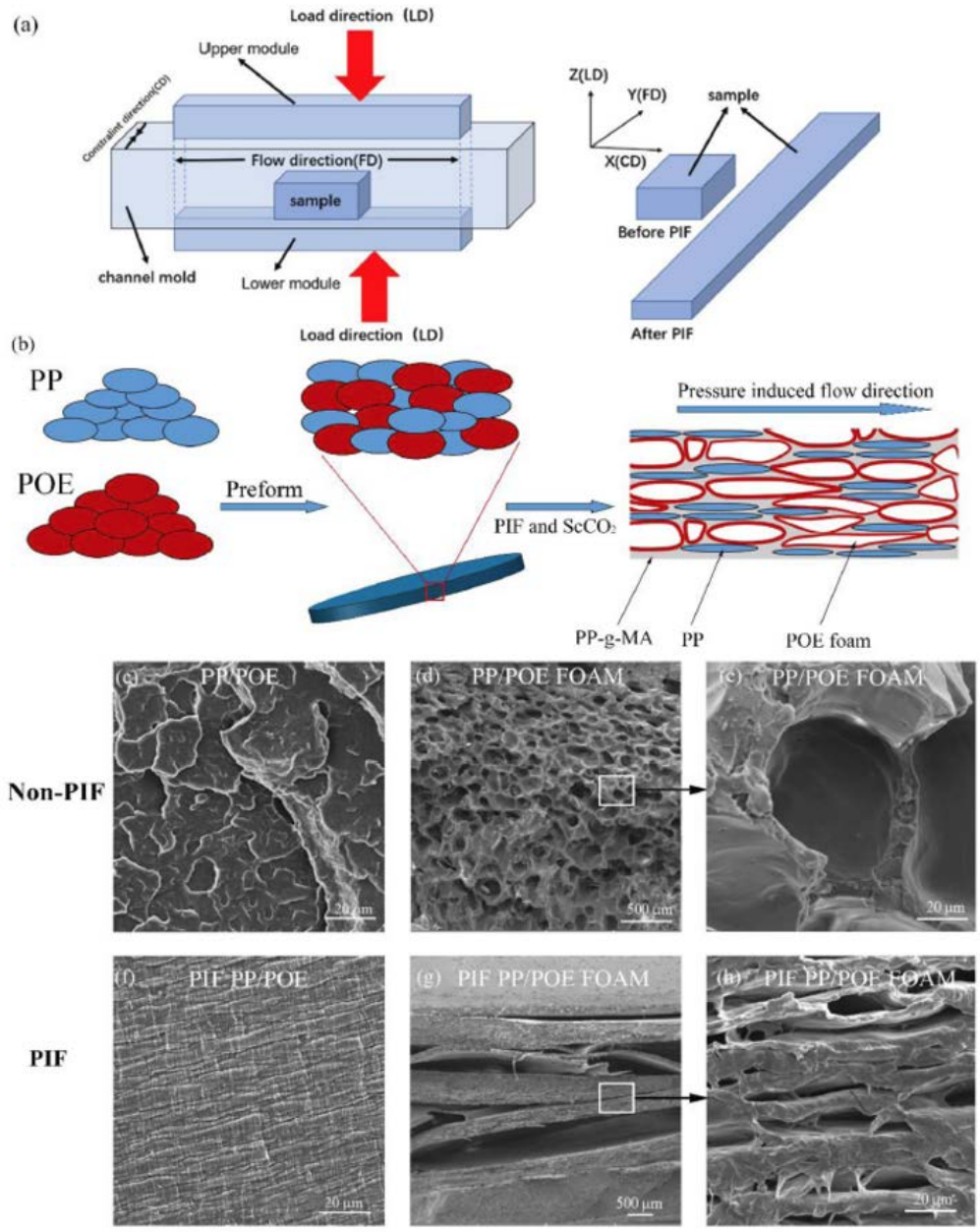

Fig. 2-30. (a) Schematic of the apparatus for PIF processing; (b) Schematic illustration of PIF PP/POE foam preparation. The SEM image of the cross-section of PP/POE(c), PP/POE foam(d), PP/POE foam at high magnification (e), PIF PP/POE (f), PIF PP/POE foam (g), PIF PP/POE foam at high magnification(h)[88].

2.5. Conclusions

The demand for the development of functional foams are emphasized in terms of toughness, electrical and sound insulation properties. The requisite introduction of toughening, electrical and sound insulation properties have been discussed, together with detailed reviews of various improvement methods.

The properties of polymer foams are strongly related to the cell structure, such as cell size, cell density, and VF. However, the relationship between cell size and properties is still imprecise. Since the cell structure can be accurately controlled using core-back FIM process, it is possible to study the effect of cell size on properties at a given void friction. This facilitates the preparation of high-performance foams and broadens their range of applications.

2.6. References

[1] L. Kishbaugh, M. Berry, 14 - Microcellular Injection Molding, in: M. Kutz (Ed.), Applied Plastics Engineering Handbook (Third Edition), William Andrew Publishing2024, pp. 297-311.

[2] L. Sorrentino, M. Aurilia, S. Iannace, Polymeric foams from high-performance thermoplastics, Adv. Polym. Technol. 30(3) (2011) 234-243. https://doi.org/10.1002/adv.20219

[3] R. Dugad, G. Radhakrishna, A. Gandhi, Recent advancements in manufacturing technologies of microcellular polymers: a review, J. Polym. Res. 27(7) (2020) 182. https://doi.org/10.1007/s10965-020-02157-7

[4] Q. Ren, M. Wu, L. Wang, W. Zheng, Y. Hikima, T. Semba, M. Ohshima, Cellulose nanofiber reinforced poly (lactic acid) with enhanced rheology, crystallization and foaming ability, Carbohydrate Polymers 286 (2022) 119320. https://doi.org/10.1016/j.carbpol.2022.119320

[5] M. Sauceau, J. Fages, A. Common, C. Nikitine, E. Rodier, New challenges in polymer foaming: A review of extrusion processes assisted by supercritical carbon dioxide, Prog. Polym. Sci. 36(6) (2011) 749-766. https://doi.org/10.1016/j.progpolymsci.2010.12.004

[6] C. Okolieocha, D. Raps, K. Subramaniam, V. Altstädt, Microcellular to nanocellular polymer foams: Progress (2004–2015) and future directions – A review, Eur. Polym. J. 73 (2015) 500-

519. https://doi.org/10.1016/j.eurpolymj.2015.11.001

[7] L. Wang, M. Ando, M. Kubota, S. Ishihara, Y. Hikima, M. Ohshima, T. Sekiguchi, A. Sato, H. Yano, Effects of hydrophobic-modified cellulose nanofibers (CNFs) on cell morphology and mechanical properties of high void fraction polypropylene nanocomposite foams, Composites, Part A 98 (2017) 166-173. https://doi.org/10.1016/j.compositesa.2017.03.028

[8] J.W.S. Lee, J. Wang, J.D. Yoon, C.B. Park, Strategies to Achieve a Uniform Cell Structure with a High Void Fraction in Advanced Structural Foam Molding, Ind. Eng. Chem. Res. 47(23) (2008) 9457-9464. https://doi.org/10.1021/ie0707016

[9] C.A. Villamizar, C.D. Han, Studies on structural foam processing II. Bubble dynamics in foam injection molding, Polym. Eng. Sci. 18(9) (1978) 699-710. https://doi.org/10.1002/pen.760180905

[10] A.K. Bledzki, H. Kirschling, M. Rohleder, A. Chate, Correlation between injection moulding processing parameters and mechanical properties of microcellular polycarbonate, J. Cell. Plast. 48(4) (2012) 301-340. https://doi.org/10.1177/0021955X12441193

[11] V. Shaayegan, L.H. Mark, A. Tabatabaei, C.B. Park, A new insight into foaming mechanisms in injection molding via a novel visualization mold, eXPRESS Polym. Lett. 10(6) (2016) 462-469. https://doi.org/10.3144/expresspolymlett.2016.44

[12] G. Wang, G. Zhao, G. Dong, Y. Mu, C.B. Park, G. Wang, Lightweight, super-elastic, and thermal-sound insulation bio-based PEBA foams fabricated by high-pressure foam injection molding with mold-opening, Eur. Polym. J. 103 (2018) 68-79. https://doi.org/10.1016/j.eurpolymj.2018.04.002

[13] M. Wu, Y. Pang, Z. Wang, F. Wu, W. Zheng, From the perspective of cells as dispersed phase in foam injection molding: Cell deformation of PP/PTFE foams, Polymer 272 (2023) 125842. https://doi.org/10.1016/j.polymer.2023.125842

[14] R.E. Lee, T. Azdast, G. Wang, X. Wang, P.C. Lee, C.B. Park, Highly expanded fine-cell foam of polylactide/polyhydroxyalkanoate/nano-fibrillated polytetrafluoroethylene composites blown with mold-opening injection molding, Int. J. Biol. Macromol. 155 (2020) 286-292. https://doi.org/10.1016/j.ijbiomac.2020.03.212

[15] V. Shaayegan, G. Wang, C.B. Park, Study of the bubble nucleation and growth mechanisms in high-pressure foam injection molding through in-situ visualization, Eur. Polym. J. 76 (2016) 2-13. https://doi.org/10.1016/j.eurpolymj.2015.11.021

[16] L. Chen, D. Rende, L.S. Schadler, R. Ozisik, Polymer nanocomposite foams, J. Mater. Chem. A 1(12) (2013) 3837-3850. https://doi.org/10.1039/c2ta00086e

[17] J.S. Colton, N.P. Suh, THE NUCLEATION OF MICROCELLULAR THERMOPLASTIC FOAM WITH ADDITIVES .1. THEORETICAL CONSIDERATIONS, Polym. Eng. Sci. 27(7) (1987) 485-492. https://doi.org/10.1002/pen.760270702

[18] J.S. Colton, N.P. Suh, THE NUCLEATION OF MICROCELLULAR THERMOPLASTIC

FOAM WITH ADDITIVES .2. EXPERIMENTAL RESULTS AND DISCUSSION, Polym. Eng. Sci. 27(7) (1987) 493-499. https://doi.org/10.1002/pen.760270703

[19] J.S. Colton, N.P. Suh, Nucleation of microcellular foam: Theory and practice, Polym. Eng. Sci. 27(7) (1987) 500-503. https://doi.org/10.1002/pen.760270704

[20] J.S. Colton, Nucleation of microcellular foams in semi-crystalline thermoplastics, Mater. Manuf. Processes 4(2) (1989) 253-262.

[21] V. Shaayegan, G. Wang, C.B. Park, Effect of foam processing parameters on bubble nucleation and growth dynamics in high-pressure foam injection molding, Chem. Eng. Sci. 155 (2016) 27-37. https://doi.org/10.1016/j.ces.2016.07.040

[22] D. Tammaro, A. Astarita, E. Di Maio, S. Iannace, Polystyrene Foaming at High Pressure Drop Rates, Ind. Eng. Chem. Res. 55(19) (2016) 5696-5701. https://doi.org/10.1021/acs.iecr.5b04911

[23] C.B. Park, D.F. Baldwin, N.P. Suh, Effect of the pressure drop rate on cell nucleation in continuous processing of microCell. Polym., Polym. Eng. Sci. 35(5) (1995) 432-440. https://doi.org/10.1002/pen.760350509

[24] Q. Ren, M. Wu, W. Li, X. Zhu, Y. Zhao, L. Wang, W. Zheng, A green fabrication method of poly (lactic acid) perforated membrane via tuned crystallization and gas diffusion process, Int. J. Biol. Macromol. 182 (2021) 1037-1046. https://doi.org/10.1016/j.ijbiomac.2021.04.105

[25] Q. Ren, M. Wu, Z. Weng, L. Wang, W. Zheng, Y. Hikima, M. Ohshima, Lightweight and strong gelling agent-reinforced injection-molded polypropylene composite foams fabricated using low-pressure CO2 as the foaming agent, J. CO2 Util. 48 (2021) 101530. https://doi.org/10.1016/j.jcou.2021.101530

[26] R. Miyamoto, S. Yasuhara, H. Shikuma, M. Ohshima, Preparation of micro/nanocellular polypropylene foam with crystal nucleating agents, Polym. Eng. Sci. 54(9) (2014) 2075-2085. https://doi.org/10.1002/pen.23758

[27] L. Wang, Y. Hikima, S. Ishihara, M. Ohshima, Fabrication of lightweight microcellular foams in injection-molded polypropylene using the synergy of long-chain branches and crystal nucleating agents, Polymer 128 (2017) 119-127. https://doi.org/10.1016/j.polymer.2017.09.025

[28] L. Wang, S. Ishihara, M. Ando, A. Minato, Y. Hikima, M. Ohshima, Fabrication of High Expansion Microcellular Injection-Molded Polypropylene Foams by Adding Long-Chain Branches, Ind. Eng. Chem. Res. 55(46) (2016) 11970-11982. https://doi.org/10.1021/acs.iecr.6b03641

[29] D. Jahani, A. Ameli, P.U. Jung, M.R. Barzegari, C.B. Park, H. Naguib, Open-cell cavity-integrated injection-molded acoustic polypropylene foams, Mater. Des. 53 (2014) 20-28. https://doi.org/10.1016/j.matdes.2013.06.063

[30] M. Ponçot, F. Addiego, A. Dahoun, True intrinsic mechanical behaviour of semi-crystalline and amorphous polymers: Influences of volume deformation and cavities shape, Int. J. Plast. 40

(2013) 126-139. https://doi.org/10.1016/j.ijplas.2012.07.007

[31] J.C.C. Yeo, J.K. Muiruri, J.J. Koh, W. Thitsartarn, X. Zhang, J. Kong, T.T. Lin, Z. Li, C. He, Bend, Twist, and Turn: First Bendable and Malleable Toughened PLA Green Composites, Adv. Funct. Mater. 30(30) (2020) 2001565. https://doi.org/10.1002/adfm.202001565

[32] X. Sun, H. Kharbas, J. Peng, L.-S. Turng, Fabrication of super ductile polymeric blends using microcellular injection molding, Manuf. Lett. 2(2) (2014) 64-68. https://doi.org/10.1016/j.mfglet.2014.02.002

[33] X. Sun, H. Kharbas, J. Peng, L.-S. Turng, A novel method of producing lightweight microcellular injection molded parts with improved ductility and toughness, Polymer 56 (2015) 102-110. https://doi.org/10.1016/j.polymer.2014.09.066

[34] J. Zhao, G. Wang, L. Zhang, B. Li, C. Wang, G. Zhao, C.B. Park, Lightweight and strong fibrillary PTFE reinforced polypropylene composite foams fabricated by foam injection molding, Eur. Polym. J. 119 (2019) 22-31. https://doi.org/10.1016/j.eurpolymj.2019.07.016

[35] G. Wang, J. Zhao, G. Wang, H. Zhao, J. Lin, G. Zhao, C.B. Park, Strong and super thermally insulating in-situ nanofibrillar PLA/PET composite foam fabricated by high-pressure microcellular injection molding, Chem. Eng. J. 390 (2020) 124520. https://doi.org/10.1016/j.cej.2020.124520

[36] B. Zhu, W. Zha, J. Yang, C. Zhang, L.J. Lee, Layered-silicate based polystyrene nanocomposite microcellular foam using supercritical carbon dioxide as blowing agent, Polymer 51(10) (2010) 2177-2184. https://doi.org/10.1016/j.polymer.2010.03.026

[37] Y. Qin, Q. Peng, Y. Ding, Z. Lin, C. Wang, Y. Li, J. Li, Y. Yuan, X. He, Y. Li, Lightweight, Superelastic, and Mechanically Flexible Graphene/Polyimide Nanocomposite Foam for Strain Sensor Application, ACS Nano 9(9) (2015) 8933-8941. https://doi.org/10.1021/acsnano.5b02781

[38] M. Nofar, Effects of nano-/micro-sized additives and the corresponding induced crystallinity on the extrusion foaming behavior of PLA using supercritical CO2, Mater. Des. 101 (2016) 24-34. https://doi.org/10.1016/j.matdes.2016.03.147

[39] N. Najafi, M.-C. Heuzey, P.J. Carreau, D. Therriault, C.B. Park, Mechanical and morphological properties of injection molded linear and branched-polylactide (PLA) nanocomposite foams, Eur. Polym. J. 73 (2015) 455-465. https://doi.org/10.1016/j.eurpolymj.2015.11.003

[40] G. Wang, G. Zhao, G. Dong, Y. Mu, C.B. Park, Lightweight and strong microcellular injection molded PP/talc nanocomposite, Compos. Sci. Technol. 168 (2018) 38-46. https://doi.org/10.1016/j.compscitech.2018.09.009

[41] H.-Y. Mi, J.-W. Chen, L.-H. Geng, B.-Y. Chen, X. Jing, X.-F. Peng, Formation of nanoscale pores in shish-kebab structured isotactic polypropylene by supercritical CO2 foaming, Mater. Lett. 167 (2016) 274-277. https://doi.org/10.1016/j.matlet.2015.12.116

[42] L. Yang, R.H. Somani, I. Sics, B.S. Hsiao, R. Kolb, H. Fruitwala, C. Ong, Shear-Induced

Crystallization Precursor Studies in Model Polyethylene Blends by in-Situ Rheo-SAXS and Rheo-WAXD, Macromolecules 37(13) (2004) 4845-4859. https://doi.org/10.1021/ma049925f

[43] P. Xiang, L. Gou, Y. Zou, B. Chen, S. Bi, X. Chen, P. Yu, A facile strategy for preparation of strong tough poly(lactic acid) foam with a unique microfibrillated bimodal micro/nano cellular structure, Int. J. Biol. Macromol. 199 (2022) 264-274. https://doi.org/10.1016/j.ijbiomac.2021.12.187

[44] L.J. Gibson, M.F. Ashby, Cellular Solids: Structure and Properties, 2 ed., Cambridge University Press, Cambridge, 1997.

[45] D.I. Collias, D.G. Baird, R.J.M. Borggreve, Impact toughening of polycarbonate by microcellular foaming, Polymer 35(18) (1994) 3978-3983. https://doi.org/10.1016/0032-3861(94)90283-6

[46] R.P. Juntunen, V. Kumar, J.E. Weller, W.P. Bezubic, Impact strength of high density microcellular poly(vinyl chloride) foams, J. Vinyl Addit. Technol. 6(2) (2000) 93-99. https://doi.org/10.1002/vnl.10230

[47] V. Kumar, R.P. Juntunen, C. Barlow, Impact strength of high relative density solid state carbon dioxide blown crystallizable poly(ethylene terephthalate) microcellular foams, Cell. Polym. 19(1) (2000) 25-37.

[48] J.B. Bao, T. Liu, L. Zhao, G.H. Hu, X.R. Miao, X.H. Li, Oriented foaming of polystyrene with supercritical carbon dioxide for toughening, Polymer 53(25) (2012) 5982-5993. https://doi.org/10.1016/j.polymer.2012.10.011

[49] J.-B. Bao, A. Nyantakyi Junior, G.-S. Weng, J. Wang, Y.-W. Fang, G.-H. Hu, Tensile and impact properties of microcellular isotactic polypropylene (PP) foams obtained by supercritical carbon dioxide, J. Supercrit. Fluids 111 (2016) 63-73. https://doi.org/10.1016/j.supflu.2016.01.016

[50] B. Notario, J. Pinto, M.A. Rodríguez-Pérez, Towards a new generation of polymeric foams: PMMA nanocellular foams with enhanced physical properties, Polymer 63 (2015) 116-126. https://doi.org/10.1016/j.polymer.2015.03.003

[51] D. Miller, V. Kumar, Microcellular and nanocellular solid-state polyetherimide (PEI) foams using sub-critical carbon dioxide II. Tensile and impact properties, Polymer 52(13) (2011) 2910-2919. https://doi.org/10.1016/j.polymer.2011.04.049

[52] C. Barlow, V. Kumar, B. Flinn, R.K. Bordia, J. Weller, Impact Strength of High Density Solid-State Microcellular Polycarbonate Foams, J. Eng. Mater. Technol. 123(2) (2000) 229-233. https://doi.org/10.1115/1.1339004

[53] Z. Ma, S. Kang, J. Ma, L. Shao, Y. Zhang, C. Liu, A. Wei, X. Xiang, L. Wei, J. Gu, Ultraflexible and Mechanically Strong Double-Layered Aramid Nanofiber–Ti3C2Tx MXene/Silver Nanowire Nanocomposite Papers for High-Performance Electromagnetic Interference Shielding, ACS Nano 14(7) (2020) 8368-8382. https://doi.org/10.1021/acsnano.0c02401

[54] Q. Song, F. Ye, X. Yin, W. Li, H. Li, Y. Liu, K. Li, K. Xie, X. Li, Q. Fu, L. Cheng, L. Zhang, B.

Wei, Carbon Nanotube–Multilayered Graphene Edge Plane Core–Shell Hybrid Foams for Ultrahigh-Performance Electromagnetic-Interference Shielding, Adv. Mater. 29(31) (2017) 1701583. https://doi.org/10.1002/adma.201701583

[55] Y. Li, X. Lan, F. Wu, J. Liu, P. Huang, Y. Chong, H. Luo, B. Shen, W. Zheng, Steam-chest molding of polypropylene/carbon black composite foams as broadband EMI shields with high absorptivity, Compos. Commun. 22 (2020) 100508. https://doi.org/10.1016/j.coco.2020.100508

[56] N. Yousefi, X. Sun, X. Lin, X. Shen, J. Jia, B. Zhang, B. Tang, M. Chan, J.-K. Kim, Highly Aligned Graphene/Polymer Nanocomposites with Excellent Dielectric Properties for High-Performance Electromagnetic Interference Shielding, Adv. Mater. 26(31) (2014) 5480-5487. https://doi.org/10.1002/adma.201305293

[57] C.-W. Nan, Y. Shen, J. Ma, Physical Properties of Composites Near Percolation, Annu. Rev. Mater. Res. 40 (2010) 131-151. https://doi.org/10.1146/annurev-matsci-070909-104529

[58] J. Li, P.C. Ma, W.S. Chow, C.K. To, B.Z. Tang, J.-K. Kim, Correlations between Percolation Threshold, Dispersion State, and Aspect Ratio of Carbon Nanotubes, Adv. Funct. Mater. 17(16) (2007) 3207-3215. https://doi.org/10.1002/adfm.200700065

[59] M. Safdari, M.S. Al-Haik, Synergistic electrical and thermal transport properties of hybrid polymeric nanocomposites based on carbon nanotubes and graphite nanoplatelets, Carbon 64 (2013) 111-121. https://doi.org/10.1016/j.carbon.2013.07.042

[60] X. Ma, B. Shen, L. Zhang, Y. Liu, W. Zhai, W. Zheng, Porous superhydrophobic polymer/carbon composites for lightweight and self-cleaning EMI shielding application, Compos. Sci. Technol. 158 (2018) 86-93. https://doi.org/10.1016/j.compscitech.2018.02.006

[61] M.H. Al-Saleh, U. Sundararaj, Microstructure, electrical, and electromagnetic interference shielding properties of carbon nanotube/acrylonitrile–butadiene–styrene nanocomposites, J. Polym. Sci., Part B: Polym. Phys. 50(19) (2012) 1356-1362. https://doi.org/10.1002/polb.23129

[62] C. Liang, M. Hamidinejad, L. Ma, Z. Wang, C.B. Park, Lightweight and flexible graphene/SiC-nanowires/poly(vinylidene fluoride) composites for electromagnetic interference shielding and thermal management, Carbon 156 (2020) 58-66. https://doi.org/10.1016/j.carbon.2019.09.044

[63] J. Li, Y.-J. Tan, Y.-F. Chen, H. Wu, S. Guo, M. Wang, Constructing multiple interfaces in polydimethylsiloxane/multi-walled carbon nanotubes nanocomposites by the incorporation of cotton fibers for high-performance electromagnetic interference shielding and mechanical enhancement, Appl. Surf. Sci. 466 (2019) 657-665. https://doi.org/10.1016/j.apsusc.2018.10.079

[64] X. Cui, J. Chen, Y. Zhu, W. Jiang, Lightweight and conductive carbon black/chlorinated poly(propylene carbonate) foams with a remarkable negative temperature coefficient effect of resistance for temperature sensor applications, J. Mater. Chem. C 6(35) (2018) 9354-9362.

https://doi.org/10.1039/C8TC02123F

[65] J. Li, G. Zhang, H. Zhang, X. Fan, L. Zhou, Z. Shang, X. Shi, Electrical conductivity and electromagnetic interference shielding of epoxy nanocomposite foams containing functionalized multi-wall carbon nanotubes, Appl. Surf. Sci. 428 (2018) 7-16. https://doi.org/10.1016/j.apsusc.2017.08.234

[66] M. Hamidinejad, B. Zhao, A. Zandieh, N. Moghimian, T. Filleter, C.B. Park, Enhanced Electrical and Electromagnetic Interference Shielding Properties of Polymer–Graphene Nanoplatelet Composites Fabricated via Supercritical-Fluid Treatment and Physical Foaming, ACS Appl. Mater. Interfaces 10(36) (2018) 30752-30761. https://doi.org/10.1021/acsami.8b10745

[67] A. Ameli, M. Nofar, C.B. Park, P. Pötschke, G. Rizvi, Polypropylene/carbon nanotube nano/microcellular structures with high dielectric permittivity, low dielectric loss, and low percolation threshold, Carbon 71 (2014) 206-217. https://doi.org/10.1016/j.carbon.2014.01.031

[68] N. Athanasopoulos, A. Baltopoulos, M. Matzakou, A. Vavouliotis, V. Kostopoulos, Electrical conductivity of polyurethane/MWCNT nanocomposite foams, Polym. Compos. 33(8) (2012) 1302-1312. https://doi.org/10.1002/pc.22256

[69] S. Wang, Y. Huang, C. Zhao, E. Chang, A. Ameli, H.E. Naguib, C.B. Park, Theoretical modeling and experimental verification of percolation threshold with MWCNTs' rotation and translation around a growing bubble in conductive polymer composite foams, Compos. Sci. Technol. 199 (2020) 108345. https://doi.org/10.1016/j.compscitech.2020.108345

[70] S. Wang, A. Ameli, V. Shaayegan, Y. Kazemi, Y. Huang, H.E. Naguib, C.B. Park, Modelling of Rod-Like Fillers' Rotation and Translation near Two Growing Cells in Conductive Polymer Composite Foam Processing, Polymers 10(3) (2018) 261.

[71] S. Wang, Y. Huang, E. Chang, C. Zhao, A. Ameli, H.E. Naguib, C.B. Park, Evaluation and modeling of electrical conductivity in conductive polymer nanocomposite foams with multiwalled carbon nanotube networks, Chem. Eng. J. 411 (2021) 128382. https://doi.org/10.1016/j.cej.2020.128382

[72] R.F. Barron, Industrial noise control and acoustics, CRC Press 2002.

[73] H.-j. Yu, G.-c. Yao, X.-l. Wang, B. Li, Y. Yin, K. Liu, Sound insulation property of Al-Si closed-cell aluminum foam bare board material, Trans. Nonferrous Met. Soc. China 17(1) (2007) 93-98. https://doi.org/10.1016/S1003-6326(07)60054-5

[74] J.S. Bolton, N.M. Shiau, Y.J. Kang, SOUND TRANSMISSION THROUGH MULTI-PANEL STRUCTURES LINED WITH ELASTIC POROUS MATERIALS, J. Sound Vib. 191(3) (1996) 317-347. https://doi.org/10.1006/jsvi.1996.0125

[75] C.M. Lee, Y. Xu, A modified transfer matrix method for prediction of transmission loss of multilayer acoustic materials, J. Sound Vib. 326(1) (2009) 290-301. https://doi.org/10.1016/j.jsv.2009.04.037

[76] J.-Z. Liang, X.-H. Jiang, Soundproofing effect of polypropylene/inorganic particle composites, Composites, Part B 43(4) (2012) 1995-1998. https://doi.org/10.1016/j.compositesb.2012.02.020

[77] L. Xu, T. Han, J. Li, Y. Xiong, S. Guo, The cell growth-induced orientation of mica in lightweight flexible poly (vinyl chloride) foams and its enhancement on sound insulation, Compos. Sci. Technol. 145 (2017) 78-88. https://doi.org/10.1016/j.compscitech.2017.03.037

[78] J.-W. Lee, J.-C. Lee, J. Pandey, S.-H. Ahn, Y.J. Kang, Mechanical Properties and Sound Insulation Effect of ABS/Carbon-black Composites, J. Compos. Mater. 44(14) (2010) 1701-1716. https://doi.org/10.1177/0021998309357673

[79] G. Liao, Research and development of Heavy metal particles/NBR-PVC blend foam sound insulation comopsites, Zhejiang Sci-Tech University (China)2018.

[80] D. Jahani, A. Ameli, M. Saniei, W. Ding, C.B. Park, H.E. Naguib, Characterization of the Structure, Acoustic Property, Thermal Conductivity, and Mechanical Property of Highly Expanded Open-Cell Polycarbonate Foams, Macromol. Mater. Eng. 300(1) (2015) 48-56. https://doi.org/10.1002/mame.201400125

[81] J. Zhao, G. Wang, Z. Chen, Y. Huang, C. Wang, A. Zhang, C.B. Park, Microcellular injection molded outstanding oleophilic and sound-insulating PP/PTFE nanocomposite foam, Composites, Part B 215 (2021) 108786. https://doi.org/10.1016/j.compositesb.2021.108786

[82] M. Wu, W. Yan, C. Liu, D. Yan, W. Zheng, Microcellular Injection Molded PP/CNT Foams and Their Sound Insulation Properties, Eng. Plast. Appl. 51(1) (2023) 46-51.

[83] B. Xue, J. Zhang, Y. Bao, Acoustically and thermally insulating epoxy foams prepared by non-traditional expandable microspheres, Polym. Eng. Sci. 59(4) (2019) 799-806. https://doi.org/10.1002/pen.25008

[84] K.H. Yoon, S.T. Yoon, O.O. Park, Damping properties and transmission loss of polyurethane. I. Effect of soft and hard segment compositions, J. Appl. Polym. Sci. 75(5) (2000) 604-611. https://doi.org/10.1002/(SICI)1097-4628(20000131)75:5<604::AID-APP2>3.0.CO;2-#

[85] H. Zhou, B. Li, G. Huang, Sound absorption characteristics of polymer microparticles, J. Appl. Polym. Sci. 101(4) (2006) 2675-2679. https://doi.org/10.1002/app.23911

[86] J.D. McRae, H.E. Naguib, N. Atalla, Mechanical and acoustic performance of compression-molded open-cell polypropylene foams, J. Appl. Polym. Sci. 116(2) (2010) 1106-1115. https://doi.org/10.1002/app.31581

[87] T. Han, X. Wang, Y. Xiong, J. Li, S. Guo, G. Chen, Light-weight poly(vinyl chloride)-based soundproofing composites with foam/film alternating multilayered structure, Composites, Part A 78 (2015) 27-34. https://doi.org/10.1016/j.compositesa.2015.07.013

[88] Z. Du, F. Chen, Y. Fei, J. Jin, P. Li, T. Kuang, Y. Xiao, S. Ruan, H. Lu, High sound insulation property of prepared polypropylene/polyolefin elastomer blends by combining pressure-induced-flow processing and supercritical CO2 foaming, Compos. Commun. 28 (2021) 100958.

https://doi.org/10.1016/j.coco.2021.100958

Chapter 3: Super toughened blends of PLA and PBAT injection-molded foams via enhancing interfacial compatibility and cellular structure

As the first step of this study, a preliminary feasibility study of toughening PLA blend foams is depicted in this chapter. Polymer foams and toughening methods are first briefly described to emphasize the motivation. Inspired by the concept of blending toughening strategies for solid PLA, we have explored the toughening of PLA foams by incorporating PBAT and a chain extender (ADR). The effect of ADR content on cell structure and mechanical properties was investigated. Discussion on the toughening mechanism of PLA blend foams is also presented.

3.1. Abstract

Biodegradable PLA foams have drawn increasing attention due to environmental challenges and petroleum crisis. However, it still remains a challenge to prepare PLA foams with fine cellular structures and high impact property, which significantly hinders its widespread application. Herein, phase interface-enhanced PLA/PBAT blend foam, modified by a reactive compatibilizer through a simple reactive extrusion, was produced via a core-back FIM technique. The obtained PLA blend foams displayed an impact strength as high as 49.1 kJ/m^2, which was 9.3 and 6.4 times that of the unmodified PLA/PBAT blend and its corresponding foam, respectively. It proved that the interfacial adhesion and cell size both strongly affected the impact strength of injection-molded PLA/PBAT foams, and two major conclusions were proposed. First, enhancing interfacial adhesion could cause a brittle-tough transition of PLA/PBAT foams. Additionally, for foams with high interfacial adhesion, small cell size (<12 μm) was more favorable for the stretching of cells and extension of the whitened region in comparison with big cell size (cell size > 60 μm), leading to the drastic toughening of PLA blends. This study provides a feasible, industrially scalable and practical strategy to prepare super toughened and fully biodegradable PLA materials.

3.2. Introduction

PLA, as a vital kind of bio-based and biodegradable polymer, has attracted increased attention due to the resource shortage crisis and serious environmental pollution

caused by the extensive use of petroleum-based polymers[1, 2]. Besides, the advantages of excellent biocompatibility, high strength, and good processability, have promoted its applications in many fields including biomedical devices, textiles, and packaging[3-8]. Nevertheless, compared with commercial PP and PE resins, the inherent brittleness, high density, and high cost of PLA resin suppress its wide application where light weight and good toughness are required[2, 9].

Foaming is a feasible method to obviously reduce the weight of polymeric products as well as offer many benefits [10]. Compared with solid counterparts, microcellular plastic foams usually exhibit good impact strength, excellent thermal and sound insulation properties, and thus have been applied in many fields, including packaging, automobiles, safety equipment and construction industries[11, 12]. However, the extremely low melt strength of PLA is the biggest problem for foaming[13, 14]. Cell coalescence and cell collapse are easy to occur due to the weak resistance of cell walls during cell growth, which inevitably leads to open cells and nonuniform bubble size distribution. So far, extensive effective approaches have been applied, including chain extension[15, 16], blending[17-19], compounding[20, 21], and cross-linking[22, 23] to improve the foaming ability of PLA. Among these methods, blending is a simple, cost-effective, and feasible approach for industrial production. For instance, Liu et al.[17] studied the influence of PBAT on the crystallization and foamability of PLA, and found that with the increase in PBAT content from 0 to 7%, the cell density of PLA increased from 2.01×10^{6} cells/cm^{3} to 1.74×10^{7} cells/cm^{3}, and the expansion ratio increased from 4.87 to 10.94.

Besides the poor foamability of PLA, the low toughness is another major challenge

that hinders its broad application. Substantial attempts have been made to enhance the toughness of PLA[24-28]. Blending with other polymers, such as PU, poly(ethylene-co-octene) (POE), poly(ethylene-co-glycidyl methacrylate) (EGMA), poly(ethylene) (PE), and ethylene-co-vinyl acetate (EVA), is regarded as the most efficient and economic approach to improve the toughness of PLA[29]. Furthermore, toughening PLA by blending PBAT has become a hotspot due to the high toughness of PBAT together with the biodegradable property of the final blend[30]. To obtain a ductile PLA blend, the compatibilization between the PLA and PBAT should be improved due to the complete phase separation between PLA and PBAT. Several approaches, such as adding reactive compatibilizers[31, 32], catalysts[22], and initiators[33], could be applied to improve the compatibility between PLA and PBAT, leading to the obvious toughening of PLA. For example, Wang et al.[32] prepared a PLA/PBAT (60/40) blend with improved elongation at break (579.9%) and impact strength (29.6 kJ/m^2) by using multifunctional epoxide (Joncryl ADR 4370S) as a reactive compatibilizer. Wu et al.[34] developed a super-tough PLA/PBAT blend through reactive melt blending, which displayed an outstanding impact strength of 61.9 kJ/m^2 and elongation at break of 278%.

However, few investigations had been conducted to improve the toughness of PLA foams[35-37]. Najafi et al.[36] evaluated the effect of long-chain branched (LCB) structure and nanoclay on the PLA foaming and its mechanical properties. It revealed that the LCB-PLA with 0.5 wt% clay exhibited an improved cell structure and enhanced specific impact strength compared with pure PLA. However, the absolute impact strength of LCB-PLA with 0.5 wt% clay (13.3 kJ/m^2) was still lower

than the corresponding solid sample (13.8 kJ/m^2). Lee et al.[37] reported that adding polyhydroxyalkanoate (PHA) and nano-fibrillated PTFE led to the improvement of the specific impact strength, while the absolute impact strength was reduced in comparison with the corresponding solid sample. It looks increasingly urgent to enhance the toughness of PLA foam from the perspective of industrial application. Based on the previous analysis, the inclusion of PBAT and reactive compatibilizers could enhance the melt strength, and further improve the foamability of PLA. To our best knowledge, however, there is no reported literature using PBAT and ADR to toughen PLA foams.

In this work, PLA/PBAT blend foam with a superior impact strength of 49.1 kJ/m^2 was obtained by using core-back FIM. In specific, chain extender ADR was used to improve the compatibility of biodegradable PLA and PBAT. The effect of ADR content on compatibility, rheological behavior, cell structure and mechanical properties of PLA/PBAT blend was comprehensively investigated. The toughening mechanism was also discussed and analyzed. Except for the compatibility between PLA and PBAT, the cell size would strongly influence the impact strength of PLA/PBAT blend foams. The existence of small cells would improve the impact strength and vice versa. This study offered a feasible method to fabricate fully biobased PLA foams with high ductility, promoting its widespread application in areas like packaging and construction.

3.3. Experimental section

3.3.1. Materials

PLA (4032D) with a density of 1.24 g/cm^3 was kindly provided by Natureworks LLC. The D-LA content is approximately 2%. PBAT (TH801T) was purchased from Xinjiang Blue Ridge Tunhe Sci. &Tech. Co., Ltd. Joncryl ADR-4468 (ADR) was obtained from BASF, with a molecular weight of 7250 g/mol and an epoxy equivalent weight of 310 g/mol. The chemical structure of PLA, PBAT and ADR was depicted in Fig. 3-1. N_2 with a purity of 99%, supplied by Ningbo Huayu Gas Inc, was used as the physical blowing agent in FIM experiments.

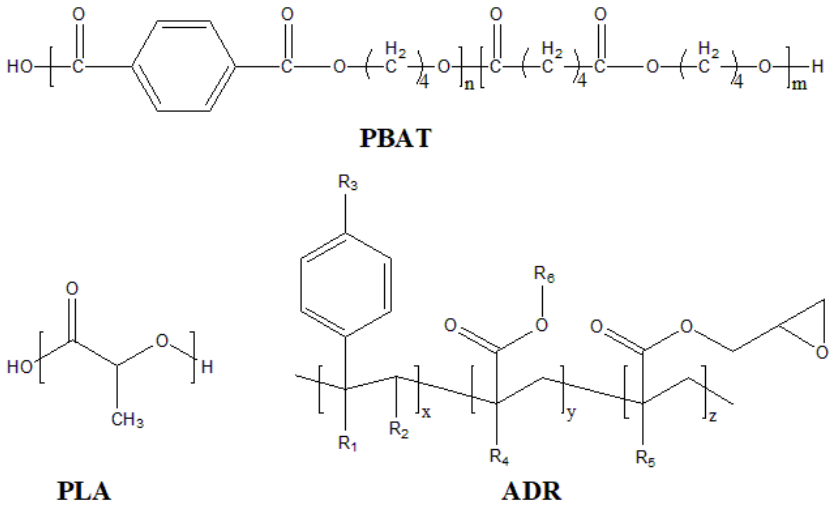

Fig. 3-1. Structure of PBAT, PLA and ADR, where R1–R5 are H, CH_3, a higher alkyl group, or combinations of them; R6 is an alkyl group, and *x*, *y*, and *z* are each between 1 and 20.

3.3.2. Blend preparation

PLA and PBAT pellets were first dried at 80 ℃ overnight to remove any moisture. The dried PLA and PBAT pellets were melt blended by using a corotating twin-

screw extruder (SHL-52, Nanjing Haili Extrusion Equipment Co. Ltd., China) with a rotary speed of 40 rpm The screw diameter and length/diameter ratio were 52 mm and 44, respectively. The temperature profile was set as 150-200 ℃ from the feed zone to the die. The weight ratio of PLA/PBAT was fixed at 70/30. Various amounts of ADR (0, 0.5, 1, and 1.5 phr) were added into the mixture during the melting blending process, and the resulting blends were marked as B, B0.5, B1 and B1.5, respectively. To evaluate the effect of ADR content on the rheological behavior of PLA and PBAT, PLA and PBAT with different ADR contents (0, 0.5, 1, and 1.5 phr) were prepared through the same extrusion process. Each extrudate was quenched in a water bath and pelletized by the cutting chamber.

3.3.3. Core-back FIM process

PLA/PBAT blend foams were prepared by using a 100-ton FIM machine (Systec 100/420-310C, Demag Plastics Group, Germany), equipped with a Mucell SCF delivery system, T100, Trexel Inc., USA. Generally, core-back FIM process consists of four stages, including injection, dwelling, core-back and cooling[38]. In the foaming process, the uniformly mixed polymer/gas solution is injected to fill the entire mold cavity, and cell nucleation occurs at the gate. The gate-nucleated cells will dissolve back into the melt due to the high packing pressure during the dwelling stage. Then, the cell nucleation is induced by core-back (mold-opening) operation, and a very uniform cell structure can be achieved. A tensile test bar mold was used in this study. Except for the thickness (3 mm), other dimensions of this mold are in line with the Standard GB/T 1040. Other detailed processing parameters are shown in Table 3-1. Then, the density and VFs of injection molded unfoamed and foamed

samples were measured and shown in Table 3-2.

Table 3-1. Processing parameters used for the FIM experiments.

PARAMETERS	SOLID	FOAM
Melt temperature (℃)	200	200
Mold temperature (℃)	80	80
Injection speed (mm/s)	100	100
Injection pressure (MPa)	150	150
Back pressure (MPa)	20	20
Packing pressure (MPa)	60	60
Dwelling time (sec)	10	25
Core-back distance (mm)	N/A	1
N_2 content (wt%)	N/A	0.8

Table 3-2. Density and VF of the unfoamed and foamed samples

Solid	Density(g/cm^3)	Foam	Density(g/cm^3)	VF
B	1.239 ± 0.003	B foam	0.878 ± 0.004	0.29
B0.5	1.239 ± 0.004	B0.5 foam	0.871 ± 0.003	0.30
B1	1.240 ± 0.002	B1 foam	0.875 ± 0.012	0.29
B1.5	1.239 ± 0.001	B1.5 foam	0.909 ± 0.001	0.27

3.3.4. Fourier transform infrared spectrometry (FTIR) and ^1H nuclear magnetic resonance (NMR)

To prove that ADR reacted with PLA and PBAT completely, PLA, PBAT, ADR and B1.5 were dissolved in dichloromethane (CH_2Cl_2), dropped onto the tableted potassium bromide, and were evaluated through FTIR (NICOLET 6700, Thermo Fisher Scientific, USA). The detailed process could be found in the reference[32]. To further investigate the interactions between PLA/PBAT blend and ADR, the PLA blends were heat pressed into disk-shaped samples in a hot-press. The disks with thickness of 1 mm were then characterized on an FTIR (Cary660 + 620, Agilent,

USA) with ATR mode at a resolution of 2 cm^{-1} and an accumulation of 32 scans. ^{1}H NMR spectra were collected on a spectrometer (AVANCE NEO 600, Bruker, Switzerland) using $CDCl_3$ as the solvent. The operating frequency was 600 MHz.

3.3.5. Gel permeation chromatography (GPC)

Molecular weight and polydispersity index (PDI) were studied using a GPC (PL-GPC 220, Polymer Laboratories, UK) at room temperature, using chloroform as solvent and a PS standard as reference. The solutions were filtered before measurement.

3.3.6. Extraction in chloroform

The gel content of PLA/PBAT blends with different ADR content was measured using a Soxhlet extractor. About 0.3 g of samples were wrapped in filter paper and extracted in boiling chloroform for 24 h. Then, the extracted samples were dried to a constant weight and the gel fraction was calculated using equation (1):

$$Gel\ fraction = \left(m_1 / m_0\right) \times 100\% \quad (3\text{-}1)$$

where m_0 and m_1 were the original and extracted weight of samples.

3.3.7. PLA/PBAT blend morphology analysis

A Hitachi-S4800 scanning electron microscopy (SEM) was used to investigate samples' morphology. The injection molded PLA/PBAT samples with various ADR content were cryofractured in liquid nitrogen. Both the cryofractured and impact-fractured surfaces were coated with a layer of platinum before observation.

3.3.8. Rheological behavior analysis

The extruded PLA/PBAT blends with various ADR content were first compressed

into disks of 1 mm in thickness with a diameter of 25 mm at 190 ℃ and 10 MPa. Rheological behaviors of PLA/PBAT blends with various ADR contents under oscillatory shear flow were conducted with an ARES rotational rheometer (HR-3, TA, USA) under a nitrogen atmosphere. The frequency sweep was performed in the frequency range of 0.01—100 rad/s with a strain of 1%, at a temperature of 190 ℃. Then, the dynamic temperature step testing was applied to evaluate the rheological behavior of PLA and PBAT with various ADR contents in the temperature range of 190–80 ℃ with a constant strain of 1%.

3.3.9. Foam morphology characterization

A SEM (EVO18, Zeiss Group, Germany) was used to investigate the cell structure of PLA/PBAT blends with various ADR content. Specimens cut from the central part of the injection molded foams were cryogenically fractured and coated with a layer of platinum before observation. The quantitative information of cell structure was evaluated thought ImageJ software (National Institutes of Health, USA). The cell density, N_0 (cells/cm^3), was determined according to the following equation (2):[39]

$$N_0 = (\frac{n}{A})^{3/2}\Phi \tag{3-2}$$

where n is the number of cells in the micrograph, A the area of the selected micrograph, Φ the expansion ratio of the foamed sample. The Φ was calculated using equation (3):

$$\Phi = \frac{\rho_s}{\rho_f} \tag{3-3}$$

where ρ_s and ρ_f are the density of the solid and its foamed sample, respectively. Water displacement method (ISO 1183-1987) was applied to determine ρ_s and ρ_f.

The VF, which is defined as the ratio of the volume of voids in the foam to the total volume of the foam, was determined using equation (4): [39]

$$VF = \frac{\rho_f}{\rho_s} \tag{3-4}$$

3.3.10. Thermal analysis

Thermal properties were investigated with a differential scanning calorimeter (DSC, DSC/TGA1, Mettler-Toledo) under a nitrogen atmosphere. All samples (about 5–8 mg) cut from the core (foamed) layer of the injection molded foams were sealed in an aluminum pan and heated from 25 to 190 ℃ at a heating rate of 10 ℃/min.

3.3.11. Mechanical test

Tensile properties of the injection-molded samples were evaluated using an Instron 5567 universal testing instrument (Instron, USA) with a crosshead speed of 20 mm/min. Izod impact tests were conducted according to the GB/T 1843-2008 standard on an impact tester (GT-7045-HML, Gotech Testing Machines Inc.). At least five specimens were tested for each condition to get an average value.

3.4. Results and discussion

3.4.1. Reaction between PLA/PBAT and ADR

In order to study the reaction between PLA/PBAT and ADR, FTIR spectroscopy

was applied to characterize the structures of pure PLA, PBAT, ADR, PLA/PBAT blend and PLA/PBAT/ADR blends, which is shown in Fig. 3-2. The characteristic absorption peaks at 908 and 850 cm^{-1} (Fig. 3-2a), corresponding to the C-O stretching vibration of epoxy group in ADR. These peaks disappeared in the B1.5 blend, indicating that ADR had reacted with PLA and PBAT completely. According to the results previously reported[31, 32], the epoxy group of ADR could easily react with the terminal hydroxyl and carboxyl groups of PLA and PBAT. This could be proved by the results depicted in Fig. 3-2b. The sharp absorption peaks at 1749 and 1714 cm^{-1} were assigned to the C=O stretching vibrations in PLA and PBAT, respectively. The weaker peaks at 1250–1050 cm^{-1} were caused by the stretching vibration of C-O-C and the vibration of C-O from carboxyl groups. The intensity of these peaks was enhanced by adding ADR, which suggested the reaction between carboxyl/hydroxyl groups and epoxy groups.

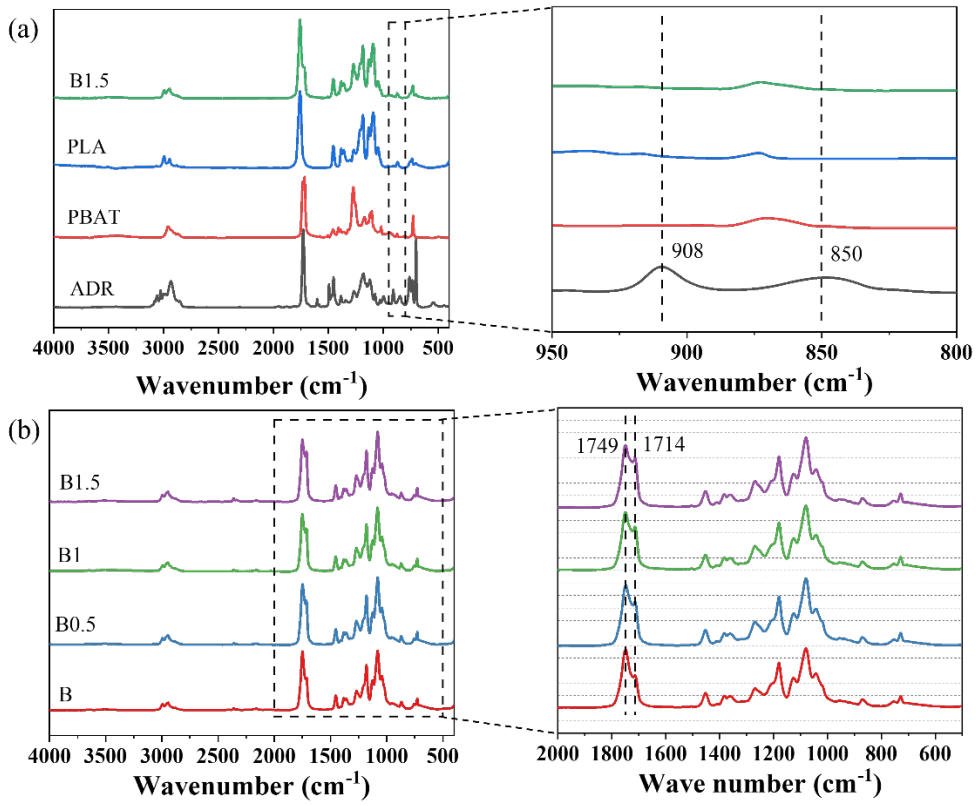

Fig. 3-2. FTIR spectra of samples: (a) ADR, PBAT, PLA and B1.5; (b) B, B0.5, B1 and B1.5.

The result was also confirmed by ^{1}H NMR measure. Fig. 3-3 shows the ^{1}H NMR spectra of pure PBAT, pure PLA, ADR, B0 and B1.5. The main peaks of PBAT, PLA and ADR were consistent with the literature[7, 8]. For example, the peak at 8.1 ppm (peak a in Fig. 3-3a) corresponded to the benzene ring of PBAT. The peaks at 1.57 (h) and 5.15 (i) ppm were assigned to the CH and CH_3 of PLA. The peaks at 6.5-7.2 (j) and 2.3-3.1 (k+l) ppm belonged to the benzene ring and the epoxy group of ADR. The spectrum of B1.5 was similar to B1, as shown in Fig. 3-3d. However, the weak peak at 7.1 (j in Fig. 3-3d') ppm proved the existence of the benzene ring of ADR. This behavior can be attributed to the low ADR content. This result confirmed the

reaction between ADR and PLA/PBAT. The possible reaction process between PLA/PBAT and ADR during reactive extrusion is described in Fig. 3-4.

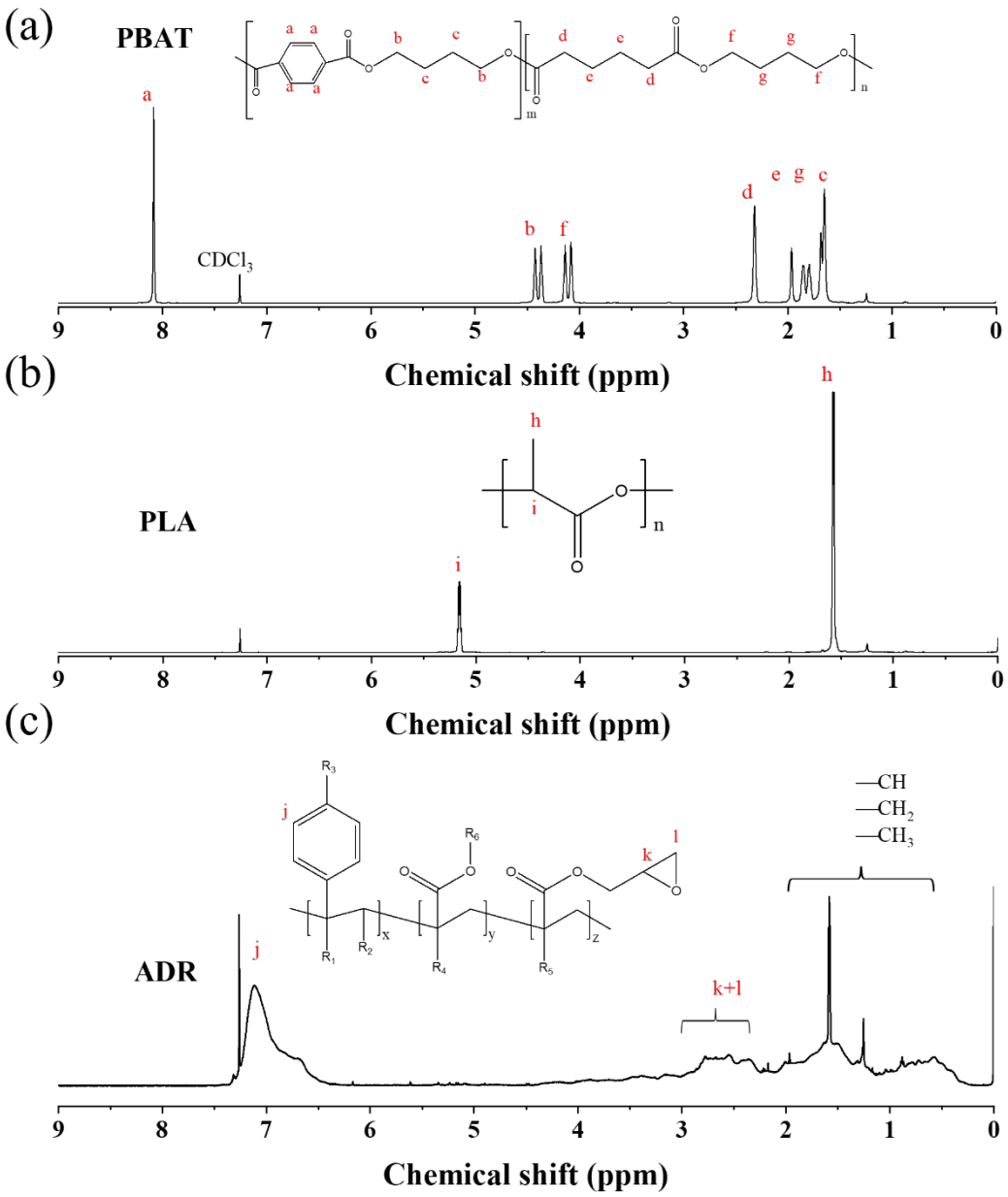

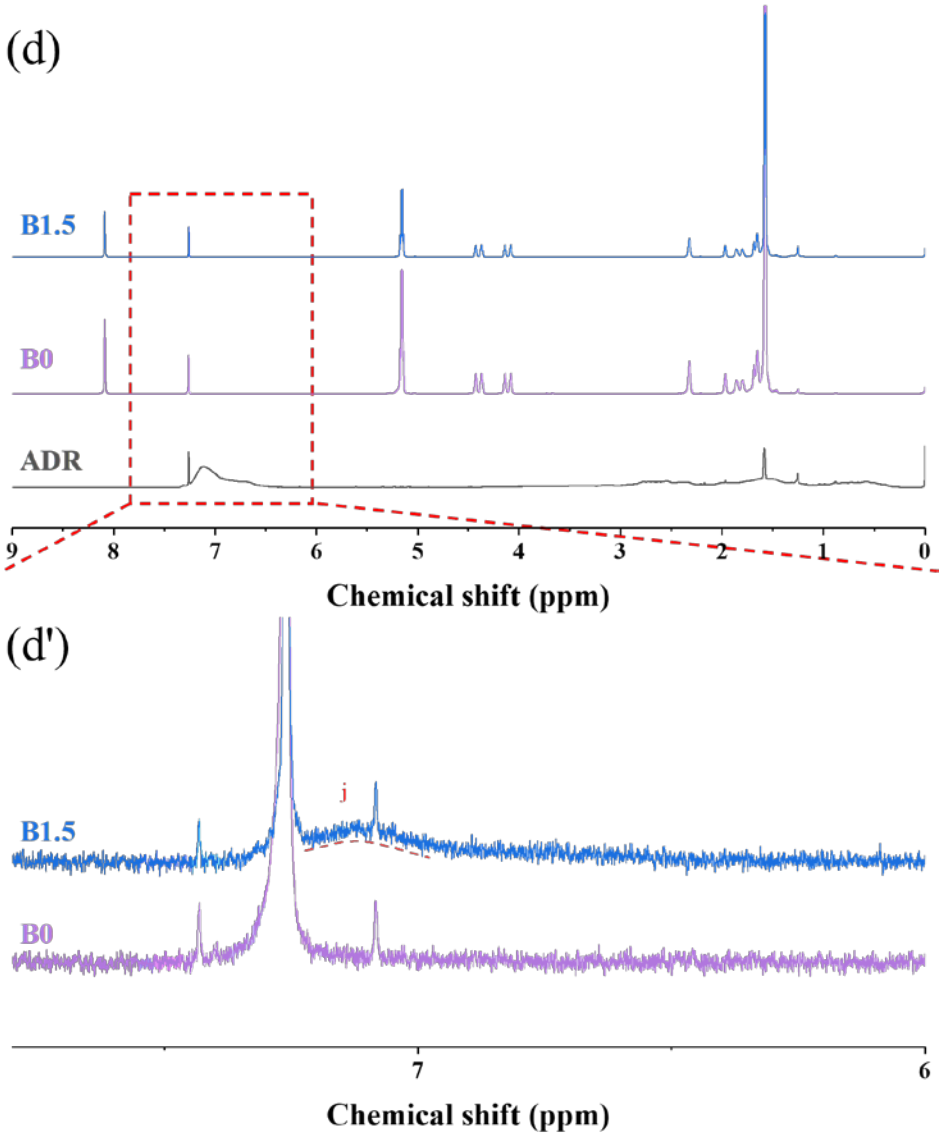

Fig. 3-3. ^{1}H NMR spectra for (a) pure PBAT, (b) pure PLA, (c) pure ADR, and (d, d') B0 and B1.5.

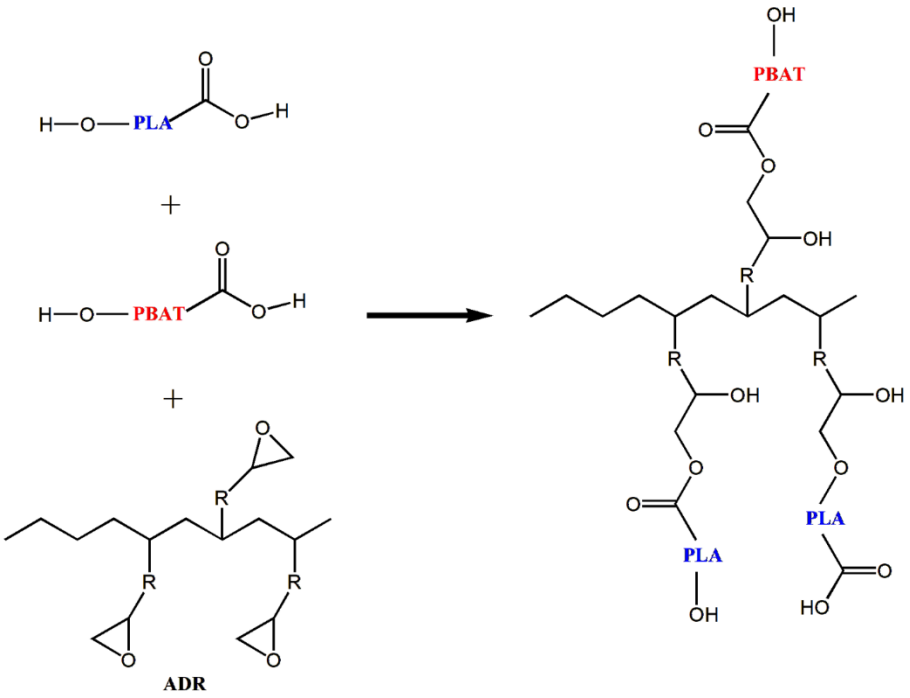

Fig. 3-4. Possible reactions between PLA/PBAT and ADR during reactive extrusion.

The occurrence of chain extension reactions preliminarily confirmed by FTIR spectra and ^{1}H NMR spectra would lead to a change in chemical structure and molecular weight. Thus, GPC was applied to further investigate the molecular weight and molecular weight distribution of samples, as shown in Table 3-3. It is obviously shown that after adding ADR, the M_w significantly improved from 144849 g/mol for B to 285155 g/mol for B1, and the corresponding PDI increased from 1.58 to 2.37. When ADR content increased to 1.5 phr, the molecular weight of B1.5 blend was somewhat lower than that of B1 blend, but the PDI was further increased to 2.57. It may be attributed to the slightly cross-linking of B1.5 blend. The extraction result depicted that only B1.5 had a gel fraction of about 5 wt%. Thus, the insoluble macromolecules (with high molecular weight) would be removed

during the filtering stage before GPC analysis. These results strongly proved that the added ADR could react with PLA/PBAT to improve the M_w of PLA/PBAT blends.

Table 3-3. Molecular weight of PLA/PBAT blends with different ADR content.

Sample	Mn	Mw	PDI
B	91152	144849	1.59
B0.5	96028	194619	2.03
B1	120210	285155	2.37
B1.5	103905	266574	2.57

3.4.2. Phase morphology of PLA/PBAT blends

Phase morphologies of injection-molded PLA/PBAT blends is shown in Fig. 3-5 From the SEM images perpendicular to the flow direction, B showed a typical “sea-island” structure where PBAT phases were dispersed in the PLA matrix. The relatively large size of dispersed phases (0.4–1.2 μm) and poor interface indicated the immiscibility between the pure PLA and PBAT resin. After adding ADR, the size of PBAT phases was dramatically decreased and the phase interface gradually became unobvious, especially when the ADR content was over 1 phr. Similar results have been reported in references[40]. This clearly indicated the formation of PLA-co-PBAT copolymer during reactive extrusion, which significantly enhanced the interface adhesion between PLA and PBAT.

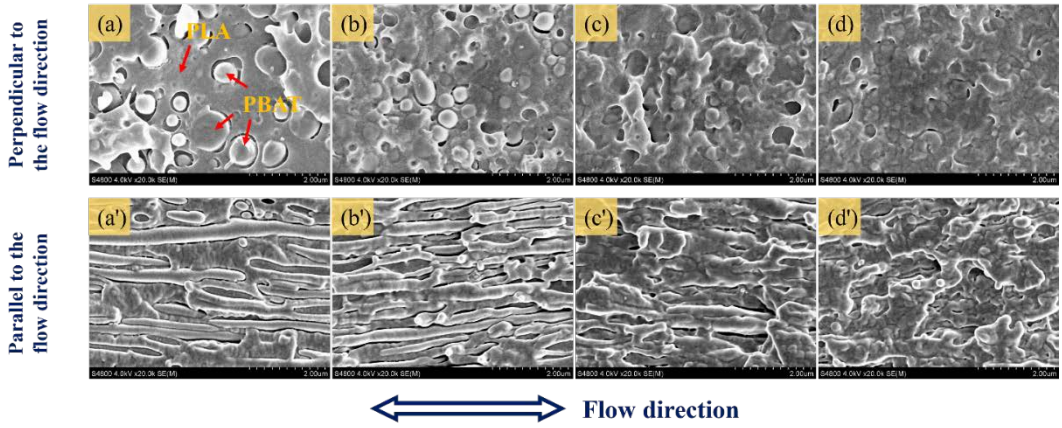

Fig. 3-5. SEM images of the unfoamed specimens (a, a') B, (b, b') B0.5, (c, c') B1 and (d, d') B1.5. (a-d) and (a'-d') were taken from the views perpendicular and parallel to the flow direction, respectively.

Interestingly, PBAT phases with fibrillar structure, which was arranged towards the flow direction, were found in the SEM images parallel to the flow direction (the enlarged images were shown in Fig. 3-6. This phenomenon was strongly related to the flow field during the injection molding process [41, 42]. SEM images of the B exhibited PBAT fibrils with high aspect ratios, and the length of some fibrils was even over 20 μm. Compared with B (PLA/PBAT blend), the PLA/PBAT/ADR blends showed a more refined fibrillar structure, especially for B1.5. This could be attributed to two facts. First, the formation of PLA-co-PBAT could act as a compatibilizer and reduce the interfacial tension, leading to the decreasing size of the dispersed phase (PBAT phase). In addition, the viscosity ratio ($\eta_{\text{dispersed phase}}/\eta_{\text{matrix phase}}$) was lower than 1 in this study, which was beneficial to the fibrillation of the dispersed phase under the flow field[43].

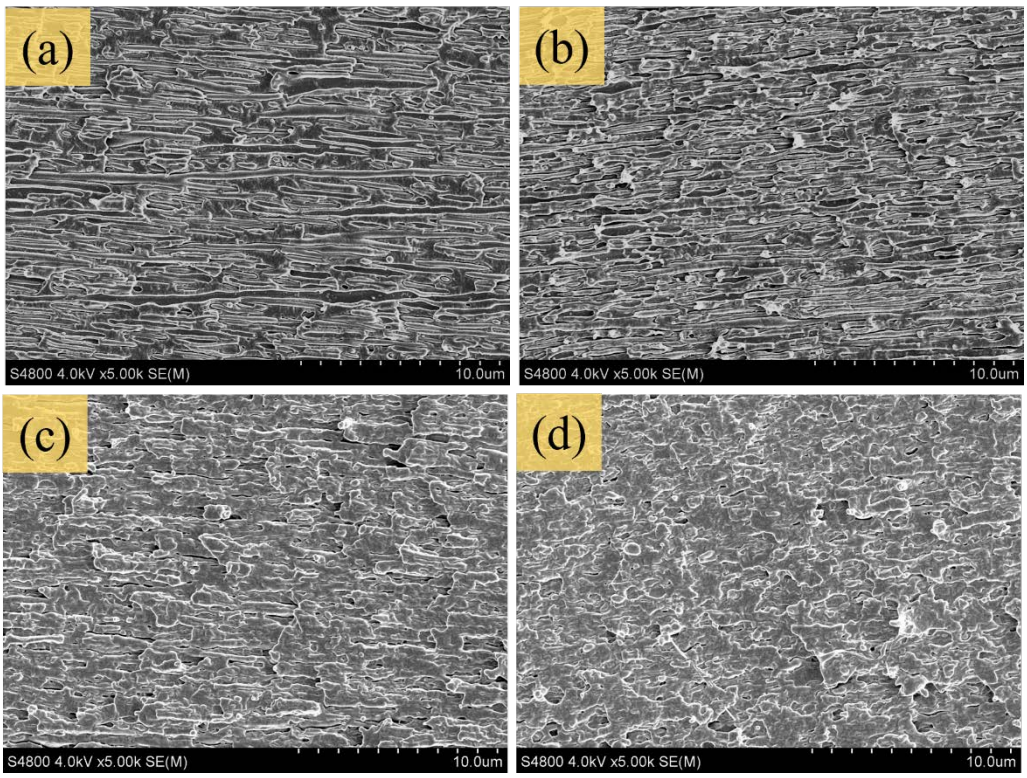

Fig. 3-6. SEM images of (a) B, (b) B0.5, (c) B1 and (d) B1.5 obtained from the view parallel to the flow direction.

3.4.3. Rheology behavior of PLA/PBAT blends

Rheological behavior plays a crucial role in the foaming process, and thus dynamic frequency tests were conducted to study the effect of ADR on the linear viscoelastic responses of PLA/PBAT blend. Fig. 3-7a shows the evolution of complex viscosity (η*) as a function of frequency. With the increase in ADR content, the shear-thinning tendency became more and more stronger. It may be attributed to the chain extension reaction between PLA/PBAT and ADR[31]. As expected, the increase in ADR content led to the increment of η* due to the improvement of dispersion and the enhancement of the interaction between PLA and PBAT (Fig. 3-5). Fig. 3-7b depicts the variation of storage modulus (G'). At high frequencies, the G' values of B1 and

B1.5 were higher than that of B and B0.5, indicating that the former owned a higher entanglement molar mass[44]. At low frequencies, adding ADR dramatically increased the G' values, confirming the existence of some branched chains.

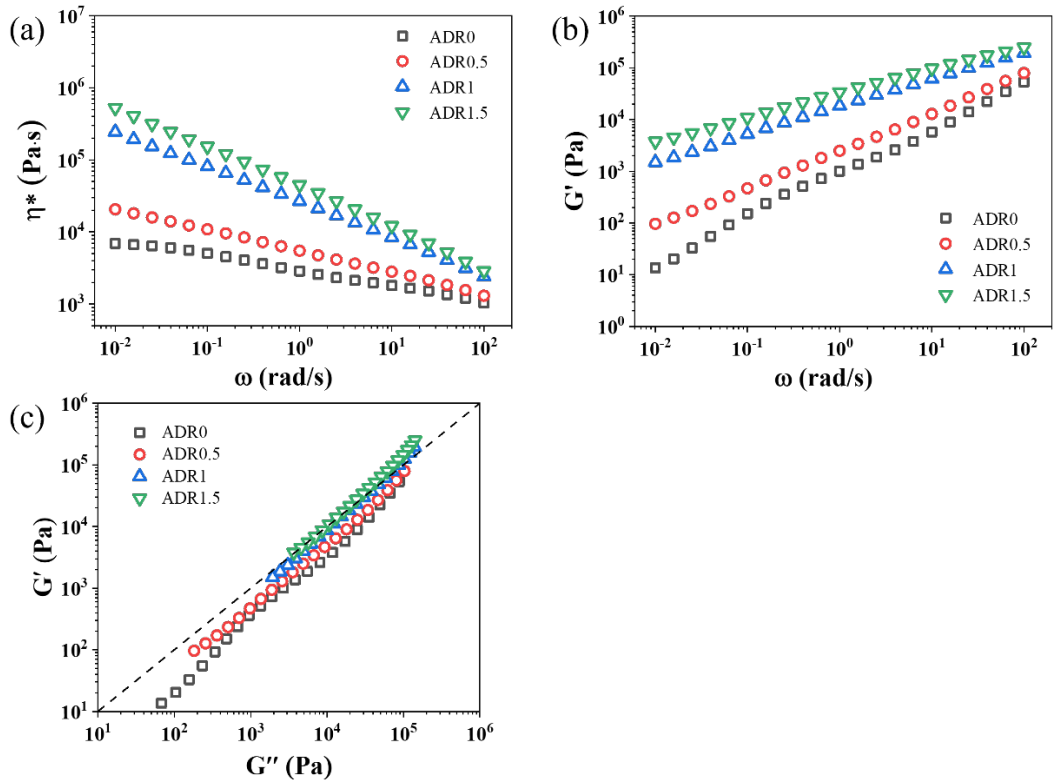

Fig. 3-7. The rheological behavior of B, B0.5, B1 and B1.5 specimens as a function of frequency at 190 °C: (a) complex viscosity (η*), (b) storage modulus (G'), and (c) Han plot.

To further investigate the impact of the introduction of ADR on the rheology behavior, the Han plot of B, B0.5, B1 and B1.5 are shown in Fig 3c. Han-plot can be used to characterize the homogeneity and compatibilization of polymeric blends[45]. A nonlinear correlation of B was observed (Fig. 3-7c), meaning that PLA and PBAT were immiscible. After adding ADR, however, the blends exhibited a good linear correlation, especially for B1 and B1.5. It could be attributed to the

formation of PLA-co-PBAT copolymer, and thus leading to the enhancement of the compatibility between PLA and PBAT. This phenomenon further confirmed the above result of phase morphology analysis (Fig. 3-5). In addition, with the increase in ADR content, a transition of liquid-like behavior (G" > G', for B and B0.5) to solid-like behavior (G' > G", for B1 and B1.5) could be found, which was due to the long-chain branching and the compatibilization modification of PLA/PBAT blend.

3.4.4. Cellular structure of injection-molded foams

Fig. 3-8 shows the typical SEM images of B, B0.5, B1 and B1.5 foams, and the corresponding quantitative cell parameters are presented in Fig. 3-9. Interestingly, even without adding ADR, PLA/PBAT blend foam showed a tiny cell size (~8.6 μm) and high cell density (1.2×10^9 cells/cm^3). It may be due to the fact that blending with PBAT greatly increased the interfacial area of disperse phases, which strongly improved the cell nucleation density during the foaming process[46]. Thus, even with the significantly enhanced viscoelastic response, compared with B foam, the cell structure of B1 foam was just slightly improved. Surprisingly, a bimodal cell structure was found in B1 and B1.5 foams. When the ADR content increased from 1 to 1.5 phr, the big cell size increased from 11.2 to 60.1 μm while the small cell size enlarged from 3.7 to 7.2 μm. According to the previous literature, a bimodal cell structure could be generated in a polymer blend with a large viscosity difference[47], and thus a more comprehensive evaluation of the difference between PLA and PBAT at various ADR content was needed.

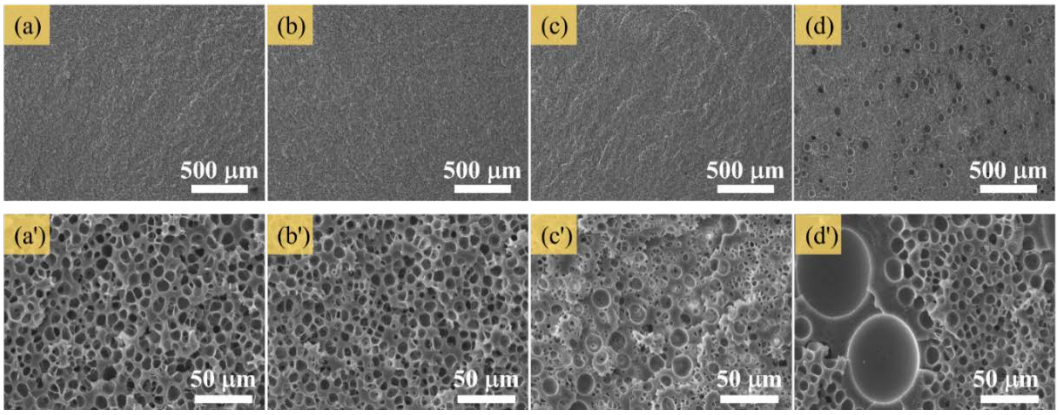

Fig. 3-8. Typical SEM images of (a, a') B, (b, b') B0.5, (c, c') B1 and (d, d') B1.5 foams. (a'-d') were the magnified images of (a-d).

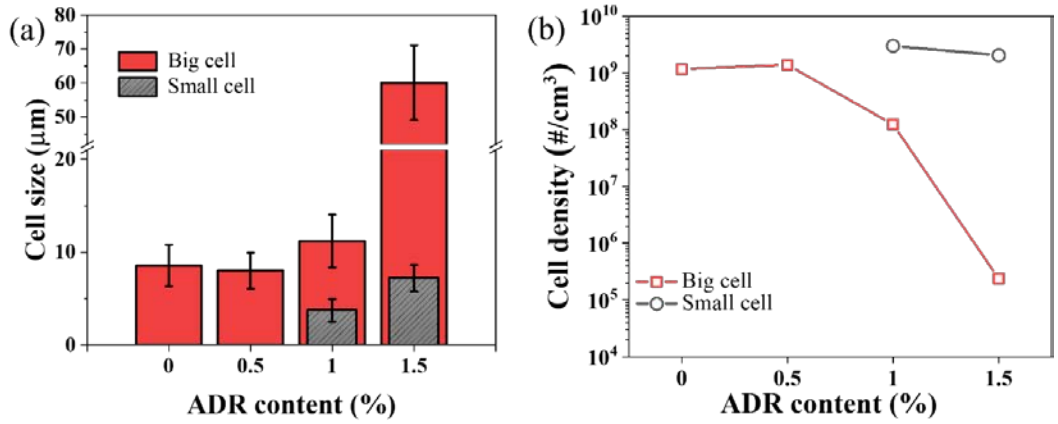

Fig. 3-9. (a) Cell size and (b) cell density of B, B0.5, B1 and B1.5 foams.

Fig. 3-10 shows the complex viscosities of PLA and PBAT separately after reaction-blending with various ADR content over a temperature range from 190 to 80 ℃. As expected, with the decrease in temperature, the η* of pure PLA or PBAT first enhanced slowly and then increased rapidly at a certain temperature due to the onset of crystallization. After adding ADR, the η* was greatly enhanced throughout the whole temperature range. This could be attributed to the increased molecular weight

and the formation of branched chains. However, the effect of ADR on the η* of PLA and PBAT was different, resulting in an increase in the difference of η* between PLA and PBAT ($\Delta_{\eta*}$) with increasing ADR content. For example, $\Delta_{\eta*}$ significantly increased from 26744 to 61842 Pa·s with the increase in ADR content from 0 to 1.5 phr when the temperature was 120 ℃. Thus, it was believed that the formation of the bimodal cell structure of B1 and B1.5 foams was strongly related to the increased viscosity difference ($\Delta_{\eta*}$).

Based on the above results, a possible formation mechanism of the bimodal cell structure for the modified PLA/PBAT blend is presented in Fig. 3-11. At the core-back stage, the movable mold was rapidly opened to induce foaming, and then numerous cell nuclei were formed, especially at the phase interfacial area (Fig. 3-11a and a')[48]. During the cell growth stage, as for the PLA/PBAT blends with high ADR content (i.e., B1 and B1.5), the gas preferred to move to the cells in PBAT phases or interfacial area. This could be attributed to the fact that PBAT phase exhibited a lower complex viscosity compared with PLA phase. With the increase in ADR content, more gas would move to cells in PBAT phase due to the enhanced $\Delta_{\eta*}$ (Fig. 3-10), and these cells would coalesce into one big cell. Consequently, large cells could be found in PBAT phase, small cells existed in PLA phase, as shown in Fig. 3-11c'. For PLA/PBAT blends with low ADR content (i.e., B and B0.5), a lower $\Delta_{\eta*}$ suggested that the cell size difference of cells in PBAT and PLA phase became smaller. Thus, cell structure with relatively uniform cell distribution could be obtained in some extent for the B and B0.5 foams, as shown in Fig. 3-11c.

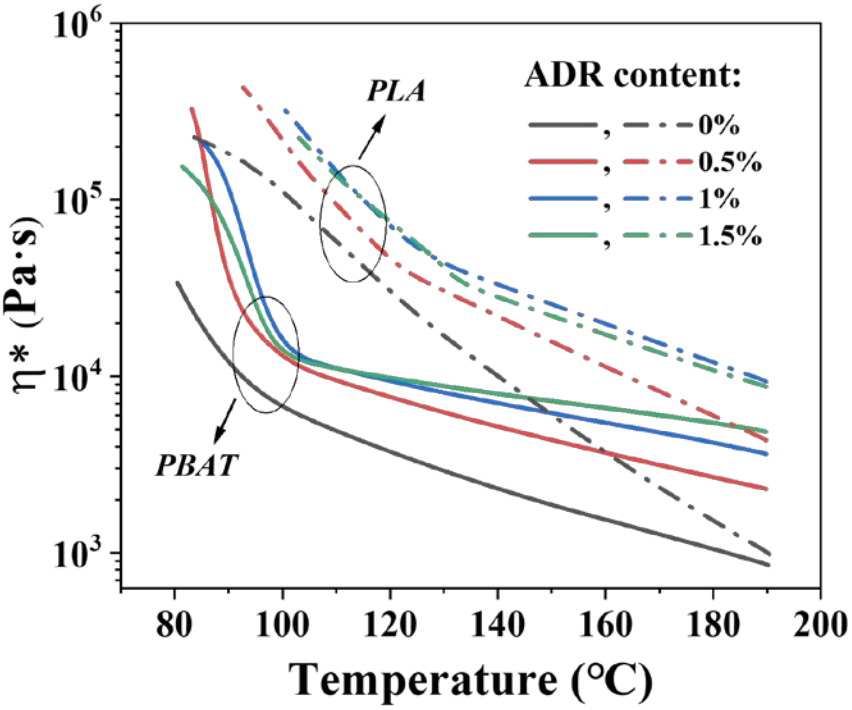

Fig. 3-10. Rheological behavior of PLA and PBAT with various ADR content as a function of temperature at a frequency of 1 rad/s.

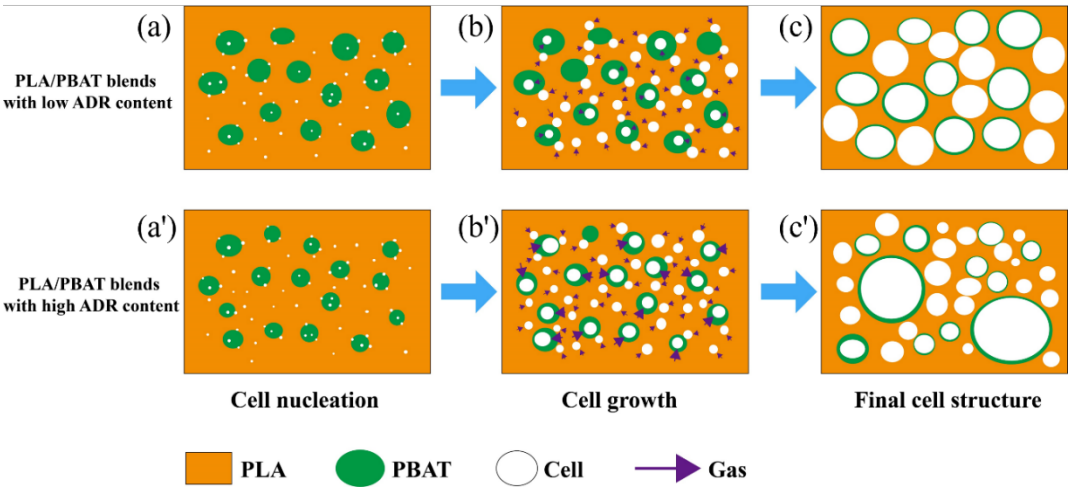

Fig. 3-11. Schematic of the formation mechanism of the bimodal cell structure for the modified PLA/PBAT blends: (a, a') Cell nucleation, (b, b') Cell growth, (c, c') Final cell structure.

3.4.5. Crystallization behaviors

The first melting curves of the core layer of injection-molded B, B0.5, B1, B1.5 and their corresponding foamed samples are shown in Fig. 3-12. The related thermal parameters are listed in Table 3-4. It is obvious that all samples showed strong cold crystallization peaks in temperature range of 92 – 102 ℃ resulting from the slow crystallization rate of PLA. For solid samples, notably, the cold crystallization temperature increased from 96.2 to 102.3 ℃ while the melt temperature decreased from 170.0 to 165.5 ℃, with the increase in ADR content from 0 to 1.5 phr. This was caused by the limited mobility of PLA chains after the chain extension reaction caused between PLA and ADR. Similar results also could be found in foamed samples. After adding ADR, the degree of crystallinity (X_c) of solid samples was reduced due to the improved molecular entanglement. For example, the X_c decreased from 9.6% for B to 6.7% for B1.5. However, for foamed samples, the X_c seemed independent with ADR content (13.3–16.3%). It could be attributed to the fact that the introduction of the physical foaming agent (N_2) could act as a plasticizer to increase the mobility of polymer chains[49, 50], which compensated for the disadvantage induced by adding ADR. Compared with solid samples, the foamed samples presented lower cold crystallization temperature and melt temperature, but with a higher degree of crystallinity, indicating that foaming could accelerate the formation of more crystals. Since both the solid and foamed samples had low crystallinity, the effect of crystallinity on mechanical properties could be neglected in the following discussion.

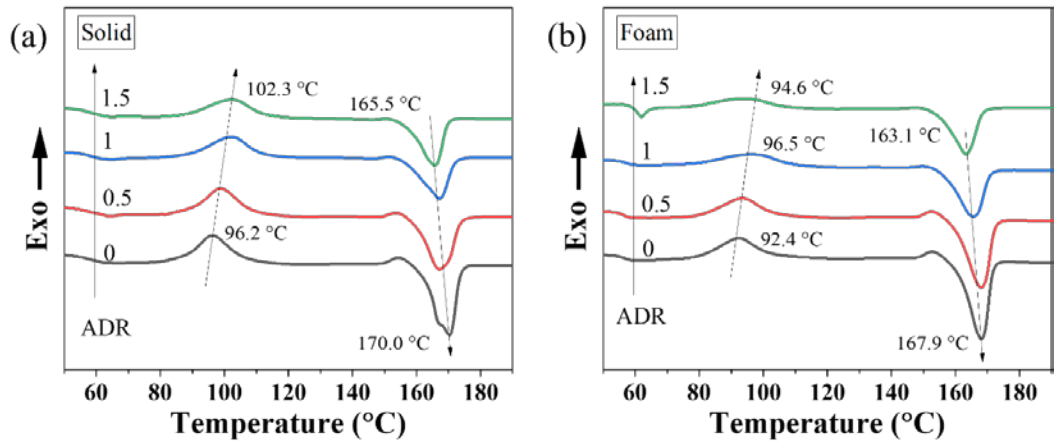

Fig. 3-12. First heating curves (10 ℃/min) of the unfoamed specimens (a) B, B0.5, B1, and B1.5 and (b) their corresponding foamed samples.

Table 3-4. Thermal parameters of B, B0.5, B1, B1.5 and their corresponding foamed samples from DSC curves

Solid	T_{cc} (℃)	T_m (℃)	X_c (%)	Foam	T_{cc} (℃)	T_m (℃)	X_c (%)
B	96.2	170.0	9.6	B foam	92.4	167.9	14.4
B0.5	98.8	166.9	6.8	B0.5 foam	93.3	167.9	14.9
B1	102.2	167.0	3.0	B1 foam	96.5	165.5	13.3
B1.5	102.3	165.5	6.7	B1.5 foam	94.6	163.1	16.3

3.4.6. Tensile properties

Fig. 3-13 shows the yield strength and elongation at break of B, B0.5, B1, B1.5 and their corresponding foamed samples. The typical stress-strain curves of these samples are displayed in Fig. 3-14. With the increase in ADR content, the tensile strength of solid samples gradually decreased from 45.8 to 40.1 MPa. This result was different from what had been reported in the literature[32]. It may be caused by the morphology transformation of PLA/PBAT blends after adding ADR[43]. In

specific, the length of PBAT fibrils significantly reduced with increasing ADR content (Fig. 3-6). After foaming, however, the cells changed the special phase morphology of PLA/PBAT blends, leading to a different result that the yield strength of foamed sample gradually improved from 21.8 to 22.8 MPa.

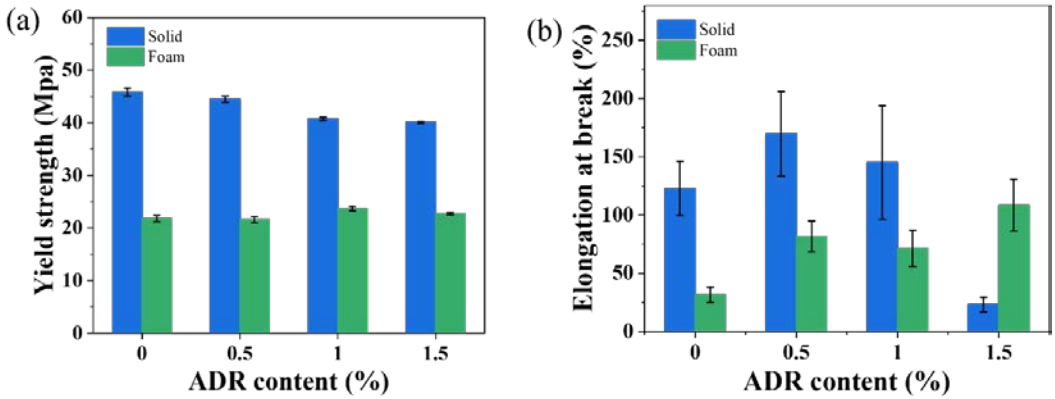

Fig. 3-13. (a) Tensile strength and (b) elongation at break of the unfoamed specimens B, B0.5, B1, B1.5 and their corresponding foamed samples.

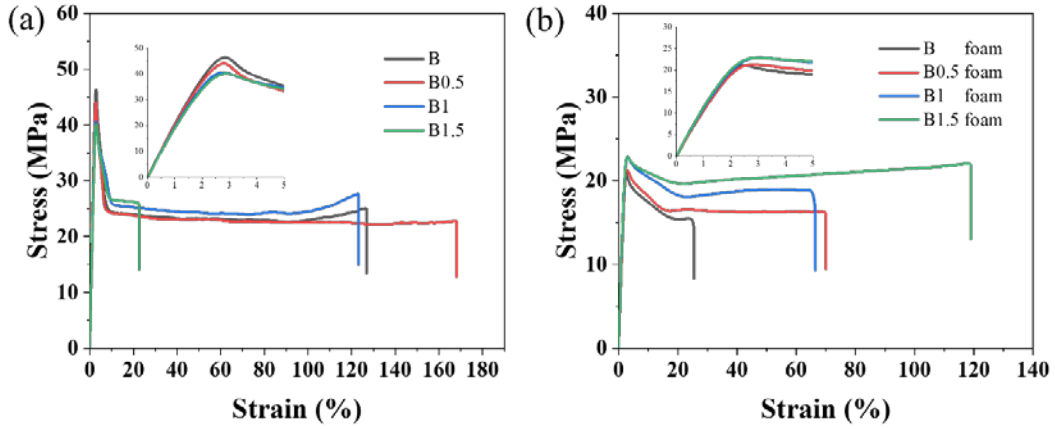

Fig. 3-14. Stress-strain curves of (a) B, B0.5, B1, B1.5 and (b) their corresponding foamed samples.

When the ADR content was below 1 phr, the enhanced compatibility between PLA and PBAT could improve the elongation at break for both solid and foamed samples.

For instance, the elongation at break of solid samples increased from 123 to 170% when ADR content increased to 0.5 phr, while that of foamed samples increased from 32 to 82%. With the further increase in ADR, however, the elongation at break of B1.5 was unexpectedly decreased to 23%. It may be attributed to the fact that the mobility of polymer chains was significantly confined due to the excessive chain extension reaction and the cross-linking when ADR content was 1.5 phr[51-53]. Interestingly, B1.5 foam showed an improved elongation at break in tensile testing compared with the solid B1.5 and foamed samples with lower ADR content. This may be due to the existence of bimodal cell structure in B1.5 foam, in which the small cells could induce matrix craze, shear yielding and large plastic zone, while the big cells could transform crack propagation direction from across the sample into the tensile direction[54, 55].

3.4.7. Impact properties

Fig. 3-15 shows the impact strength of PLA/PBAT blends samples. With the increase in ADR content, the impact strength of solid samples first almost unchanged (~5.3 kJ/m^2 for both B and B0.5), and then suddenly increased to an extremely high level (30.8 kJ/m^2 for B1 and 46.4 kJ/m^2 for B1.5). It should be noticed that B1 and B1.5 were not completely fractured during the impact test as shown in the digital picture of the inset in Fig. 3-15a. As expected, the enhanced interfacial adhesion could cause this result. This changing trend of the impact strength was consistent with the results of the phase morphology of PLA/PBAT blends (Fig. 3-5). Specifically, poor interfacial adhesion usually led to a low impact strength, and vice versa, as previous literature reported[32]. Interestingly, the impact

strength of foamed samples first slightly improved from 7.7 kJ/m^2 for B foam to 12.2 kJ/m^2 for B0.5 foam, and then significantly enhanced to 49.1 kJ/m^2 for B1 foam, more than 59.4% higher than that of solid, and 6.4 and 9.3 times that of B foam and B, respectively. Noticeably, B1 foam belongs to super toughened PLA materials (notched impact strength>35 kJ/m^2[56]). When the ADR content increased to 1.5 phr, however, the impact strength abruptly reduced to 28.7 kJ/m^2, which was even lower than its corresponding solid sample. It should be mentioned that when ADR content was over 0.5 phr, the foamed samples were not completely fractured during the impact test as shown in the digital picture of the inset in Fig. 3-15b. Obviously, except for the interfacial adhesion, the cell structure also strongly affected the final impact strength of PLA/PBAT blend foams. Considering the fact that the foamed samples exhibited a higher impact strength than solid samples, except B1.5 foam, it was reasonable that the existence of big cells (60 μm for B1.5 foam) would extremely damage the toughness, but small cells (<12 μm for B, B0.5, B1.5) would enhance the toughness.

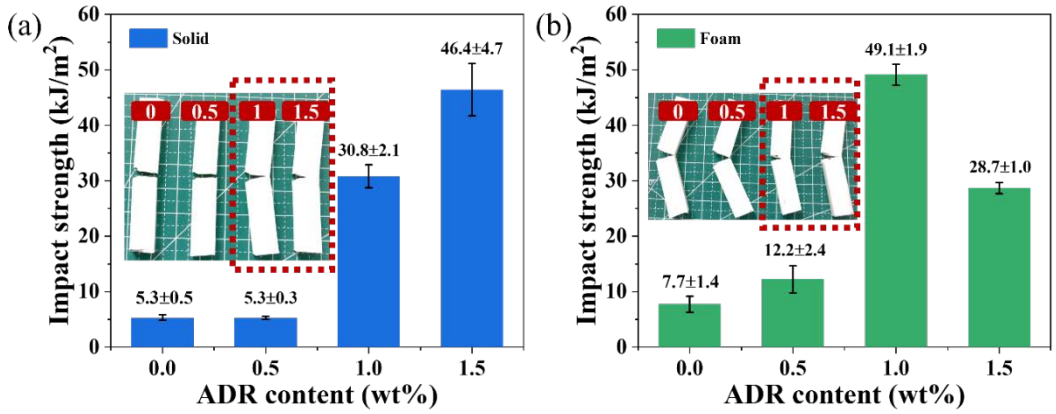

Fig. 3-15. Impact strength of the unfoamed specimens (a) B, B0.5, B1, B1.5 and (b) their corresponding foamed samples.

To further investigate the fracture mechanism during the impact test, the SEM images of impact-fractured surfaces of solid (Fig. 3-16) are evaluated. By comparing Fig. 3-16a1–d1, it is clearly observed that the whole impact-fractured surfaces of B and B0.5 were rather smooth. Furthermore, debonding and stretching of PBAT phase were found in the magnified SEM images of B and B0.5 (Fig. 3-16a2–a4 and b2–b4), due to the poor interfacial adhesion. Clearly, B and B0.5 samples showed brittle fractures during the impact test. However, for B1 and B1.5 samples, attributed to the enhanced interfacial adhesion, both samples were not completely fractured and the whole impact-fractured surface became rough. In specific, plastic deformation was revealed in the magnified SEM images of B1 and B1.5, especially in the later crack propagation zone (Fig. 3-16c4 and d4). As expected, increasing interfacial adhesion led to a brittle-tough transition in the solid samples, in which the impact energy dissipation changed from craze to yielding of the matrix.

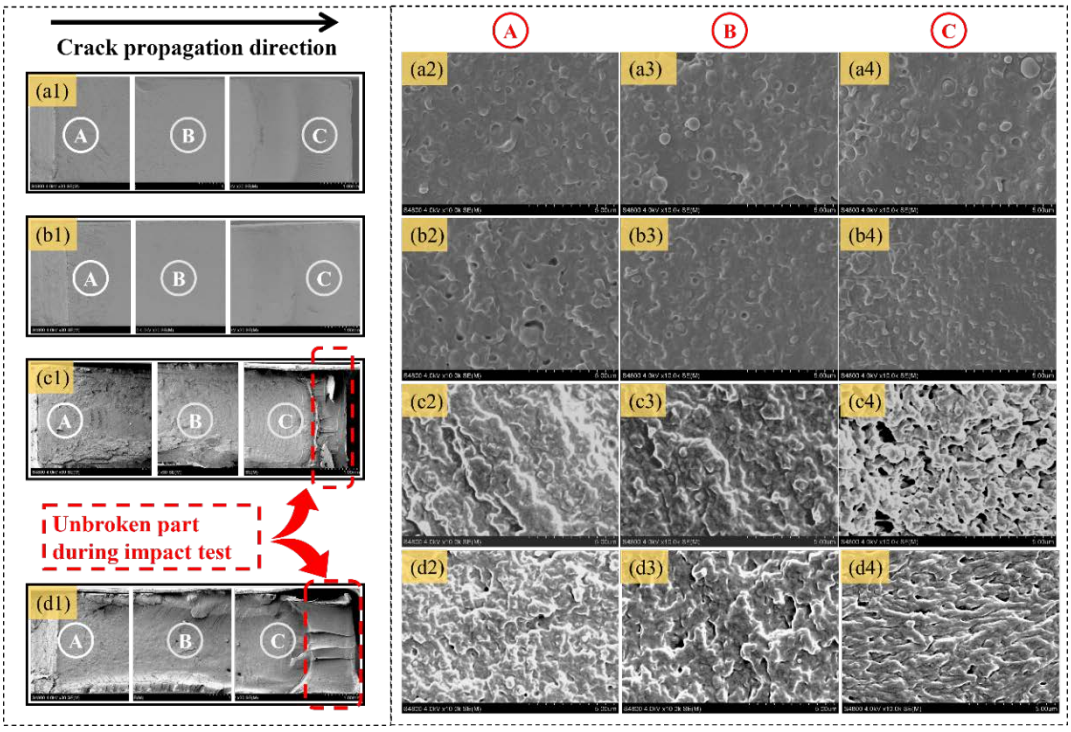

Fig. 3-16. SEM images of impact-fractured surfaces of (a) B, (b) B0.5, (c) B1, (d) B1.5. Number 1 represent the whole impact-fractured surface morphology at low magnification. Number 2, 3, and 4 represent the magnified images obtained from the crack initiation zone (position A), the early crack propagation zone (position B) and the later crack propagation zone (position C), respectively.

Compared with solid samples, the macro-deformation processes of foamed samples became more complicated due to the introduction of cell structure, as shown in Fig. 3-17. From the perspective of the whole morphology (Fig. 3-17a1–d1), B foam and B0.5 foam showed the much smoother impact-fractured surface than B1 foam and B1.5 foam. Interestingly, the unbroken part area of B1 foam was much larger than that of B1.5 foam, proving the rationality of the big difference in impact strength between those two samples (Fig. 3-15b). In the initiation zone (position A), deformed cell structure could be found in all samples due to the huge impact force.

For B and B0.5 foams with low interfacial adhesion, the cells preserved their original shape after the impact test in both the early crack propagation zone (position B) and the later crack propagation zone (position C). In addition, fibrillar PBAT phases could be found in B and B0.5 foams as shown in Fig. 3-18, which were the magnified images of the early crack propagation zone (position B). It confirmed that the PBAT phase was elongated during the impact process due to the poor interfacial adhesion between PLA and PBAT, but the PLA phase still showed brittle fracture, leading to the low impact strength. When ADR content increased to high levels (1 or 1.5 phr ADR content), the enhanced interfacial adhesion caused the disappearance of fibrillar PBAT, and the appearance of plastic deformation is shown in Fig. 3-18. More interestingly, the cell walls of B1 and B1.5 foams in the later crack propagation zone were extremely stretched. The obvious plastic deformation suggested the high fracture resistance, resulting in the enhanced ductility of B1foam and B1.5 foam in comparison with B foam and B0.5 foam. With the increase in ADR content from 1 to 1.5 phr, the big cell size increased from 11.2 to 60.2 μm, resulting in a thicker cell wall around the big cells (Fig. 3-17d3). Based on the SEM images of Fig. 3-17c3 and d3, it could be induced that the presence of the thicker cell wall of B1.5 foam would prevent the deformation of the cell wall, leading to the impaired impact strength compared with B1 foam.

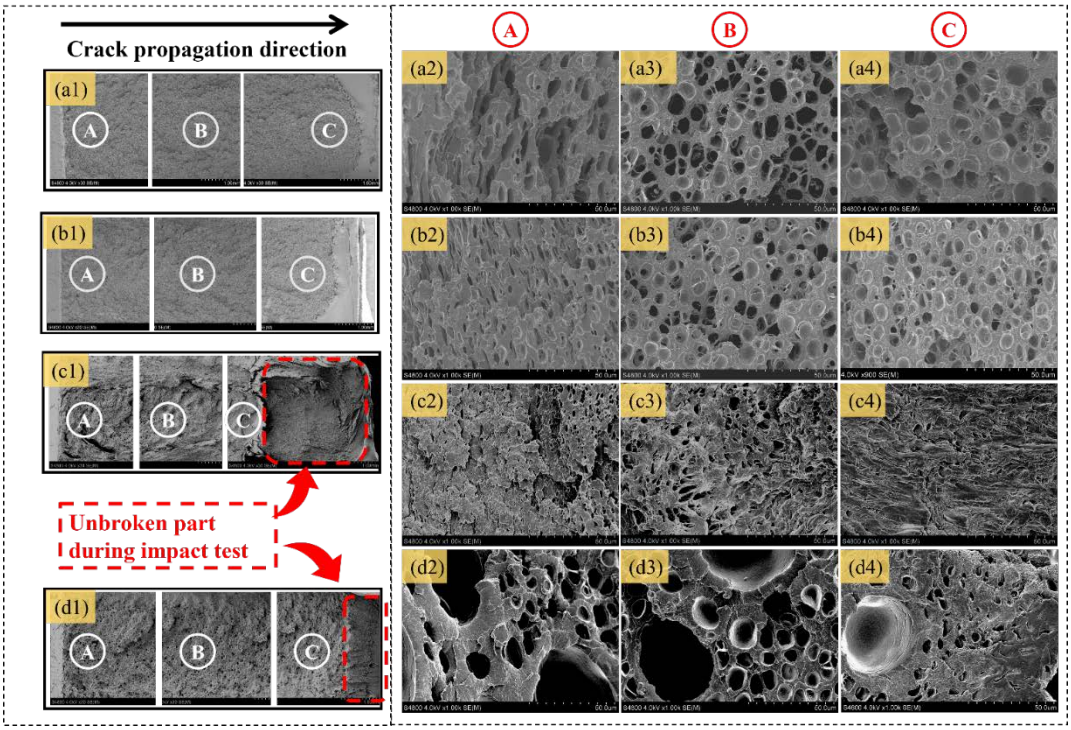

Fig. 3-17. SEM images of impact-fractured surfaces of (a) B foam, (b) B0.5 foam, (c) B1foam, (d) B1.5 foam. Number 1 represent the whole impact-fractured surface morphology at low magnification. Number 2, 3, and 4 represent the magnified images obtained from the crack initiation zone (position A), the early crack propagation zone (position B) and the later crack propagation zone (position C), respectively.

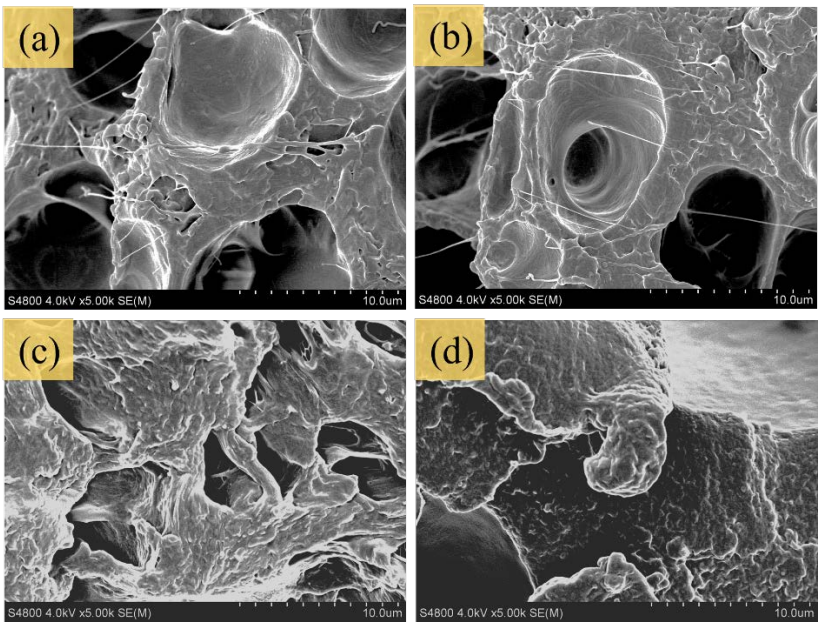

Fig. 3-18. SEM images of (a) B, (b) B0.5, (c) B1, (d) B1.5 foam at the early crack propagation zone.

Apart from the impact-fractured surfaces, SEM images of B1 foam and B1.5 foam in whitened region were studied, as shown in Fig. 3-19. Cellular deformation was clearly observed in the whitened region for B1 foam, and the deformation zone (marked by red dashed boxes) was much larger than B1.5 foam. This phenomenon undisputed proved that small cells were favorable to deformation during the impact test, leading to larger energy dissipation. Based on the previous analysis, the schematic of the impact-fractured surface morphology of PLA/PBAT blend foams is exhibited in Fig. 3-20. There were two main factors that would affect the impact behavior of PLA/PBAT blend foams, including interfacial adhesion and cell size. Two main conclusions could be proposed. First, independent of cell size, interfacial adhesion was the key factor that could lead to the brittle-tough transition of PLA/PBAT blend foams. Second, for PLA/PBAT blend foams with good interfacial

adhesion, small cell size (<12 μm) was conducive to the development of matrix yielding (small-scale plastic deformation) into cell stretching (large-scale plastic deformation), and extended the area of the whitened region (Fig. 3-19), which would extremely enhance the impact strength of PLA/PBAT blend foams.

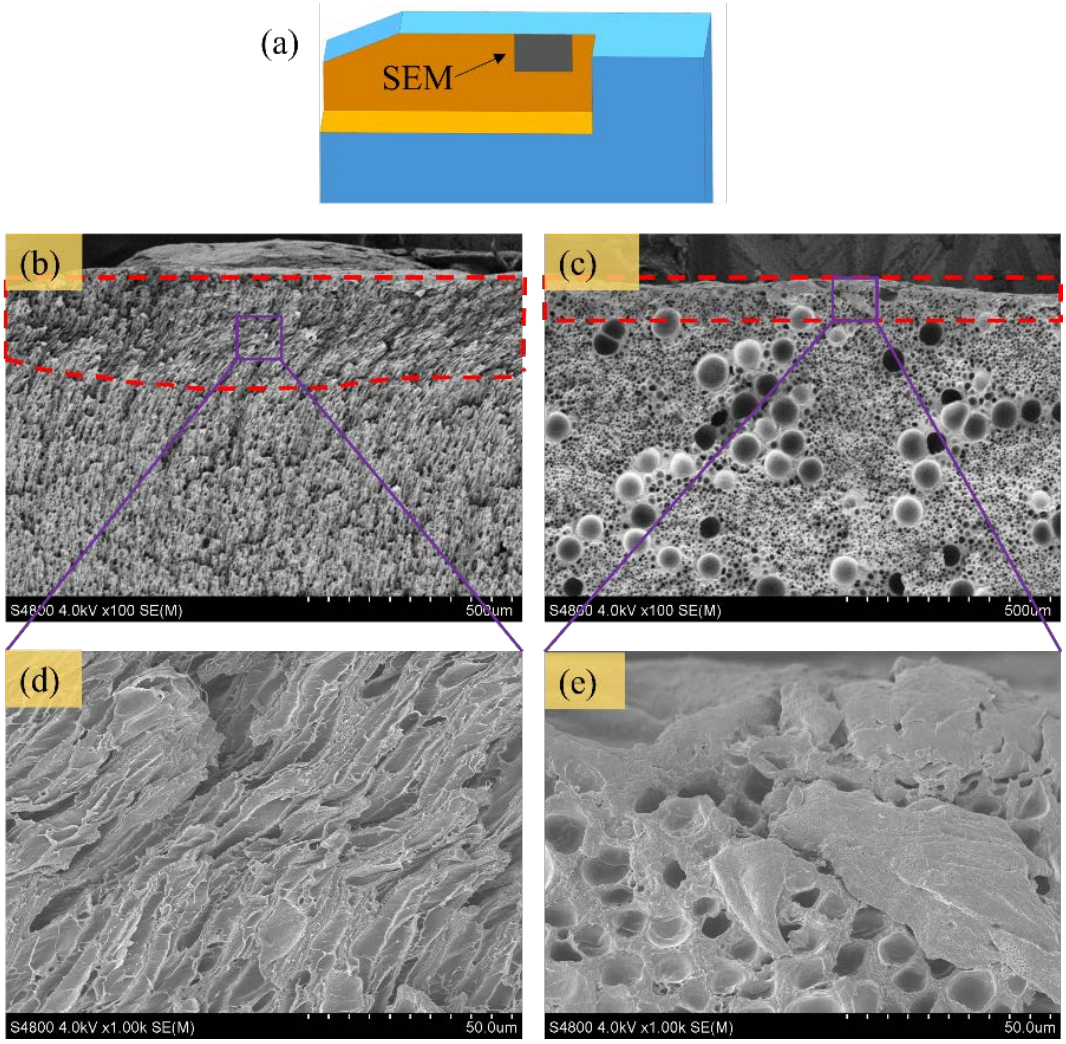

Fig. 3-19. (a) Schematic of sample position for SEM. SEM images of (b, d) B1 foam and (c, e) B1.5 foam in whitened region perpendicular to the impact-fractured surface.

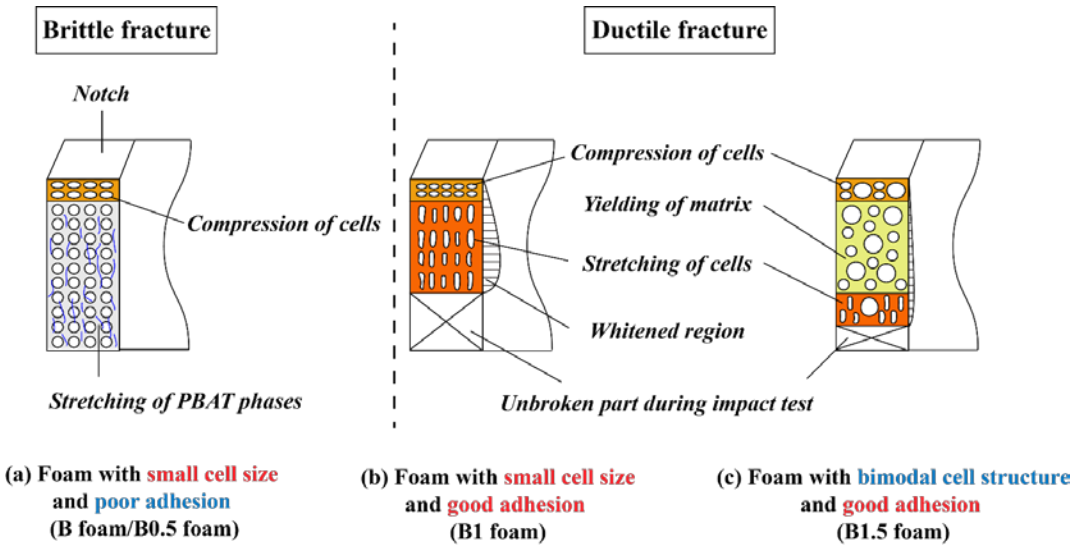

Fig. 3-20. Schematic of the impact-fractured surface morphology of PLA/PBAT blend foams.

3.5. Conclusion

In this work, super toughened PLA/PBAT blend foams were successfully obtained through a reactive extrusion and the followed core-back FIM. When the ADR content increased to 1 phr, the impact strength of foamed sample reached 49.1 kJ/m^2, which were about 59.4% higher than that of its solid, and 9.3 and 6.4 times than that of the unmodified PLA/PBAT blend and its foam, respectively. In addition, the elongation at break of PLA/PBAT/ADR (1 wt%) foam increased to 71%, which was about 2.2 times that of the unmodified PLA/PBAT foam. FTIR, NMR and GPC analysis showed that the chain extension reaction between ADR and PLA/PBAT led to the increase in the molecular weights. SEM and rheological results confirmed that the formation of PLA-co-PBAT copolymer could significantly improve the

compatibility between PLA and PBAT. For solid blend samples, the impact strength was strongly related to the compatibility. In contrast, as for the foamed PLA/PBAT blends, except for the compatibility, the thin cell walls (the corresponding cell size < 12 μm in this study) were prone to plastic deformation compared with thick cell walls (the corresponding cell size > 60 μm) and absorbed a large amount of energy. The enhanced compatibility and small cell size were responsible for the super toughness of injection-molded PLA/PBAT blend foam.

3.6. References

[1] C. Albano, J. Reyes, M. Ichazo, J. González, M. Brito, D. Moronta, Analysis of the mechanical, thermal and morphological behaviour of polypropylene compounds with sisal fibre and wood flour, irradiated with gamma rays, Polym. Degrad. Stab. 76(2) (2002) 191-203. https://doi.org/10.1016/S0141-3910(02)00014-9

[2] Q. Ju, Z. Tang, H. Shi, Y. Zhu, Y. Shen, T. Wang, Thermoplastic starch based blends as a highly renewable filament for fused deposition modeling 3D printing, Int. J. Biol. Macromol. 219 (2022) 175-184. https://doi.org/10.1016/j.ijbiomac.2022.07.232

[3] P. Wang, S. Gao, X. Chen, L. Yang, X. Wu, S. Feng, X. Hu, J. Liu, P. Xu, Y. Ding, Effect of hydroxyl and carboxyl-functionalized carbon nanotubes on phase morphology, mechanical and dielectric properties of poly(lactide)/poly(butylene adipate-co-terephthalate) composites, Int. J. Biol. Macromol. 206 (2022) 661-669. https://doi.org/10.1016/j.ijbiomac.2022.02.183

[4] Y. Kwon, K.T. Kim, Crystallization-driven self-assembly of block copolymers having monodisperse poly(lactic acid)s with defined stereochemical sequences, Macromolecules 54(22) (2021) 10487-10498. https://doi.org/10.1021/acs.macromol.1c01825

[5] H. Xu, L. Ke, M. Tang, H. Shang, Z.-L. Zhang, W. Xu, Y.-N. Fu, Y. Wang, D. Tang, D. Huang, S. Zhang, H.-R. Yang, X. He, J. Gao, Pea pod-mimicking hydroxyapatite nanowhisker-reinforced poly(lactic acid) composites with bone-like strength, Int. J. Biol. Macromol. 216 (2022) 114-123. https://doi.org/10.1016/j.ijbiomac.2022.06.211

[6] H. Shang, K. Xu, X. Li, S. Lu, L. Ke, H.-R. Yang, J. Gao, D. Tang, D. Huang, X. He, H. Xu, B. Shen, UV-protective and high-transparency poly(lactic acid) biocomposites for ecofriendly packaging of perishable fruits, Int. J. Biol. Macromol. 222 (2022) 927-937. https://doi.org/10.1016/j.ijbiomac.2022.09.219

[7] S. Deng, H. Bai, Z. Liu, Q. Zhang, Q. Fu, Toward Supertough and Heat-Resistant Stereocomplex-Type Polylactide/Elastomer Blends with Impressive Melt Stability via in Situ Formation of Graft Copolymer during One-Pot Reactive Melt Blending, Macromolecules 52(4) (2019) 1718-1730. https://doi.org/10.1021/acs.macromol.8b02626

[8] D.D. Wu, Y. Guo, A.P. Huang, R.W. Xu, P. Liu, Effect of the multi-functional epoxides on the thermal, mechanical and rheological properties of poly(butylene adipate-co-terephthalate)/polylactide blends, Polym. Bull. 78(10) (2021) 5567-5591. https://doi.org/10.1007/s00289-020-03379-x

[9] T. Kuboki, Mechanical properties and foaming behavior of injection molded cellulose fiber reinforced polypropylene composite foams, J. Cell. Plast. 50(2) (2014) 129-143. https://doi.org/10.1177/0021955x13504776

[10] L.M. Matuana, Solid state microcellular foamed poly(lactic acid): Morphology and property characterization, Bioresour. Technol. 99(9) (2008) 3643-3650. https://doi.org/10.1016/j.biortech.2007.07.062

[11] L. Wang, Y. Hikima, M. Ohshima, A. Yusa, S. Yamamoto, H. Goto, Development of a simplified foam injection molding technique and its application to the production of high void fraction polypropylene foams, Ind. Eng. Chem. Res. 56(46) (2017) 13734-13742. https://doi.org/10.1021/acs.iecr.7b03382

[12] B. Zhao, M. Hamidinejad, S. Wang, P.W. Bai, R.C. Che, R. Zhang, C.B. Park, Advances in electromagnetic shielding properties of composite foams, J. Mater. Chem. A 9(14) (2021) 8896-8949. https://doi.org/10.1039/d1ta00417d

[13] M. Nofar, C.B. Park, Poly (lactic acid) foaming, Prog. Polym. Sci. 39(10) (2014) 1721-1741. https://doi.org/10.1016/j.progpolymsci.2014.04.001

[14] J. Liu, L. Lou, W. Yu, R. Liao, R. Li, C. Zhou, Long chain branching polylactide: Structures and properties, Polymer 51(22) (2010) 5186-5197. https://doi.org/10.1016/j.polymer.2010.09.002

[15] M. Li, S. Li, B. Liu, T. Jiang, D. Zhang, L. Cao, L. He, W. Gong, Rheological behavior, crystallization properties, and foaming performance of chain-extended poly (lactic acid) by functionalized epoxy, RSC Adv. 11(52) (2021) 32799-32809. https://doi.org/10.1039/D1RA06382K

[16] R. Al-Itry, K. Lamnawar, A. Maazouz, Reactive extrusion of PLA, PBAT with a multi-functional epoxide: Physico-chemical and rheological properties, Eur. Polym. J. 58 (2014) 90-102. https://doi.org/10.1016/j.eurpolymj.2014.06.013

[17] W. Liu, P. Chen, X.D. Wang, F.C. Wang, Y.J. Wu, Effects of poly(butyleneadipate-co-terephthalate) as a macromolecular nucleating agent on the crystallization and foaming behavior of biodegradable poly(lactic acid), Cell. Polym. 36(2) (2017) 75-96. https://doi.org/10.1177/026248931703600202

[18] X. Wang, W. Liu, H. Zhou, B. Liu, H. Li, Z. Du, C. Zhang, Study on the effect of dispersion

phase morphology on porous structure of poly (lactic acid)/poly (ethylene terephthalate glycol-modified) blending foams, Polymer 54(21) (2013) 5839-5851. https://doi.org/10.1016/j.polymer.2013.08.050

[19] G. Wang, J. Zhao, G. Wang, H. Zhao, J. Lin, G. Zhao, C.B. Park, Strong and super thermally insulating in-situ nanofibrillar PLA/PET composite foam fabricated by high-pressure microcellular injection molding, Chem. Eng. J. 390 (2020) 124520. https://doi.org/10.1016/j.cej.2020.124520

[20] J. Chai, G. Wang, A. Zhang, G. Dong, S. Li, J. Zhao, G. Zhao, Microcellular injection molded lightweight and tough poly (L-lactic acid)/in-situ polytetrafluoroethylene nanocomposite foams with enhanced surface quality and thermally-insulating performance, J. Biol. Macromol. 215 (2022) 57-66. https://doi.org/10.1016/j.ijbiomac.2022.06.091

[21] Q. Ren, M. Wu, L. Wang, W. Zheng, Y. Hikima, T. Semba, M. Ohshima, Cellulose nanofiber reinforced poly (lactic acid) with enhanced rheology, crystallization and foaming ability, Carbohydr. Polym. 286 (2022) 119320. https://doi.org/10.1016/j.carbpol.2022.119320

[22] Z. Xu, X. Lin, H. Liu, The application of blocked polyfunctional isocyanate as a cross-linking agent in biodegradable extruded poly(lactic acid) foam, Iran. Polym. J. 28(5) (2019) 417-424. https://doi.org/10.1007/s13726-019-00710-w

[23] A. Pietrosanto, A. Apicella, P. Scarfato, L. Incarnato, L. Di Maio, Development of Novel Blown Shrink Films from Poly(Lactide)/Poly(Butylene-Adipate-co-Terephthalate) Blends for Sustainable Food Packaging Applications, Polym. 14(14) (2022) 2759. https://doi.org/10.3390/polym14142759

[24] K. Hamad, M. Kaseem, M. Ayyoob, J. Joo, F. Deri, Polylactic acid blends: The future of green, light and tough, Prog. Polym. Sci. 85 (2018) 83-127. https://doi.org/10.1016/j.progpolymsci.2018.07.001

[25] H. Bai, C. Huang, H. Xiu, Y. Gao, Q. Zhang, Q. Fu, Toughening of poly(l-lactide) with poly(ε-caprolactone): Combined effects of matrix crystallization and impact modifier particle size, Polymer 54(19) (2013) 5257-5266. https://doi.org/10.1016/j.polymer.2013.07.051

[26] S. Lin, W. Guo, C. Chen, J. Ma, B. Wang, Mechanical properties and morphology of biodegradable poly(lactic acid)/poly(butylene adipate-co-terephthalate) blends compatibilized by transesterification, Mater. Des. (1980-2015) 36 (2012) 604-608. https://doi.org/10.1016/j.matdes.2011.11.036

[27] J. Huang, J. Fan, L. Cao, C. Xu, Y. Chen, A novel strategy to construct co-continuous PLA/NBR thermoplastic vulcanizates: Metal-ligand coordination-induced dynamic vulcanization, balanced stiffness-toughness and shape memory effect, Chem. Eng. J. 385 (2020) 123828. https://doi.org/10.1016/j.cej.2019.123828

[28] H. Xu, J. Zhou, K. Odelius, Z. Guo, X. Guan, M. Hakkarainen, Nanostructured Phase Morphology of a Biobased Copolymer for Tough and UV-Resistant Polylactide, ACS Appl.

Polym. Mater. 3(4) (2021) 1973-1982. https://doi.org/10.1021/acsapm.1c00057

[29] D. Sun, T. Gu, X. Qi, J. Yang, Y. Lei, Y. Wang, Highly-toughened biodegradable poly(L-lactic acid) composites with heat resistance and mechanical-damage-healing ability by adding poly(butylene adipate-co-butylene terephthalate) and carbon nanofibers, Chem. Eng. J. 424 (2021) 130558. https://doi.org/10.1016/j.cej.2021.130558

[30] J. Chen, C. Rong, T. Lin, Y. Chen, J. Wu, J. You, H. Wang, Y. Li, Stable co-continuous PLA/PBAT blends compatibilized by interfacial stereocomplex crystallites: Toward full biodegradable polymer blends with simultaneously enhanced mechanical properties and crystallization rates, Macromolecules 54(6) (2021) 2852-2861. https://doi.org/10.1021/acs.macromol.0c02861

[31] R. Al-Itry, K. Lamnawar, A. Maazouz, Improvement of thermal stability, rheological and mechanical properties of PLA, PBAT and their blends by reactive extrusion with functionalized epoxy, Polym. Degrad. Stab. 97(10) (2012) 1898-1914. https://doi.org/10.1016/j.polymdegradstab.2012.06.028

[32] X. Wang, S. Peng, H. Chen, X. Yu, X. Zhao, Mechanical properties, rheological behaviors, and phase morphologies of high-toughness PLA/PBAT blends by in-situ reactive compatibilization, Composites, Part B 173 (2019) 107028. https://doi.org/10.1016/j.compositesb.2019.107028

[33] P. Ma, X. Cai, Y. Zhang, S. Wang, W. Dong, M. Chen, P.J. Lemstra, In-situ compatibilization of poly(lactic acid) and poly(butylene adipate-co-terephthalate) blends by using dicumyl peroxide as a free-radical initiator, Polym. Degrad. Stab. 102 (2014) 145-151. hhttps://doi.org/10.1016/j.polymdegradstab.2014.01.025

[34] N. Wu, H. Zhang, Mechanical properties and phase morphology of super-tough PLA/PBAT/EMA-GMA multicomponent blends, Mater. Lett. 192 (2017) 17-20. https://doi.org/10.1016/j.matlet.2017.01.063

[35] F. Huang, W. Liu, J. Lai, J. Wu, A. Huang, L. Geng, X. Peng, Enhanced heat resistance and expansion ratio of biodegradable poly (lactic acid)/poly (butylene adipate-co-terephthalate) composite foams via synergistic effect of nucleating agent and chain extension, J. Polym. Eng. 43(4) (2023) 297-309. https://doi.org/10.1515/polyeng-2022-0284

[36] N. Najafi, M.-C. Heuzey, P.J. Carreau, D. Therriault, C.B. Park, Mechanical and morphological properties of injection molded linear and branched-polylactide (PLA) nanocomposite foams, Eur. Polym. J. 73 (2015) 455-465. https://doi.org/10.1016/j.eurpolymj.2015.11.003

[37] R.E. Lee, T. Azdast, G. Wang, X. Wang, P.C. Lee, C.B. Park, Highly expanded fine-cell foam of polylactide/polyhydroxyalkanoate/nano-fibrillated polytetrafluoroethylene composites blown with mold-opening injection molding, J. Biol. Macromol. 155 (2020) 286-292. https://doi.org/10.1016/j.ijbiomac.2020.03.212

[38] V. Shaayegan, G. Wang, C.B. Park, Study of the bubble nucleation and growth mechanisms in high-pressure foam injection molding through in-situ visualization, Eur. Polym. J. 76 (2016) 2-

13. https://doi.org/10.1016/j.eurpolymj.2015.11.021

[39] P. Tiwary, C.B. Park, M. Kontopoulou, Transition from microcellular to nanocellular PLA foams by controlling viscosity, branching and crystallization, Eur. Polym. J. 91 (2017) 283-296. https://doi.org/10.1016/j.eurpolymj.2017.04.010

[40] Y. Zhao, B. Zhao, B. Wei, Y. Wei, J. Yao, H. Zhang, X. Chen, Z. Shao, Enhanced compatibility between poly(lactic acid) and poly (butylene adipate-co-terephthalate) by incorporation of N-halamine epoxy precursor, Int. J. Biol. Macromol. 165 (2020) 460-471. https://doi.org/10.1016/j.ijbiomac.2020.09.142

[41] K. Friedrich, M. Evstatiev, S. Fakirov, O. Evstatiev, M. Ishii, M. Harrass, Microfibrillar reinforced composites from PET/PP blends: processing, morphology and mechanical properties, Compos. Sci. Technol. 65(1) (2005) 107-116. https://doi.org/10.1016/j.compscitech.2004.06.008

[42] Z.-M. Li, M.-B. Yang, B.-H. Xie, J.-M. Feng, R. Huang, In-situ microfiber reinforced composite based on PET and PE via slit die extrusion and hot stretching: Influences of hot stretching ratio on morphology and tensile properties at a fixed composition, Polym. Eng. Sci. 43(3) (2003) 615-628. https://doi.org/10.1002/pen.10050

[43] L.C. Arruda, M. Magaton, R.E.S. Bretas, M.M. Ueki, Influence of chain extender on mechanical, thermal and morphological properties of blown films of PLA/PBAT blends, Polym. Test. 43 (2015) 27-37. https://doi.org/10.1016/j.polymertesting.2015.02.005

[44] R. Al-Itry, K. Lamnawar, A. Maazouz, Rheological, morphological, and interfacial properties of compatibilized PLA/PBAT blends, Rheol. Acta 53(7) (2014) 501-517. https://doi.org/10.1007/s00397-014-0774-2

[45] C.D. Han, J. Kim, Rheological technique for determining the order–disorder transition of block copolymers, J. Polym. Sci., Part B: Polym. Phys. 25(8) (1987) 1741-1764. https://doi.org/10.1002/polb.1987.090250815

[46] P. Gong, M. Ohshima, Effect of interfacial tension on the cell structure of poly(methyl methacrylate)/bisphenol A polycarbonate blends foamed with CO_2, J. Appl. Polym. Sci. 131(5) (2014). https://doi.org/10.1002/app.39228

[47] K. Taki, K. Nitta, S.-I. Kihara, M. Ohshima, CO_2 foaming of poly(ethylene glycol)/polystyrene blends: Relationship of the blend morphology, CO2 mass transfer, and cellular structure, J. Appl. Polym. Sci. 97(5) (2005) 1899-1906. https://doi.org/10.1002/app.21930

[48] W. Zhai, H. Wang, J. Yu, J. Dong, J. He, Foaming behavior of polypropylene/polystyrene blends enhanced by improved interfacial compatibility, J. Polym. Sci., Part B: Polym. Phys. 46(16) (2008) 1641-1651. https://doi.org/10.1002/polb.21498

[49] M. Takada, S. Hasegawa, M. Ohshima, Crystallization kinetics of poly(L-lactide) in contact with pressurized CO_2, Polym. Eng. Sci. 44(1) (2004) 186-196. https://doi.org/10.1002/pen.20017

[50] D.-c. Li, T. Liu, L. Zhao, X.-s. Lian, W.-k. Yuan, Foaming of poly(lactic acid) based on its nonisothermal crystallization behavior under compressed carbon dioxide, Ind. Eng. Chem. Res. 50(4) (2011) 1997-2007. https://doi.org/10.1021/ie101723g

[51] Y. Zhang, J. Li, L. Shen, H. Lin, Y. Shan, The observation of PP/EVA blends in which isotactic PP was preradiated with different radiation absorbed doses, J. Appl. Polym. Sci. 134(28) (2017) 45057. https://doi.org/10.1002/app.45057

[52] S. Dalai, C. Wenxiu, Radiation effects on poly(propylene) (PP)/ethylene–vinyl acetate copolymer (EVA) blends, J. Appl. Polym. Sci. 86(13) (2002) 3420-3424. https://doi.org/10.1002/app.11365

[53] V. Ojijo, S.S. Ray, Super toughened biodegradable polylactide blends with non-linear copolymer interfacial architecture obtained via facile in-situ reactive compatibilization, Polymer 80 (2015) 1-17. https://doi.org/10.1016/j.polymer.2015.10.038

[54] J. Zhao, Y. Qiao, G. Wang, C. Wang, C.B. Park, Lightweight and tough PP/talc composite foam with bimodal nanoporous structure achieved by microcellular injection molding, Mater. Des. 195 (2020) 109051. https://doi.org/10.1016/j.matdes.2020.109051

[55] X. Sun, H. Kharbas, J. Peng, L.-S. Turng, A novel method of producing lightweight microcellular injection molded parts with improved ductility and toughness, Polymer 56 (2015) 102-110. https://doi.org/10.1016/j.polymer.2014.09.066

[56] V. Nagarajan, A.K. Mohanty, M. Misra, Perspective on Polylactic Acid (PLA) based Sustainable Materials for Durable Applications: Focus on Toughness and Heat Resistance, ACS Sustainable Chem. Eng. 4(6) (2016) 2899-2916. https://doi.org/10.1021/acssuschemeng.6b00321

Chapter 4: Cell structure and adhesion in polymer blend foams: Cell size-induced brittle-tough transition

In Chapter 3, a super toughened PLA/PBAT foam was prepared by introducing PBAT and a chain extender. The enhanced interfacial adhesion could cause a brittle-tough transition of PLA/PBAT foams. In addition, the existence of big cells (cell size > 60 μm) can damage the impact toughness even for PLA/PBAT foams with good interfacial adhesion.

Building on the results in Chapter 3, the next step is to figure out the relationship between cell size and impact strength. Herein, PLA/PBAT blend foams with various cell sizes but a fixed VF were prepared by using core-back FIM technique. The tests of impact strength were conducted. Besides, the effect of interfacial adhesion on impact strength was also considered. Finally, the cell size-induced toughening mechanism was discussed.

4.1. Abstract

The mechanical properties of polymeric foams are closely associated with their cellular structure. However, the study of how cell structure influences the mechanical behavior of polymeric foams is complicated by the interrelated variations in cell size and expansion ratio. Herein, we explored the relationship between cell size and impact strength in PLA/rubber blend foams by controlling the cell size while keeping the expansion ratio constant. This was achieved using the core-back FIM technique. Surprisingly, a cell size-induced brittle-tough transition occurred at a specific critical cell size. Foams exhibited brittleness when the cell size exceeded this critical threshold, whereas smaller cell sizes resulted in toughness. Furthermore, we found that enhancing the interfacial adhesion effectively increased the critical cell size. The fracture behavior of foams across a spectrum of cell sizes was extensively examined using impact test and SENTB techniques, leading to the proposal of a cell size-induced toughening mechanism. Below the critical cell size, the proximity of the cells facilitated a robust interaction of stress fields generated by adjacent cells, coupled with the beneficial role of rubber particles in hindering the progression of cell-induced crazes to cracks, thereby absorbing significant energy. Conversely, when the cell size surpassed the critical value, the diminished interaction among cells allowed cell-induced crazes to develop directedly into cracks, resulting in reduced impact strength. This proposed toughening mechanism is likely applicable across a broad range of brittle polymer/rubber blend foams, suggesting a universal strategy for enhancing the resilience of polymeric foam materials.

4.2. Introduction

Thermoplastic foams have been extensively used across various sectors s such as packaging, automotive, and construction due to their notable advantages including superior impact resistance, good acoustic and thermal properties, and reduced densities[1-4]. The excellent mechanical properties of these foams are favorable for their wide applications. Beyond the intrinsic qualities of the foam precursors, the cellular structure parameters, including density and cell size, markedly affect the final mechanical properties[5-7]. Specifically, the modulus or strength of microcellular foam is predominantly determined by the relative density, as elucidated by Gibson and Ashby[8]. However, focusing solely on density's impact on strength can yield inconsistent outcomes. For instance, the impact strength of PP foams initially increased with a decrease in relative density up to a point (around 0.6) and then decreased [9]. Conversely, the impact strength of PS foams consistently reduced with a decrease in relative density[10]. Given the variation in cell size attendant on density changes, both density and cell size are essential in discussing the determinants of the impact strength of polymeric foams.

Contradictory findings have emerged regarding the relationship between cell size and the impact strength of polymeric foams. Barlow et al[11] prepared PC foams with different cell sizes (6–18 μm) while maintaining a constant relative density (0.7), and found that the impact strength enhanced with the increase of cell size. Conversely, Bao et al compared the impact strength of PS foams with different cell sizes and the same relative density, revealing a decline in impact strength with the

enlargement of cell size at the same relative density (0.3 or 0.56). This disparity in outcomes underscores the necessity for further comprehensive investigations to elucidate the relationship between cell size and impact strength within polymeric foams.

PLA, recognized for its bio-based and biodegradable nature, has become one of the most commercially viable polymers, attributed to its excellent properties such as high stiffness, high strength, and good transparency[12, 13]. Despite these advantages, the inherent brittleness of PLA limits its foams' broader applications, with only a limited number of studies addressing this challenge. For instance, Xiang et al.[14] prepared strong and tough PLA foams through a process of PIF followed by supercritical CO_2 foaming. The orientation of crystals, alongside the presence of micro-/nano-cells, resulted in PLA foam obtained at 40 ℃ with an impressive impact strength of 32.3 kJ/m^2. However, the PIF process necessitates specialized equipment capable of exerting an internal pressure as high as 180 MPa, rendering this method less feasible for large-scale industrial production. Najafi et al[15] demonstrated that adding 0.5 wt% clay into long-chain branched PLA could improve the cell structure, leading to a significant improvement in the specific impact strength from 13.9 to 19.1 (kJ·m^{-2})/(g·cm^{-3}). It should be noticed that these impact strengths were derived from tests on unnotched samples, and the toughness improvement was only about 37%. This incremental progress underscores the growing necessity to advance the toughness of PLA foams to expand their application spectrum. In this regard, conducting a systematic investigation into the correlation between cell size and impact properties of PLA foams could yield

valuable insights, potentially paving the way for developing more robust PLA foam products.

Building on the concept of blending toughening strategies for solid PLA[16, 17], we have explored the toughening of PLA foams by incorporating PBAT and a chain extender, ADR (which is known to react with both PLA and PBAT, thereby enhancing the interfacial adhesion between PLA and PBAT), as detailed in our previous work[18]. We studied the effect of ADR content on the cell structure and impact strength of PLA/PBAT (70/30) blend foams. The findings indicated that the optimal impact strength, reaching 49.1 kJ/m^2 was achieved by adding 1phr ADR, which was 6.4 times relative to the impact strength of the unmodified PLA/PBAT blend foams. However, increasing the ADR content to 1.5 phr leaded to a diminished impact strength of 28.7 kJ/m^2 due to the formation of larger cells from approximately 12 to 60 μm), despite improved interfacial adhesion between PLA and PBAT. This outcome emphatically demonstrates proved that the cell structure would heavily influence the impact strength of PLA foams.

In this study, based on our preceding investigations into PLA/PBAT blend foams, both the unmodified PLA/PBAT blend and a phase interface-enhanced PLA/PBAT blend (incorporating 1 phr chain extender ADR) were selected for foam preparation. These foams were fabricated with various cell sizes but maintained a fixed VF (either 30% or 40%) using core-back foaming injection molding (FIM). The relationship between cell size and impact strength of the PLA/PBAT foams was systematically evaluated. The cell size-induced toughening mechanism was also proposed. The presence of cells was found to initiate crazes due to a lower stress

required for initiation. For foams with cell size below a critical threshold, cell-induced crazes would develop stably between neighboring cells, leading to high impact strength. In contrast, for larger cell sizes, the cell-induced crazes would transition directly to cracks, resulting in a diminished impact strength.

4.3. Experimental section

4.3.1. Materials

An extrusion-grade PLA 4032D with a density of 1.24 g/cm^3 and an MFR of 7 g/10 min (210 ℃, 2.16 kg) was purchased from NatureWorks LLC. PBAT TH801T was kindly provided by Xinjiang Blue Ridge Tunhe Sci.&Tech. Co., Ltd. The reactive compatibilizer with the trade name of Joncryl ADR-4468 (ADR) was obtained from BASF. Its molecular weight and epoxy equivalent weight were 7250 g/mol and 310 g/mol, respectively. N_2 with a purity of 0.99 was supplied by Ningbo Huayu Gas Inc.

4.3.2. Blend preparation

Prior to blending, pellets of PLA and PBAT were died under vacuum at 80 ℃ overnight. A corotating twin-screw extruder (SHL-52, Nanjing Haili Extrusion Equipment Co. Ltd., China) was used to prepare PLA/PBAT/ADR blends at weight ratios of 70/30/0 and 70/30/1) with a rotary speed of 40 rpm. The temperature profile was set as 150-200 ℃ from the hopper to the die. Blends were first introduced into a water bath for cooling, and then pelletized by a cutting chamber.

4.3.3. FIM with core-back operation

A 100-ton FIM machine (Systec 100/420-310C, Demag Plastics Group, Germany),

equipped with a Mucell SCF delivery system (T100, Trexel Inc., USA), was applied for the FIM experiments. The core-back FIM process comprises four stages: injection, dwelling, core-back, and cooling[19]. Initially, a full shot is applied to completely fill out the mold cavity, inducing cell nucleation at the gate. High packing pressure during the dwelling step could causes these gate-nucleated cells to redissolve back into the melt. Subsequently, a precisely controlled core-back step can provide a driving force for cell nucleation, achieving foams with a predetermined VF. Uniform cell structures can be obtained after cooling. The utilized two-plate mold has a tensile test bar mold cavity. Its dimensions meet the Standard GB/T 1040 with the exception of thickness (3 mm). To prepare foams with various cell sizes, different dwelling times (5–30 s) and N_2 content (0.6–1 wt%) were employed. In addition, various core-back distances of 1 and 2 mm were applied to adjust the VF. The densities and VFs of the resultant foams are detailed in Table 4-1, facilitating the preparation of foams with distinct cell sizes while maintaining a consistent VF (approximately 30% or 40%). More detailed processing parameters are listed in Table 4-2.

Table 4-1. Density and VF of foamed samples

	Core-back distance (mm)	Density (g/cm^3)	VF
PLA/PBAT foams	1	0.90 ± 0.01	28%
	2	0.75 ± 0.03	40%
PLA/PBAT/ADR foams	1	0.8 ± 0.04	30%
	2	0.72 ± 0.04	42%

Table 4-2. Processing parameters used for the FIM experiments.

PARAMETERS	SOLID	FOAM
Melt temperature (℃)	200	200
Mold temperature (℃)	80	80
Injection speed (mm/s)	100	100
Injection pressure (MPa)	150	150
Back pressure (MPa)	20	20
Packing pressure (MPa)	60	60
Dwelling time (sec)	10	5–30
Core-back distance (mm)	N/A	1, 2
N_2 content (wt%)	N/A	0.6–1

4.3.4. PLA/PBAT blend morphology analysis

The phase morphology of the PLA/PBAT samples was investigated using a Hitachi-S4800 SEM. The injection-molded PLA/PBAT samples with various ADR contents were cryofractured in liquid nitrogen. Before observation, both the cryofractured and impact-fractured surfaces were coated with a layer of platinum. The weight-average particle size, D_w, was calculated through equation:

$$D_w = \frac{\sum_{i=1}^{N} n_i D_i^2}{\sum_{i=1}^{N} n_i D_i} \quad (4\text{-}1)$$

where n_i is the number of PBAT particles, D_i the diameter of PBAT particle.

A JEM-1230 transmission electron microscopy (TEM) was also used to analyze phase morphology at 80 kV. The specimens with a thickness of ~120 nm were sliced using a LEICA EM FC7 ULTRA-MICROTOME. Before observation, Ruthenium tetroxide (RuO_4) vapor was applied to selectively stain the PBAT phases at room temperature for 4 hours.

4.3.5. Rheological behavior analysis

Disk-shaped specimens, each with a diameter of 25 mm and a thickness of 1 mm, were prepared through hot pressing before rheological testing. The rheological properties of PLA, PBAT, PLA/PBAT blends with different ADR contents were investigated using an ARES rotational plate rheometer (HR-3, TA, USA) under a nitrogen atmosphere. Tests were conducted across a frequency range of 0.01–100 rad/s at a constant temperature of 190 °C and a strain amplitude of 1%.

4.3.6. Foam characterization

For the assessment of cell size and cell density, the cellular structure of the foamed samples were investigated using a SEM (EVO18, Zeiss Group, Germany). Prior to observation, specimens cut from the central part of the injection-molded foams were cryogenically fractured and subsequently coated with platinum before imaging. Then, Image J software (National Institutes of Health, US)- was applied to analyze SEM images. The cell density, N_0 (cells/cm^3), was calculated from the following equation:[20]

$$N_0 = \left(\frac{n}{A}\right)^{3/2} \Phi \tag{4-2}$$

$$\Phi = \frac{\rho_s}{\rho_f} \tag{4-3}$$

where n is the number of cells in the selected micrograph, A is the area of the micrograph, and Φ the expansion ratio of the foamed sample. ρ_s and ρ_f are the densities of the solid and its foamed counterpart, respectively. Water displacement method (ISO 1183-1987) was applied to determine ρ_s and ρ_f.

The VF, which is defined as the ratio of the volume of voids in the foam to the total

volume of the foam, was determined using equation: [20]

$$VF = \frac{\rho_f}{\rho_s} \tag{4-4}$$

The average cell size, d (μm), and the cell wall thickness, τ (μm), were obtained from the following equations (4–6):[21]

$$d = \frac{\sum_{i=1}^{N} n_i d_i}{\sum_{i=1}^{N} n_i} \tag{4-5}$$

$$\ln \sigma = \sqrt{\frac{\sum_{i=1}^{N} n_i \left(\ln d_i - \ln d\right)^2}{\sum_{i=1}^{N} n_i}} \tag{4-6}$$

$$\tau = d\left[\left(\frac{\pi}{6\varphi}\right)^{1/3} \exp\left(1.5\ln^2 \sigma\right) - \exp\left(0.5\ln^2 \sigma\right)\right] \tag{4-7}$$

where d_i is the cell size, n_i the number of cell, and σ the size distribution of cells.

4.3.7. Thermal analysis

A DSC (DSC3+, Mettler-Toledo) was used to study the thermal properties under a nitrogen atmosphere. The testing specimens cut from the core (foamed) layer of foams, with specimen sizes in the range of 5–8 mg. The test procedure consisted of a heating cycle in the temperature range of 25–190 ℃ with a heating rate of 10 ℃/min.

4.3.8. Mechanical properties

Izod impact tests were conducted according to the GB/T 1843-2008 standard using an impact tester (GT-7045-HML, Gotech Testing Machines Inc.). Additionally, SENTB test was conducted to investigate the fracture behavior of the foamed samples, using an Instron 5567 universal testing instrument (Instron, USA). The corresponding process is depicted in Fig. 4-1. Both Izod impact tests and bending tests specimens were of identical dimensions. Prior to testing, the surface layer of each specimen was meticulously removed. At least five specimens were tested for each condition and the mean values were reported.

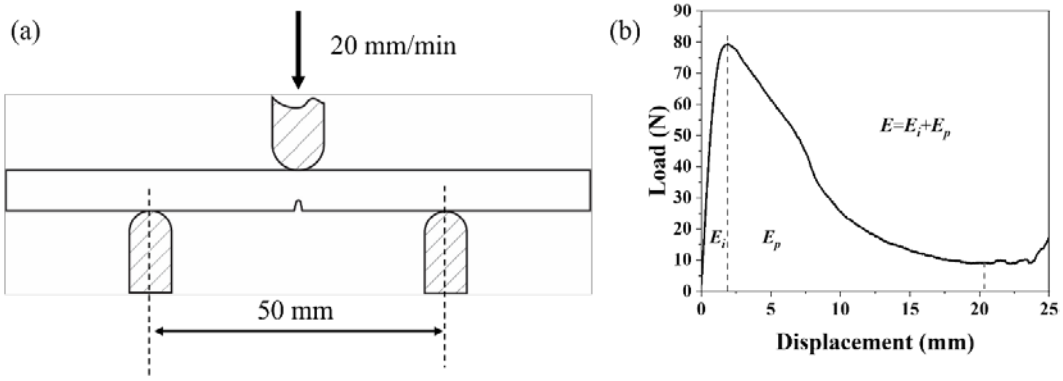

Fig. 4-1. (a) Schematic of SENTB. (b) A typical load-displacement curve.

4.4. Results and discussion

4.4.1. Phase morphology

The interaction between the terminal carboxyl groups and hydroxyl groups with the epoxy group of ADR facilitated the formation of PLA-co-PBAT copolymer, which was pivotal for improving the interfacial adhesion between PLA and PBAT in the PLA/PBAT blends[22-24]. The comprehensive examination of the reaction between

PLA/PBAT and ADR was discussed in our previous work through a series of characterization methods, including FTIR, ^{1}H NMR spectra and GPC[18]. Given the detailed analysis provided in that study, this aspect would not be reiterated herein. Fig. 4-2a and b shows the SEM images of PLA/PBAT blends with and without ADR corporation, and Fig. 4-2a' and 2b' are the corresponding TEM images. In the absence of ADR, the PLA/PBAT blend exhibits a distinct sea-island structure, attributed to suboptimal interfacial adhesion between PLA and PBAT. Conversely, the introduction of ADR resulted in a notable reduction in the size of PBAT dispersed phase, which became enveloped by the PLA matrix, indicative of improved compatibility. Fig. 4-2c to e display the phase morphology of PLA/BAT blend foams with different cell sizes. Compared to the solid sample, the PBAT particles within the foamed specimens exhibited a slight elongation during the foaming process. However, the dimensions of the PBAT particle remained almost unchanged, within a range of 0.51 to 0.68 μm, throughout the foaming. This observation indicated that variations in the particle size of PBAT had a negligible impact on the impact strength of the blend foams, thus directing the focus of discussion away from particle size variation towards other influential factors.

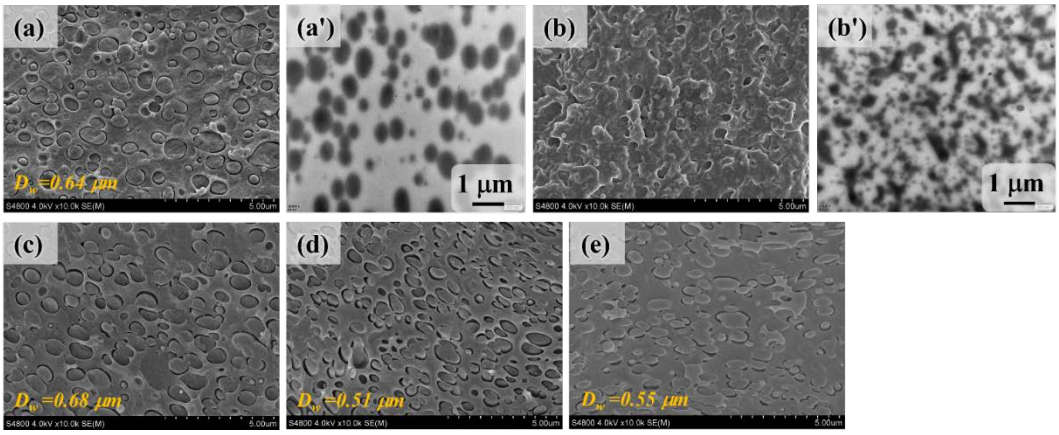

Fig. 4-2. Phase morphology of (a, a') PLA/PBAT, (b, b') PLA/PBAT/ADR, and (c–e) PLA/PBAT foams with various cell sizes: (c) 43.6 μm, (d) 19.2 μm, and (e) 11.2 μm. (a–e) obtained by SEM, and (a', b') by TEM. The VF of PLA/PBAT foams was 30%.

4.4.2. Rheological behavior

The rheological behavior of the PLA, PBAT, and PLA/PBAT blends with and without ADR, as subjected to frequency sweeps, are depicted in Fig. 4-3. For the pure PLA and PBAT, a Newtonian plateau was observed at low frequencies, followed by a typical shear-thinning behavior at higher frequencies. In contrast, the PLA/PBAT blend exhibited a distinct non-terminal behavior at low frequency region, which was ascribed to the shape relaxation phenomenon. This phenomenon involved the shape deformation of the dispersed phase within the matrix during the oscillatory shear deformation, leading to the increase of the storage modules of PLA/PBAT at low frequencies [25, 26]. Additionally, the addition of ADR into the blend markedly enhanced both the complex viscosity and storage modulus, a result of the chain extension reaction between ADR and PLA/PBAT[23]. Besides, the shear-thinning tendency of the PLA/PBAT blend became more obvious with the introduction of ADR.

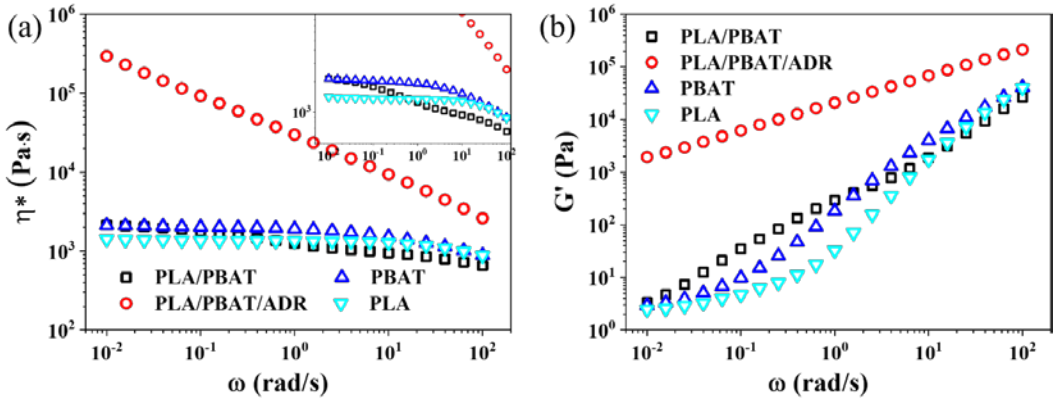

Fig. 4-3. The dependence angular frequencies of (a) complex viscosity and (b) storage modulus at 190 ℃.

4.4.3. Cellular structure

Generally, the formation of foams consists of two steps, including cell nucleation and cell growth. During the cell nucleation step, the inclusion of a higher content of physical blowing agent or nucleating agent additives are effective methods to accelerate cell nucleation. This efficacy is due to the fact that physical blowing agents can enhance the driving force for cell nucleation, whereas nucleating agents can significantly lower the energy barrier for heterogeneous nucleation according to the traditional cell nucleation theory[27, 28]. During the cell growth stage, an increase in melt strength could suppress the growth of nucleated cells, leading to a smaller cell size. As the melt strength is strongly related with the melt temperature, foams with smaller cell sizes could be achieved by extending the dwelling times in the FIM process. To examine the relationship between cell size and impact strength without introducing additional variables, N_2 content and dwelling time were selected as the primary parameters to modulate the cellular structure of the injection-molded foams. Consequently, different N_2 contents and dwelling times were employed to prepare foams with various cell sizes. Fig. 4-4 and 4-5 show the SEM images of PLA/PBAT foams with VF of 30% and 40%, respectively, while Fig. 4-6 and 4-7 illustrate the corresponding cell size distributions. The cell sizes ranged from 43.6 to 11.2 μm for foams with a VF of 30% and from 22.8 to 6.4 μm for those with a 40% VF of. To further characterize the cell structure, Fig. 4-8 demonstrates

the relationship between cell size and two other critical parameters–cell density and cell wall thickness– for foams with VFs of 30% and 40%. There was a clear correlation among these parameters: as cell size increased, cell density decreased, whereas cell wall thickness increased. This variation in cell size resulted in cell wall thicknesses ranging from 3.2 to 13.3 μm for foams with a 30% VF and from 1.3 to 3.6 μm for foams with a 40% VF.

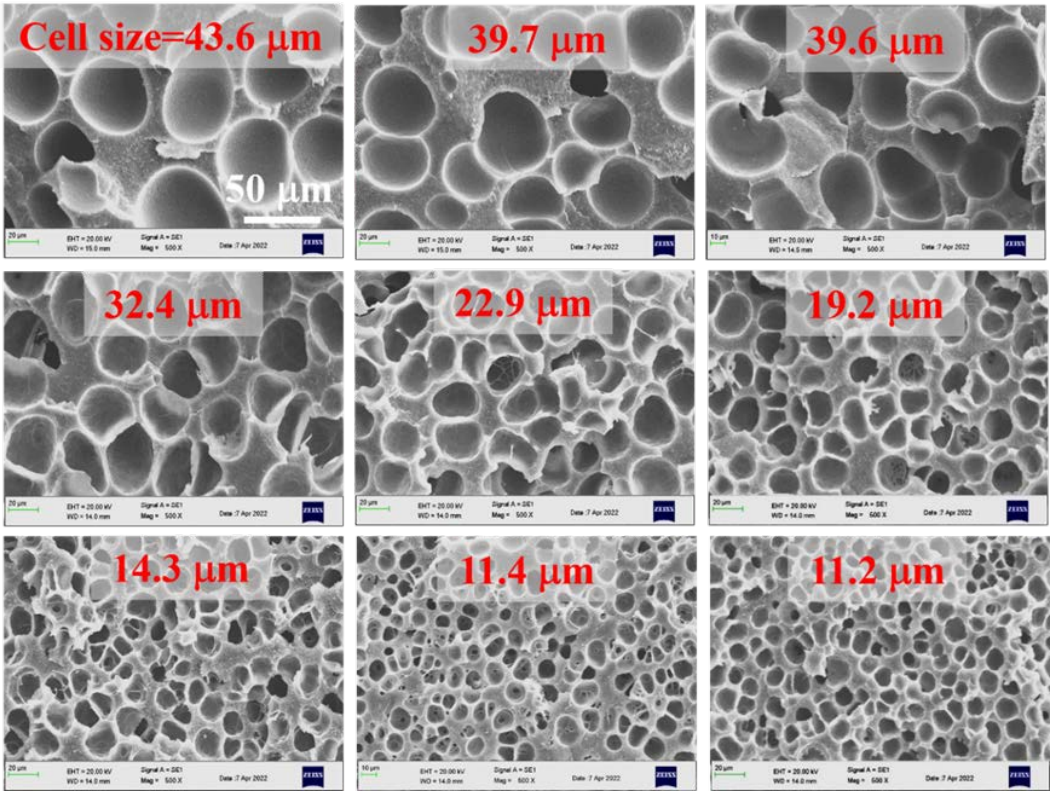

Fig. 4-4. SEM images of PLA/PBAT foams with different cell sizes and a fixed VF of 30%.

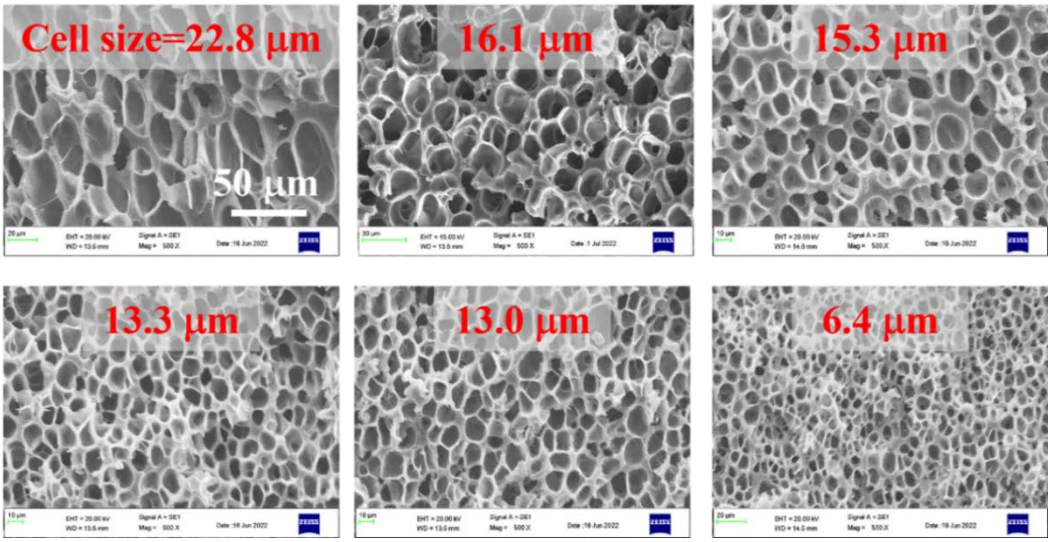

Fig. 4-5. SEM images of PLA/PBAT foams with different cell sizes and a fixed VF of 40%.

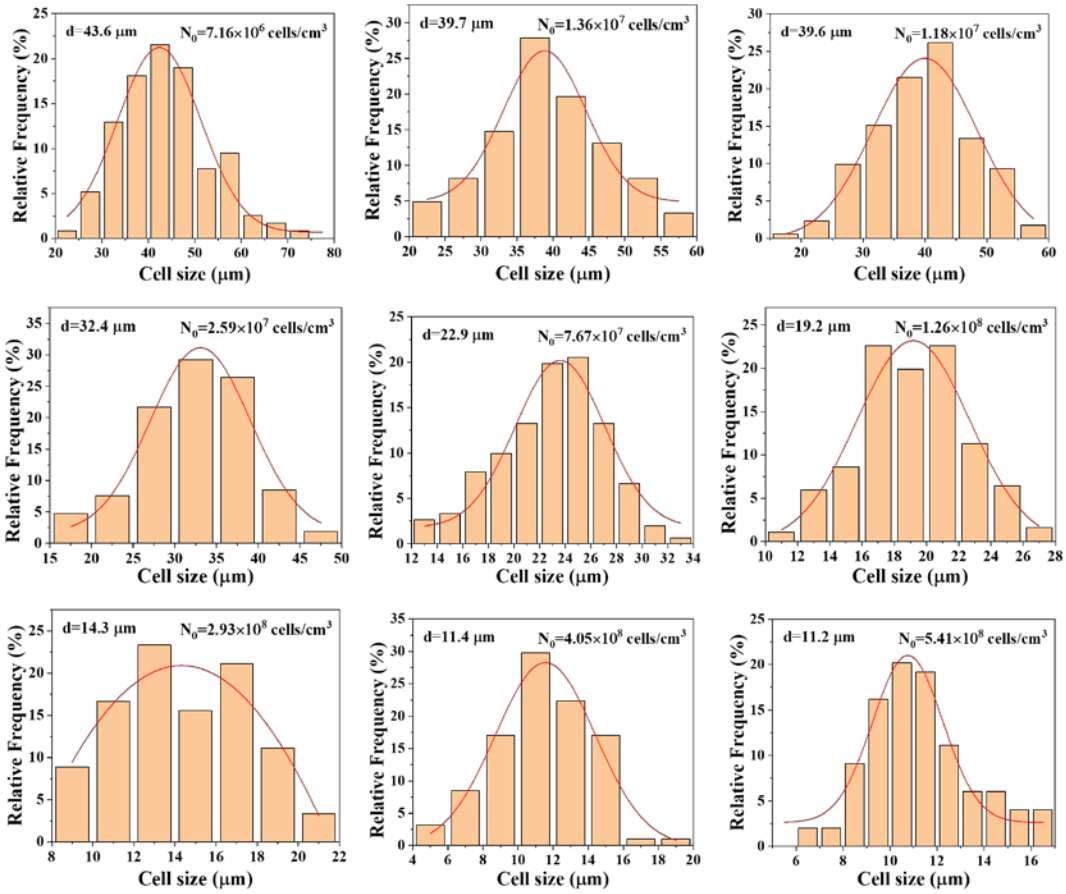

Fig. 4-6. Cell size distribution of PLA/PBAT foams with a VF of 30%.

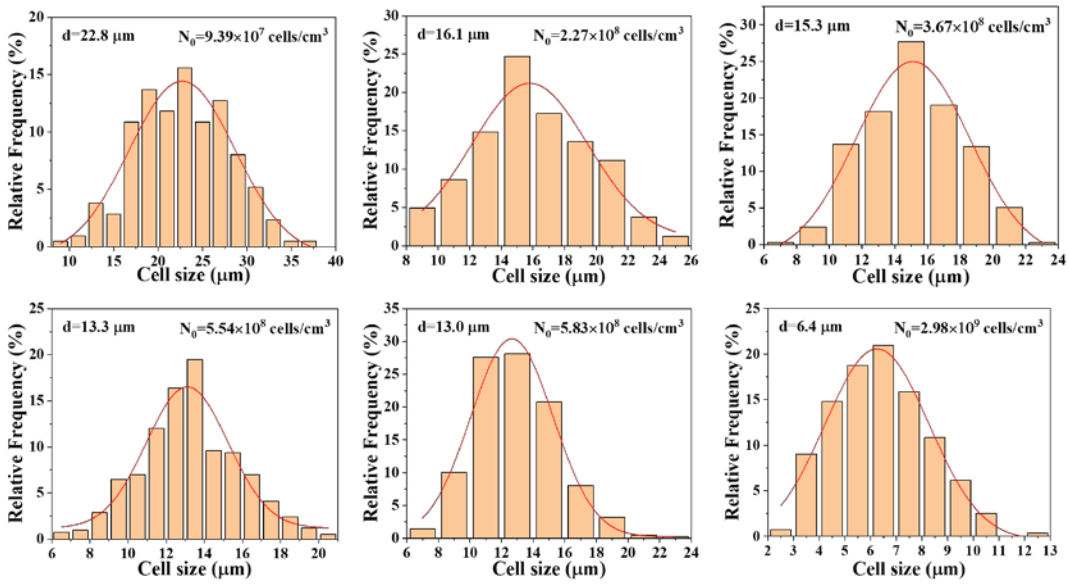

Fig. 4-7. Cell size distribution of PLA/PBAT foams with a VF of 40%.

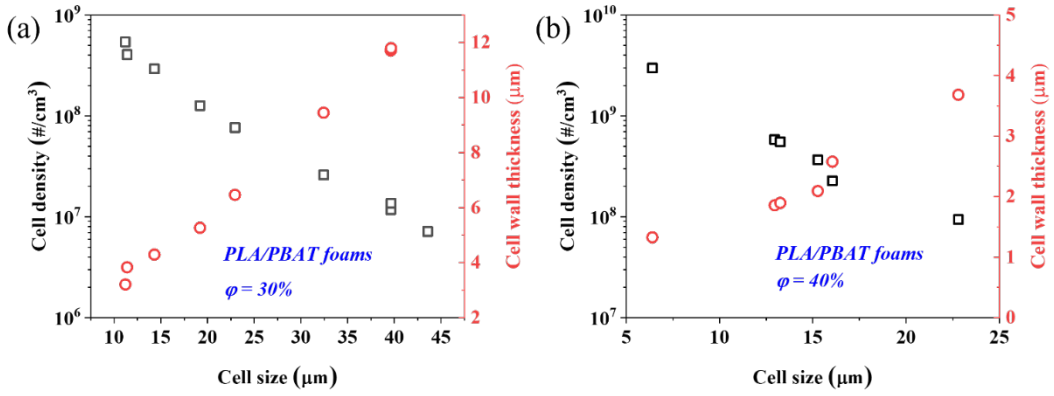

Fig. 4-8. Cell size dependence of cell density and cell wall thickness for PLA/PBAT foams with VF of (a) 30% and (b) 40%.

Following the same preparation methodology, PLA/PBAT/ADR foams with a range of cell sizes were produced, corresponding to VFs of 30% and 40%, as shown in Fig. 4-9 and 4-10. The distribution of cell size for these foams is further depicted in Fig. 4-11 and 4-12. Fig. 4-13. presents the cell size dependence of cell density and cell wall thickness for foams with VFs of 30% and 40%. For foams with a 30% VF,

the cell wall thickness varied between 1.2 and 41.4 μm, whereas foams with a 40% VF exhibited cell wall thicknesses ranging from 1.8 to 14.4 μm.

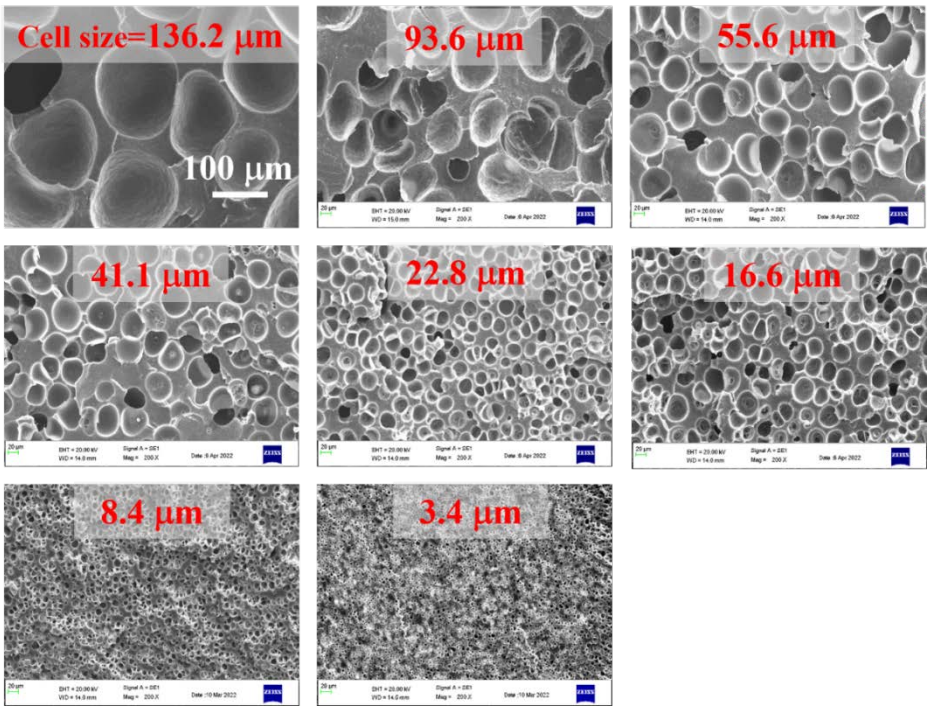

Fig. 4-9. SEM images of PLA/PBAT/ADR foams with different cell sizes and a fixed VF of 30%.

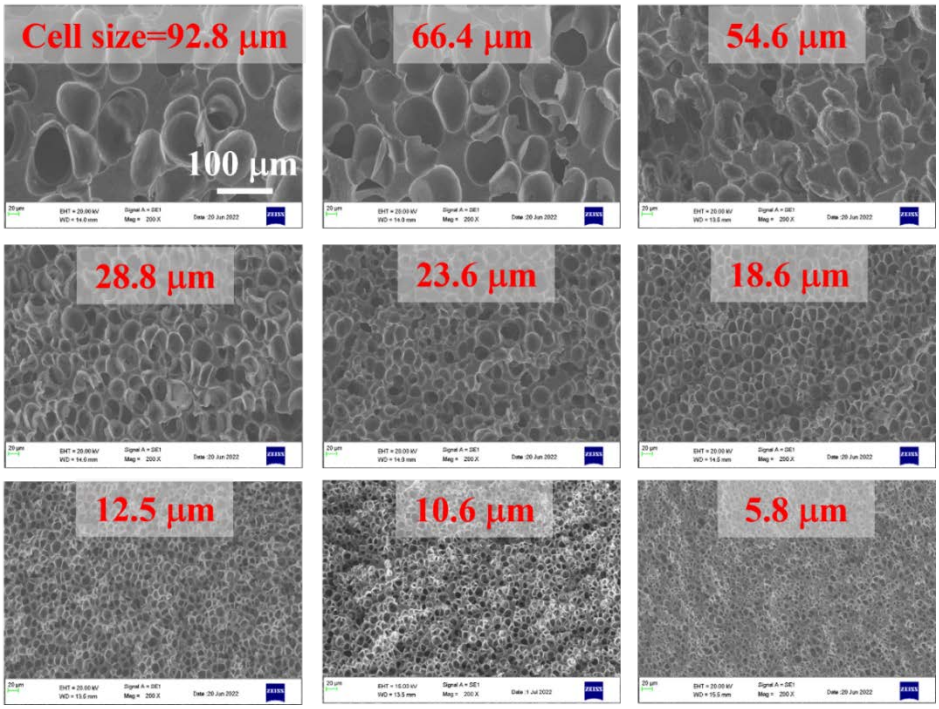

Fig. 4-10. SEM images of PLA/PBAT/ADR foams with different cell sizes and a fixed VF of 40%.

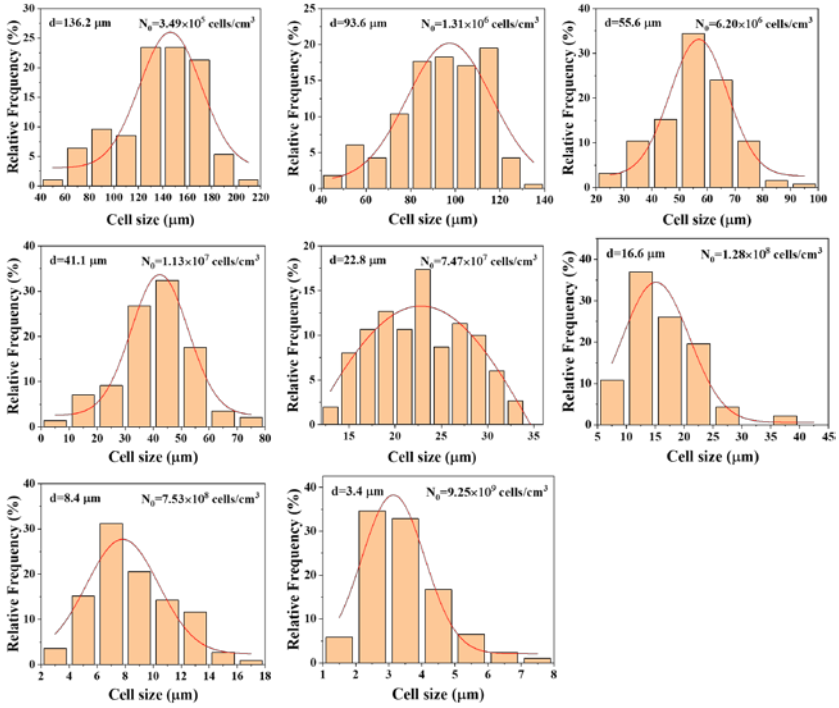

Fig. 4-11. Cell size distribution of PLA/PBAT/ADR foams with a VF of 30%.

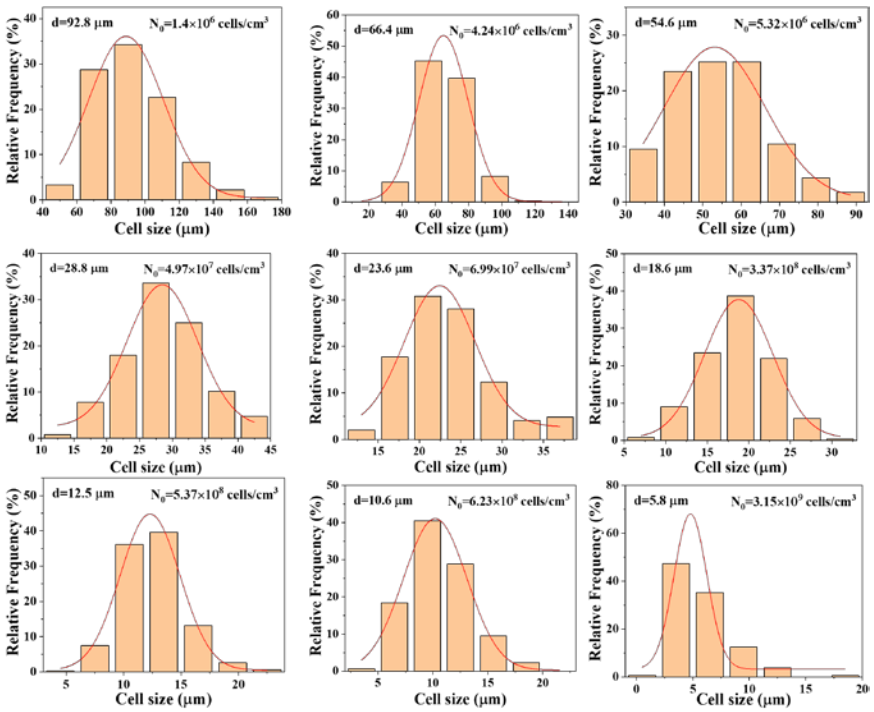

Fig. 4-12. Cell size distribution of PLA/PBAT/ADR foams with a VF of 40%.

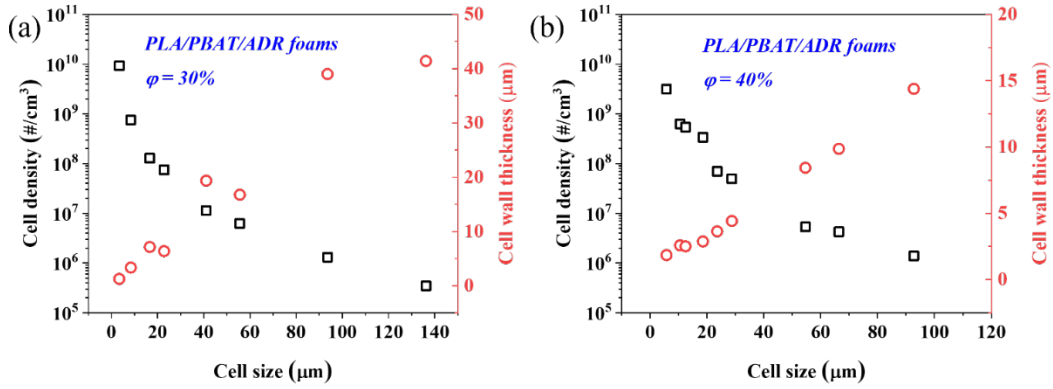

Fig. 4-13. Cell size dependence of cell density and cell wall thickness for PLA/PBAT/ADR foams with VF of (a) 30% and (b) 40%.

4.4.4. Thermal behavior

Considering the potential impact of foaming on the crystallization properties of polymers[29, 30], a comprehensive analysis of the thermal behavior of PLA/PBAT and PLA/PBAT/ADR foams was conducted. The first heating thermograms of

PLA/PBAT and PLA/PBAT/ADR foams were analyzed, as shown in Fig. 4-14. Given the extensive variety of samples, a pragmatic approach was adopted whereby three distinct foams–representing the maximum, minimum, and medium cell sizes–were selected for detailed thermal analysis within each set defined by a fixed VF. An intriguing observation emerged from this analysis: a direct correlation between decreased cell size and increased crystallinity across all foam variants. For instance, for the PLA/PBAT/ADR foams with a fixed VF of 40%, the crystallinity improved from 4.8 to 18.6% by decreasing the cell size from 92.8 to 5.8 μm. This phenomenon could be attributed to the reduced cell wall thickness associated with the reduction of cell size (as evidenced in Fig. 4-8 and 4-13), suggesting that a thinner cell wall might subject the matrix to a more pronounced shear field during the foaming process, thereby fostering a higher crystallinity[31, 32]. In summary, although the crystallinity levels across all foams were found to be relatively low, their effect on mechanical properties was considered negligible and thus will not be a focal point in subsequent discussions regarding mechanical performance.

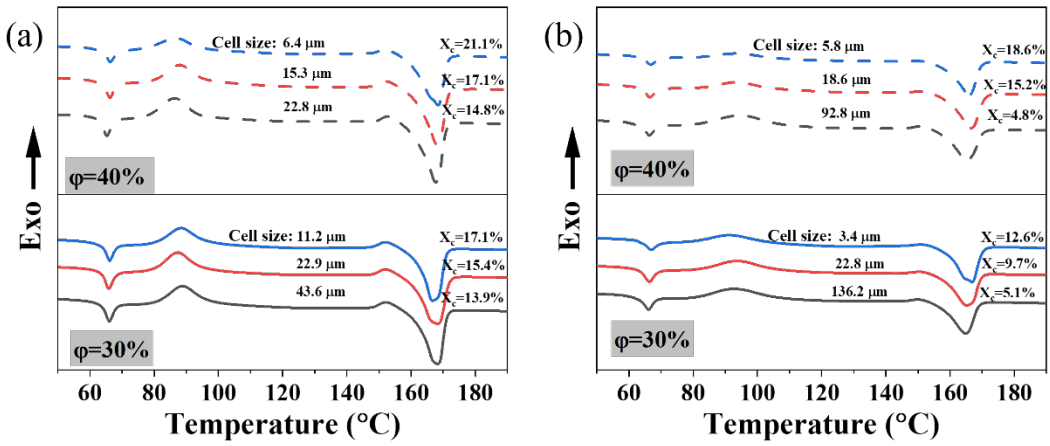

Fig. 4-14. First heating curves of obtained foams with different cell sizes under VFs of 30% and 40%: (a) PLA/PBAT foams, (b) PLA/PBAT/ADR foams.

4.4.5. Impact strength

Fig. 4-15 shows the impact strength of PLA/PBAT and PLA/PBAT foams. Interestingly, there was a critical cell size: approximately 15 μm for PLA/PBAT foams and 30 μm for PLA/PBAT/ADR foams. When the cell size was greater than this critical value, the impact strength stabilized at a relatively low level (approximately 5 kJ/m^2 for PLA/PBAT foams and 20 kJ/m^2 for PLA/PBAT foams), irrespective of cell size variations. Conversely, a reduction in cell size below this critical point resulted in a significant enhancement in impact strength. For example, reducing the cell size from 22.9 to 11.2 μm in PLA/PBAT foams with a VF of leaded to an impact strength increased from 4.8 to 13.4 kJ/m^2, marking a substantial enhancement of 179%. Similarly, when cell size reduced to 3.4 μm, the resulting PLA/PBAT/ADR foam (φ=30%) reached the super toughness with an impact strength of 53.6 kJ/m^2, which represented an increase of 175% relative to foams with a cell size of 41.4 μm. To isolate the influence of VF on the impact strength, the specific impact strength across various cell sizes is depicted in Fig. 4-15b and 4-15d. Notably, all the data points were in line with a single principal curve (represented by the gray line) for both the PLA/PBAT foams and PLA/PBAT/ADR foams. Above the critical cell size (e.g., ~15 μm for PLA/PBAT foams), the specific impact strength was similar to that of solid sample, indicating the same fracture mechanism across these conditions. Below the critical cell size, the marked improvement in specific impact strength strongly proved that the introduction of smaller cells could toughen the PLA/PBAT (or PLA/PBAT/ADR) foams by altering

the fracture mechanism upon impact. The specific impact strength for PLA/PBAT foams increased from ~5 to 15.5 (kJ·m^{-2})/(g·cm^{-3}), and from ~25 to 62.2 (kJ·m^{-2})/(g·cm^{-3}) for PLA/PBAT/ADR foams, corresponding to increases of up to 200% and 150%, respectively.

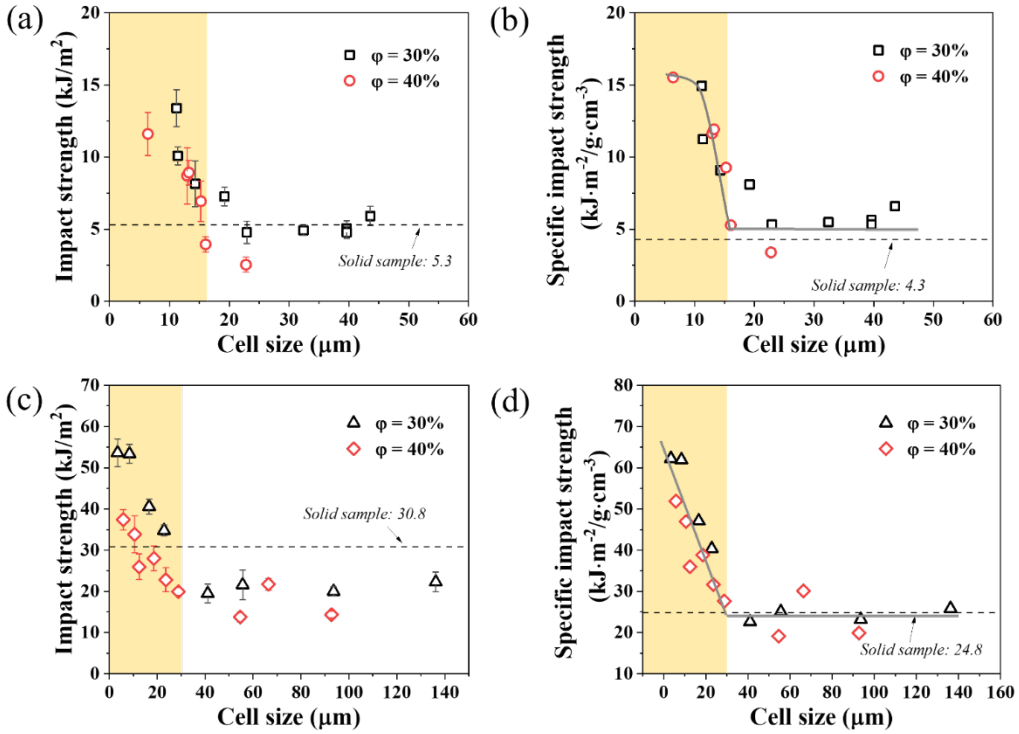

Fig. 4-15. Impact strength of (a, b) PLA/PBAT foams and (d, e) PLA/PBAT/ADR foams: (a, c) impact strength *vs.* cell size, (b, d) specific impact strength *vs.* cell size. Dashed line represents the solid sample.

To verify the prior hypothesis, the impact-fractured surfaces of foamed samples were further analyzed. Across all the PLA/PBAT foams (Fig. 4-16a and 4-16b), the cell structures largely maintained their original morphology post-impact, indicating the absence of significant macro-deformations. Fig. 4-16a' reveals the rather smooth

surface of PLA matrix as well as the evident stretching and debonding of the PBAT phase. This was mainly due to the poor interfacial compatibility and conclusively demonstrated that the PLA/PBAT foam with larger cells (d=43.6 μm) exhibited brittle fracture characteristics. In contrast, a reduction in the cell size to 11.2 μm promoted the onset of plastic deformation within the PLA matrix (Fig. 4-16b'), leading to a notable increase of impact strength from 5.9 to 13.4 kJ/m^2. Furthermore, Fig. 4-16c and 4-16c' shows the SEM images of the impact fracture surface of PLA/PBAT/ADR foam characterized by a larger cell size (136.2 μm). Here, the PLA matrix displayed signs of yielding, with no PBAT particles discernible on the fracture surface. It should be also noticed that the cell morphology remained unchanged after the impact testing. Despite this, the impact strength recorded at 22.3 kJ/m^2 significantly higher than that of the PLA/PBAT foams, which could be attributed to the enhanced interfacial adhesion between PLA and PBAT[18]. Upon reducing the cell size to 3.4 μm (Fig. 4-16d and 4-16d'), surprisingly, extensive yielding, large deformation of cells, and the presence of secondary cracks were found. These characteristics were advantageous for energy dissipation during impact testing, leading to a super high impact strength of 53.6 kJ/m^2.

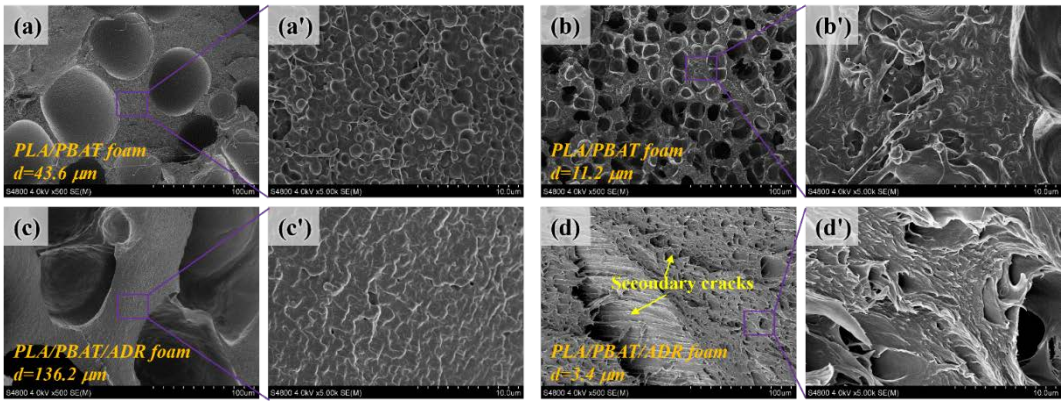

Fig. 4-16. SEM images of impact fractured surfaces of (a, b) PLA/PBAT foams and (c, d) PLA/PBAT/ADR foams. (a'– d') are the enlarged images of (a– d), respectively. The VF of all samples was 30%.

To further evaluate the fracture behaviors, SENTB tests were conducted. Prior to testing, three representative samples were selected from the PLA/PBAT (or PLA/PBAT/ADR) foams, representing the highest, medium, and lowest impact strength. Fig. 4-17 shows the typical load-displacement curves and their corresponding values for fracture energy (E), crack initiation energy (E_i), and crack propagation energy (E_p) across foams with various cell sizes. For the PLA/PBAT foams, a reduction in resulted in a marked improvement in E, which can be attributable to enhancements in both E_i and E_p, with E_p making a particularly significant contribution. Specifically, as the cell size was decreased from 22.8 to 6.4 μm, E_i increased from 0.05 to 0.18 J, and Ep from 0.09 to 1.26 J, resulting in a substantial elevation of E from 0.14 to 1.44 J. This undoubtfully revealed that reducing the cell size in PLA/PBAT foams could not only inhibit crack initiation but also hinder crack propagation, enhancing the material's overall fracture resistance. A comparable trend was observed in the PLA/PBAT/ADR foams. Upon decreasing the cell size from 92.8 to 5.8 μm, the E_i, E_p, and E improved from 0.15, 0.78 and 0.93 J to 0.25, 1.47 and 0.72 J, respectively. This evidences the critical role of cell size in dictating the fracture mechanisms of these foams, with smaller cell sizes substantially improving their resistance to crack initiation and propagation.

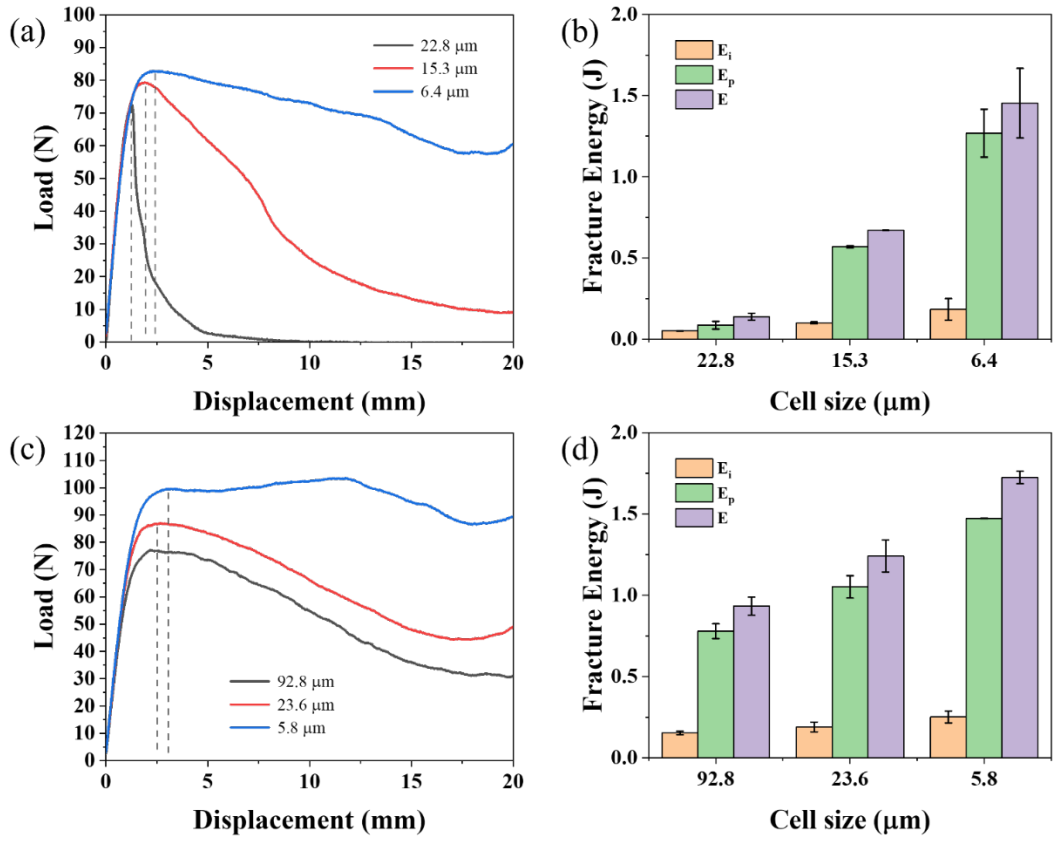

Fig. 4-17. (a, c) Load-displacement curves and (b, d) variation of fracture energy parameters (E, E_i and E_p) of foams with various cell sizes: (a, b) PLA/PBAT foams, (b, d) PLA/PBAT/ADR foams. The VF of all samples was 40%.

4.4.6. Discussion

Drawing upon the findings discussed earlier, a notable transition from brittle to tough behavior was observed in the PLA/PBAT (and PLA/PBAT/ADR) foams, which firmly proved that the energy dissipation mechanism changed by reducing the cell size. Traditionally, for brittle polymers, enhancing toughness typically involves the incorporation of rubber particles in a single distribution. However, adding a dual distribution of rubber particles has revealed a surprising effect in augmenting toughness. Fowler et al[33] added styrene-butadiene-styrene (SBS)

copolymer and/or methyl methacrylate-butadiene-styrene (MBS) copolymer to increase the toughness of acrylonitrile-styrene (SAN) copolymer. Individually, neither an SBS (with particle diameters ranging from 1 to 5 μm) nor an MBS (particle diameter = 0.18 μm) copolymer could significantly enhance the toughness of SAN. Nonetheless, a great improvement in the toughness was found when incorporating both types of rubber particles, which was similarly observed in ABS and PS system[34, 35]. The authors proposed that the larger rubber particles might initiate crazes due to a lower initiation stress, while smaller particles could act as reinforcing agents by bending the craze path[36]. This synergistic toughening mechanism could potentially elucidate the observed increase in impact strength for PLA/PBAT foams with smaller cells. Nevertheless, the specific reason why this synergistic effect was predominantly observed in PLA/PBAT foams with smaller cells warranted further investigation.

To elucidate the dependence of impact strength on cell size in PLA/PBAT foams, attention should be directed towards the interaction of stress fields between two neighboring cells. In this context, Goodier's solution[37] for the distribution of stress around a spherical inclusion within a big elastic matrix was applied. Fig. 4-18a shows the schematics of the hoop stress along the equatorial plane in matrix. The maximum stress at the equator is about $2\sigma_0$ and reduces rapidly and reach the external stress σ_0 with the distance from the rubber particle surface improve[38]. When two particles are close enough (Fig. 4-18b), the interaction between their stress fields (the sum of two stress fields) can reduce the craze-initiation stress, facilitating the formation of stable crazes bridged between two rubber particles, as

reported by Matsuo et al[38]. In this study, both PBAT particles and cells contribute to the stress fields, thereby influencing the fracture behavior, as depicted in Fig. 4-18c. In foams with large cells, the interaction between neighboring cells was minimal due to the thick cell wall thickness (as indicated in Fig. 5 and 6, where an increase in cell size correlates with thicker cell walls), even when considering the stress field generated by PBAT particles. In contrast, for foams with small cells, the reduced thickness of cell wall was sufficiently small, and thus the crazes could stably develop between neighboring cells and bridge with each other. This could significantly enhance the toughness of PLA/PBAT foams (or PLA/PBAT/ADR foams).

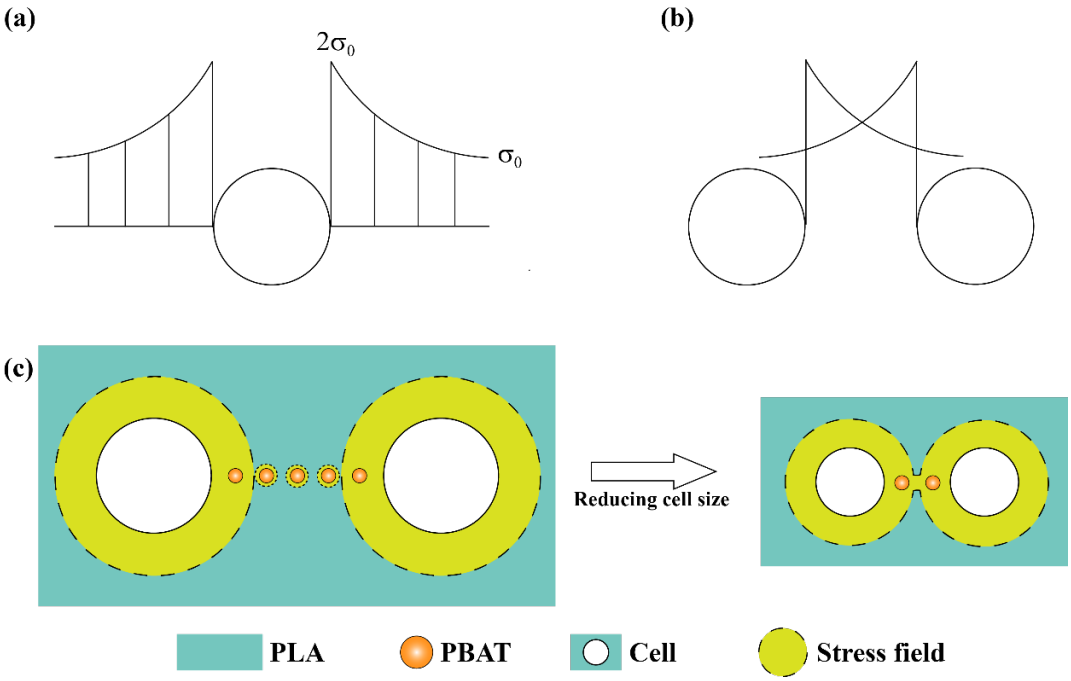

Fig. 4-18. Schematics of stress concentration (a) around a rubber particle and between two rubber particles. (c) Schematics of stress field distribution before and after reducing cell size.

Fig. 4-19 shows the schematic of the cell size-induced toughening mechanism in foams. The pivotal element in determining the synergistic toughening mechanism in PLA/PBAT (and PLA/PBAT/ADR) foams hinged on whether the cell wall thickness was sufficiently small. Such a condition facilitated the stabilization of cell-induced crazes between neighboring cells through the intensified interaction of stress fields, which was ascribed to both the neighboring cells and the presence of PBAT particles located at the inner surfaces of the cells. For foams with large cells (~15 and ~30 μm for PLA/PBAT foams and PLA/PBAT/ADR foams, respectively), the introduction of large cells did not alter the fracture behavior of the PLA/PBAT (or PLA/PBAT/ADR) foams. Consequently, these foams displayed similar specific impact strengths as their solid counterparts, as illustrated in Fig. 4-15. For foams with small cells, however, the robust interaction between the stress fields could prevent the cell-induced crazes from evolving into cracks, thereby substantiating the observed enhancements in E_i and E_p upon reducing the cell size (Fig. 4-17). Moreover, the existence of small PBAT particles would influence the yield process such that shear yielding may take place alongside crazing. This occurs because crazing and shear yielding can synergistically interact to improve the material's toughness [39]. Consequently, a reduction in cell size leaded to the manifestation of shear yielding within PLA/PBAT foams. In PLA/PBAT/ADR foams, this phenomenon extended to extreme deformation of cells, as evidenced in Fig. 4-16. This integrated understanding elucidated how a reduction in cell size not only enhanced the foam's energy dissipation capabilities but also introduced mechanisms such as shear yielding that significantly contributed to the material's overall

toughness.

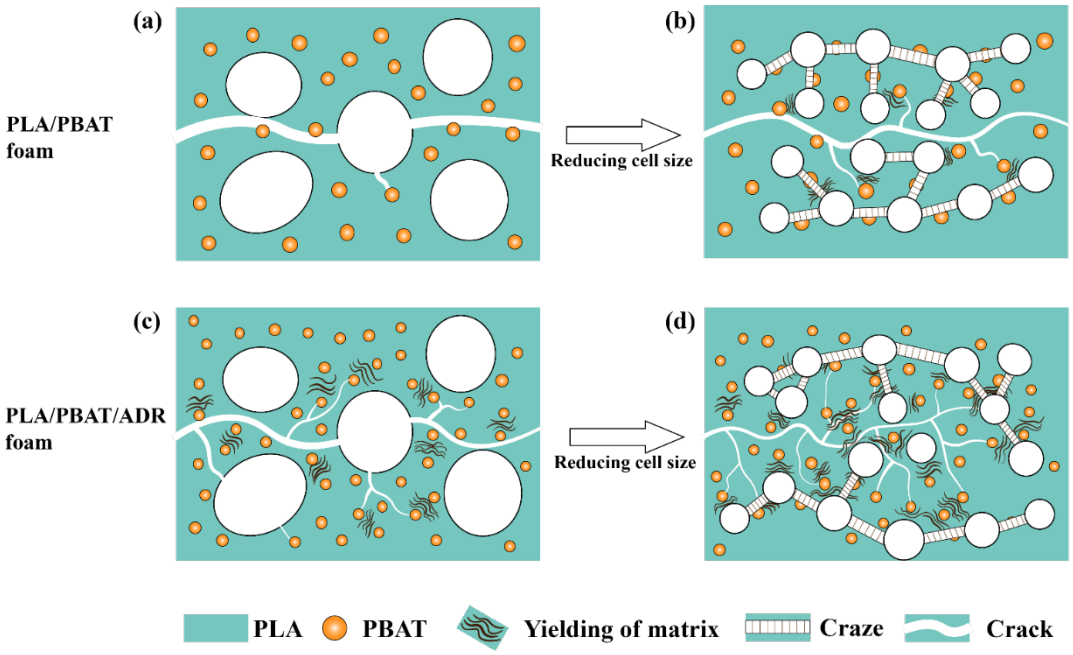

Fig. 4-19. Schematic of the cell size-induced toughening mechanism of (a, b) PLA/PBAT foams and (c, d) PLA/PBAT/ADR.

4.5. Conclusion

This work elucidated the relationship between cell size and impact strength in PLA/PBAT blend foams, uncovering a significant brittle-tough transition as cell sizes decreased below a critical threshold. Specifically, the specific impact strength remained constant at approximately 5 $(kJ \cdot m^{-2})/(g \cdot cm^{-3})$ for cell size larger than ~15 μm. However, it significantly increased to 15.5 $(kJ \cdot m^{-2})/(g \cdot cm^{-3})$ when the cell size reduced below ~15 μm, marking s substantial enhancement of 200%. Furthermore, it was found that enhancing the interfacial adhesion could elevate the critical cell size to ~30 μm, while also dramatically increasing the specific impact strength from

~25 to 62.2 $(kJ \cdot m^{-2})/(g \cdot cm^{-3})$ upon reducing cell size. Through comprehensive investigations via impact testing and SENTB, along with the morphological assessments of the cell structure and the impact-fractured surface, a cell size-induced toughening mechanism was proposed. In foams with smaller cells, which corresponded to thinner cell wall thickness, a strong interaction of stress fields from neighboring cells, along with the presence of PBAT particles at the cells' inner surfaces, effectively prevented the transition of cell-induced crazes to cracks. This led to a larger stable craze region, thereby enhancing impact strength. Conversely, in foams characterized by larger cells, the cell-induced crazes could directly develop into cracks due to the minimal interaction between cells, leading to a reduced impact strength.

4.6. References

[1] M.O. Okoroafor, K.C. Frisch, 1 - INTRODUCTION TO FOAMS AND FOAM FORMATION, in: A.H. Landrock (Ed.), Handbook of Plastic Foams, William Andrew Publishing, Park Ridge, NJ, 1995, pp. 1-10.

[2] L. Wang, Y. Hikima, M. Ohshima, A. Yusa, S. Yamamoto, H. Goto, Development of a Simplified Foam Injection Molding Technique and Its Application to the Production of High Void Fraction Polypropylene Foams, Ind. Eng. Chem. Res. 56(46) (2017) 13734-13742. https://doi.org/10.1021/acs.iecr.7b03382

[3] M. Xu, M. Wu, X. Li, J. Tang, W. Ma, X. Zhu, Q. Ren, L. Wang, W. Zheng, Biodegradable nanofibrillated microcellular PBS/PLA foams for selective oil absorption, Int. J. Biol. Macromol. 254 (2024) 127844. https://doi.org/10.1016/j.ijbiomac.2023.127844

[4] Q. Ren, M. Wu, L. Wang, W. Zheng, Y. Hikima, T. Semba, M. Ohshima, Light and strong poly (lactic acid)/cellulose nanofiber nanocomposite foams with enhanced rheological and crystallization property, J. Supercrit. Fluids 190 (2022) 105758. https://doi.org/10.1016/j.supflu.2022.105758

[5] J. Zhao, Y. Qiao, G. Wang, C. Wang, C.B. Park, Lightweight and tough PP/talc composite foam with bimodal nanoporous structure achieved by microcellular injection molding, Mater. Des.

195 (2020) 109051. https://doi.org/10.1016/j.matdes.2020.109051

[6] Q. Ren, M. Wu, Z. Weng, L. Wang, W. Zheng, Y. Hikima, M. Ohshima, Lightweight and strong gelling agent-reinforced injection-molded polypropylene composite foams fabricated using low-pressure CO2 as the foaming agent, J. CO2 Util. 48 (2021) 101530. https://doi.org/10.1016/j.jcou.2021.101530

[7] L. Wang, Y. Hikima, S. Ishihara, M. Ohshima, Fabrication of lightweight microcellular foams in injection-molded polypropylene using the synergy of long-chain branches and crystal nucleating agents, Polymer 128 (2017) 119-127. https://doi.org/10.1016/j.polymer.2017.09.025

[8] L.J. Gibson, M.F. Ashby, Cellular Solids: Structure and Properties, 2 ed., Cambridge University Press, Cambridge, 1997.

[9] J.-B. Bao, A. Nyantakyi Junior, G.-S. Weng, J. Wang, Y.-W. Fang, G.-H. Hu, Tensile and impact properties of microcellular isotactic polypropylene (PP) foams obtained by supercritical carbon dioxide, J. Supercrit. Fluids 111 (2016) 63-73. https://doi.org/10.1016/j.supflu.2016.01.016

[10] J.B. Bao, T. Liu, L. Zhao, G.H. Hu, X.R. Miao, X.H. Li, Oriented foaming of polystyrene with supercritical carbon dioxide for toughening, Polymer 53(25) (2012) 5982-5993. https://doi.org/10.1016/j.polymer.2012.10.011

[11] C. Barlow, V. Kumar, B. Flinn, R.K. Bordia, J. Weller, Impact Strength of High Density Solid-State Microcellular Polycarbonate Foams, J. Eng. Mater. Technol. 123(2) (2000) 229-233. https://doi.org/10.1115/1.1339004

[12] H. Urayama, T. Kanamori, Y. Kimura, Properties and Biodegradability of Polymer Blends of Poly(L-lactide)s with Different Optical Purity of the Lactate Units, Macromol. Mater. Eng. 287(2) (2002) 116-121. https://doi.org/10.1002/1439-2054(20020201)287:2<116::AID-MAME116>3.0.CO;2-Z

[13] S. Pradeep, H. Kharbas, L.-S. Turng, A. Avalos, J. Lawrence, S. Pilla, Investigation of Thermal and Thermomechanical Properties of Biodegradable PLA/PBSA Composites Processed via Supercritical Fluid-Assisted Foam Injection Molding, Polymers 9(1) (2017) 22. https://doi.org/10.3390/polym9010022

[14] P. Xiang, L. Gou, Y. Zou, B. Chen, S. Bi, X. Chen, P. Yu, A facile strategy for preparation of strong tough poly(lactic acid) foam with a unique microfibrillated bimodal micro/nano cellular structure, Int. J. Biol. Macromol. 199 (2022) 264-274. https://doi.org/10.1016/j.ijbiomac.2021.12.187

[15] N. Najafi, M.-C. Heuzey, P.J. Carreau, D. Therriault, C.B. Park, Mechanical and morphological properties of injection molded linear and branched-polylactide (PLA) nanocomposite foams, Eur. Polym. J. 73 (2015) 455-465. https://doi.org/10.1016/j.eurpolymj.2015.11.003

[16] X. Wang, S. Peng, H. Chen, X. Yu, X. Zhao, Mechanical properties, rheological behaviors, and phase morphologies of high-toughness PLA/PBAT blends by in-situ reactive compatibilization, Composites, Part B 173 (2019) 107028. https://doi.org/10.1016/j.compositesb.2019.107028

[17] X.P. Zhao, H. Hu, X. Wang, X.L. Yu, W.Y. Zhou, S.X. Peng, Super tough poly(lactic acid) blends: a comprehensive review, RSC Adv. 10(22) (2020) 13316-13368. https://doi.org/10.1039/d0ra01801e

[18] M. Wu, Q. Ren, X. Zhu, W. Li, H. Luo, F. Wu, L. Wang, W. Zheng, P. Cui, X. Yi, Super toughened blends of poly(lactic acid) and poly(butylene adipate-co-terephthalate) injection-molded foams via enhancing interfacial compatibility and cellular structure, Int. J. Biol. Macromol. 245 (2023) 125490. https://doi.org/10.1016/j.ijbiomac.2023.125490

[19] V. Shaayegan, G. Wang, C.B. Park, Study of the bubble nucleation and growth mechanisms in high-pressure foam injection molding through in-situ visualization, Eur. Polym. J. 76 (2016) 2-13. https://doi.org/10.1016/j.eurpolymj.2015.11.021

[20] P. Tiwary, C.B. Park, M. Kontopoulou, Transition from microcellular to nanocellular PLA foams by controlling viscosity, branching and crystallization, Eur. Polym. J. 91 (2017) 283-296. https://doi.org/10.1016/j.eurpolymj.2017.04.010

[21] Z.H. Liu, X.D. Zhang, X.G. Zhu, Z.N. Qi, F.S. Wang, Effect of morphology on the brittle ductile transition of polymer blends: 1. A new equation for correlating morphological parameters, Polymer 38(21) (1997) 5267-5273. https://doi.org/10.1016/S0032-3861(97)00075-X

[22] J. Andrzejewski, J. Cheng, A. Anstey, A.K. Mohanty, M. Misra, Development of Toughened Blends of Poly(lactic acid) and Poly(butylene adipate-co-terephthalate) for 3D Printing Applications: Compatibilization Methods and Material Performance Evaluation, ACS Sustainable Chem. Eng. 8(17) (2020) 6576-6589. https://doi.org/10.1021/acssuschemeng.9b04925

[23] R. Al-Itry, K. Lamnawar, A. Maazouz, Improvement of thermal stability, rheological and mechanical properties of PLA, PBAT and their blends by reactive extrusion with functionalized epoxy, Polym. Degrad. Stab. 97(10) (2012) 1898-1914. https://doi.org/10.1016/j.polymdegradstab.2012.06.028

[24] L.C. Arruda, M. Magaton, R.E.S. Bretas, M.M. Ueki, Influence of chain extender on mechanical, thermal and morphological properties of blown films of PLA/PBAT blends, Polym. Test. 43 (2015) 27-37. https://doi.org/10.1016/j.polymertesting.2015.02.005

[25] M. Iza, M. Bousmina, R. Jérôme, Rheology of compatibilized immiscible viscoelastic polymer blends, Rheol. Acta 40(1) (2001) 10-22. https://doi.org/10.1007/s003970000112

[26] M. Bousmina, P. Bataille, S. Sapieha, H.P. Schreiber, Comparing the effect of corona treatment and block copolymer addition on rheological properties of polystyrene/polyethylene blends, J. Rheol. 39(3) (1995) 499-517. https://doi.org/10.1122/1.550709

[27] J.S. Colton, N.P. Suh, Nucleation of microcellular foam: Theory and practice, Polym. Eng. Sci. 27(7) (1987) 500-503. https://doi.org/10.1002/pen.760270704

[28] J.S. Colton, N.P. Suh, THE NUCLEATION OF MICROCELLULAR THERMOPLASTIC FOAM: PROCESS MODEL AND EXPERIMENTAL RESULTS, Adv. Manuf. Processes 1(3-

4) (1986) 341-364. https://doi.org/10.1080/10426918608953169

[29] D.-c. Li, T. Liu, L. Zhao, X.-s. Lian, W.-k. Yuan, Foaming of Poly(lactic acid) Based on Its Nonisothermal Crystallization Behavior under Compressed Carbon Dioxide, Ind. Eng. Chem. Res. 50(4) (2011) 1997-2007. https://doi.org/10.1021/ie101723g

[30] M. Takada, S. Hasegawa, M. Ohshima, Crystallization kinetics of poly(L-lactide) in contact with pressurized CO2, Polym. Eng. Sci. 44(1) (2004) 186-196. https://doi.org/10.1002/pen.20017

[31] R.H. Somani, B.S. Hsiao, A. Nogales, H. Fruitwala, S. Srinivas, A.H. Tsou, Structure Development during Shear Flow Induced Crystallization of i-PP: In Situ Wide-Angle X-ray Diffraction Study, Macromolecules 34(17) (2001) 5902-5909. https://doi.org/10.1021/ma0106191

[32] H. Fang, Y. Zhang, J. Bai, Z. Wang, Shear-Induced Nucleation and Morphological Evolution for Bimodal Long Chain Branched Polylactide, Macromolecules 46(16) (2013) 6555-6565. https://doi.org/10.1021/ma4012126

[33] M.E. Fowler, H. Keskkula, D.R. Paul, Mechanical behavior of dual-rubber-modified SAN, J. Appl. Polym. Sci. 35(6) (1988) 1563-1571. https://doi.org/10.1002/app.1988.070350613

[34] L. Morbitzer, D. Kranz, G. Humme, K.H. Ott, Structure and properties of abs polymers. X. Influence of particle size and graft structure on loss modulus temperature dependence and deformation behavior, J. Appl. Polym. Sci. 20(10) (1976) 2691-2704. https://doi.org/10.1002/app.1976.070201007

[35] S.Y. Hobbs, The effect of rubber particle size on the impact properties of high impact polystyrene (HIPS) blends, Polym. Eng. Sci. 26(1) (1986) 74-81. https://doi.org/10.1002/pen.760260112

[36] M.E. Fowler, H. Keskkula, D.R. Paul, Synergistic toughening in rubber modified blends, Polymer 28(10) (1987) 1703-1711. https://doi.org/10.1016/0032-3861(87)90013-9

[37] J.N. Goodier, Concentration of Stress Around Spherical and Cylindrical Inclusions and Flaws, J. Appl. Mech. 1(2) (2021) 39-44. https://doi.org/10.1115/1.4012173

[38] M. Matsuo, T.T. Wang, T.K. Kwei, Crazing of polystyrene containing two rubber balls: A model for ABS plastics, Journal of Polymer Science Part A-2: Polym. Phys. 10(6) (1972) 1085-1095. https://doi.org/10.1002/pol.1972.160100610

[39] C.B. Bucknall, D. Clayton, W.E. Keast, Rubber-toughening of plastics, J. Mater. Sci. 7(12) (1972) 1443-1453. https://doi.org/10.1007/BF00574936

Chapter 5: Toughened polylactide blend foams: Combined effects of cell size and matrix crystallization

In Chapter 4, we concluded that reducing cell size can lead to a brittle-tough transition in PLA/PBAT foams. However, those PLA/PBAT foams showed low crystallinities of PLA matrix (< 21%). It is well known that the PLA crystallinity in PLA/elastomer blend can strongly influence the impact toughness. To obtain PLA foams with better ductility, the effect of PLA crystallinity on impact strength for PLA/PBAT foams must be considered and studied deeply.

In this chapter, CO_2 treatment was used to improve the crystallinity of the PLA matrix of PLA/PBAT foams. The combined effects of cell size and PLA matrix crystallinity on the impact strength were comprehensively studied. Discussions on mechanical performance are presented, proposing a general strategy for the fabrication of toughened PLA blend foams.

5.1. Abstract

It is well known that increasing matrix crystallization is a good method to improve the impact toughness of semicrystalline polymer/elastomer blends. Is tailoring the crystalline structure still applicable to their foamed materials? The answer is yes, but other parameters should also be considered. Herein, using PLA/PBAT (70/30) blend foam as an example, the combined effects of matrix crystallization and cell size on the toughness have been studied. The PLA crystallinity was tailored by CO_2 treatment and cell size was well controlled by changing processing parameters. Interestingly, the impact strength was greatly enhanced with the reduction of cell size, indicating the occurrence of cell size-induced brittle-tough transition. By increasing the PLA crystallinity, the critical cell size for brittle-tough transition decreased from 15 to 12 μm. When the cell size surpassed the critical value, PLA/PBAT foams were all fractured through crazing. When cell size was below the critical valve, the dominant mechanism for foams with lowly crystalline PLA was multiple crazing, while that for foams with highly crystalline PLA was shear yielding, which was favorable to energy dissipation. This study could not only offer new insights into the synergistic effects of cell size and matrix crystallization on the toughening of PLA foam but also establish a general framework for preparing PLA foams with excellent toughness.

5.2. Introduction

PLA, as a biodegradable and renewably sourced polymer, has been considered as an

auspicious alternative to petroleum-based polymers, such as PET and PS[1, 2]. Thanks to its high strength, modulus and good processability, it has been applied in packaging, agriculture and medical field[3-5]. However, due to the inherent brittleness of PLA, it is still hard to obtain PLA foams with high toughness, which greatly limits its wide applications. To modify the properties of PLA foams, we can look for inspiration from the strategy of toughening PLA, which has been well studied in recent years.

Blending with some immiscible elastomers, such as PBAT[6, 7], polybutylene succinate (PBS)[8, 9], polycaprolactone (PCL)[10], and ethylene-glycidyl methacrylate (EGMA)[11], was considered to be a cost-effective method to enhance the toughness of PLA. Besides, enhancing the interface compatibility between PLA matrix and elastomers, the toughening efficiency can be further improved[12]. Han et al.[6] reported that epoxidized soybean oil (ESO) could be used as a compatibilizer for PLA/PBAT blend since ESO could react with terminated hydroxyl groups of both PLA and PBAT. By adding 5 phr ESO into PLA/PBAT (70/30) blend, the impact strength greatly improved from 8.8 to 36.7 kJ/m^2, exhibiting an increase of over 300%. Wang et al.[13] prepared the PLA/PBAT reactive blends with multifunctional epoxide ADR by melt blending and found that ADR can effectively promote impact toughness and the elongation at break of the blends.

Tailoring the crystallization of PLA matrix in a PLA/elastomer blend was also an effective strategy for toughening PLA[14-18]. Usually, increasing the crystallinity of PLA can enhance the impact toughness of PLA/elastomer blends. For example,

Bai et al[17] prepared PLA/PCL blends with various matrix crystallinity ranging from 10 to 50 % by changing NA content and found that the impact strength improved linearly with the increase of PLA matrix crystallinity. Deng et al[15] found that thermal annealing could improve the PLA crystallinity in PLA/EGMA blend, leading to the significant enhancement of impact strength from 35 to 98 kJ/m^2.

For PLA/elastomer foams, cell structure should also be taken into account when considering the factors influencing the mechanical properties. Fortunately, Chapter 4 has comprehensively investigated the relationship between cell size and impact toughness of PLA/PBAT foams. The results showed that a brittle-tough transition can be found by reducing cell size. When the cell size was greater than the critical value, foams would be brittle; when smaller, foams would be tough. It should be noticed that all foams showed low crystallinities of PLA matrix (< 21%). Considering that the impact toughness is strongly related with the crystallization of PLA matrix in PLA/elastomer blend, as discussed above, the interesting question naturally arises: whether the critical cell size varies with the PLA crystallinity. However, as far as we know, the combined effects of matrix crystallinity and cell size on the impact behavior have not been investigated so far.

In this work, PLA/PBAT (70/30) blend foams with different cell sizes but a fixed VF of 40% were successfully prepared using core-back foaming injection molding (FIM). The degree of PLA matrix crystallinity was tailored through CNT treatment, which was regarded as an efficient method to improve the crystallinity of PLA by using high-pressure CO_2 as a plasticizer[19, 20]. The combined effects of cell size and PLA matrix crystallization on the impact strength were comprehensively

investigated. The toughing mechanism was also proposed. Interestingly, cell size-induced brittle-tough transition occurred at a critical cell size for both high and low PLA matrix crystallinity. Furthermore, the critical cell size reduced by increasing the PLA matrix crystallinity. When cell size was below the critical value, the high PLA crystallinity was effective in initiating the shear yielding of PLA matrix, while the low PLA crystallinity was favorable for the multiple crazing of PLA matrix. When the cell size was above the critical value, however, PLA/PBAT foams were all fractured through crazing. More importantly, this work could provide an effective method to fabricate PLA blend foams with high impact toughness via tailoring cell size and PLA matrix crystallization.

5.3. Experimental section

5.3.1. Materials

PLA (4032D) was obtained from Natureworkds LLC, with a density of 1.24 g/cm^3. PBAT (TH801T) was kindly provided by Xinjiang Blue Ridge Tunhe Sci. & Tech. Co., Ltd. N_2 with a purity of 99%, supplied by Ningbo Huayu Gas Inc., was used as the physical blowing agent in FIM experiments.

5.3.2. Blend preparation

PLA and PBAT were first dried at 80 ℃ for 8 h to remove moisture. PLA/PBAT blend with a weight ratio of 70/30 was prepared using a corotating twin-screw extruder (SHL-52, Nanjing Haili Extrusion Equipment Co. Ltd., China) with a rotary speed of 40 rpm. The screw diameter and length/diameter ratio were 52 mm and 44, respectively. The temperature profile was set as 150-180 ℃ from the feed

zone to the die. Extrudate was quenched in a water bath and pelletized by the cutting chamber.

5.3.3. Core-back FIM process

PLA/PBAT blend foams were obtained by using a 100-ton FIM machine (Systec 100/420-310C, Demag Plastics Group, Germany), equipped with a Mucell SCF delivery system, T100, Trexel Inc., USA. injection, dwelling, core-back and cooling are the four steps generally occurring in the core-back process. First, a full shot is used in the injection step, and cell nucleation occurs at the gate due to the low pressure in the cavity. Then, the gate-nucleated cells would dissolve back into the melt under high pressure during the dwelling step. A uniform cell nucleation is induced by core-back operation and a fine cell structure can be achieved after cooling. A tensile test bar mold was applied in this work. Except for the thickness (3 mm), other dimensions of this mold are in line with the Standard GB/T 1040. The core-back distance was set as 2 mm, and the corresponding VF was 40%. To obtain foams with various cell sizes, different dwelling times and N_2 content were used. Detailed processing parameters can be found in Table 5-1.

Table 5-1. Processing parameters used for the FIM experiments.

PARAMETERS	SOLID	FOAM
Melt temperature (℃)	200	200
Mold temperature (℃)	80	80
Injection speed (mm/s)	100	100
Injection pressure (MPa)	150	150
Back pressure (MPa)	20	20
Packing pressure (MPa)	60	60
Dwelling time (sec)	10	15, 20, 25
Core-back distance (mm)	N/A	2
N_2 content (wt%)	N/A	0.7, 0.8, 1

5.3.4. CO_2 treatment

A self-made high-pressure autoclave was applied for CO_2 treatment, as shown in Fig. 5-1. The pristine samples were placed into the autoclave, and then CO_2 was inflated. The samples were saturated under 5 MPa and 20 ℃ for 120 h. After saturation, the autoclave was cooled down to 0 ℃ and CO_2 was depressurized slowly. The obtained samples were first placed in a refrigerator (0 ℃) for 12 h to prevent foaming and then placed in an air environment over 1 month to desorb the residual CO_2. Due to the low modulus of the PLA/PBAT/CO_2 blend, as well as the fact that the permeability of CO_2 is greater than air in the polymer during the aging process[21, 22], a slight shrinkage of foams could be observed. The VF of PLA/PBAT foams was reduced from 40% to 28%.

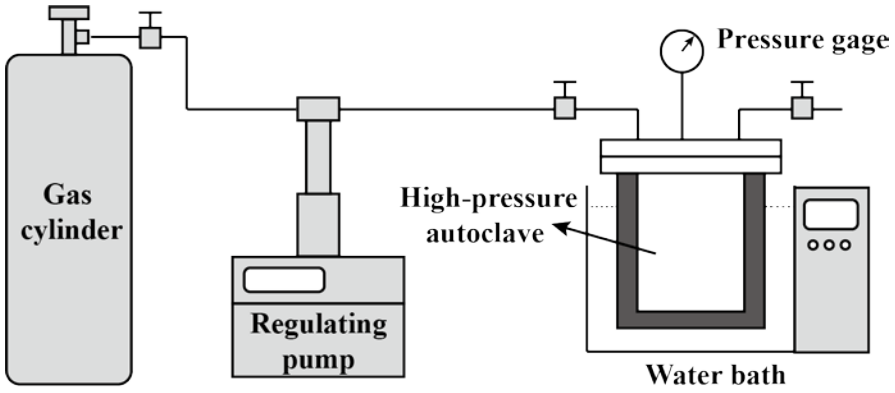

Fig. 5-1. Illustration of CO_2 treatment equipment.

5.3.5. SEM

The phase morphology of PLA/PBAT foams was evaluated by a Hitachi-S4800 SEM. Samples for the SEM observation were cryo-fractured in liquid nitrogen. An ImageJ software (National Institutes of Health, USA) was used to quantify the weight average particle size of PBAT (D_w), which was calculated through the

equation:

$$D_w = \frac{\sum_{i=1}^{N} n_i D_i^2}{\sum_{i=1}^{N} n_i D_i} \quad (5\text{-}1)$$

where n_i is the number of PBAT particles, and D_i the diameter of PBAT particle.

The deformation behavior of the impact-fracture samples was investigated by using Hitachi-S4800 SEM. In addition to the impact-fractured surface, the deformation region beneath the impact-fractured surface, which can be obtained by cryo-fracturing along a plane perpendicular to the thickness direction, was also evaluated. A SEM (EVO18, Zeiss Group, Germany) was used to study the cell morphology of PLA/PBAT foams. Specimens cut from the central part of the injection molded foams were cryogenically fractured and platinum-coated before observation. ImageJ software (National Institutes of Health, USA) was used to examine the cell structure. The cell density, N_0 (cells/cm^3), was determined using the following equation (1):[23]

$$N_0 = (\frac{n}{A})^{3/2} \Phi \quad (5\text{-}2)$$

where n, A and Φ are the number of cells in the micrograph, the area of the selected micrograph and the expansion ratio of the foamed sample, respectively. The Φ was calculated according to the equation (2):

$$\Phi = \frac{\rho_p}{\rho_f} \quad (5\text{-}3)$$

where ρ_s and ρ_f are the density of the solid and its foamed sample, respectively.

Water displacement method (ISO 1183-1987) was applied to determine ρ_s and ρ_f.

5.3.6. DSC

Thermal properties were investigated with a DSC (DSC/TGA1, Mettler-Toledo) under dry nitrogen atmosphere. All samples (about 5–8 mg) taken from the core layer of the injection molded foams were put into an aluminum pan and scanned from 25 to 190 ℃ at a heating rate of 10 ℃/min. The degree of crystallinity of PLA (X_c) was determined using equation

$$X_c = \frac{\Delta H_m - \Delta H_c}{\omega_f \Delta H_m^0} \tag{5-4}$$

where ΔH_m is the enthalpy of melting, ΔH_c the enthalpy of crystallization for PLA during heating process, ΔH_m^0 the melting enthalpy of completely crystalline PLA, ω_f the weight percent of PLA in the sample. The value of ΔH_m^0 was 93.6 J/g according to the literature [24, 25].

5.3.7. Wide-angle X-ray diffraction (WAXD)

2D WAXD measurements were conducted using a Small-angle X-ray Scattering (Xeuss 3.0 UHR, XENOCS SAS, France), with a Cu Kα radiation source (λ = 0.1542 nm). 2D patterns were collected by a Dectris EIGER2 Si 500K CCD detector (512 × 1028 pixels with a pixel size of 75 μm), and it was placed 45 mm away from the specimen. 2D WAXD intensity curves as a function of q could be obtained by integration in the azimuthal angular range of a whole circle from the specimen 2D patterns. q can be transformed into 2θ by the following relationship

$$q = 4\pi \sin\theta / \lambda \tag{5-5}$$

5.3.8. Mechanical test

Izod impact tests were conducted according to the GB/T 1843-2008 standard on an impact tester (GT-7045-HML, Gotech Testing Machines Inc.). To evaluate the mechanism of impact fracture, SENTB test was applied through a universal testing instrument (Instron 5567, Instron, USA) with a crosshead speed of 1 mm/s, as shown in Fig. 5-2 The side surfaces were analyzed through SEM after reaching the desired level of deformation. Prior to the measurement of mechanical tests, the surface layers of all specimens were removed and polished. The average value reported was obtained from at least five specimens.

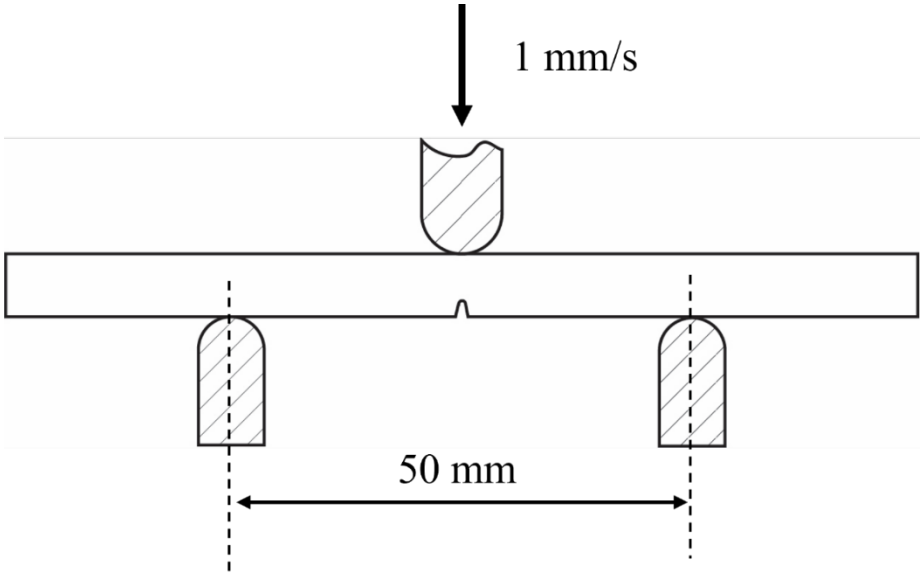

Fig. 5-2. Illustration of SENTB test

5.4. Results and discussion

5.4.1. Cell structure evolution during CO_2 treatment

To tailor the cell size in a wide range, PLA/PBAT foams were obtained by foaming injection molding under various N_2 content (0.7 – 1.0 wt%) and dwelling time (15 – 25). Increasing gas content will significantly accelerate cell nucleation according to the cell nucleation theory[26]. Besides, the temperature of polymer melt reduces with a longer dwelling time, while crystallization will also occur for semicrystalline polymers, leading to the enhancement of melt strength. It will restrain cell growth during foaming[27]. As a result, untreated PLA/PBAT foams with cell sizes ranging from 6.4 – 22.8 μm were obtained, as shown in Fig. 5-3. Fig. 5-4 shows the SEM images of CO_2 treated PLA/PBAT foams and their corresponding cell size distribution. After CO_2 treatment, the cell sizes of all samples were slightly reduced, as depicted in Fig. 5-5, which led to a small decrease in VF from ~40% to ~ 28%. Foam shrinkage is a universal phenomenon for elastomer foams prepared through supercritical CO_2 foaming. It can be attributed to the fact that the permeability of CO_2 is greater than air in the polymer during the aging process, which leads to the negative pressure inside the cell. The cell wall cannot resist the negative pressure due to the low modulus of elastomers, resulting in foam shrinkage[21, 22]. The shrinkage in PLA/PBAT foams indicated that the CO_2 saturated PLA/PBAT blend exhibited an extremely low modulus.

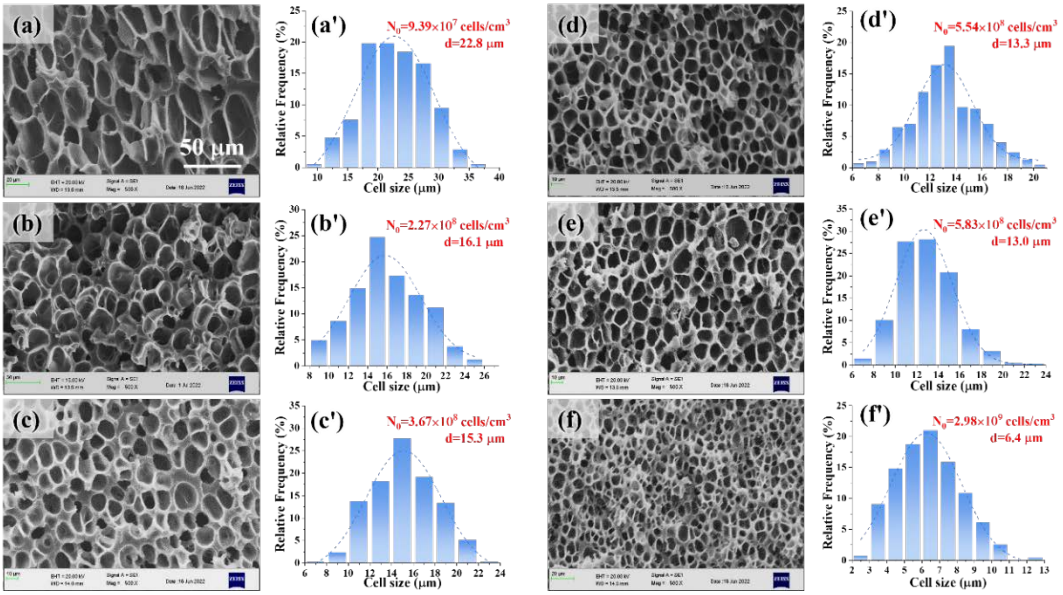

Fig. 5-3. (a–f) SEM images of untreated PLA/PBAT foams with different cell sizes and (a'–f') their corresponding cell size distribution. The VF of all samples was ~40%.

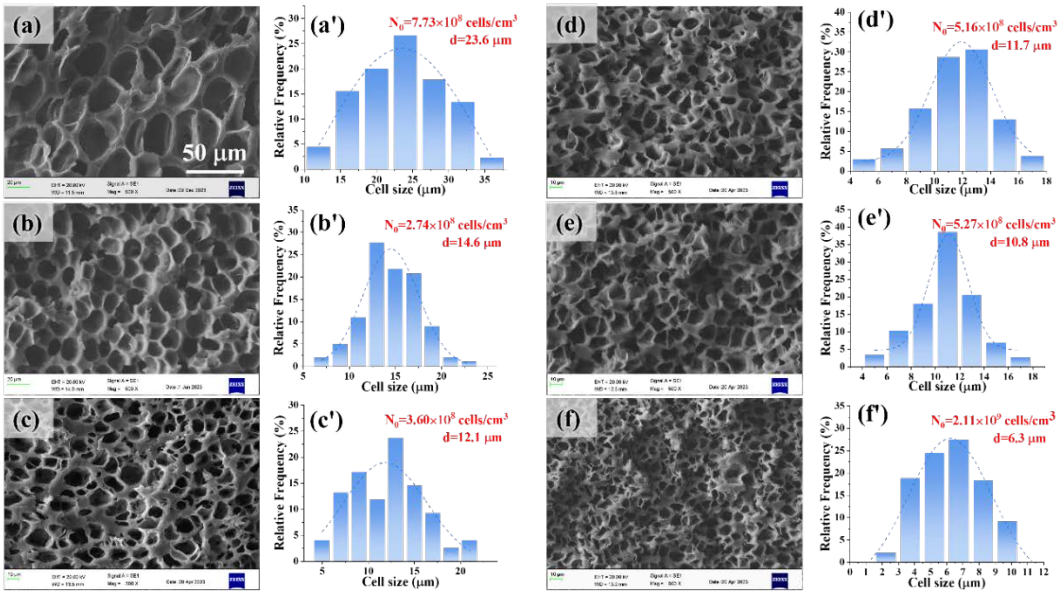

Fig. 5-4. (a–f) SEM images of CO_2 treated PLA/PBAT foams with different cell sizes and (a'–f') their corresponding cell size distribution. The VF of all samples was ~28%.

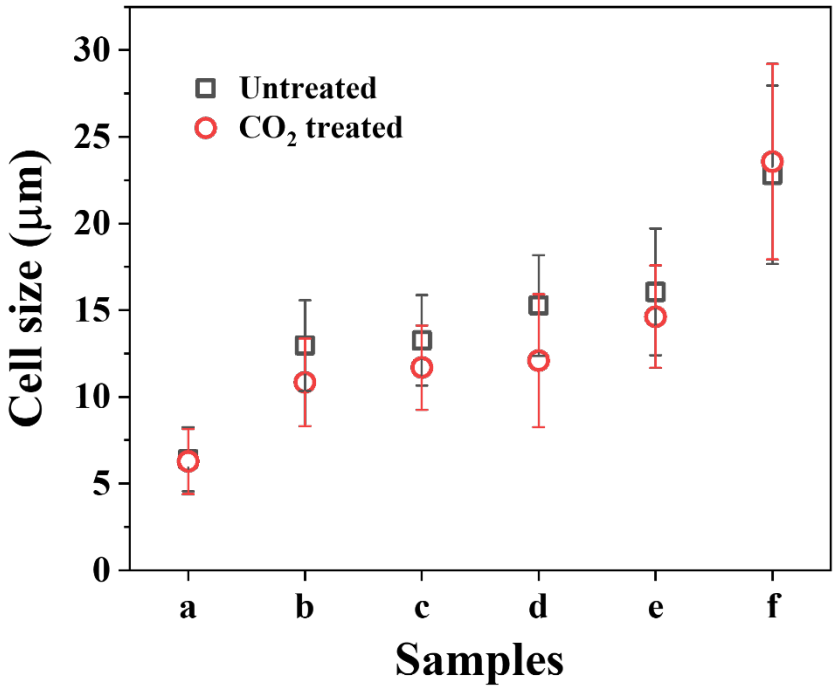

Fig. 5-5. Comparison of cell size of PLA/PBAT foams before and after CO_2 treatment. Sample a–f correspond to SEM a–f in Fig. 5-3 and 5-4.

5.4.2. Crystalline structure development during CO_2 treatment

Due to the effective plasticization effect of the dissolved CO_2 in the PLA matrix, it can improve the PLA molecular mobility, and thus accelerate the crystallization of PLA, even at room temperature and below[19, 28]. To investigate the effect of CO_2 treatment on mechanical performance, the crystallization behavior should be comprehensively evaluated.

The samples before and after CO_2 treatment were first analyzed by DSC, as shown in Fig. 5-6. The corresponding thermal parameters are listed in Table 5-2. As expected, all untreated samples appeared cold crystallization temperature (T_{cc1}) because of the low crystallization kinetics of PLA[29]. In addition, a small exothermic peak appeared before the melting peak of PLA due to the phase transition from α'-form crystal to α-one[30]. It was inevitable that all untreated

foams showed low degrees of crystallinity (14.8 – 21.1%). After CO_2 treatment, however, the thermograms were appreciably different from those in untreated foams. The cold crystallization peaks almost disappeared, suggesting that the crystallization of PLA was greatly improved through CO_2 treatment. The degree of crystallinity of all CO_2 treated samples was above 45%. It also should be noticed that all samples showed similar melting temperature (T_m) at about 168 °C, indicating that cell size and CO_2 treatment did not influence the thickness of PLA lamellae.

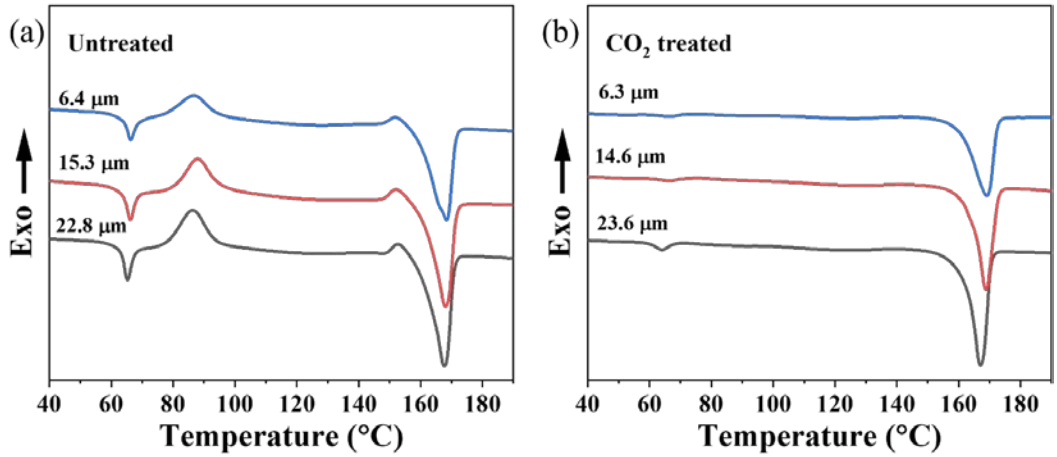

Fig. 5-6. First heating curves of PLA/PBAT foams (a) before and (b) after CO_2 treatment.

Table 5-2. Thermal parameters of PLA/PBAT foams before and after CO_2 treatment

	Cell size (mm)	T_{cc1} (°C)	T_{cc2} (°C)	T_m (°C)	X_c (%)
Untreated foams	6.4	86.6	151.7	168.0	21.1
	15.3	88.0	152.1	167.8	17.1
	22.8	86.3	152.6	167.3	14.8
CO_2 treated foams	6.3	–	–	168.9	48.6
	12.1	–	–	168.4	50.9
	23.6	–	–	166.7	56.7

To further analyze the crystalline structure of PLA/PBAT foams, One-dimensional (1D)-WAXD results of samples before and after CO_2 treatment were presented in Fig. 5-7. The diffraction peaks at 2θ = 16.6°, 18.9°, and 23.1° corresponded to the reflections of 110/200, 203, and 115, indicating the typical crystal structure of order α[31, 32]. Due to the low content of α'-form crystal in untreated foams (the small exothermic peak before the melting peak of PLA in Fig. 5-6a), the diffraction peaks of α'-form crystal cannot be found in WAXD profiles. Thus, it can be noticed that the crystal structure of foams was almost unchanged after CO_2 treatment.

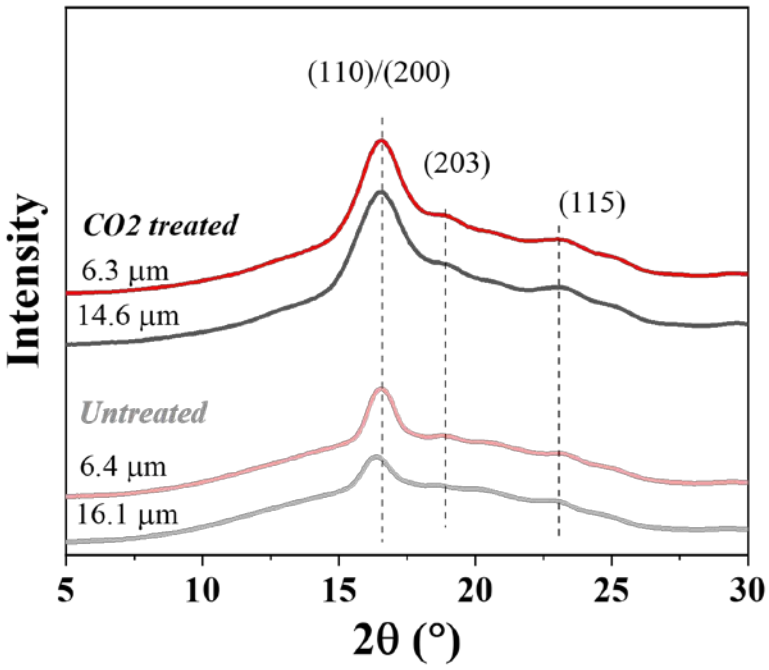

Fig. 5-7. 1-D WAXD diffraction profiles of PLA/PBAT foams before and after CO_2 treatment.

5.4.3. Phase morphology changes during CO_2 treatment

It is well known that the fracture toughness of rubber-toughened blends is mainly

dependent on the morphology of the dispersed rubber particles[33]. Fig. 5-8 exhibits the phase morphologies of solid and foamed samples before and after CO_2 treatment, and D_w was also shown in SEM images. As expected, due to the poor interfacial adhesion between PLA and PBAT, all samples displayed the typical sea-island structure, where PBAT phases were dispersed in the PLA matrix. Round-like PBAT particles were depicted in solid samples. However, the PBAT phases were slightly elongated after foaming. It could be attributed to the biaxial flow during the foam processing[34, 35]. Except for the shape of the PBAT phase, foaming had a lesser impact on particle size. For instance, the particle size of the untreated solid sample was 0.63 μm, while that of those untreated foamed samples was in the range of 0.51–0.68 μm. After CO_2 treatment, the PBAT phase size slightly increased, suggesting the thermodynamically spontaneous tendency towards an equilibrium state[36, 37]. For example, the particle size increased from 0.55 μm for untreated foam (cell size = 6.4 μm) to 0.64 μm for CO_2 treated foam (cell size = 6.3 μm). The unnoticeable improvement in particle size during CO_2 treatment indicated that phase morphology can be ignored when considering the factors that impacted mechanical properties before and after CO_2 treatment.

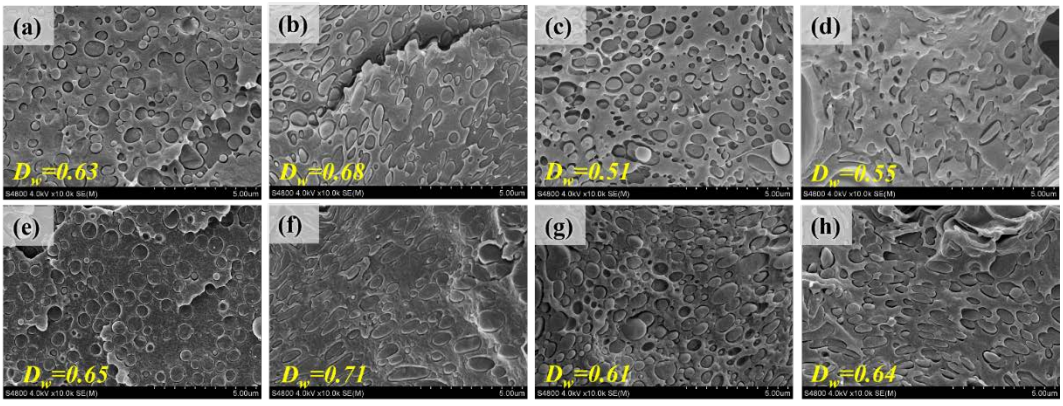

Fig. 5-8. SEM image of solid and foamed PLA/PBAT foams (a–d) before and (e–h) after CO_2 treatment. (a, e) were obtained from solid samples. The cell sizes of untreated foams (b, c, d) were 22.8, 15.3 and 6.4 μm, respectively. The cell sizes of treated foams (f, g, h) were 23.6, 14.6 and 6.3 μm, respectively.

5.4.4. Mechanical properties induced by PLA matrix crystallinity

Fig. 5-9a depicts the impact strength of PLA/PBAT foams with various cell sizes but almost the same low PLA crystallinity. Interestingly, a rapid improvement in impact strength can be observed by reducing the cell size. With the decrease of cell size from 22.8 to 6.4 μm, the impact strength increased from 2.5 to 11.6 kJ/m^2, showing an increase of 360%. Besides, there existed a critical cell size, ~15 μm, below which the impact strength increased significantly. Sufficient research has proved that PLA crystallinity has a key role in toughing PLA/rubber blend[17, 38]. However, it is still unknown if there is a cell size-induced brittle-tough transition for PLA/PBAT foams with high crystalline PLA. Fig. 5-9b shows the impact strength of PLA/PBAT foams with high crystalline PLA under different cell sizes. Similarly, brittle-tough transition can be found with the reduction of cell size, and the critical cell size was ~12 μm. When the cell size reduced to 6.3 μm, the resulting foam showed an impact strength of 30.2 kJ/m^2, 10.4 times that of foam with a cell size of 23.6 μm. It is obvious that both cell size and PLA crystallinity can influence the impact toughness of PLA/PBAT foams. Fig. 5-9c gives the specific impact strength as a function of cell size for foams with low and high PLA crystallinity. Based on the impact toughness under various cell sizes and different PLA crystallinity,

PLA/PBAT foams can be divided into two types. For foams with cell size above 12 μm (region I), the impact strength was almost independent of the PLA crystallinity. For foams with cell size below 12 μm (region II), however, improving the PLA crystallinity can extremely enhance the impact toughness. For example, the impact strength greatly increased from 15.5 to 33.9 kJ·m^{-2}/g·cm^{-3} by improving the PLA crystallinity for foam with a cell size of about 6 μm.

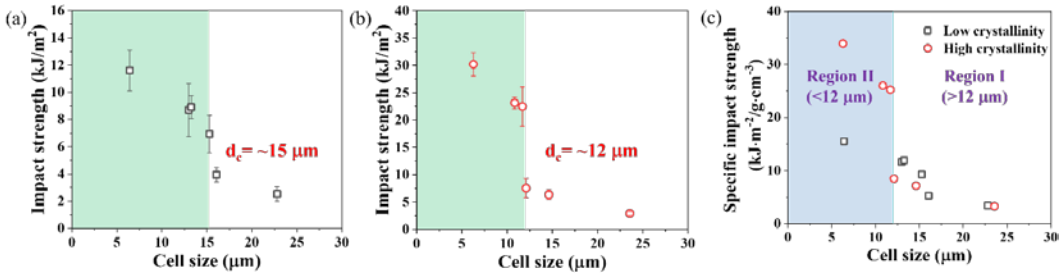

Fig. 5-9. Notched Izod impact strength as a function of cell size for foams with (a) low and (b) high PLA crystallinity. (c) Specific impact strength as a function of cell size for foams with low and high PLA crystallinity.

To clearly understand how the cell size and PLA crystallinity affect the impact strength, the impact fractured surfaces of foams obtained from region I and region II were investigated, as shown in Fig. 5-10. For foams with big cell sizes (Fig. 5-10a and b), they were all completely broken. The corresponding magnified images (Fig. 5-10a' and b') show some fibrillar PBAT phases (indicated by red arrows) but no plastic deformation in the matrix, which was a typical brittle fracture. Thus, they all exhibited low impact toughness of 9.3 kJ·m^{-2}/g·cm^{-3} (d=15.3 μm) and 7.2 kJ·m^{-2}/g·cm^{-3} (d=14.6 μm). For foams with small cell sizes (Fig. 5-10c and d), they were all partially broken, indicating that just reducing cell size could improve impact

strength for both PLA/PBAT foams with highly and lowly crystalline PLA. As shown in Fig. 5-10c', not only the fibrillation of PBAT phases but also the plastic deformation in the PLA matrix were found. It proved that small cell size was favorable for the shear yielding of PLA matrix. After increasing the crystallinity of PLA, as shown in Fig. 5-10d', extensive cell deformation appeared, indicating a great improvement in impact toughness. It was well consistent with their impact performance, where the impact strength of foams with low crystallinity and high crystallinity was 15.5 and 33.9 $kJ \cdot m^{-2}/g \cdot cm^{-3}$, respectively.

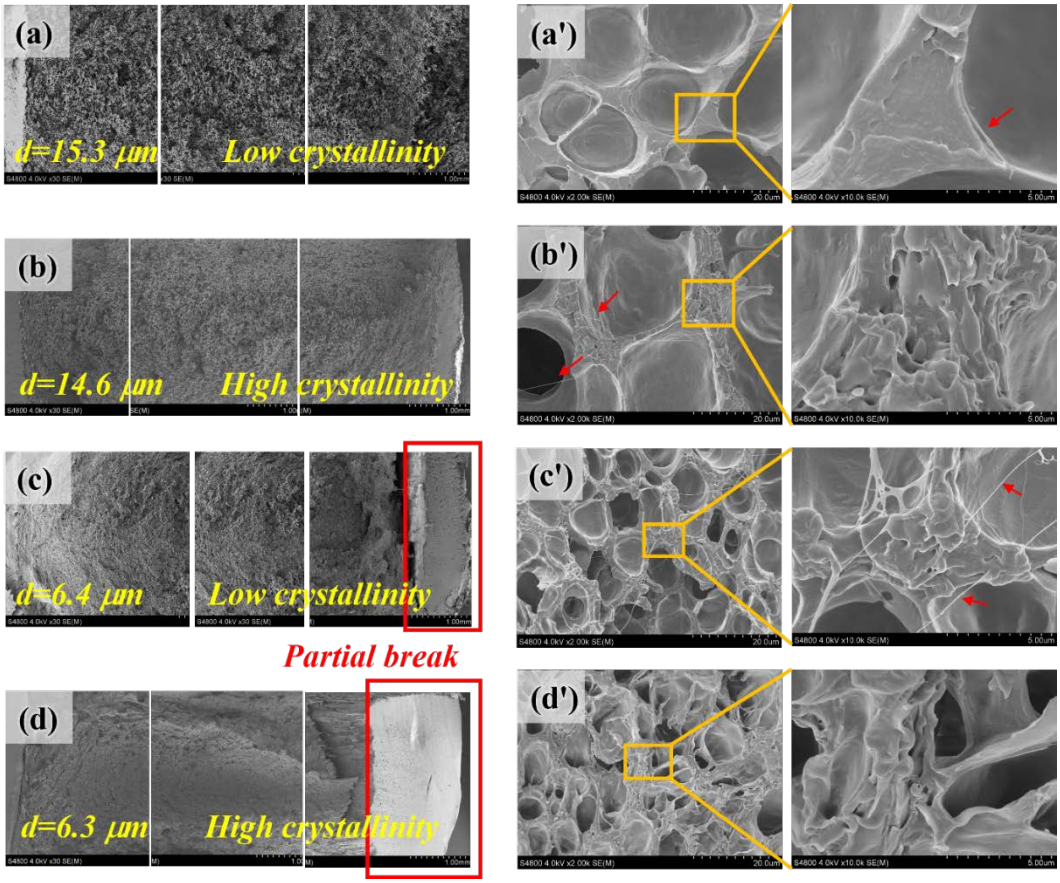

Fig. 5-10. SEM images of impact-fractured surfaces of PLA/PBAT foams with various cell sizes: (a) 15.3 μm, (b) 14.6 μm, (c) 6.4 μm, and (d) 6.3 μm. (a, c) and (b, d) had low and high PLA crystallinity, respectively. (a'–d') were the magnified images of (a–d).

In addition to the impact-fractured surfaces, SEM images of cross sections underneath the impact-fractured surfaces for PLA/PBAT foams obtained from region I and region II were evaluated, as shown in Fig. 5-11. For foams with big cells (Fig. 5-11a and b), the phase morphology near the impact-fractured surfaces was unaffected after impact test. After reducing the cell size to about 6 μm, however, the deformation region was extremely expanded, as shown in Fig. 5-11c and d. For example, severe cell deformation can be found in foam with low crystallinity of PLA (Fig. 5-11c), especially near the impact-fractured surface (Position 1). With the increase of distance from the impact-fractured surface, the cell deformation degree gradually weakened (Position 2), and finally disappeared (Position 3). By increasing the crystallinity of PLA, the thickness of the deformation region significantly increased from 150 to 550 μm, which naturally led to enhanced impact strength. According to the previous analysis, a schematic of the morphology of the impact-fractured surfaces for PLA/PBAT foams was depicted in Fig. 5-12.

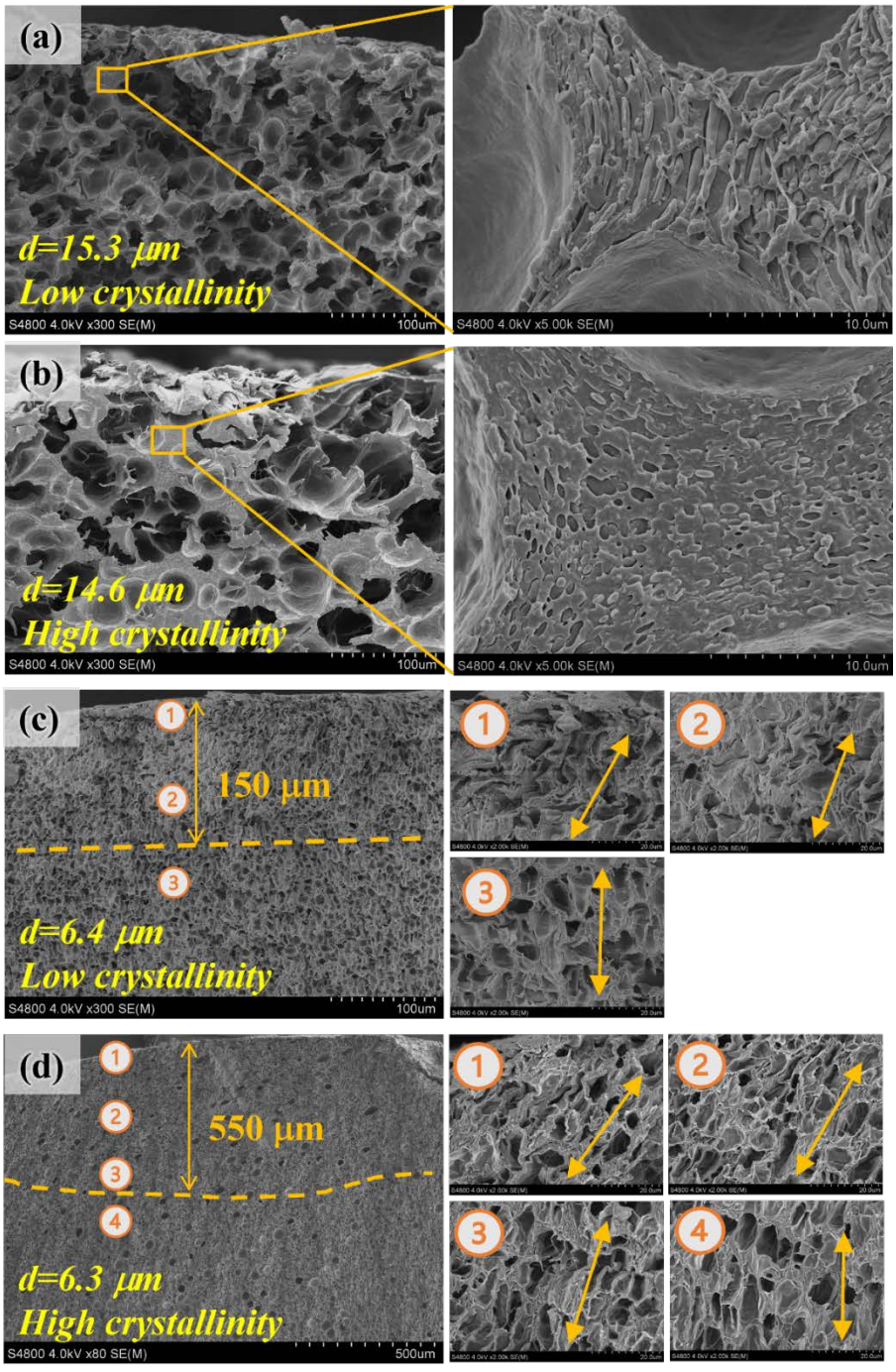

Fig. 5-11. SEM images of cross sections underneath the impact-fractured surfaces for PLA/PBAT foams with various cell sizes: (a) 15.3 μm, (b) 14.6 μm, (c) 6.4 μm, and (d) 6.3 μm. (a, c) and (b, d) had low and high PLA crystallinity, respectively.

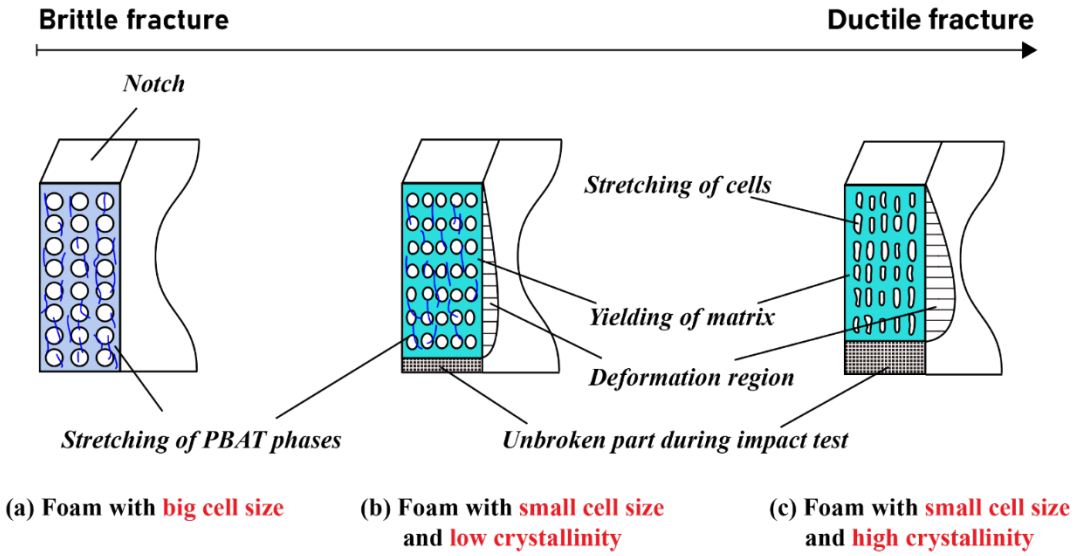

Fig. 5-12. Schematic of the impact-fractured surfaces for PLA/PBAT foams with different cell sizes and various PLA crystallinity.

SENTB tests were performed on PLA/PBAT foams to investigate their fracture mechanisms in terms of the development of a damage zone. Fig. 5-13 shows SEM images of the polished surfaces of samples, after some deformation in SENTB tests at 1 mm/s. For foams with big cell sizes (Fig. 5-13a and b), cracking or crazing occurred in front of the notch tip. It seems that crazing was the main fracture mechanism in PLA/PBAT foams with big cells regardless of the PLA crystallinity. For foam with small cell size and low crystallinity of PLA (Fig. 5-13c), surprisingly, the damage zone greatly enlarged, indicating the enhancement in impact toughness. Besides, the damage zone was bent inwards, suggesting that shear yielding should have appeared as well. Considering the observation of the damage zone and its impact performance, multiple crazing of the PLA matrix was the main fracture mechanism. For foam with small cell size and high PLA crystallinity (Fig. 5-13d), it seems that crazing and shear yielding first occurred, and then the crazes developed

into cracks. Therefore, the cracks did not directly appear below the notch tip. Combined with the great enhancement of impact strength(Fig. 5-9b) by reducing cell size from 14.6 to 6.3 μm, the dominant fracture mechanism changed from crazing to shear yielding.

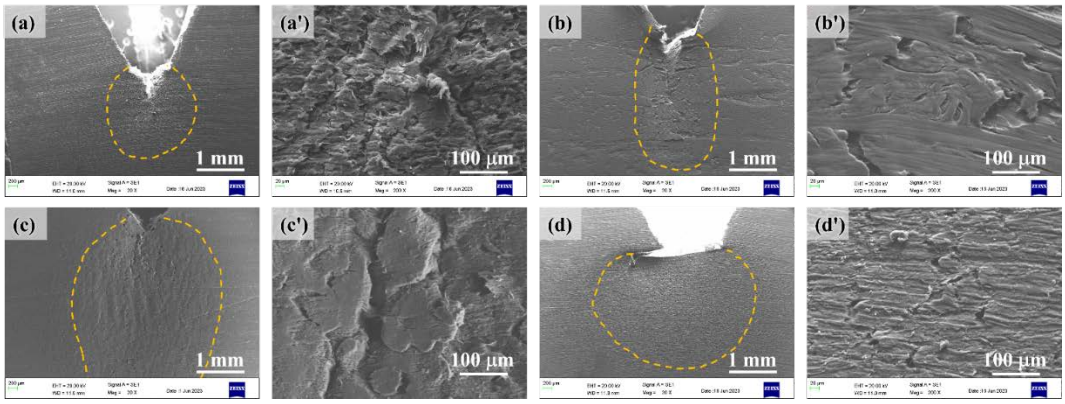

Fig. 5-13. SEM images taken from the polished surfaces of PLA/PBAT foams with various cell sizes: (a) 15.3 μm, (b) 14.6 μm, (c) 6.4 μm, and (d) 6.3 μm. (a, c) and (b, d) had low and high PLA crystallinity, respectively. (a'–d') were the magnified images of (a–d).

5.4.5. Discussion

Based on the previous results, it is obvious that cell size-induced brittle-tough transition occurred both for PLA/PBAT foams with lowly crystalline PLA and for foams with highly crystalline PLA. The cell size-induced brittle-tough transition for PLA/PBAT foams with low crystalline PLA as well as the corresponding toughing mechanism have been comprehensively studied in Chapter 4. It seems that this toughening mechanism was also applicable in PLA/PBAT foams with high crystallinity of PLA. The larger cells could easily initiate crazes due to a lower initiation stress compared with the smaller PBAT particles. When the cell size was

above the critical value(~15 μm for foams with high crystallinity of PLA and ~12 μm for foams with low crystallinity of PLA), the cell-induced crazes would develop to cracks due to the negligible interaction between neighboring cells, leading to a low impact strength. It was obvious that crazing was the main fracture mechanism for foams with big cells and was independent of the PLA crystallinity. However, when the cell size reduced to the critical value, the corresponding cell wall thickness was small enough. The strong interaction of stress fields caused by the neighboring cells as well as the existence of PBAT particles can hinder the transition of cells-induced crazes to cracks, and thus the damage zone significantly expanded(Fig. 5-13c and 10d), which was the typical feature of multiple crazing. Besides, the presence of PBAT particles could also induce the shear yielding of the PLA matrix. Probably due to the big internal structure differences between amorphous polymers and semicrystalline polymers, where semicrystalline polymers usually consisted of crystalline lamellae and amorphous regions, the highly crystalline PLA was more prone to shear yield in comparison with lowly crystalline PLA. Thus, the dominant fracture mechanism for foams with lowly crystalline PLA was multiple crazing, while that for foams with highly crystalline PLA was shear yielding. Since shear yielding is more effective in energy dissipation compared with crazing[39, 40], the foams with highly crystalline PLA exhibited extremely high impact strength in comparison with foams with lowly crystalline PLA (Fig. 5-9c), when the cell size below the critical value.

5.5. Conclusion

In this work, the synergistic effect of cell size and PLA matrix crystallization on the toughening of PLA/PBAT blend foams was first demonstrated through our experiments. A brittle-tough transition occurred only when the PLA crystallinity matched the cell size. By increasing the PLA crystallinity, the critical cell size for brittle-tough transition reduced from 15 to 12 μm. When the cell size was above the critical value, PLA/PBAT foams were all fractured through crazing. When the cell size was below the critical value, the fracture mechanism would transfer to a combination of multiple crazing and shear yielding. However, the primary mechanism for foams with lowly crystalline PLA was multiple crazing, while that for foams with highly crystalline PLA was shear yielding, which was effective in energy dissipation. This study could offer a general strategy for the preparation of toughened PLA blend foams.

5.6. References

[1] V.H. Sangeetha, H. Deka, T.O. Varghese, S.K. Nayak, State of the art and future prospectives of poly(lactic acid) based blends and composites, Polym. Compos. 39(1) (2018) 81-101. https://doi.org/10.1002/pc.23906

[2] M.W. Halloran, J.A. Nicell, R.L. Leask, M. Marić, Toughening Poly(lactide) with Bio-Based Poly(farnesene) Elastomers, ACS Appl. Polym. Mater. 4(8) (2022) 6276-6287. https://doi.org/10.1021/acsapm.2c01183

[3] M. Nofar, D. Sacligil, P.J. Carreau, M.R. Kamal, M.-C. Heuzey, Poly (lactic acid) blends: Processing, properties and applications, Int. J. Biol. Macromol. 125 (2019) 307-360. https://doi.org/10.1016/j.ijbiomac.2018.12.002

[4] J.-h. Wu, T.-g. Hu, H. Wang, M.-h. Zong, H. Wu, P. Wen, Electrospinning of PLA Nanofibers: Recent Advances and Its Potential Application for Food Packaging, J. Agric. Food Chem. 70(27)

(2022) 8207-8221. https://doi.org/10.1021/acs.jafc.2c02611

[5] J. Li, M. Xu, H. He, Q. Gao, Y. Zhang, H. Zhang, Q. Gu, B. Xue, Z. Zhu, Enhancing Tensile Strength and Toughness via Moderate Orientation of Amorphous Molecular Chains in Biobased Biodegradable Poly(lactic acid), ACS Appl. Polym. Mater. 4(10) (2022) 6969-6977. https://doi.org/10.1021/acsapm.2c00898

[6] Y. Han, J. Shi, L. Mao, Z. Wang, L. Zhang, Improvement of Compatibility and Mechanical Performances of PLA/PBAT Composites with Epoxidized Soybean Oil as Compatibilizer, Ind. Eng. Chem. Res. 59(50) (2020) 21779-21790. https://doi.org/10.1021/acs.iecr.0c04285

[7] R. Li, L. Wu, B.-G. Li, Poly (l-lactide)/PEG-mb-PBAT blends with highly improved toughness and balanced performance, Eur. Polym. J. 100 (2018) 178-186. https://doi.org/10.1016/j.eurpolymj.2018.01.037

[8] B. Xue, H.-Z. He, Z.-X. Huang, Z. Zhu, F. Xue, S. Liu, B. Liu, Fabrication of super-tough ternary blends by melt compounding of poly(lactic acid) with poly(butylene succinate) and ethylene-methyl acrylate-glycidyl methacrylate, Composites, Part B 172 (2019) 743-749. https://doi.org/10.1016/j.compositesb.2019.05.098

[9] F. Wu, M. Misra, A.K. Mohanty, Tailoring the toughness of sustainable polymer blends from biodegradable plastics via morphology transition observed by atomic force microscopy, Polym. Degrad. Stab. 173 (2020) 109066. https://doi.org/10.1016/j.polymdegradstab.2019.109066

[10] C. Zhang, T. Zhai, L.-S. Turng, Y. Dan, Morphological, Mechanical, and Crystallization Behavior of Polylactide/Polycaprolactone Blends Compatibilized by l-Lactide/Caprolactone Copolymer, Ind. Eng. Chem. Res. 54(38) (2015) 9505-9511. https://doi.org/10.1021/acs.iecr.5b02134

[11] H.T. Oyama, Super-tough poly(lactic acid) materials: Reactive blending with ethylene copolymer, Polymer 50(3) (2009) 747-751. https://doi.org/10.1016/j.polymer.2008.12.025

[12] V. Nagarajan, A.K. Mohanty, M. Misra, Perspective on Polylactic Acid (PLA) based Sustainable Materials for Durable Applications: Focus on Toughness and Heat Resistance, ACS Sustainable Chem. Eng. 4(6) (2016) 2899-2916. https://doi.org/10.1021/acssuschemeng.6b00321

[13] X. Wang, S. Peng, H. Chen, X. Yu, X. Zhao, Mechanical properties, rheological behaviors, and phase morphologies of high-toughness PLA/PBAT blends by in-situ reactive compatibilization, Composites, Part B 173 (2019) 107028. https://doi.org/10.1016/j.compositesb.2019.107028

[14] J. Zhao, H. He, Z. Zhu, Fabrication of Biodegradable Poly(Lactic Acid) Composites with High Toughness via In Situ Fibrillation Method and Facile Annealing Process, Ind. Eng. Chem. Res. 62(9) (2023) 3952-3961. https://doi.org/10.1021/acs.iecr.2c04359

[15] L. Deng, C. Xu, X. Wang, Z. Wang, Supertoughened Polylactide Binary Blend with High Heat Deflection Temperature Achieved by Thermal Annealing above the Glass Transition Temperature, ACS Sustainable Chem. Eng. 6(1) (2018) 480-490. https://doi.org/10.1021/acssuschemeng.7b02751

[16] Y. Xia, S. Qian, W. Lu, Z. Zhang, H. Cheng, K. Sheng, A strategy to prepare high-robust and ultra-tough polylactic acid/polycaprolactone/talc composites with thermo-resistance, Polym. Compos. 44(12) (2023) 8750-8765. https://doi.org/10.1002/pc.27734

[17] H. Bai, H. Xiu, J. Gao, H. Deng, Q. Zhang, M. Yang, Q. Fu, Tailoring Impact Toughness of Poly(l-lactide)/Poly(ε-caprolactone) (PLLA/PCL) Blends by Controlling Crystallization of PLLA Matrix, ACS Appl. Mater. Interfaces 4(2) (2012) 897-905. https://doi.org/10.1021/am201564f

[18] W. Zhou, X. Chen, K. Yang, H. Fang, Z. Xu, Y. Ding, Achieving morphological evolution and interfacial enhancement in fully degradable and supertough polylactide/polyurethane elastomer blends by interfacial stereocomplexation, Appl. Surf. Sci. 572 (2022) 151393. https://doi.org/10.1016/j.apsusc.2021.151393

[19] J. Chai, G. Wang, B. Li, G. Wan, L. Zhang, G. Zhao, Strong and ductile poly (lactic acid) achieved by carbon dioxide treatment at room temperature, J. CO2 Util. 33 (2019) 292-302. https://doi.org/10.1016/j.jcou.2019.06.006

[20] J. Chai, G. Wang, A. Zhang, S. Li, J. Zhao, G. Zhao, C.B. Park, Ultra-ductile and strong in-situ fibrillated PLA/PTFE nanocomposites with outstanding heat resistance derived by CO2 treatment, Composites, Part A 155 (2022). https://doi.org/10.1016/j.compositesa.2022.106849

[21] J. Zhang, D. Hu, S. Wei, Z. Xi, W. Zhen, L. Zhao, Effects of chain composition of PBAT on the supercritical CO2 foaming and degradation behavior, J. CO2 Util. 72 (2023) 102500. https://doi.org/10.1016/j.jcou.2023.102500

[22] W. Zhai, J. Jiang, C.B. Park, A review on physical foaming of thermoplastic and vulcanized elastomers, Polym. Rev. 62(1) (2022) 95-141. https://doi.org/10.1080/15583724.2021.1897996

[23] M. Wu, F. Wu, Q. Ren, Z. Weng, H. Luo, L. Wang, W. Zheng, Effect of crystalline structure on the cell morphology and mechanical properties of polypropylene foams fabricated by core-back foam injection molding, J. Appl. Polym. Sci. 138(46) (2021) 51370. https://doi.org/10.1002/app.51370

[24] W. Li, Q. Ren, X. Zhu, M. Wu, Z. Weng, L. Wang, W. Zheng, Enhanced heat resistance and compression strength of microcellular poly (lactic acid) foam by promoted stereocomplex crystallization with added D-Mannitol, J. CO2 Util. 63 (2022) 102118. https://doi.org/10.1016/j.jcou.2022.102118

[25] Q. Ren, M. Wu, L. Wang, W. Zheng, Y. Hikima, T. Semba, M. Ohshima, Light and strong poly (lactic acid)/cellulose nanofiber nanocomposite foams with enhanced rheological and crystallization property, J. Supercrit. Fluids 190 (2022) 105758. https://doi.org/10.1016/j.supflu.2022.105758

[26] J.S. Colton, N.P. Suh, Nucleation of microcellular foam: Theory and practice, Polym. Eng. Sci. 27(7) (1987) 500-503. https://doi.org/10.1002/pen.760270704

[27] L. Wang, Y. Hikima, S. Ishihara, M. Ohshima, Fabrication of lightweight microcellular foams

in injection-molded polypropylene using the synergy of long-chain branches and crystal nucleating agents, Polymer 128 (2017) 119-127. https://doi.org/10.1016/j.polymer.2017.09.025

[28] H. Marubayashi, S. Akaishi, S. Akasaka, S. Asai, M. Sumita, Crystalline Structure and Morphology of Poly(l-lactide) Formed under High-Pressure CO2, Macromolecules 41(23) (2008) 9192-9203. https://doi.org/10.1021/ma800766h

[29] S. Saeidlou, M.A. Huneault, H. Li, C.B. Park, Poly(lactic acid) crystallization, Prog. Polym. Sci. 37(12) (2012) 1657-1677. https://doi.org/10.1016/j.progpolymsci.2012.07.005

[30] P. Pan, W. Kai, B. Zhu, T. Dong, Y. Inoue, Polymorphous Crystallization and Multiple Melting Behavior of Poly(l-lactide): Molecular Weight Dependence, Macromolecules 40(19) (2007) 6898-6905. https://doi.org/10.1021/ma071258d

[31] J. Zhang, K. Tashiro, H. Tsuji, A.J. Domb, Disorder-to-Order Phase Transition and Multiple Melting Behavior of Poly(l-lactide) Investigated by Simultaneous Measurements of WAXD and DSC, Macromolecules 41(4) (2008) 1352-1357. https://doi.org/10.1021/ma0706071

[32] H. Tsuji, K. Ohsada, Y. Arakawa, Stereocomplex- and homo-crystallization behavior, polymorphism, and thermal properties of enantiomeric random copolymers of l- and d-lactic acids from the melt, Polymer 228 (2021) 123954. https://doi.org/10.1016/j.polymer.2021.123954

[33] H. Bai, C. Huang, H. Xiu, Y. Gao, Q. Zhang, Q. Fu, Toughening of poly(l-lactide) with poly(ε-caprolactone): Combined effects of matrix crystallization and impact modifier particle size, Polymer 54(19) (2013) 5257-5266. https://doi.org/10.1016/j.polymer.2013.07.051

[34] M. Okamoto, P.H. Nam, P. Maiti, T. Kotaka, T. Nakayama, M. Takada, M. Ohshima, A. Usuki, N. Hasegawa, H. Okamoto, Biaxial Flow-Induced Alignment of Silicate Layers in Polypropylene/Clay Nanocomposite Foam, Nano Lett. 1(9) (2001) 503-505. https://doi.org/10.1021/nl010051+

[35] C.L.T. III, P. Moldenaers, MICROSTRUCTURAL EVOLUTION IN POLYMER BLENDS, Annual Review of Fluid Mechanics 34(1) (2002) 177-210. https://doi.org/10.1146/annurev.fluid.34.082301.144051

[36] Y. Pang, X. Dong, Y. Zhao, C.C. Han, D. Wang, Time evolution of phase structure and corresponding mechanical properties of iPP/PEOc blends in the late-stage phase separation and crystallization, Polymer 48(21) (2007) 6395-6403. https://doi.org/10.1016/j.polymer.2007.08.032

[37] L. Zhu, X. Shen, J. Gu, C. Li, X. Xu, Analysis of phase structure and evolution of PP/PEOc blends during quiescent molten-state annealing process from SEM patterns. Part I: droplet/matrix morphology, Colloid Polym. Sci. 291(4) (2013) 1009-1017. https://doi.org/10.1007/s00396-012-2824-6

[38] D.-x. Sun, T. Gu, X.-d. Qi, J.-h. Yang, Y.-z. Lei, Y. Wang, Highly-toughened biodegradable poly(L-lactic acid) composites with heat resistance and mechanical-damage-healing ability by

adding poly(butylene adipate-co-butylene terephthalate) and carbon nanofibers, Chem. Eng. J. 424 (2021) 130558. https://doi.org/10.1016/j.cej.2021.130558

[39] R.A.C. Deblieck, D.J.M. van Beek, K. Remerie, I.M. Ward, Failure mechanisms in polyolefines: The role of crazing, shear yielding and the entanglement network, Polymer 52(14) (2011) 2979-2990. https://doi.org/10.1016/j.polymer.2011.03.055

[40] A. Salehi, M. Kheradmandkeysomi, S.S. Rahman, R. Rahmati, A. Afzal, R. Li, C.B. Park, Fabricating super-tough polypropylene nanocomposites incorporating silane cross-linked in-situ nano-fibrillated ethylene-1-butene copolymer, Mater. Today Chem. 35 (2024) 101856. https://doi.org/10.1016/j.mtchem.2023.101856

Chapter 6: Enhanced EC and EMI shielding performance through cell size-induced CNS alignment in PP/CNS foam

In this chapter, the necessity of developing CPC foams with enhanced EC was emphasized. To explore the influence of cell size on electrical properties, PP/CNS foams with different cell sizes were obtained using core-back FIM technique. The dispersion of CNS in PP matrix and the electrical properties were evaluated. Then the mechanism of EC improvement was discussed.

6.1. Abstract

The incorporation of cell structure within CPCs presents significant advantages in terms of EC and EMI shielding performance. In addition to the commonly reported strategies in the literature, such as increasing the content of conductive fillers and adjusting the VF of CPC foams, we propose that enlarging cell size is also an effective means of improving EC and EMI shielding properties. Herein, PP/CNS nanocomposite foams with a fixed VF were produced using core-back foaming injection molding (FIM) technique, and their cell sizes were well-controlled by modifying the N_2 content. The results reveal that as the cell size increased from 71 to 317 μm, the EC and EMI SE increased from 1.43×10^{-3} to 5.07×10^{-3} S/cm and from 48.5 to 59.2 dB, respectively. The enhanced EC was attributed to the slightly aligned CNS and the shorter actual conductive paths. Furthermore, our novel CPC foams demonstrated a maximum specific SE reached 329 $dB\cdot cm^2/g$, exhibiting superior EMI shielding performance compared to other existing CPC foams. This study offers a feasible strategy for the fabrication of CPC foams with exceptional EMI shielding properties.

6.2. Introduction

Due to the thriving development of electronic devices, extensively utilized in cutting domains such as communication, military and aerospace, escalating electromagnetic pollution has emerged as a potential hazard to equipment functionality and human well-being[1-3]. Consequently, there is an urgent need to develop lightweight

materials with outstanding EMI shielding performance. CPCs, comprising polymer and conductive fillers, offer advantageous attributes, such as lightweight, cost-effectiveness, corrosion resistance and ease of processability, in comparison to metal-based materials[4-6]. Furthermore, the incorporation of cell structures into CPCs presents an additional avenue for reducing weight and enhancing the electrical properties of CPCs, even at lower filler contents[7, 8]. For instance, Ameli et al.[9] prepared composite foams of PP/CF with an expansion ratio of 1.3-fold and found that cell growth could change CFs' orientation and improve their interconnectivity. Consequently, this led to a reduction in the percolation threshold (from 8.75 to 7 vol.%) and significant improvements in EC (increased by six orders of magnitude) and specific EMI SE (increased by 65%). Similarly, Hamidinejad et al.[10] reported similar results in a system comprising HDPE/GNP. Through foaming, they were able to lower the percolation threshold from 19 to 7.2 vol% with a foaming degree of 26% and enhance the EMI SE from 21.8 to 31.6 dB with a GNP content of 19 vol%.

Numerous studies have demonstrated that the reduction in percolation threshold and enhancement of electrical performance primarily occur in CPC foams incorporating 1D and 2D conductive fillers, such as MWCNTs[11-13], CF[14], GNP[15], and stainless-steel fiber[16]. This behavior can be attributed to the biaxial flow induced by cell growth during foaming, which would cause the rod-like fillers to align along the cell boundaries, thereby improving the interconnectivity among the conductive fillers and facilitating the formation of the conductive path[17-19]. Ameli et al[18] investigated the effect of relative density on the EC of PP/MWCNT foams. They

observed that as the relative density decreased from 1 (solid) to 0.7, the EC initially increased due the slight orientation of MWCNTs around the cells, which were favorable for the MWCNT interconnections. However, with the further decrease of relative density, the EC gradually decreased due to the full orientation of MWCNTs perpendicular to the radial direction, resulting in a reduction in MWCNT interconnections. This explanation was supported by the works of Du et al.[20] and Gong et al.[21], who demonstrated that the highest EC was achieved when the CNT exhibited slight alignment, rather than high alignment or isotropy, within the matrix. Considering the effect of location and orientation of conductive filler on the EC of CPC foams, Monte Carlo simulations were applied to investigate the EC under various VFs[22-24]. The simulation result showed that increasing the VF (below 20%) improves the EC, while further increases in VF (>30%) lead to a decrease in the EC.

Although considerable studies have explored the relationship between VF/conductive filler content and EC, limited research has been published regarding the impact of cell size on EC. Zhao et al[11] investigated the effect of VF of poly(vinylidene fluoride) (PVDF)/MWCNT on EC and EMI shielding properties. The results showed that the EC and EMI shielding properties declined with the increase of VF for foams with low MWCNT content (1 and 2 wt%) but improved for foams with high MWCNT content (5 and 8 wt%). It also should be noticed that the cell size varied from ~5 to ~20 μm for foams with MWCNT content of 8 wt%, for example. The non-uniform cell structure could be found for foams with high MWCNT contents (5 and 8 wt%). Regrettably, however, the influence of cell

structure on electrical properties of PVDF/MWCNT was not discussed in this reference. In fact, it was very common just mainly focusing on the effect VF/conductive filler content on EC but ignoring the influence of cell size in previous reported literature[14, 25-27].Foams can be characterized by various parameters, including cell size, cell density, cell wall thickness, and VF, and these parameters are interconnected [28, 29]. For foams with the same VF, increasing cell size would cause the increase of cell wall thickness[17, 30] and the reduction of cell density. If rod-like fillers are dispersed within the cell wall, the fillers near the cell boundary tend to orient themselves perpendicular to the radial direction. The degree of orientation would decrease as the distance between the filler and the cell boundary increase. Consequently, the thinner cell wall would promote greater filler alignment, which may subsequently influence the final EC.

Our previous results proved that the EMI SE improved with the increase of VF (0–80%) for CPC foams with high filler content[31]. In addition, a higher VF suggested a thinner cell wall thickness, which was favorable for the alignment of rod-like fillers. In this work, PP/CNS nanocomposite foams with 5 wt% CNS content and 78% VF were prepared using core-back FIM. The effect of cell size on the EC and EMI shielding performance of PP/CNS nanocomposite foams was investigated in detail. The results revealed that increasing the cell size enhanced the EC due to the slightly aligned CNS and the shorter real conductive paths, leading to a higher EMI SE. This work provides a straightforward method to obtain lightweight PP/CNS foams with outstanding EMI shielding properties.

6.3. Experimental section

6.3.1. Materials

A commercial-grade long chain branched PP (WB140HMS), with a melt flow rate of 2.1 g/10 min (ISO 1133), supplied by Borealis Ltd. CNS (ATHLOS 200), a type of branched MWCNT, was purchased from Cabot Corporation. The CNS is coated with polyethylene glycol (PEG) and has a density of 0.135 g/cm^3 (ASTM D7481). N_2 (99% purity) provided by Huayu Gas Inc., China, was selected as the physical blowing agent.

6.3.2. Sample preparation

Fig. 6-1. Shows the fabrication process of PP/CNS foams. Before compounding, both the PP and CNS were dried at 80 ℃ for 8 h to remove moisture. Before compounding, both the PP and CNS were dried at 80 ℃ for 8 h to remove moisture. PP and CNS were compounded using a twin screw extruder (AK 36, Nanjing KY Chemical Machinery Co. Ltd., China) at 170–220 ℃. The CNS content was fixed at 5 wt%. A 100-ton foaming injection molding (FIM) machine (Systec 100/420-310C, Demag Plastics Group, Germany), equipped with a Mucell SCF delivery system (T100, Trexel Inc., USA) was applied to conduct the core-back FIM experiments. A rectangular mold cavity (150 × 110 × 2 mm^3) equipped with pressure and temperature transducers was applied in this study, as shown in Fig. 6-2. The core-back FIM experiments consisted of four steps: filling, dwelling, core-back, and cooling. In this work, a core-back distance of 7 mm was used to prepare foams with a VF of 78%. The dwelling time was 3.5 s, and the corresponding foaming temperature was 105 ℃ determined by the cavity temperature transducers. To obtain

foams with various cell sizes, three different N_2 contents (0.6 wt%, 0.8 wt%, 1 wt%) were selected to conduct experiments. Table 6-1 depicts the detailed processing conditions.

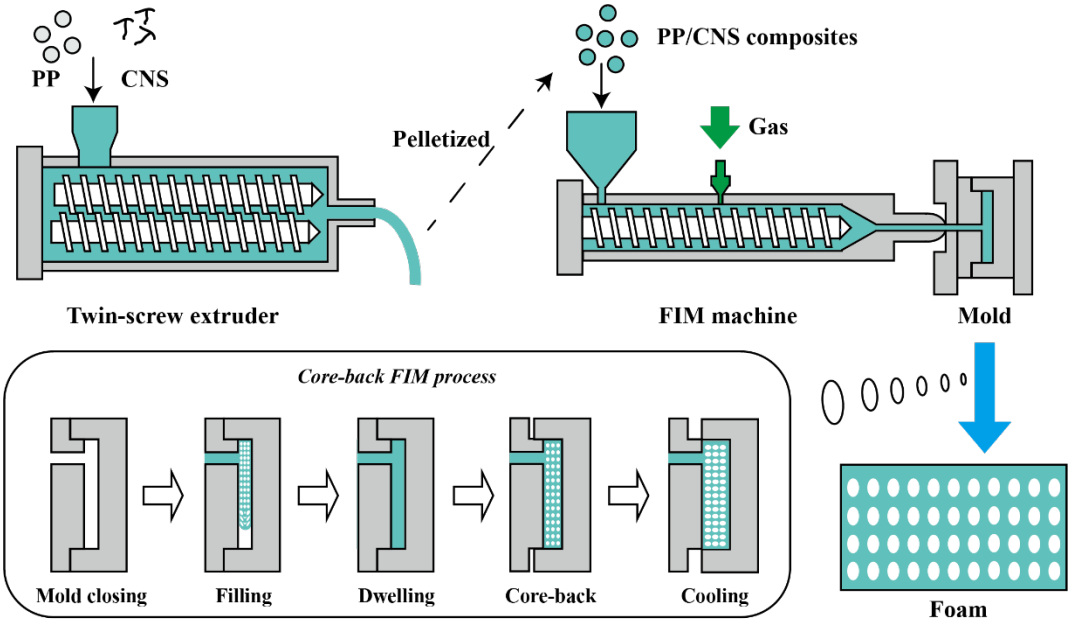

Fig. 6-1. Schematic of the preparation process of PP/CNS nanocomposite foams.

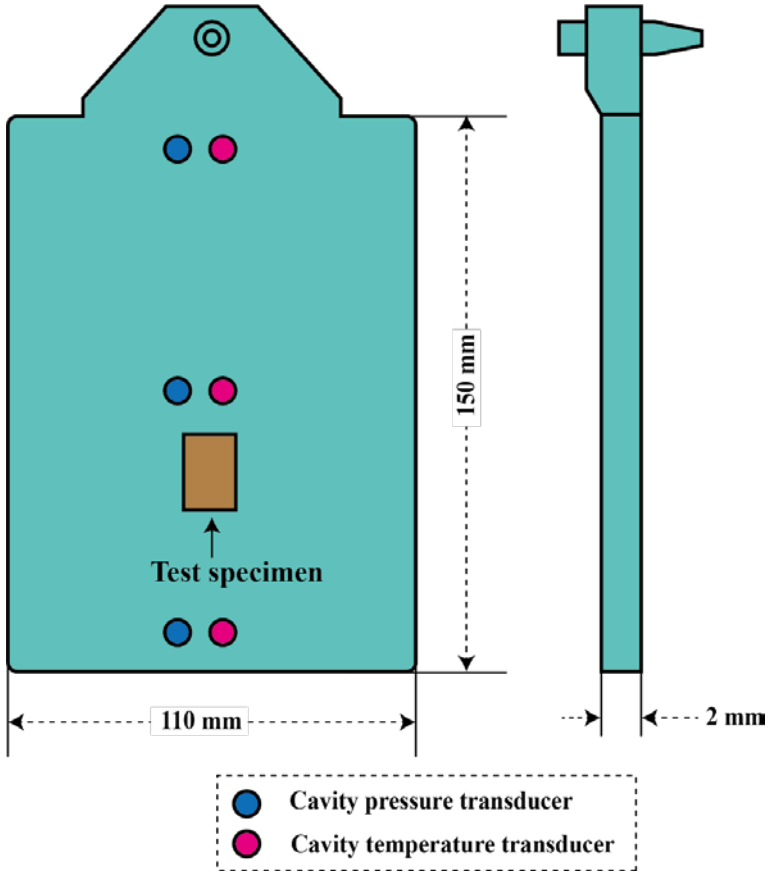

Fig. 6-2. Schematic of mold cavity and specimen preparations.

Table 6-1. Processing parameters used in the core-back FIM process.

Parameters	Values
Melt temperature (℃)	220
Mold temperature (℃)	100
Injection speed (mm/s)	150
Injection pressure (MPa)	140
Back pressure (MPa)	20
Packing pressure (MPa)	40
Shot size (mm)	55
Dwelling time (sec)	3.5
Core-back distance (mm)	7
N_2 content (wt%)	0.6, 0.8, 1

6.3.3. Thermal analysis

The crystallization behavior of pure PP and PP/CNS nanocomposite was measured using a DSC (DSC/TGA1, Mettler-Toledo) under a nitrogen atmosphere. Specimens weighing approximately 5-8 mg were first heated from 25℃ to 200℃ and kept for 5 min to remove thermal history. Subsequently, they were cooled down to 25℃ and reheated to 200℃. The heating and cooling rates were fixed at 10℃/min.

6.3.4. Rheological analysis

The rheological properties of pure PP and PP/CNS nanocomposite under oscillatory shear flow were investigated with an ARES rotational rheometer (HR-3, TA). A parallel-plate geometry (ϕ=25 mm) with a thickness of 1 mm was heat compressed for this test. The frequency sweep test was conducted over a frequency range of 0.01−100 rad/s at 200 ℃. The strain amplitude was 0.1%.

6.3.5. SEM

Prior to observation, the SEM specimens cut from the middle of the solid and foam (Fig. 6-2) were cryogenically fractured after being immersed in liquid nitrogen for 20 min, and then spurted with a layer of Pt (platinum). A Hitachi S4800 SEM was used to investigate the dispersion of CNS in PP/CNS nanocomposite and its corresponding foams. A Zeiss EVO 18 SEM was applied to characterize the cell morphology. Image J software (National Institutes of Health, USA) was used to analyze cell structure of foams, and the cell density N_0 was determined as by equation [32]:

$$N_0 = (\frac{n}{A})^{3/2}\Phi \tag{6-1}$$

where n is the number of cells, A denotes the area of the SEM micrograph, and

Φ denotes the expansion ratio of the foamed sample. The Φ was calculated using equation [32]:

$$\Phi = \frac{\rho_s}{\rho_f} \tag{6-2}$$

where ρ_s and ρ_f represent the density of the unfoamed and foamed specimens, respectively. The water displacement method (ASTM D792-00) was used to measure those densities. The VF is defined as the ratio of the volume of voids in the foam to the total volume of the foam, and was determined according to the following equation [32]:

$$VF = \frac{\rho_f}{\rho_s} \tag{6-3}$$

The cell wall thickness was calculated according to the Gibson and Ashby equations[33]. Spherical cells were assumed by tetrakaidekahedral pores. For foams with closed cells, the cell wall thickness t was given by equation:

$$t = \frac{l\left(\rho_f / \rho\right)}{1.18}, \quad d = Bl \tag{6-4}$$

where l is the edge length, d denotes the average cell size and B is a constant that related to the assumed cellular shape. For a tetrakaidekahedral pore, B was 2.828.

6.3.6. Transmission electron microscope (TEM)

A JEOL 2100 TEM was used to investigate the CNS dispersion in PP matrix. Before observation, a ultramicrotomy was applied to obtain PP/CNS foam samples for TEM.

6.3.7. EC and EMI shielding performance measurement

EC of foams was analyzed with a two-probe method using an electrochemical workstation (CHI660E, Chenhua Co., China) at room temperature. Three specimens were tested and the average results were reported.

A vector network analyzer (VNA, Keysight N5225A) was used to measure the EMI shielding performance through the wave-guide method in X band (8.2–12.4 Hz). Before measurement, the unfoamed and foamed specimens were cut into rectangles with dimensions of 22.86×10.16 mm^2 (the thickness of unfoamed and foamed specimens were 2 mm and 9 mm, respectively), as shown in Fig. 6-2. The EMI SE can be calculated by the S parameters (S_{11} and S_{21}) by the following equations[34]:

$$R = \left|S_{11}\right|^2, \quad T = \left|S_{21}\right|^2, \quad A' = 1 - T' - R' \tag{6-5}$$

$$SE_{ref} = 10\log\left(\frac{1}{1-R}\right), \quad SE_{abs} = -10\log\left(\frac{T}{1-R}\right) \tag{6-6}$$

$$SE_{total} = 10\log\left(\frac{1}{T}\right) = SE_{ref} + SE_{abs} \tag{6-7}$$

where R', A', T' are the coefficients of reflection, absorption and transmission, respectively. SE_{ref}, SE_{abs} and SE_{total} are SE's reflection, absorption and transmission, respectively.

6.4. Results and discussion

6.4.1. CNS dispersion in PP matrix

Thanks to the surface modification of CNS, Fig. 6-3a depicts a good dispersion of CNS in PP matrix. Probably due to the relatively high content of CNS (5 wt%), some small aggregations can be found in Fig. 6-3b (indicated by red dotted circles). It is

well known that the homogeneous distributed CNS could not only significantly improve the foamability of PP by strengthening melt strength and crystallization rate, but also benefit the formation of conductive path[35-38].

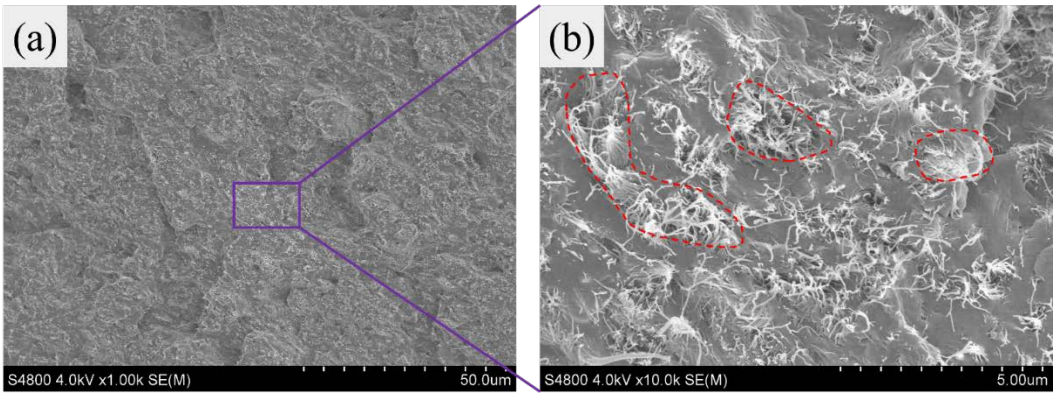

Fig. 6-3. SEM images of PP/CNS nanocomposite. (b) is the magnified image of one section of (a).

6.4.2. Cell structure

Fig. 6-4 and 6-5 show the rheology and crystallization behavior of pure PP and PP/CNS nanocomposite (detailed discussion can be found in supporting information). The enhanced melt strength and crystallization rate of PP/CNS nanocomposite were favorable for the preparation of foams with fine cell structure. Fig. 6-6 depicts the SEM images and cell size distribution of pure PP and PP/CNS nanocomposite foams, and the corresponding quantitative information is listed in Table 6-2. Under the same process condition, the cell size of PP/CNS foam was 10 times smaller than that of PP foam and its cell density was improved by two orders of magnitude. Generally, the final cell structure was determined by two steps, including cell nucleation and cell growth. In the cell nucleation step, the nucleation rate of cells was significantly enhanced due to the existence of CNS and the preformed PP crystallites which were induced by the introduction of CNS during

dwelling step[37, 39]. During the cell growth step, cell collapse was largely suppressed owing to the strengthened melt strength of PP/CNS nanocomposite (Fig. 6-4). To obtain PP/CNS foams with different cell sizes, a series of different N_2 content was applied since increasing the gas content would reduce the activation energy required for cell nucleation, leading to a higher nucleation rate and smaller cell size. Thus, the cell size varied from 317 to 71 μm with the increase of N_2 content from 0.6 to 1 wt%. Injection molded foams exhibit a typical sandwich structure, where the middle is foamed layer and the two sides are surface layers. It was necessary to evaluate the surface layer thickness since it would affect the electrical properties and EMI shielding performance of PP/CNS foams. Fig. 6-7 shows that the surface layer thicknesses of PP/CNS foams were in the range of 250–280 μm, which were much smaller than the samples' thickness (9 mm). Thus, the effect of the surface layer thickness on EMI SE could be ignored.

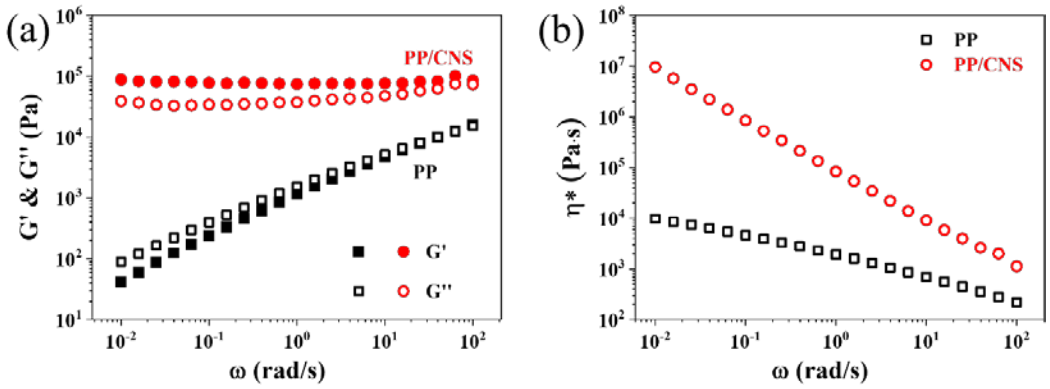

Fig. 6-4. Rheological behavior of pure PP and PP/CNS nanocomposite.

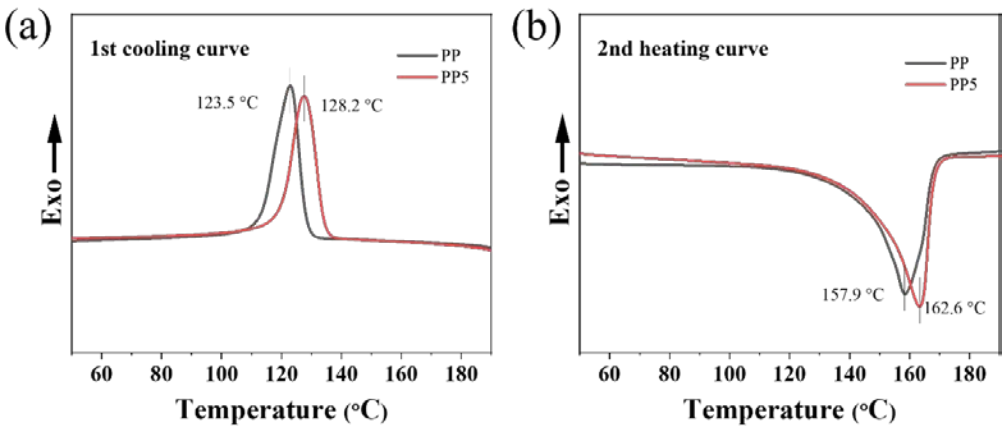

Fig. 6-5. Crystallization behavior of pure PP and PP/CNS nanocomposite in (a) 1st cooling and (b) 2nd heating.

Table 6-2. Cell structure parameters of PP and PP/CNS foams

Foam	N_2 content (wt%)	d (mm)	N_0 (cells/cm^3)	t[a] (μm)
PP	1	726	1.01×10^4	-
PP/CNS	0.6	317	7.51×10^4	20.9
PP/CNS	0.8	142	1.05×10^6	9.4
PP/CNS	1	71	8.72×10^6	4.7

[a] Thickness of cell wall, which was calculated from equation (6-4).

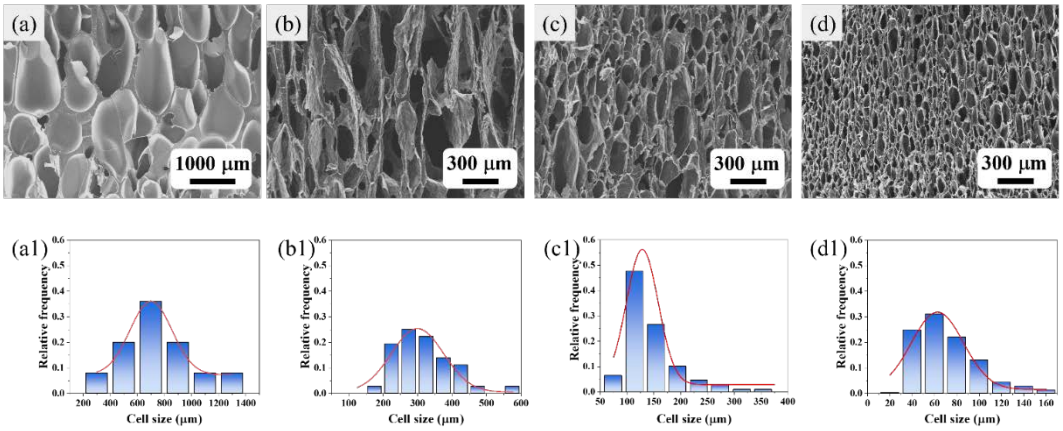

Fig. 6-6. SEM images of (a) PP and (b–d) PP/CNS nanocomposite foams fabricated under various N_2 content: (a)1 wt%, (b) 0.6 wt%, (c) 0.8 wt%, (d) 1 wt%. (a1—d1) were the

corresponding cell size distribution of (a—d).

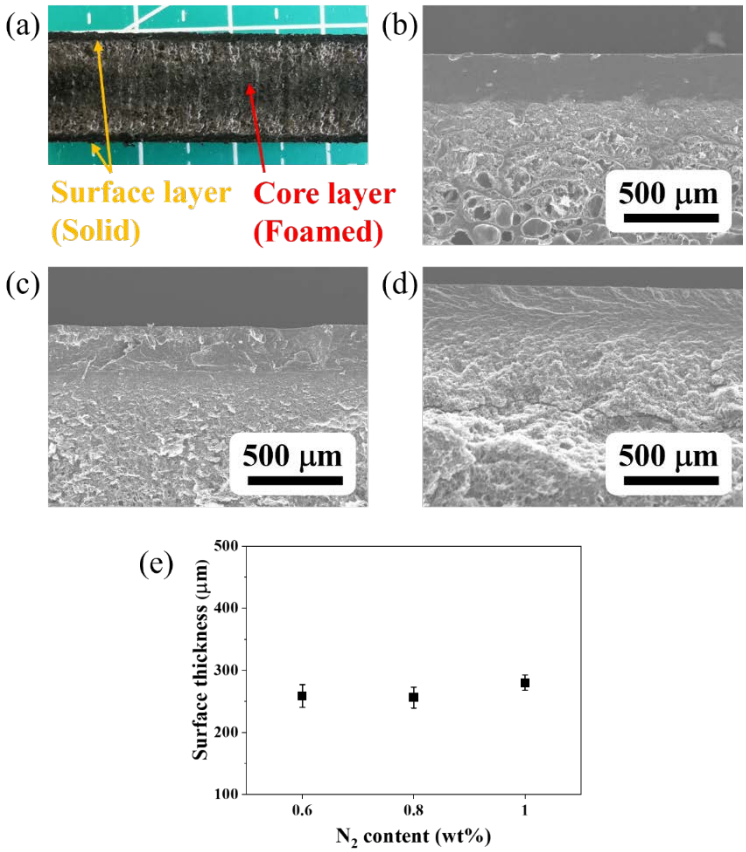

Fig. 6-7. (a) Optical photograph of foamed sample. SEM images of the surface layer of PP/CNS foams under N_2 content of (b) 0.6 wt%, (c)0.8 wt% and (d) 1 wt%. (e) Surface layer thickness of PP/CNS foams fabricated under different N_2 content.

6.4.3. EC of PP/CNS foams

Intensive studies have reported that foaming could significantly improve the EC and decrease the percolation threshold of CPCs by adding 1D fillers (such as CNT, stainless-steel fiber and CF) or 2D fillers (GNP)[9, 10, 16, 18]. Fig. 6-8a depicts the EC of solid and foamed samples. It is noteworthy that all foamed samples exhibited higher EC than the solid sample (9.59×10^{-4} S/cm).This can be attributed to the

growth of cells re-arranged the CNS (CNS paralleled to the boundary of cells), leading to enhanced interconnectivity and EC[10]. Interestingly, the EC of PP/CNS foams increased with the decrease of N_2 content. As the cell structure was strongly related to the applied N_2 content, the relationship between EC and cell size was displayed in Fig. 6-8b. Remarkably, by increasing the cell size from 71 to 317 mm, the EC improved from 1.43×10^{-3} to 5.07×10^{-3} S/cm. This phenomenon has not been previously reported in the existing literature, which mainly focused on the effect of conductive filler content and density (expansion ratio) on the EC of CPC foams[27, 40, 41].

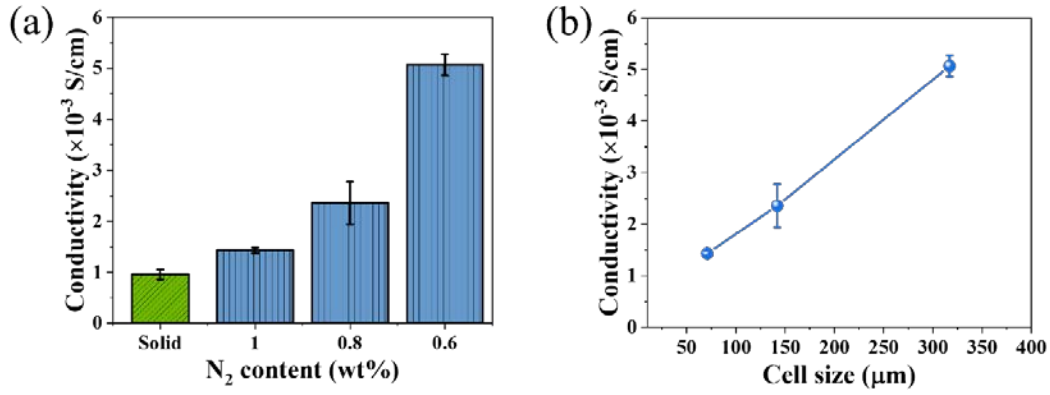

Fig. 6-8. EC of PP/CNS solid and foamed samples as a function of (a) N_2 content and (b) Cell size.

Considering the fact that the EC was mainly influenced by the interconnectivity of CNS, it was necessary to investigate the dispersion of CNS in the cell wall of PP/CNS foams. According to the equation (6-2), we could find the relationship between cell wall thickness (t) and cell size (d): $t \propto d$. By reducing the cell size, the calculated cell wall thicknesses of PP/CNS foams decreased from 20.9 to 4.7

μm, as shown in Table 6-2. Fig. 6-9 shows the SEM images of cell walls for PP/CNS foams with various cell sizes. Fig. 6-10 shows the TEM images of PP/CNS foams with different cell wall thicknesses. Due to the biaxial flow of matrix during foaming[17], CNS aligned along the cell boundary, which was particularly evident in foams with thin cell walls (Fig. 6-9c, 6-9d and 6-10a). For example, CNS aligned along the cell boundary in a thin cell wall (0.8 μm) as shown in Fig. 6-10a. However, for foams with a thicker cell wall, the dispersion of CNS would be strongly related to its distance from the cell boundary as shown in SEM (Fig. 6-9a and b) and TEM (Fig. 6-10) images. (b1–b4) were the magnified TEM images captured from different distances from the cell boundary in Fig. 6-10b. CNS near the cell boundary (b1 in Fig. 6-10) was strictly paralleled to the cell boundary. With the increase of the distance from the cell boundary (from 0 to 11 μm), the degree of CNS orientation gradually impaired (b2 and b3 in Fig. 6-10). The CNS more than 17 μm from the cell boundary was not affected by the biaxial flow of the matrix and was randomly dispersed in the matrix (b4 in Fig. 6-10). Thus, it was obvious that the degree of CNS orientation gradually impaired as the distance from the cell boundary increased, as depicted in the corresponding schematic diagram in Fig. 6-11a. Du et al.[20] systematically investigated the relationship between EC of PMMA/SWNT and the alignment of SWNT through experiment and theoretical simulation. They found that the highest EC was achieved with slightly aligned fillers, rather than highly aligned or randomly dispersed fillers. Additionally, a thicker cell wall indicated a higher quantity of CNS presented, which was further beneficial for the interconnectivity of CNS. Thus, PP/CNS foam with a thick cell wall (big cell size) was more prone to

forming a conductive path, as illustrated in Fig. 6-11b and c.

In addition, with the increase of cell wall thickness, more amount of CNS formed the conductive path, leading to the reduced resistivity of the path. Fig. 6-11d and e depict the possible schematic of conductive path for PP/CNS foams with small and big cells. The reduction in cell size would lead to an increase of tortuosity, defined as the ratio between the length of the real path and the shortest length between two points[42]. PP/CNS foams with smaller cell sizes have longer conductive paths and definitely showed higher volume resistance compared to foams with larger cell sizes. Based on the previous analysis, under the same expansion ratio, foams with a bigger cell size (thicker cell wall) exhibited a higher EC.

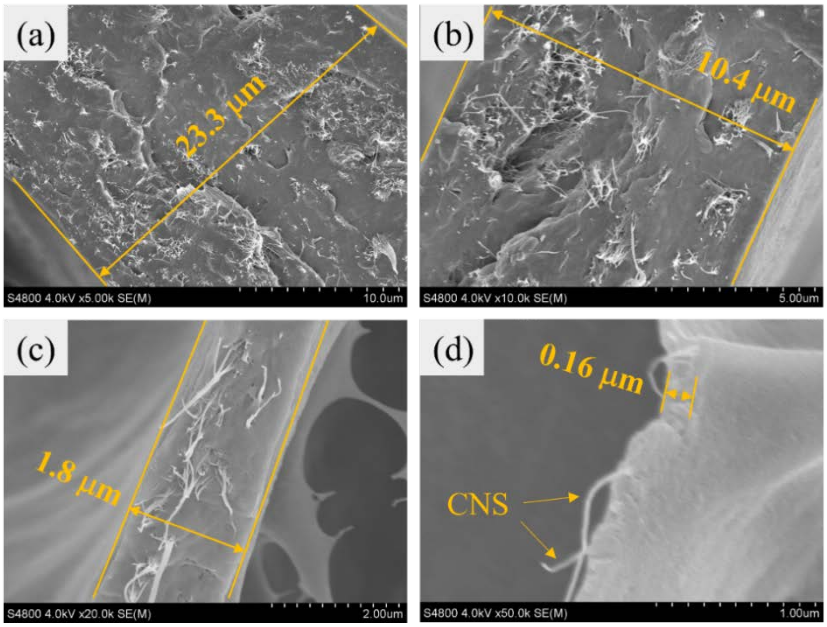

Fig. 6-9. SEM images of the cell wall for PP/CNS foams with different cell sizes: (a) 317 μm, (b) 142μm, (c, d) 71 μm.

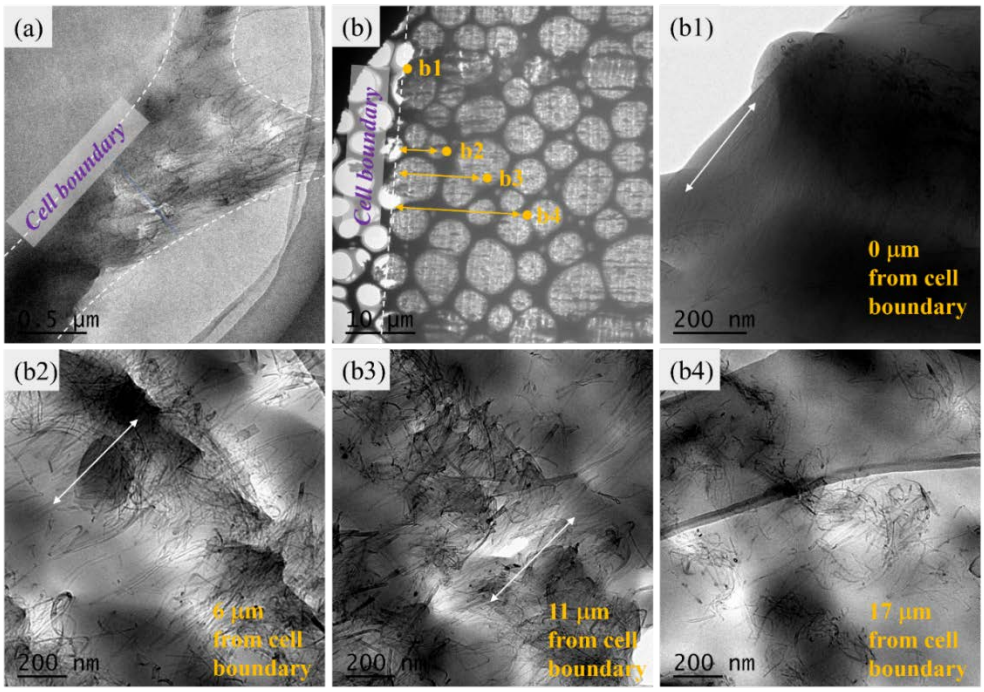

Fig. 6-10. TEM images of PP/CNS foams with different cell wall thicknesses: (a) 0.8 μm, (b) over 40 μm. (b1-b4) are the magnified images captured from different distances from cell boundary in (b): (b1) 0 μm, (b2) 6 μm, (b3) 11 μm, (b4) 17 μm.

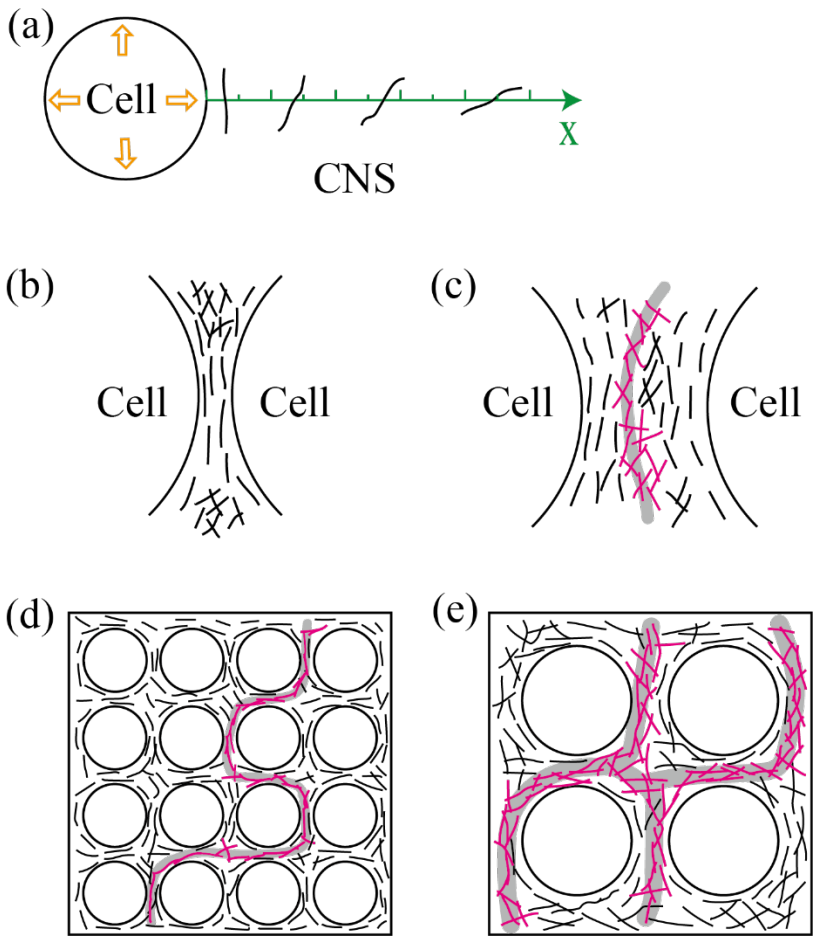

Fig. 6-11. (a) Schematic diagram of the degree of CNS orientation at different locations away from the boundary of cell. (b, c) CNS dispersion in PP matrix of cell wall with (b) small and (c) large thickness. (d, e) Conductive path of PP/CNS foams with (d) small cell size (thin cell wall) and (e) big cell size (thick cell wall).

6.4.4. EMI shielding performance

The EMI shielding performance of both solid and foamed samples in X band was evaluated. As shown in Fig. 6-12a, all foamed samples exhibited much higher SE_{total} than the solid sample. Excepted the enhanced EC, the increased thickness and the introduction of cell structure were also responsible for this enhancement. As

anticipated, with the increase of cell size from 71 to 317 μm, the improved EC (Fig. 6-8b) leaded to an enhancement of SE_{total} from 48.5 to 59.2 dB. Further analysis indicated that the increasement in SE_{total} was mainly from the contribution of SE_{abs} via the internal multiple reflections[43, 44], as shown in Fig. 6-12b. The high level of EC would impair the capability of microwave absorption, resulting a reflection-dominant shielding mechanism for solid and foamed samples (R'>0.7, Fig. 6-12c). Generally, the thickness of testing sample would strongly influence the finial SE_{total}. Thus, to fairly evaluate the EMI shielding performance of CPC foams, the concept of the specific SE (specific SE, defined as the ratio of SE to mass density and thickness of sample) was applied[45]. Fig. 6-12d compares the EMI shielding performance of various CPC foams. Among them, PP/CNS foams exhibited superior performance in terms of both EMI SE and specific SE in comparison with other CPC foams, with the highest specific SE reaching 329 $dB \cdot cm^2/g$. Remarkably, even in the case of PP foams with relatively low CNS loading, we achieved CPC foams with outstanding EMI shielding performance simply by controlling the cell size. This novel strategy provides a viable means to tailor the EMI shielding performance of CPC foams.

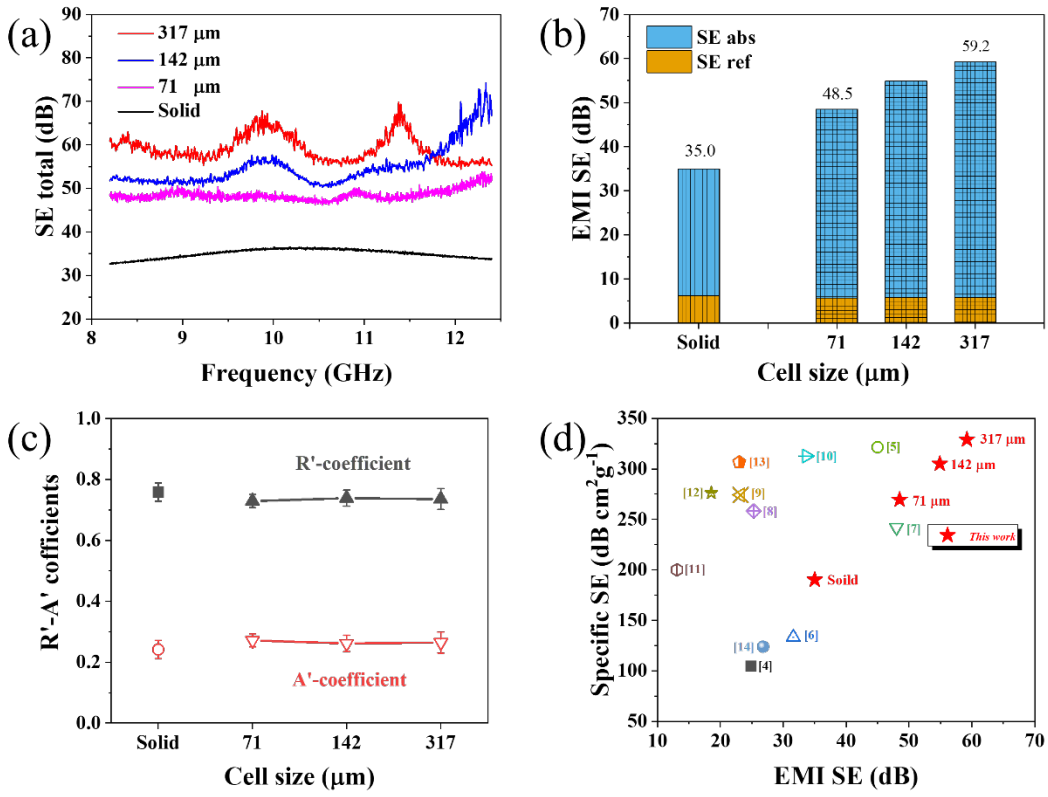

Fig. 6-12. (a-c) EMI shielding properties of PP/CNS nanocomposite and the corresponding foams in X band: (a) SE total, (b) SE abs and SE ref, (c) R' and A' coefficients. (d) Comparison of the EMI shielding performance of our result with other reported CPC foams. The reference numbers listed in Table 6-3.

Table 6-3. Comparison of the EMI shielding performance of CPC foams.

material	Filler content	Thickness	EMI SE	ρ	Specific SE	Specific SE	Ref.
PP	10 vol% CF	3.2	24.9	0.74	104.7	33.7	[9]
PLA	5 wt% nanographite	2	45	0.7	321.4	64.3	[46]
HDPE	19.0 vol% GNP	3	31.6	0.782	133.4	40.4	[10]
PP	1.1 vol% stainless steel fiber	3.1	48	0.64	241.9	75	[16]
PS/PMMA	2 vol% MWCNT	2	25.3	0.49	258.2	51.6	[47]
PS	7 wt% MWCNT	1.8	23.2	0.47	274.2	49.4	[48]
Natural rubber	6.4 wt% CNT	1.3	33.7	0.83	312.69	40.7	[49]
PMMA	7 wt% Fe_3O_4@MWCNTs	2.5	13.1	0.26	200	50	[50]
PS	7 wt% CNT	1.2	18.56	0.56	276.2	33.1	[51]
PLLA	10 wt% MWCNT	2.5	23	0.3	306.6	77	[52]
PVDF	10 wt% Ni-chains	2	26.8	1.08	124	24.8	[53]
PP	5 wt% CNS	2	35.0	0.92	190.2	38.0	This article
PP	5 wt% CNS	9	48.5	0.20	269.4	242.5	This article
PP	5 wt% CNS	9	54.9	0.20	305.0	274.5	This article
PP	5 wt% CNS	9	59.2	0.20	328.9	296.0	This article

6.5. Conclusion

In this work, PP/CNS foams with different cell sizes ranging from 71 to 317 μm were fabricated using core-back FIM. The dispersion of CNS was strongly related with the cell structure of PP/CNS foams. Due to the slightly aligned CNS and the shorter real conductive paths of foams with bigger cell size (thicker cell wall), the EC increased from 1.43×10^{-3} to 5.07×10^{-3} S/cm when the cell size increased from 71 to 317 μm. As a result, the EMI SE improved from 48.5 to 59.2 dB and the highest specific SE reached 329 dB·cm^2/g. This study provided a new strategy to prepare CPC foam with high EMI shielding performance.

6.6. References

[1] P. Xie, Y. Liu, M. Feng, M. Niu, C. Liu, N. Wu, K. Sui, R.R. Patil, D. Pan, Z. Guo, R. Fan, Hierarchically porous Co/C nanocomposites for ultralight high-performance microwave absorption, Adv. Compos. Hybrid. Mater. 4(1) (2021) 173-185. https://doi.org/10.1007/s42114-020-00202-z

[2] P. Song, B. Liu, H. Qiu, X. Shi, D. Cao, J. Gu, MXenes for polymer matrix electromagnetic interference shielding composites: A review, Compos. Commun. 24 (2021) 100653. https://doi.org/10.1016/j.coco.2021.100653

[3] W. Gu, J. Sheng, Q. Huang, G. Wang, J. Chen, G. Ji, Environmentally Friendly and Multifunctional Shaddock Peel-Based Carbon Aerogel for Thermal-Insulation and Microwave Absorption, Nano-Micro Lett. 13(1) (2021) 102. https://doi.org/10.1007/s40820-021-00635-1

[4] G. Sang, P. Xu, T. Yan, V. Murugadoss, N. Naik, Y. Ding, Z. Guo, Interface Engineered Microcellular Magnetic Conductive Polyurethane Nanocomposite Foams for

Electromagnetic Interference Shielding, Nano-Micro Lett. 13(1) (2021) 153. https://doi.org/10.1007/s40820-021-00677-5

[5] R. Asmatulu, P.K. Bollavaram, V.R. Patlolla, I.M. Alarifi, W.S. Khan, Investigating the effects of metallic submicron and nanofilms on fiber-reinforced composites for lightning strike protection and EMI shielding, Adv. Compos. Hybrid. Mater. 3(1) (2020) 66-83. https://doi.org/10.1007/s42114-020-00135-7

[6] X. Lv, Y. Tang, Q. Tian, Y. Wang, T. Ding, Ultra-stretchable membrane with high electrical and thermal conductivity via electrospinning and in-situ nanosilver deposition, Compos. Sci. Technol. 200 (2020) 108414. https://doi.org/10.1016/j.compscitech.2020.108414

[7] Y. Zhang, K. Ruan, X. Shi, H. Qiu, Y. Pan, Y. Yan, J. Gu, Ti3C2Tx/rGO porous composite films with superior electromagnetic interference shielding performances, Carbon 175 (2021) 271-280. https://doi.org/10.1016/j.carbon.2020.12.084

[8] L. Wang, P. Song, C.-T. Lin, J. Kong, J. Gu, 3D Shapeable, Superior Electrically Conductive Cellulose Nanofibers/Ti_3C_2Tx MXene Aerogels/Epoxy Nanocomposites for Promising EMI Shielding, Research 2020 (2020). https://doi.org/10.34133/2020/4093732

[9] A. Ameli, P.U. Jung, C.B. Park, Electrical properties and electromagnetic interference shielding effectiveness of polypropylene/carbon fiber composite foams, Carbon 60 (2013) 379-391. https://doi.org/10.1016/j.carbon.2013.04.050

[10] M. Hamidinejad, B. Zhao, A. Zandieh, N. Moghimian, T. Filleter, C.B. Park, Enhanced Electrical and Electromagnetic Interference Shielding Properties of Polymer–Graphene Nanoplatelet Composites Fabricated via Supercritical-Fluid Treatment and Physical Foaming, ACS Appl. Mater. Interfaces 10(36) (2018) 30752-30761. https://doi.org/10.1021/acsami.8b10745

[11] B. Zhao, R. Wang, Y. Li, Y. Ren, X. Li, X. Guo, R. Zhang, C.B. Park, Dependence of electromagnetic interference shielding ability of conductive polymer composite foams with hydrophobic properties on cellular structure, J. Mater. Chem. C 8(22) (2020) 7401-7410. https://doi.org/10.1039/D0TC00987C

[12] X. Zhi, H.-B. Zhang, Y.-F. Liao, Q.-H. Hu, C.-X. Gui, Z.-Z. Yu, Electrically conductive polycarbonate/carbon nanotube composites toughened with micron-scale voids, Carbon 82

(2015) 195-204. https://doi.org/10.1016/j.carbon.2014.10.062

[13] B. Zhao, M. Hamidinejad, C. Zhao, R. Li, S. Wang, Y. Kazemi, C.B. Park, A versatile foaming platform to fabricate polymer/carbon composites with high dielectric permittivity and ultra-low dielectric loss, J. Mater. Chem. A 7(1) (2019) 133-140. https://doi.org/10.1039/C8TA05556D

[14] A. Ameli, P.U. Jung, C.B. Park, Through-plane electrical conductivity of injection-molded polypropylene/carbon-fiber composite foams, Compos. Sci. Technol. 76 (2013) 37-44. https://doi.org/10.1016/j.compscitech.2012.12.008

[15] M. Salari, N.D. Sansone, Z. Razzaz, S.M. Taromsari, M. Leroux, C.B. Park, P.C. Lee, Insights into synergy-induced multifunctional property enhancement mechanisms in hybrid graphene nanoplatelet reinforced polymer composites, Chem. Eng. J. 463 (2023) 142406. https://doi.org/10.1016/j.cej.2023.142406

[16] A. Ameli, M. Nofar, S. Wang, C.B. Park, Lightweight Polypropylene/Stainless-Steel Fiber Composite Foams with Low Percolation for Efficient Electromagnetic Interference Shielding, ACS Appl. Mater. Interfaces 6(14) (2014) 11091-11100. https://doi.org/10.1021/am500445g

[17] M. Okamoto, P.H. Nam, P. Maiti, T. Kotaka, T. Nakayama, M. Takada, M. Ohshima, A. Usuki, N. Hasegawa, H. Okamoto, Biaxial Flow-Induced Alignment of Silicate Layers in Polypropylene/Clay Nanocomposite Foam, Nano Lett. 1(9) (2001) 503-505. https://doi.org/10.1021/nl010051+

[18] A. Ameli, M. Nofar, C.B. Park, P. Pötschke, G. Rizvi, Polypropylene/carbon nanotube nano/microcellular structures with high dielectric permittivity, low dielectric loss, and low percolation threshold, Carbon 71 (2014) 206-217. https://doi.org/10.1016/j.carbon.2014.01.031

[19] V. Shaayegan, A. Ameli, S. Wang, C.B. Park, Experimental observation and modeling of fiber rotation and translation during foam injection molding of polymer composites, Composites, Part A 88 (2016) 67-74. https://doi.org/10.1016/j.compositesa.2016.05.013

[20] F. Du, J.E. Fischer, K.I. Winey, Effect of nanotube alignment on percolation conductivity in carbon nanotube/polymer composites, Phys. Rev. B 72(12) (2005) 121404.

https://doi.org/10.1103/PhysRevB.72.121404

[21] S. Gong, Z.H. Zhu, S.A. Meguid, Anisotropic electrical conductivity of polymer composites with aligned carbon nanotubes, Polymer 56 (2015) 498-506. https://doi.org/10.1016/j.polymer.2014.11.038

[22] S. Wang, A. Ameli, V. Shaayegan, Y. Kazemi, Y. Huang, H.E. Naguib, C.B. Park, Modelling of Rod-Like Fillers' Rotation and Translation near Two Growing Cells in Conductive Polymer Composite Foam Processing, Polymers 10(3) (2018) 261.

[23] S. Wang, Y. Huang, E. Chang, C. Zhao, A. Ameli, H.E. Naguib, C.B. Park, Evaluation and modeling of electrical conductivity in conductive polymer nanocomposite foams with multiwalled carbon nanotube networks, Chem. Eng. J. 411 (2021) 128382. https://doi.org/10.1016/j.cej.2020.128382

[24] S. Wang, Y. Huang, C. Zhao, E. Chang, A. Ameli, H.E. Naguib, C.B. Park, Theoretical modeling and experimental verification of percolation threshold with MWCNTs' rotation and translation around a growing bubble in conductive polymer composite foams, Compos. Sci. Technol. 199 (2020) 108345. https://doi.org/10.1016/j.compscitech.2020.108345

[25] Y. Liu, Y. Guan, J. Lin, Y. Li, J. Zhai, X. Li, Mold-opening foam injection molded strong PP/CF foams with high EMI shielding performance, J. Mater. Res. Technol. 17 (2022) 700-712. https://doi.org/10.1016/j.jmrt.2022.01.049

[26] J. Li, G. Zhang, H. Zhang, X. Fan, L. Zhou, Z. Shang, X. Shi, Electrical conductivity and electromagnetic interference shielding of epoxy nanocomposite foams containing functionalized multi-wall carbon nanotubes, Appl. Surf. Sci. 428 (2018) 7-16. https://doi.org/10.1016/j.apsusc.2017.08.234

[27] N. Athanasopoulos, A. Baltopoulos, M. Matzakou, A. Vavouliotis, V. Kostopoulos, Electrical conductivity of polyurethane/MWCNT nanocomposite foams, Polym. Compos. 33(8) (2012) 1302-1312. https://doi.org/10.1002/pc.22256

[28] Q. Ren, M. Wu, Z. Weng, X. Zhu, W. Li, P. Huang, L. Wang, W. Zheng, M. Ohshima, Promoted formation of stereocomplex in enantiomeric poly(lactic acid)s induced by cellulose nanofibers, Carbohydr. Polym. 276 (2022) 118800. https://doi.org/10.1016/j.carbpol.2021.118800

[29] Q. Ren, M. Wu, L. Wang, W. Zheng, Y. Hikima, T. Semba, M. Ohshima, Cellulose nanofiber reinforced poly (lactic acid) with enhanced rheology, crystallization and foaming ability, Carbohydr. Polym. 286 (2022) 119320. https://doi.org/10.1016/j.carbpol.2022.119320

[30] B. Notario, J. Pinto, M.A. Rodriguez-Perez, Nanoporous polymeric materials: A new class of materials with enhanced properties, Prog. Mater. Sci. 78-79 (2016) 93-139. https://doi.org/10.1016/j.pmatsci.2016.02.002

[31] M. Wu, F. Wu, Q. Ren, X. Jia, H. Luo, B. Shen, L. Wang, W. Zheng, Tunable electromagnetic interference shielding performance of polypropylene/carbon black composites via introducing microcellular structure, Compos. Commun. 36 (2022) 101363. https://doi.org/10.1016/j.coco.2022.101363

[32] P. Gong, P. Buahom, M.-P. Tran, M. Saniei, C.B. Park, P. Pötschke, Heat transfer in microcellular polystyrene/multi-walled carbon nanotube nanocomposite foams, Carbon 93 (2015) 819-829. https://doi.org/10.1016/j.carbon.2015.06.003

[33] L.J. Gibson, M.F. Ashby, Cellular Solids: Structure and Properties, 2 ed., Cambridge University Press, Cambridge, 1997.

[34] X. Jia, Y. Li, B. Shen, W. Zheng, Evaluation, fabrication and dynamic performance regulation of green EMI-shielding materials with low reflectivity: A review, Composites, Part B 233 (2022) 109652. https://doi.org/10.1016/j.compositesb.2022.109652

[35] B. Krause, C. Barbier, K. Kunz, P. Pötschke, Comparative study of singlewalled, multiwalled, and branched carbon nanotubes melt mixed in different thermoplastic matrices, Polymer 159 (2018) 75-85. https://doi.org/10.1016/j.polymer.2018.11.010

[36] J. Wang, Y. Kazemi, S. Wang, M. Hamidinejad, M.B. Mahmud, P. Pötschke, C.B. Park, Enhancing the electrical conductivity of PP/CNT nanocomposites through crystal-induced volume exclusion effect with a slow cooling rate, Composites, Part B 183 (2020) 107663. https://doi.org/10.1016/j.compositesb.2019.107663

[37] J. Zhao, G. Wang, C. Wang, C.B. Park, Ultra-lightweight, super thermal-insulation and strong PP/CNT microcellular foams, Compos. Sci. Technol. 191 (2020) 108084. https://doi.org/10.1016/j.compscitech.2020.108084

[38] L. Wang, M. Wu, Q. Ren, Z. Weng, W. Li, X. Zhu, W. Zheng, X. Yi, Strong and high void

fraction PP/CNS nanocomposite foams fabricated by core-back foam injection molding, J. Appl. Polym. Sci. n/a(n/a) (2022) e53521. https://doi.org/10.1002/app.53521

[39] J.S. Colton, N.P. Suh, Nucleation of microcellular foam: Theory and practice, Polym. Eng. Sci. 27(7) (1987) 500-503. https://doi.org/10.1002/pen.760270704

[40] B. Zhao, M. Hamidinejad, S. Wang, P.W. Bai, R.C. Che, R. Zhang, C.B. Park, Advances in electromagnetic shielding properties of composite foams, J. Mater. Chem. A 9(14) (2021) 8896-8949. https://doi.org/10.1039/d1ta00417d

[41] X.-B. Xu, Z.-M. Li, L. Shi, X.-C. Bian, Z.-D. Xiang, Ultralight Conductive Carbon-Nanotube–Polymer Composite, Small 3(3) (2007) 408-411. https://doi.org/10.1002/smll.200600348

[42] M.T.Q.S. da Silva, M. do Rocio Cardoso, C.M.P. Veronese, W. Mazer, Tortuosity: A brief review, Materials Today: Proceedings 58 (2022) 1344-1349. https://doi.org/10.1016/j.matpr.2022.02.228

[43] Y. Li, J. Liu, S. Wang, L. Zhang, B. Shen, Self-templating graphene network composites by flame carbonization for excellent electromagnetic interference shielding, Composites, Part B 182 (2020) 107615. https://doi.org/10.1016/j.compositesb.2019.107615

[44] W.-L. Song, M.-S. Cao, L.-Z. Fan, M.-M. Lu, Y. Li, C.-Y. Wang, H.-F. Ju, Highly ordered porous carbon/wax composites for effective electromagnetic attenuation and shielding, Carbon 77 (2014) 130-142. https://doi.org/10.1016/j.carbon.2014.05.014

[45] B. Shen, Y. Li, W. Zhai, W. Zheng, Compressible Graphene-Coated Polymer Foams with Ultralow Density for Adjustable Electromagnetic Interference (EMI) Shielding, ACS Appl. Mater. Interfaces 8(12) (2016) 8050-8057. https://doi.org/10.1021/acsami.5b11715

[46] G. Wang, G. Zhao, S. Wang, L. Zhang, C.B. Park, Injection-molded microcellular PLA/graphite nanocomposites with dramatically enhanced mechanical and electrical properties for ultra-efficient EMI shielding applications, J. Mater. Chem. C 6(25) (2018) 6847-6859. https://doi.org/10.1039/c8tc01326h

[47] F. Zou, J. Chen, X. Liao, P. Song, G. Li, Efficient electrical conductivity and electromagnetic interference shielding performance of double percolated polymer composite foams by phase coarsening in supercritical CO2, Compos. Sci. Technol. 213 (2021) 108895.

https://doi.org/10.1016/j.compscitech.2021.108895

[48] J. Chen, X. Liao, W. Xiao, J. Yang, Q. Jiang, G. Li, Facile and Green Method To Structure Ultralow-Threshold and Lightweight Polystyrene/MWCNT Composites with Segregated Conductive Networks for Efficient Electromagnetic Interference Shielding, ACS Sustainable Chem. Eng. 7(11) (2019) 9904-9915. https://doi.org/10.1021/acssuschemeng.9b00678

[49] Y. Zhan, M. Oliviero, J. Wang, A. Sorrentino, G.G. Buonocore, L. Sorrentino, M. Lavorgna, H. Xia, S. Iannace, Enhancing the EMI shielding of natural rubber-based supercritical CO2 foams by exploiting their porous morphology and CNT segregated networks, Nanoscale 11(3) (2019) 1011-1020. https://doi.org/10.1039/C8NR07351A

[50] H. Zhang, G. Zhang, J. Li, X. Fan, Z. Jing, J. Li, X. Shi, Lightweight, multifunctional microcellular PMMA/Fe3O4@MWCNTs nanocomposite foams with efficient electromagnetic interference shielding, Composites, Part A 100 (2017) 128-138. https://doi.org/10.1016/j.compositesa.2017.05.009

[51] Y. Yang, M.C. Gupta, K.L. Dudley, R.W. Lawrence, Novel Carbon Nanotube−Polystyrene Foam Composites for Electromagnetic Interference Shielding, Nano Lett. 5(11) (2005) 2131-2134. https://doi.org/10.1021/nl051375r

[52] T. Kuang, L. Chang, F. Chen, Y. Sheng, D. Fu, X. Peng, Facile preparation of lightweight high-strength biodegradable polymer/multi-walled carbon nanotubes nanocomposite foams for electromagnetic interference shielding, Carbon 105 (2016) 305-313. https://doi.org/10.1016/j.carbon.2016.04.052

[53] H. Zhang, G. Zhang, Q. Gao, M. Tang, Z. Ma, J. Qin, M. Wang, J.-K. Kim, Multifunctional microcellular PVDF/Ni-chains composite foams with enhanced electromagnetic interference shielding and superior thermal insulation performance, Chem. Eng. J. 379 (2020) 122304. https://doi.org/10.1016/j.cej.2019.122304

Chapter 7: Enhanced sound insulation properties of PP/mica foams by controlling cell structure

In this chapter, a brief introduction to polymeric foams for sound insulation applications and methods of soundproofing performance enhancement are briefly introduced. PP/mica composite foams with different VFs and cell sizes were fabricated using core-back FIM technique to investigate the relationship between cell structure and sound insulation performance. Discussions on sound insulation properties and the enhancing mechanism of polymer foams are presented.

7.1. Abstract

The performance of a sound insulation foam is highly dependent on the cell structure. In this study, we prepared PP/mica composite foams with different VFs and cell sizes using core-back FIM. The results showed that increasing the VF (the sample thickness increased but the sample density remained constant) could enhance the STL from 16.8 dB for PP solid to 29.9 dB for PP foam with 75% VF. In addition, Reducing the cell size and adding mica could also improve the STL due to the increase in reflection and scattering of sound waves in cells. This study offers a convenient strategy to obtain polymeric foams with excellent sound insulation properties.

7.2. Introduction

Due to the fast development of traffic systems and modern industry, noise pollution has become a major problem of environmental pollution, and is also harmful to personal healthiness[1, 2]. Thus, various sound absorbing and sound insulation material, such as metal, concrete material, fibers, and polymer materials, were developed in noise control engineering[3-5]. Among those soundproof and damping materials, polymer materials have gained more attention thanks to their advantages like lightweight and good processibility. However, the soundproofing performance of most polymer materials needs to be enhanced to meet the requirements of practical applications due to their low

density and modulus, according to the mass and stiffness laws[6, 7].

Adding inorganic fillers was a good method to improve the sound insulation performance of polymer materials by improving their density and modulus[8-13]. For example, Liang et al.[10-14] investigated the soundproofing properties of PVC/glass bead (GB), PVC/calcium carbonate ($CaCO_3$), and PP/HGB composite, and the results showed that with the increase in the filler contents, the density of composites increased, leading to the enhancement of sound insulation properties according to the mass law. Besides, they proposed a new transmission loss equation by investigating the sound insulation mechanism of polymer/inorganic filler composites. Lee et al.[14] found that the introduction of carbon nanotube (CNT) into acrylonitrile butadiene styrene (ABS) could improve the stiffness of ABS/CNT composite, leading to the improvement of soundproofing properties.

Incorporating cell structure into polymer is another way to enhance the sound insulation properties. Generally, the sound insulation properties improved with the increase of VF, since the thickness of the tested samples was also increased, which would prolong the transmission pathway of sound waves[15, 16]. Zhao et al. studied the sound insulation performance of PP/PTFE foams, and found that when the VF was fixed, increasing the PTFE content could cause the reduction of cell size, leading to the improvement of sound insulation properties. However, we cannot get the relationship between cell size and sound insulation performance, because the influence of PTFE content cannot be eliminated. To

our best knowledge, the effect of cell size on sound insulation properties has not been investigated so far.

In this work, PP/mica composite foams with different VF and cell sizes were successfully prepared using core-back FIM. The effect of VF, mica content and cell size on sound insulation properties were systematically investigated. Besides, the mechanism of improving the sound insulation performance of PP/mica composite foams was also discussed.

7.3. Experimental section

7.3.1. Materials

A commercial-grade long chain branched PP (WB140HMS), with a melt flow rate of 2.1 g/10 min (ISO 1133), supplied by Borealis Ltd. Mica with 2000 meshes was purchased from Chuzhou Grea Minerals Co., Ltd. N_2 (99% purity) provided by Huayu Gas Inc., China, was selected as the physical blowing agent.

7.3.2. Blend preparation

Before blending, PP pellets and mica were first dried at 80 ℃ overnight to remove any moisture. The dried PP pellets and mica were compounded by using a corotating twin-screw extruder (SHL-52, Nanjing Haili Extrusion Equipment Co. Ltd., China). The temperature profile was set as 170-220 ℃. Various amounts of mica (0, 10, and 30 wt%) were added into the extruder during the compounding process, and these composites containing various mica content

were referred to as PP, PP10, PP30, respectively.

7.3.3. Core-back FIM

Before compounding, both the PP and mica were dried at 80 ℃ for 8 h to remove moisture. PP/mica composites with mica content of 0, 10 and 30 wt% were compounded using a twin screw extruder (AK 36, Nanjing KY Chemical Machinery Co. Ltd., China) at 170–220 ℃. A 100-ton foaming injection molding (FIM) machine (Systec 100/420-310C, Demag Plastics Group, Germany), equipped with a Mucell SCF delivery system (T100, Trexel Inc., USA) was applied to conduct the core-back FIM experiments. A rectangular mold cavity ($150 \times 110 \times 2$ mm^3) was applied in this study. The detailed processing parameters are listed in Table 7-1.

Table 7-1. Processing parameters used for the FIM experiments.

PARAMETERS	SOLID	FOAM
Melt temperature (℃)	230	230
Mold temperature (℃)	80	80
Injection speed (mm/s)	120	120
Injection pressure (MPa)	100	100
Back pressure (MPa)	20	20
Packing pressure (MPa)	40	40
Dwelling time (sec)	10	5–12
Core-back distance (mm)	N/A	2–6
N_2 content (wt%)	N/A	0.6–1

7.3.4. SEM

A Zesis EVO18 SEM was used to examine the cell structure of PP/CB

nanocomposite foams. Before the observation, the foamed samples were cryogenically fractured in liquid nitrogen, and then, sputtered a layer of platinum on the surface. The morphological parameters were calculated from the SEM micrographs. The cell nucleation density, N_0, was defined by equation[17]:

$$N_0 = (\frac{n}{A})^{3/2}\phi \tag{7-1}$$

where n is the number of cells, A is the area of the SEM micrograph, Φ is the volume expansion of the polymer foam, which can be calculated using equation[17]:

$$\Phi = \frac{\rho_p}{\rho_f} \tag{7-2}$$

where ρ_p and ρ_f were the density of the unfoamed and foamed polymer, respectively, and those densities can be obtained using the water displacement method.

7.3.5. Dynamic mechanical analysis (DMA)

A DMA instrument (Q800, TA, USA) was conducted to evaluate the dynamic thermos-mechanical properties of the samples in a single cantilever mode. The dimensions of the test sample were 10×2×30 mm^3. The test temperature ranged from -50 to 150 ℃ at a rate of 3 ℃/min and a frequency of 1 Hz.

7.3.6. Characterization of sound insulation

Sound insulation properties of the samples were investigated by STL, which is defined as follows:

$$STL = 10 \log_{10} \frac{E_i}{E_t} \quad (7\text{-}3)$$

where E_i and E_t are the incident sound energy and transmitted sound energy, respectively. For certain incident sound waves, the bigger the STL value, the better the sound insulation properties.

The STL values were measured according to ASTM E2611-09 by a four-microphone impedance tube (BSAW Technology Co., Beijing). This instrument includes two kinds of tubes: a small tube with a diameter of 30 mm was used for the measurement of high frequencies sound waves (1000–6300 Hz); and a large tube with a diameter of 60 mm tube was used for the measurement of low and medium frequencies sound waves (64–1600 Hz). The samples with constant mica content had the same weight but different thicknesses, and the samples' thicknesses of 2, 4, 6, and 8 mm corresponded to the VFs of 0%, 50%, 67%, and 75%. Each value represented an average of three measurements for each test sample.

7.4. Results and discussion

7.4.1. Mica dispersion in PP matrix

Fig. 7-1 shows the SEM image of mica and its dispersion in PP/mica foam. The particle sizes were in the range of 4–25 μm. It is clear that the mica platelets were oriented along the boundary of the cell (Fig. 7-1b') due to the biaxial flow during the foaming process [18].

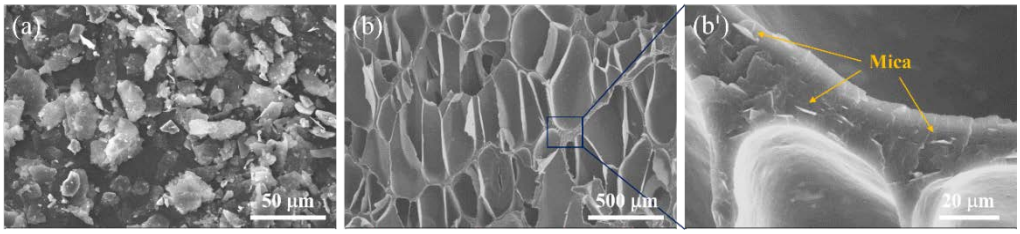

Fig. 7-1. SEM images of (a) mica particles and (b) PP/mica composite foam. (b') is the magnification of one section of (b).

7.4.2. Cell structure

Generally, foams prepared using core-back FIM technology can be divided into two layers including the skin layer and core layer (foamed layer)[19, 20]. Fig. 7-2 and 6-3 show SEM images of core and surface layers of PP/mica composite foams with various VFs, respectively. The foaming process was performed at a fixed N_2 content of 0.6 wt%. By changing the core-back distance to 2, 4, 6 mm, the foams with VFs of 50, 67 and 75% were obtained, respectively. Due to the weak melt strength of PP, all PP foams showed poor cell structure with cell size of over 500 μm (Fig. 7-3a). However, adding 10 wt% of mica into the PP matrix, PP10 mica foams exhibited a much better cell structure compared with pure PP foams, as shown in Fig. 7-2. With the further increase of mica content, cell size gradually decreased, and the cell size distribution became narrower. For instance, as for PP and PP/mica composite foams with a VF of 67%, when mica content first increased to 10 wt%, the cell size dramatically decreased from 638 μm for PP foam to 200 μm for PP10 foam (Fig. 7-4a), and cell density improved from

7.4×10^3 cells/cm^3 to 3.0 $\times10^5$ cells/cm^3 (Fig. 7-4b). With the further rising of mica content, the cell size of PP30 foam slowly reduced to 128 μm, and cell density improved to 9.8×10^5 cells/cm^3 simultaneously. Obviously, this significant improvement of the cell structure of PP/mica composite foams was caused by the addition of mica. Mica could act as a heterogeneous NA to enhance the cell nucleation rate during foaming process[21, 22]. Thus, PP/mica composite foams with small cell sizes can be obtained, and the cell size distribution became more uniform with the increase of mica content. It is clearly shown that the skin layers of pure PP foam and PP/mica composite foams were completely unfoamed, and the skin thicknesses were all in the range of 380 – 510 μm, as shown in Fig. 7-4c.

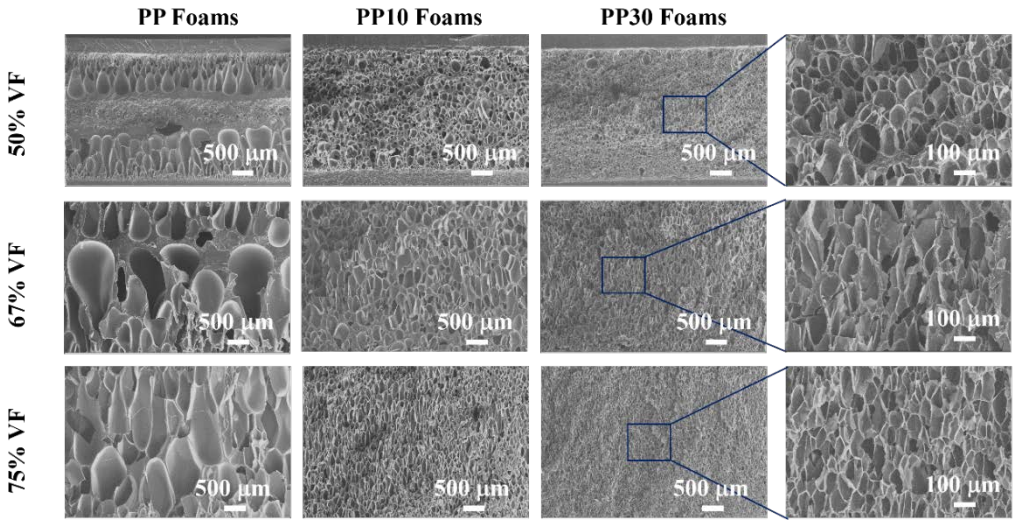

Fig. 7-2. SEM images of core layers of pure PP and PP/mica composite foams at various VFs.

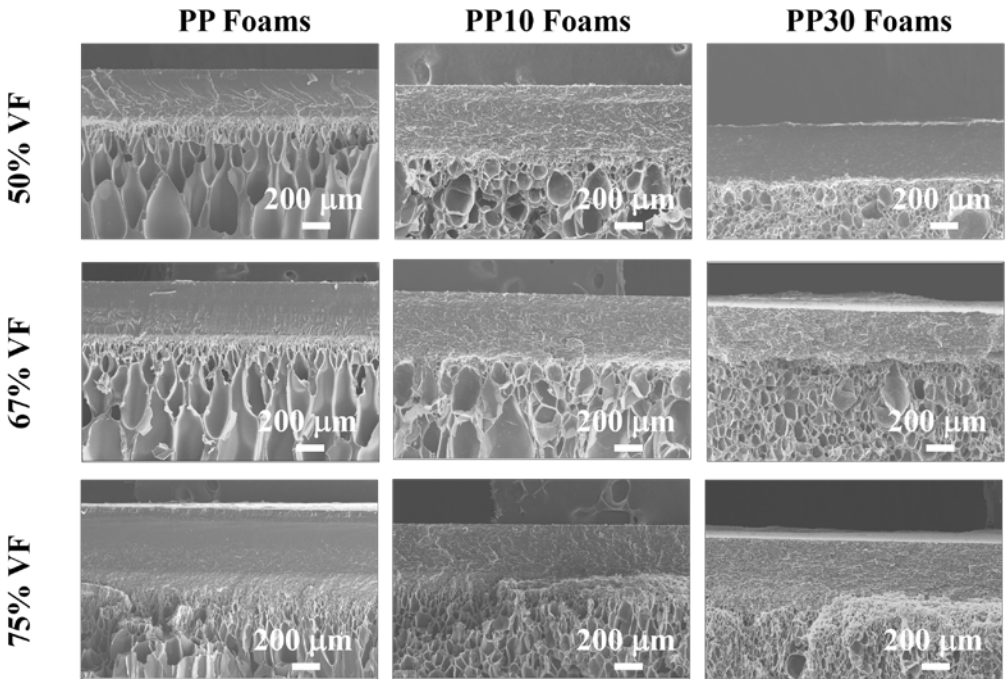

Fig. 7-3. SEM images of surface layers of pure PP and PP/mica composite foams at various VFs.

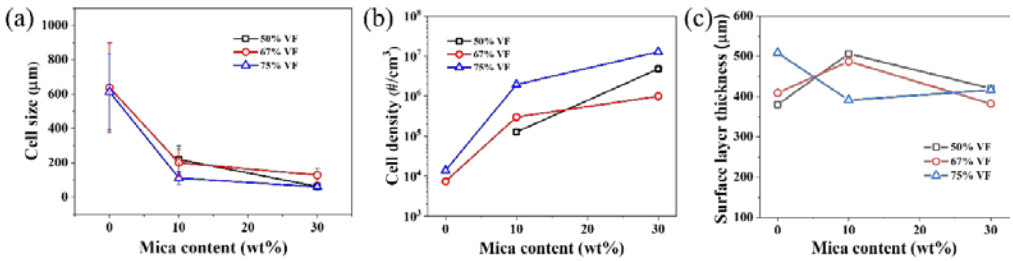

Fig. 7-4. Changes of (a) cell size, (b) cell density, and (c) skin layer thickness of pure PP and PP/mica composite foams at various VFs.

Since the cell structure was strongly related to those applied processing parameters, such as N_2 content and dwelling time [23]. To obtain PLA/PBAT foams with different cell sizes, various N_2 content and dwelling times were applied. Fig. 7-5 shows SEM images of the core layers of PP and PP30

composite foams with various cell sizes at the fixed VF of 67%. To further characterize the cell structure, the cell size dependence of cell density for pure PP foams and PP30 foams are shown in Fig. 7-7a and 7-7b, respectively. Increasing the cell size would lead to the reduction of cell density. For instance, when the cell size of PP foams increased from 32 to 638 μm, the cell density significantly decreased from 7.2×10^{7} to 7.4×10^{3} cells/cm^{3}, revealing four orders of magnitude reduction. Thus, PP foams with cell sizes varying from 638 to 32 μm and PP30 foams with cell sizes ranging from 231 to 96 μm were successfully prepared. Those foams can be applied to study the relationship between cell size and sound insulation properties. According to SEM images of the skin layers of pure PP foam and PP30 foams displayed in Fig. 7-6, and the calculated results (Fig. 7-7c and 7-7d) exhibited that the skin thicknesses of pure PP foams were in the range of 420–500 μm, while that of PP30 foams were in the range of 380–460 μm.

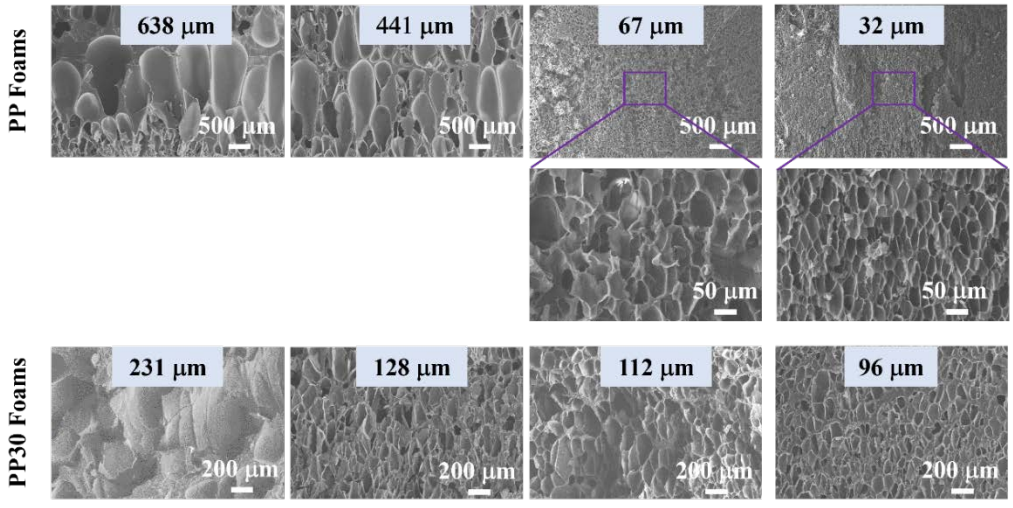

Fig. 7-5. SEM images of core layers of pure PP and PP30 foams with various cell sizes

at a fixed VF of 67%.

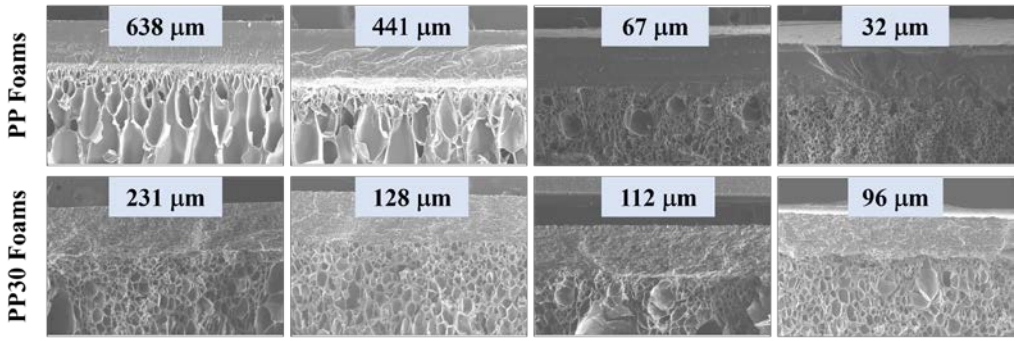

Fig. 7-6. SEM images of surface layers of pure PP and PP30 foams with various cell sizes at a fixed VF of 67%.

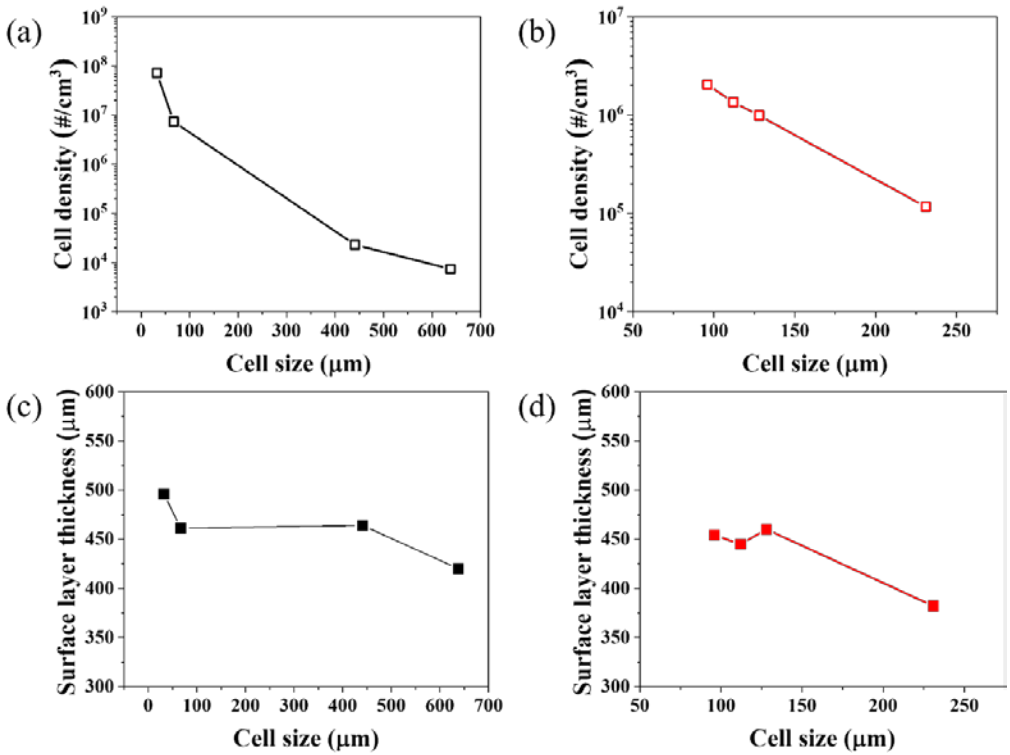

Fig. 7-7. (a, b) Cell size dependence of cell density for (a) pure PP foams and (b) PP30 foams. (c, d) Cell size dependence of cell wall thickness for (c) pure PP foams and (d) PP30 foams. VF is fixed at 67%.

7.4.3. Sound insulation properties

The STL values were tested from 64 to 6300 Hz and the average STL value was obtained from the 1/3 octave average value [24, 25]. The average STL values of PP and PP/mica composite foams are shown in Fig. 7-8 and 7-10.

In the typical curves of STL versus sound frequency of PP and PP foams (Fig. 7-8a), the lowest STL value appears at the resonance frequency of 400 Hz for solid PP. The resonance frequency shifted to a higher frequency with the increase of VF, and the resonance frequency of PP foam with 75% VF reached up to 1600 Hz. PP/mica composite foams showed a similar changing trend. Fig. 7-8d shows the average STL values of PP and PP/mica composite foams under different VF. By increasing the mica content, the average STL increased for both solid and foamed samples. For example, the average STL improved from 16.8 dB for PP solid to 23.2 dB for PP30 solid. It can be attributed to the fact that the stiffness and density of the material can significantly affect the sound insulation property [14, 26, 27]. After introducing mica into the PP matrix, the density increased from 0.9 g/cm^3 for pure PP to 1.12 g/cm^3 for PP30 (Fig. 7-9a). In addition, it is clear that the PP30 solid depicted the highest storage modulus over the entire test temperature range (Fig. 7-9b). It implies that the stiffness improved with a higher mica content. These two factors enhanced the sound insulation properties of solid samples. Fig. 7-9c shows the loss modulus of solid samples as a function of temperature. PP30 solid sample showed the highest loss modulus, indicating

that PP30 solid foam endows more dissipation of sound energy during the sound wave propagation [28, 29].

Introducing cell structure into PP and PP/mica composites could also improve the STL. The STL increased from 16.8 dB for PP solid to 29.9 dB for PP foam with 75% VF, for instance. It is mainly caused by the increase in thickness of test samples [30]. It should be noticed that all the PP solid and PP foams showed the same mass, but the thickness varied from 2 mm for the PP solid to 8 mm for the PP foam with 75% VF.

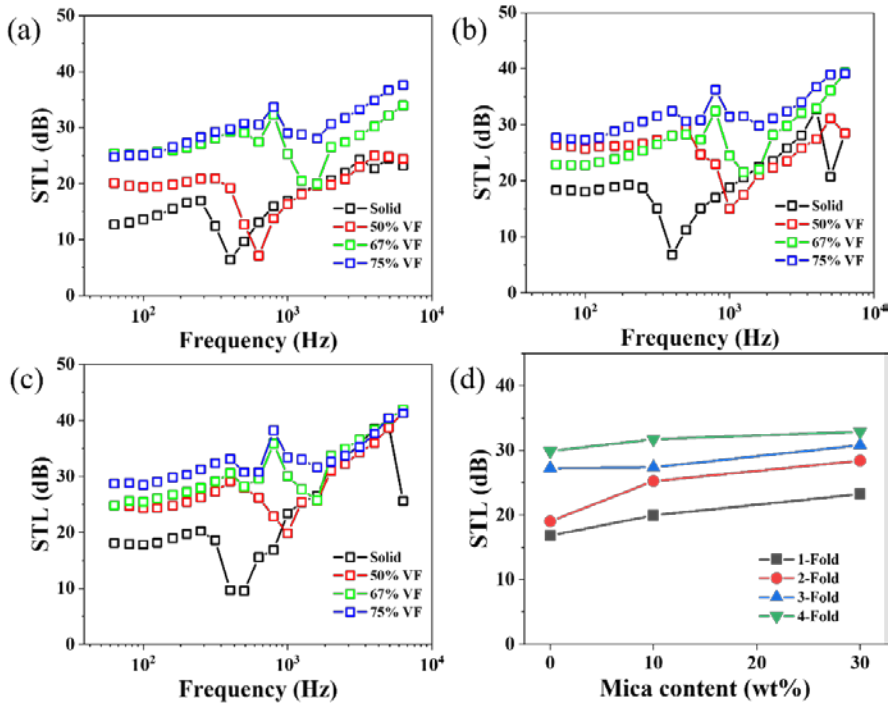

Fig. 7-8. Sound insulation properties of PP and PP/mica composite foams under different VF: (a) PP foams, (b) PP10 foams, (c) PP30 foams, and (d) average STL value.

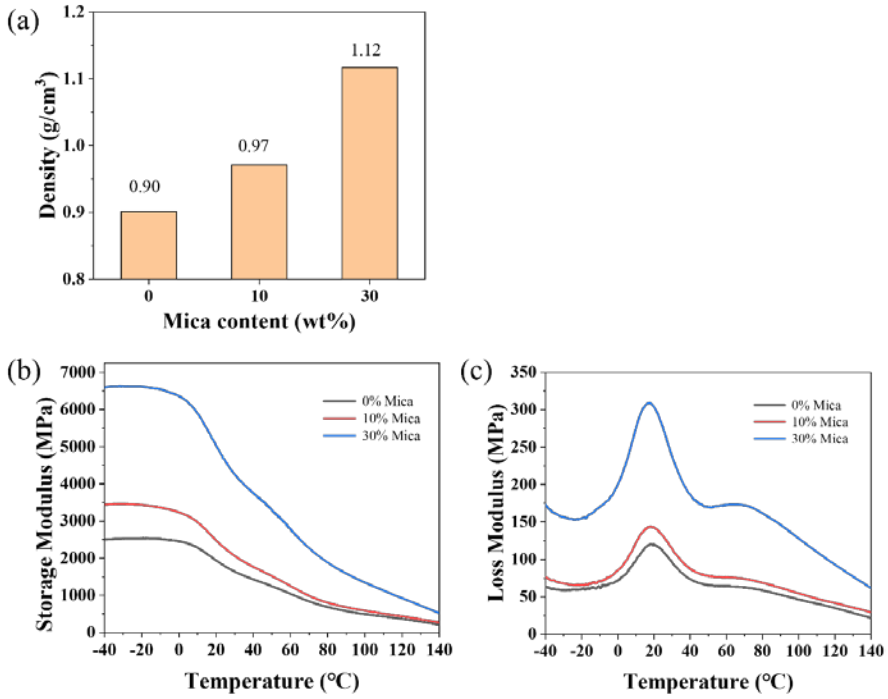

Fig. 7-9. (a) Volume density of PP and PP/mica composites. (b) The storage modulus and (c) loss modulus-temperature curves of PP and PP/mica composites.

The sound insulation properties and the average STL values of PP and PP/mica composite foams with different cell sizes are shown in Fig. 7-10. All the samples had the same VF of 67% (thickness was 6 mm). With the decrease of cell size from 638 to 32 μm, the average STL of PP foam improved from 27.2 to 33.1 dB. For PP30 foams, the average STL improved from 29.7 to 33.1 dB by reducing the cell size from 231 to 96 μm. The results strongly proved that reducing cell size could improve the sound insulation properties, and it can be explained further through Fig. 7-11a. When the incident sound energy faces the material, part of the sound energy is reflected, and the other part of the sound energy is converted into mechanical vibration and penetrates the material, so the sound energy is also decreased. By reducing the cell size, the transmission path of the

sound waves became longer, as shown in Fig. 7-11a. The scattering and the reflection of sound waves were much more violent inside the smaller cells (orange arrow), and it led to the vibration acceleration of sound waves inside small pores during the transmission process of sound waves [31, 32].

Obviously, introducing mica into PP foam could enhance the sound insulation property, as shown in Fig. 7-10c. It can be explained through Fig. 7-11b. First, the interfaces between mica and the PP matrix could scatter, diffract and refract sound wave energy, thus enhancing sound energy's dissipation. Second, adding mica into the PP matrix would also increase the density and stiffness of PP/mica foams, leading to the enhanced STL.

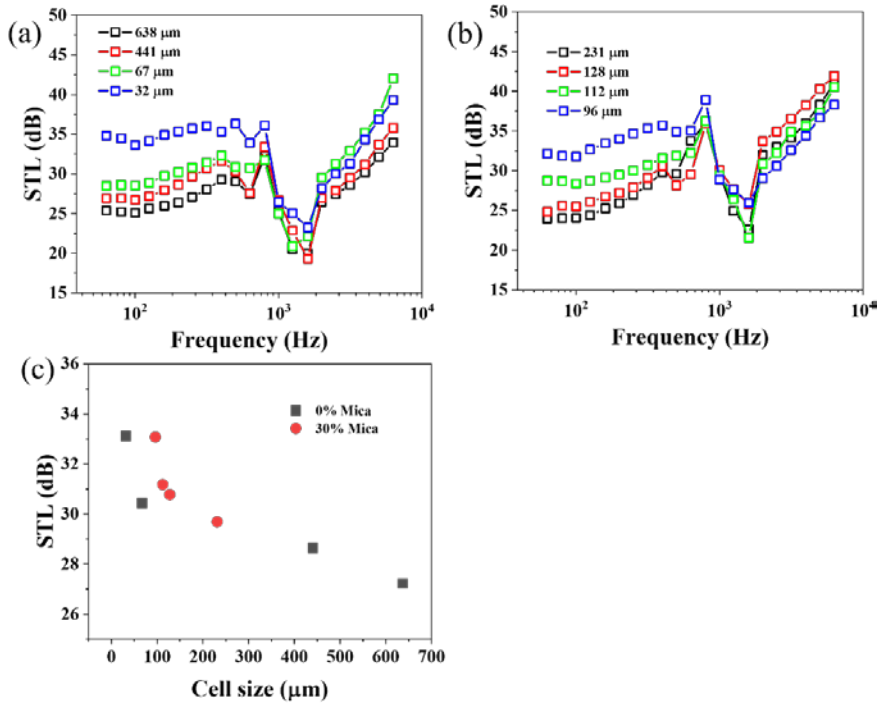

Fig. 7-10. Sound insulation properties of PP and PP/mica composite foams under different cell sizes: (a) PP foams, (b) PP30 foams, and (c) average STL value.

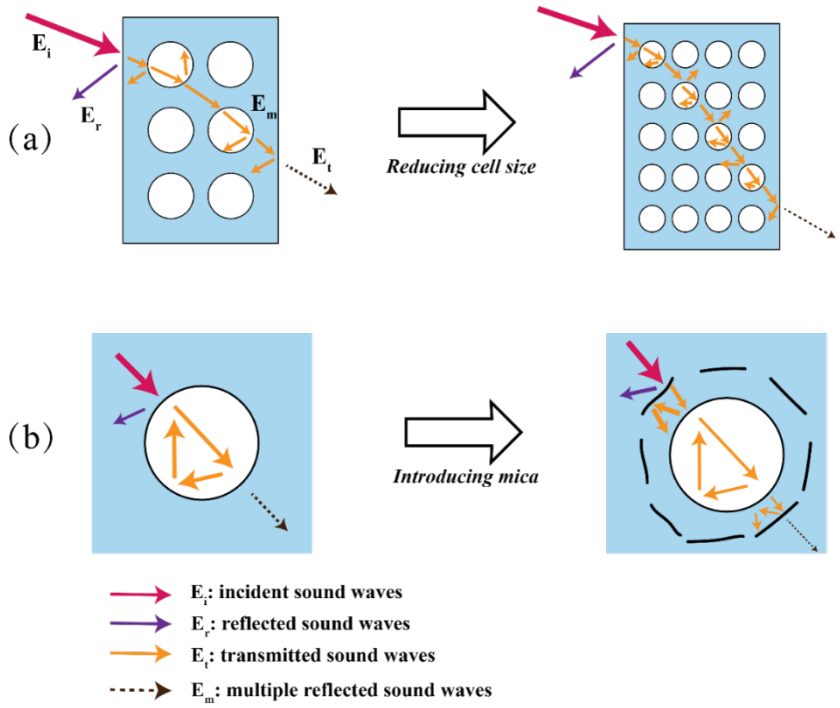

Fig. 7-11. The schematic diagram of sound waves transmission path by the effect of (a) reducing cell size and (b) introducing mica.

7.5. Conclusion

This work investigated the effects of VF, cell size and mica content on the sound insulation properties of PP/mica foams. First, the introduction of cell structure could significantly improve the STL of PP foams from 16.8 dB to 29.9 dB due to the prolonged sound transimission path. Forther more, reducing cell size or adding mica into PP matrix could enhance the scattering and reflection of sound waves in the foams, resulting the improved STL of PP foams. This study provides a feasible method for preparing good sound insulation polymeric foams.

7.6. References

[1] D. Chen, J. Li, J. Ren, Study on sound absorption property of ramie fiber reinforced poly(l-

lactic acid) composites: Morphology and properties, Composites, Part A 41(8) (2010) 1012-1018. https://doi.org/10.1016/j.compositesa.2010.04.007

[2] W. Fang, Y. Fei, H. Lu, J. Jin, M. Zhong, P. Fan, J. Yang, Z. Fei, F. Chen, T. Kuang, Enhanced sound insulation and mechanical properties based on inorganic fillers/thermoplastic elastomer composites, J. Thermoplast. Compos. Mater. 32(7) (2019) 936-950. https://doi.org/10.1177/0892705718766382

[3] A. Patnaik, M. Mvubu, S. Muniyasamy, A. Botha, R.D. Anandjiwala, Thermal and sound insulation materials from waste wool and recycled polyester fibers and their biodegradation studies, Energy Build. 92 (2015) 161-169. https://doi.org/10.1016/j.enbuild.2015.01.056

[4] X.X. Wang, H.K. Peng, T.T. Li, C.W. Lou, Y.T. Wang, J.H. Lin, Preparation and property evaluations of zeolite rigid foam composites, Polym. Compos. 40(11) (2019) 4175-4185. https://doi.org/10.1002/pc.25278

[5] A.E. Tiuc, O. Nemeş, H. Vermeşan, A.C. Toma, New sound absorbent composite materials based on sawdust and polyurethane foam, Composites, Part B 165 (2019) 120-130. https://doi.org/10.1016/j.compositesb.2018.11.103

[6] D.J. Oldham, S.N. Hillarby, The acoustical performance of small close fitting enclosure, part 1: Theoretical models, J. Sound Vib. 150(2) (1991) 261-281. https://doi.org/10.1016/0022-460X(91)90620-Y

[7] A. Berry, J. Nicolas, Structural acoustics and vibration behavior of complex panels, Appl. Acoust. 43(3) (1994) 185-215. https://doi.org/10.1016/0003-682X(94)90047-7

[8] Y. Yang, Z. Chen, T. Xu, R. Han, D. Emefa Awuye, Sound insulation and hydrophobic properties of phenolic resin modified melamine foam: role of micro-morphology, Mater. Res. Express 6(7) (2019) 075331. https://doi.org/10.1088/2053-1591/ab17bb

[9] Y. Fei, W. Fang, M. Zhong, J. Jin, P. Fan, J. Yang, Z. Fei, F. Chen, T. Kuang, Morphological Structure, Rheological Behavior, Mechanical Properties and Sound Insulation Performance of Thermoplastic Rubber Composites Reinforced by Different Inorganic Fillers, Polymers 10(3) (2018) 276.

[10] J.-Z. Liang, X.-H. Jiang, Sound insulation in polymer/inorganic particle composites. I. Theoretical model, J. Appl. Polym. Sci. 125(1) (2012) 676-681.

https://doi.org/10.1002/app.34824

[11] J.-Z. Liang, X.-H. Jiang, Soundproofing effect of polypropylene/inorganic particle composites, Composites, Part B 43(4) (2012) 1995-1998. https://doi.org/10.1016/j.compositesb.2012.02.020

[12] J.-Z. Liang, Prediction of sound transmission losses for polymer/inorganic particle composites, Polym. Compos. 36(11) (2015) 2059-2065. https://doi.org/10.1002/pc.23116

[13] J.-Z. Liang, B. Zhu, Estimation of sound transmission loss of polymer/hollow microsphere composites, J. Compos. Mater. 50(15) (2016) 2137-2142. https://doi.org/10.1177/0021998315602943

[14] J.-C. Lee, Y.-S. Hong, R.-G. Nan, M.-K. Jang, C.S. Lee, S.-H. Ahn, Y.-J. Kang, Soundproofing effect of nano particle reinforced polymer composites, J. Mech. Sci. Technol. 22(8) (2008) 1468-1474. https://doi.org/10.1007/s12206-008-0419-4

[15] D. Jahani, A. Ameli, M. Saniei, W. Ding, C.B. Park, H.E. Naguib, Characterization of the Structure, Acoustic Property, Thermal Conductivity, and Mechanical Property of Highly Expanded Open-Cell Polycarbonate Foams, Macromol. Mater. Eng. 300(1) (2015) 48-56. https://doi.org/10.1002/mame.201400125

[16] J. Zhao, G. Wang, Z. Chen, Y. Huang, C. Wang, A. Zhang, C.B. Park, Microcellular injection molded outstanding oleophilic and sound-insulating PP/PTFE nanocomposite foam, Composites, Part B 215 (2021) 108786. https://doi.org/10.1016/j.compositesb.2021.108786

[17] P. Gong, P. Buahom, M.-P. Tran, M. Saniei, C.B. Park, P. Pötschke, Heat transfer in microcellular polystyrene/multi-walled carbon nanotube nanocomposite foams, Carbon 93 (2015) 819-829. https://doi.org/10.1016/j.carbon.2015.06.003

[18] M. Okamoto, P.H. Nam, P. Maiti, T. Kotaka, T. Nakayama, M. Takada, M. Ohshima, A. Usuki, N. Hasegawa, H. Okamoto, Biaxial Flow-Induced Alignment of Silicate Layers in Polypropylene/Clay Nanocomposite Foam, Nano Lett. 1(9) (2001) 503-505. https://doi.org/10.1021/nl010051+

[19] A. Huang, X. Peng, L.-S. Turng, In-situ fibrillated polytetrafluoroethylene (PTFE) in thermoplastic polyurethane (TPU) via melt blending: Effect on rheological behavior, mechanical properties, and microcellular foamability, Polymer 134 (2018) 263-274.

https://doi.org/10.1016/j.polymer.2017.11.053

[20] G. Wang, G. Zhao, G. Dong, Y. Mu, C.B. Park, G. Wang, Lightweight, super-elastic, and thermal-sound insulation bio-based PEBA foams fabricated by high-pressure foam injection molding with mold-opening, Eur. Polym. J. 103 (2018) 68-79. https://doi.org/10.1016/j.eurpolymj.2018.04.002

[21] J.S. Colton, N.P. Suh, THE NUCLEATION OF MICROCELLULAR THERMOPLASTIC FOAM WITH ADDITIVES .1. THEORETICAL CONSIDERATIONS, Polym. Eng. Sci. 27(7) (1987) 485-492. https://doi.org/10.1002/pen.760270702

[22] J.S. Colton, N.P. Suh, THE NUCLEATION OF MICROCELLULAR THERMOPLASTIC FOAM WITH ADDITIVES .2. EXPERIMENTAL RESULTS AND DISCUSSION, Polym. Eng. Sci. 27(7) (1987) 493-499. https://doi.org/10.1002/pen.760270703

[23] L. Wang, Y. Hikima, S. Ishihara, M. Ohshima, Fabrication of lightweight microcellular foams in injection-molded polypropylene using the synergy of long-chain branches and crystal nucleating agents, Polymer 128 (2017) 119-127. https://doi.org/10.1016/j.polymer.2017.09.025

[24] L. Xia, H. Wu, S. Guo, X. Sun, W. Liang, Enhanced sound insulation and mechanical properties of LDPE/mica composites through multilayered distribution and orientation of the mica, Composites, Part A 81 (2016) 225-233. https://doi.org/10.1016/j.compositesa.2015.11.023

[25] X. Wang, F. You, F.S. Zhang, J. Li, S. Guo, Experimental and theoretic studies on sound transmission loss of laminated mica-filled poly(vinyl chloride) composites, J. Appl. Polym. Sci. 122(2) (2011) 1427-1433. https://doi.org/10.1002/app.34047

[26] C.F. Ng, C.K. Hui, Low frequency sound insulation using stiffness control with honeycomb panels, Appl. Acoust. 69(4) (2008) 293-301. https://doi.org/10.1016/j.apacoust.2006.12.001

[27] S. Chonan, Y. Kugo, Acoustic characteristics and the design of two-layered soundproof plates, J. Sound Vib. 129(3) (1989) 501-511. https://doi.org/10.1016/0022-460X(89)90438-0

[28] N.N. Najib, Z.M. Ariff, A.A. Bakar, C.S. Sipaut, Correlation between the acoustic and

dynamic mechanical properties of natural rubber foam: Effect of foaming temperature, Mater. Des. 32(2) (2011) 505-511. https://doi.org/10.1016/j.matdes.2010.08.030

[29] D. Zhou, Y. Xiong, H. Yuan, Q. Shen, G. Luo, W. Guo, Enhanced sound insulation properties of microporous PMMA foams by constructing novel multilayered and directional cell structure (MDCS), J. Appl. Polym. Sci. 137(35) (2020) 49020. https://doi.org/10.1002/app.49020

[30] X. Shi, J. Wu, X. Wang, X. Zhou, X. Xie, Z. Xue, Novel sound insulation materials based on epoxy/hollow silica nanotubes composites, Composites, Part B 131 (2017) 125-133. https://doi.org/10.1016/j.compositesb.2017.07.055

[31] T. Han, X. Wang, Y. Xiong, J. Li, S. Guo, G. Chen, Light-weight poly(vinyl chloride)-based soundproofing composites with foam/film alternating multilayered structure, Composites, Part A 78 (2015) 27-34. https://doi.org/10.1016/j.compositesa.2015.07.013

[32] R. Verdejo, R. Stämpfli, M. Alvarez-Lainez, S. Mourad, M.A. Rodriguez-Perez, P.A. Brühwiler, M. Shaffer, Enhanced acoustic damping in flexible polyurethane foams filled with carbon nanotubes, Compos. Sci. Technol. 69(10) (2009) 1564-1569. https://doi.org/10.1016/j.compscitech.2008.07.003

Chapter 8: Conclusions and future work

8.1. Conclusions

In this research, the effects of cell size on impact strength, electrical properties and sound insulation properties were comprehensively investigated. It was found that:

(a) Effect of cell structure on impact strength

Firstly, phase interface-enhanced PLA/PBAT blend foams, modified by a reactive compatibilizer through a simple reactive extrusion, were produced via a core-back FIM technique. By adding 1phr ADR, the impact strength of the foamed sample reached 49.1 kJ/m^2, approximately 9.3 and 6.4 times that of the unmodified PLA/PBAT blend and its foam, respectively. It proved that the interfacial adhesion and cell size both strongly affected the impact strength of injection-molded PLA/PBAT foams. For foams with high interfacial adhesion, small cell size (<12 μm) was more favorable for the stretching of cells and extension of the whitened region in comparison with big cell size (cell size > 60 μm), leading to the drastic toughening of PLA blends.

Subsequently, the relationship between cell size and impact strength of PLA/PBAT foams at a constant VF was studied. With the reduction of cell size, a significant brittle-tough transition occurred at a critical threshold. Furthermore, we found that enhancing the interfacial adhesion between PLA and PBAT effectively increased the critical cell size. Below the critical cell size, the

proximity of the cells facilitated a robust interaction of stress fields generated by adjacent cells, coupled with the beneficial role of rubber particles in hindering the progression of cell-induced crazes to cracks, thereby absorbing significant energy. When the cell size surpassed the critical value, however, the diminished interaction among cells allowed cell-induced crazes to develop directedly into cracks, resulting in reduced impact strength.

Finally, the combined effects of matrix crystallization and cell size of PLA/PBAT foams on the toughness were studied. The PLA crystallinity was tailored by CO_2 treatment and cell size was well controlled by changing processing parameters. A brittle-tough transition occurred only when the PLA crystallinity matched the cell size. Increasing the PLA crystallinity would lead to a decrease in critical cell size. When the cell size surpassed the critical value, PLA/PBAT foams were all fractured through crazing. When cell size was below the critical valve, the dominant mechanism for foams with lowly crystalline PLA was multiple crazing, while that for foams with highly crystalline PLA was shear yielding, which was favorable to energy dissipation.

Therefore, it can be concluded that the impact toughness of PLA/PBAT foams can be enhanced by reducing cell size, improving interfacial adhesion and increasing the PLA crystallinity.

(b) Effect of cell structure on electrical properties

Except for the commonly reported strategies, including increasing the content of conductive fillers and adjusting the VF of CPC foams, we proposed that

enlarging cell size was also an effective method of improving EC and EMI shielding properties. PP/CNS nanocomposite foams with different cell sizes were produced using core-back foaming injection molding (FIM) technique. As the cell size increased from 71 to 317 μm, the EC increased from 1.43×10^{-3} to 5.07×10^{-3} S/cm, due to the slightly aligned CNS and the shorter real conductive paths of foams with bigger cell size (thicker cell wall). Thus, the EMI SE improved from 48.5 to 59.2 dB and the highest specific SE reached 329 dB·cm^2/g.

(c) Effect of cell structure on sound insulation properties

PP/mica composite foams with different cell sizes were obtained using core-back FIM. The reduction in cell size could improve the STL of samples. With the decrease of cell size from 638 to 32 μm, the average STL of PP foam improved from 27.2 to 33.1 dB. The mechanism for the enhancement of sound insulation performance is speculated as: the scattering and the reflection of sound waves were much more violent inside the smaller cells, and it led to the vibration acceleration of sound waves inside small pores during the transmission process of sound waves. In addition, adding mica into the PP matrix could further enhance the STL since the interfaces between mica and PP can refract sound waves, and thus prolong the sound transmission path.

8.2. Future work

For the future of this research work, the following is recommended.

(a) For polymer/elastomer blend foams, the effects of crystallinity of matrix and

interfacial adhesion on cell size-impact strength relationship have been discussed. The correlations between the properties of the dispersed phase (elastomer content, size, and size distribution) and cell size-impact strength relationship could be investigated further.

(b) The mechanisms of EC enhancement induced by cell size are suggested to be studied further, especially for CPC foams under different VFs. It is believed that by optimizing the cell morphology, the electrical properties of CPC foams could be improved significantly.

(c) With the knowledge obtained in this work about the effects of cell size and VF on sound insulation properties, it is possible to conduct further research and development to improve the sound insulation properties of polymer foams. For example, a bimodal cell structure, in which big cells can increase the VF and small cells can enhance the sound energy dissipation, can be applied to prepare lightweight polymer foams with enhanced sound insulation performance.